Theoretical and Experimental Analysis of Strain in a Tire Under Static Loading and Steady-State Free-Rolling Conditions

by

Vijaykumar Krithivasan

A dissertation submitted to the Graduate Faculty of
Auburn University
in partial fulfillment of the
requirements for the Degree of
Doctor of Philosophy

Auburn, Alabama
August 6, 2011

Keywords: FEM, Strain, Slip, Tires, Lateral Force, Longitudinal Force

Approved by

Robert L. Jackson, Chair, Associate Professor of Mechanical Engineering
Song-Yul Choe, Associate Professor of Mechanical Engineering
Hareesh V. Tippur, Professor of Mechanical Engineering
Dan B. Marghitu, Professor of Mechanical Engineering

Abstract

This main objective of this work is to predict the operating conditions or the state of a tire based on a wireless sensor suit. First a three dimensional finite element model of a standard reference test tire (SRTT) was developed to better understand the tire deformation under separate cases of static loading, steady state free-rolling and steady-state rolling conditions. A parametric study of normal loading, slip angle and slip ratio was carried out to capture the influence of these parameters. The numerical analysis techniques such as the Fouier analysis, Weibull curve fitting and slope curve method were explored to relate the tire strains to the various loads on the tire. The advantages and disadvantages of the various methods, mentioned above, for strain analysis is also presented.

A wireless sensor suite comprising of analog devices (strain, pressure and temperature sensors) was developed to capture the tire deformation under loading conditions similar to those used in the finite element model. This sensor suite formed the basis for experimentally verifying the trends captured by the finite element model on a custom built tire test stand with capabilities of mimicking real-time conditions (under static loading scenario) of a tire in contact with road and steady state conditions on a FlatTrac test bed. Using the results from the experiments and the finite element model an empirical model was developed which demonstrates how the strains measured on the inner surface of the tire could be used to quantify desired parameters such as slip angle, lateral force, slip ratio, longitudinal force and normal load. This resulting empirical equations relate measured strains to the normal load, slip angle, slip ratio, lateral force and longitudinal force.

Acknowledgments

This research work that I commenced four years ago would not have culminated into this dissertation without the help and constant support of many people. I am grateful to my advisors, Professor Robert L. Jackson and Professor Song-yul Choe, for providing me with this wonderful and exciting opportunity. Their deep love and enthusiasm for research and the passion for life is very infectious. Their efforts towards ensuring the progress and well-being of their students is truly remarkable and I am a very happy beneficiary of that. I am immensely proud to have been associated with them and their Smart Tire Research Group. I would like to thank Hyundai Motor Company, South Korea, for providing support to my graduate school research.

I would like to express my gratitude to Professor Hareesh V. Tippur, Professor Dan B. Marghitu, and Professor Asheber Abebe, for serving as members of my Defense Examination Committee. I would like to thank David Howland of General Motors for the help with my research work in all possible manner. I am grateful to Dr. Marion Pottinger for sharing valuable inputs and insights in the field of tire research.

I would like to thank my colleagues in the Research Group: Dr. Jyoti Ajitsaria, Mr. Russell Green, Mr. Jeremy Dawkins, Mr. Santosh Angadi, Mr. Everett Wilson, for their significant contributions.

I am grateful to my friends Dr. Vivek Krishnan, Mr. Karthik Narayanan, Mr. Varun Rupela, Dr. Pradeep Prasad, Mr. Naren Pari, Dr. Anand Sankarraj, Dr. Shankar Balasubramanian, Mr. Raghu Viswananthan, Mr. Kashyap Yellai, Mr. John Polchow and Mr. Jake Fredrick for their encouragement.

The unwavering support and encouragement from my loving family throughout my graduate study made this day possible. The sacrifices that my parents Krithivasan and

Sathyabama have made in raising their kids cannot be described in words. I am what I am today because of them. My brother Dr. Ramkumar Krithivasan has been a pillar of support in all my endeavors. I am forever indebted to my family.

Table of Contents

List of Figures

List of Tables

Nomenclature

α_{slip}	slip angle [deg]
$\bar{I}_1$	first invariant of Cauchy-Green deformation tensor
$\bar{I}_2$	second invariant of Cauchy-Green deformation tensor
$\bar{I}_3$	determinant value of deformation gradient matrix
β	weibull shape parameter
$\delta_{\alpha_{slip}}$	slip angle strain indicator [mm/mm]
$\epsilon_{\theta\theta}$	circumferential strain [mm/mm]
ϵ_{ave_1}	average value of sensor 1 strains in the contact patch [mm/mm]
ϵ_{ave_2}	average value of sensor 2 strains in the contact patch [mm/mm]
ϵ_{ave_3}	average value of sensor 3 strains in the contact patch [mm/mm]
ϵ_{ave_4}	average value of sensor 4 strains in the contact patch [mm/mm]
ϵ_{fric}	strain due to frictional load [mm/mm]
ϵ_{norm}	strain due to normal load [mm/mm]
κ	bulk modulus [MPa]
λ	weibull scale parameter
μ	shear modulus [MPa]
ω	angular velocity [rad/s]

Ω_{SR} slip ratio or longitudinal slip expressed as %

σ_k relaxation length [mm]

a Weibull scale parameter

$A_{contact}$ contact area $[mm^2]$

A_{exp} load dependent constant fit to the experimental data

A_{fem} load dependent constant fit to FEM data

B Magic formula: stiffness factor

b Weibull shape parameter

B_{exp} load dependent constant fit to the experimental data

B_{fem} load dependent constant fit to FEM data

C Magic formula: shape factor

c Weibull height parameter

C_α load dependent constant fit to FEM data

c_Ω load dependent constant fit to FEM data

C_{pq} material constants related to distortional response

D Magic formula: peak value

D_1 material constant related to volumetric response

D_α load dependent constant fit to FEM data

d_Ω load dependent constant fit to FEM data

E Magic formula: curvature factor

E_α load dependent constant fit to FEM data

e_Ω load dependent constant fit to FEM data

E_{ext} bridge excitation voltage [V]

F_α load dependent constant fit to the experimental data

f_{fem} FEM constant

f_s sampling frequency [Hz]

f_x longitudinal force [N]

f_y lateral force [N]

f_z normal load on the tire [lbs]

G_α load dependent constant fit to the experimental data

G_f gage factor

H_α load dependent constant fit to the experimental data

H_s tire section height [mm]

p_{inf} tire inflation pressure [MPa]

S_H Magic formula: horizontal shift

S_V Magic formula: vertical shift

t time [sec]

t_d contact duration [sec]

v vehicle velocity $[mm/s]$

v_0 vehicle velocity [mm/s]

V_{out} output voltage [V]

V_o axle speed [mm/s]

v_x vehicle velocity in x-direction [mm/s]

v_y vehicle velocity in y-direction [mm/s]

W strain energy density function

W_s tire section width [mm]

w_{tread} tread width [mm]

X Magic formula: input variable

Y Magic formula: output variable

Chapter 1

Introduction

1.1 Motivation

Structural Health Monitoring (SHM) of pneumatic tires has evolved into an important area of research in the tire industry. The main focus of this research has shifted from simple pressure and temperature monitoring to wirelessly monitoring the tire deformation using strain sensing principles. The Bridgestone/Firestone tire recall of 2000 in the US resulted in the TREAD[1] act. The Transportation Recall Enhancement, Accountability and Documentation (TREAD)[1] act which requires the installation of tire pressure monitoring systems(TPMS)[2]–[6]. This has lead various tire manufacturers investigate strain characterization of the tire. Apart from the commercially available TPMS[7]–[16], tire manufacturers are exploring ways in which tire strains can be measured and used to enhance overall vehicle stability and drivability. In short, tire and car manufactures are working on developing an intelligent tire sensor suite that will monitor the state of a tire in real-time.

What is an intelligent tire? How different would it be from the current tire? A modern pneumatic tire does not sense contact conditions and does not provide any data for controlling vehicle behavior. In contrast, an intelligent tire will contain embedded sensors which will transmit data wirelessly to the vehicle system. The benefits of such a sensing system include, but are not limited to, monitoring road friction, tire forces, tire pressure, tread wear etc. during normal tire use.

Researchers in the past have developed a wide array of models to extract data from a tire. Although there are separate models to obtain the slip, normal load, etc., there does not seem to be a single sensor suite and model capable of predicting the normal load, lateral force, longitudinal force and wear.

1.2 Types of Tire Models

Ring, string and elastic (also viscoelastic) foundation models were widely used in tire stress and deformation analysis, before computational mechanics became mature enough to be used in the tire industry. These models were developed extensively by Clark et al.[17]. The equivalent tire parameters required by these models are obtained from full-scale tire experiments[18]. Given their non complex nature, these models work fairly well for predicting and understanding certain tire characteristics such as tire vibration, cornering force, braking and traction. Despite providing an insight into tire behavior, these models had drawbacks that can't be overlooked. One of the biggest drawbacks of this type of model[19] is the need to run extensive experiments to estimate tire parameters. The estimated parameters only truly apply to the tire for which they were obtained. In the string model[17] the tread is assumed to be a prestressed membrane. Bending is not considered. The ring model on the other hand includes bending and the sidewalls are modeled as an elastic foundation that simply supports the tread. Some more elaborate models where developed where shear deformations were considered. The character of these models limits their use in the current tire research.

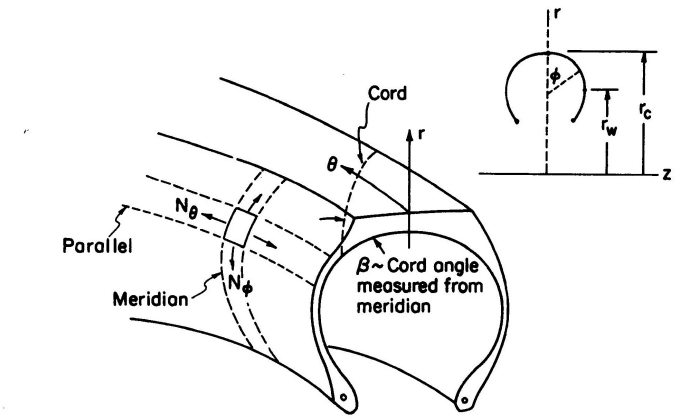

Figure 1.1: Geometry based cord model[17].

With the advent of fast computing more complex models were developed to characterize tire behavior. These models can be broadly categorized as cord and rubber models, anisotropic ply models and laminate models. This broad classification is based on the degree of complexity that needs to be incorporated into an analysis to obtain a solution.In the cord and rubber model(see Fig. 1.1) each and every cord is represented by exact dimensions and the relative positions with respect to the neighboring rubbers. The rubber in this model is assumed to be isotropic and incompressible. Other components such as the bead wires and the cords are considered as filaments with unique material properties in their normal and in-plane directions.

Anisotropic ply models are used to grant simplicity. As opposed to the cord model, the tire structure is represented by plies. The biggest advantage of such a representation is it allows computation of interply strain, something that is not quite possible in the cord network model. An added advantage of this model is that is allows non-linear strain distribution over the tire thickness. The rubber compound is treated as incompressible elements just as in the cord model. But this model can be used with finite element modeling, as it allows modeling beads as plies and layups, where the geometrical features and material properties can be specified.

The last set of models are the laminate models (nowadays referred to as finite element models), which can be viewed as ensembles of shell or solid elements or a combination of the two. In this type of model plies are grouped together into a laminate and then analysis is carried out on the entire structure. Mostly isotropic elements are used, but anisotropy and orthotropy can also be modeled with the necessary computational assistance.

Finite element modeling (FEM) (once known as laminate modeling) has been extensively employed in the tire research. Continental AG has pioneered FEM[19]of tires since 1970. Tire FEM in its first stages(a two dimensional model)[20]–[22] was used for simulation of tire inflation and tire shape change under high rotational speeds. Since then researchers have used FEM for studying tire footprint, inter-ply shear for tire durability and tire vibrations, all

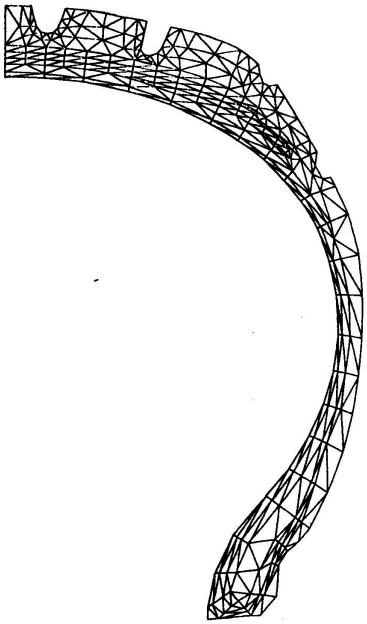

Figure 1.2: Two dimensional axisymmetric model for inflation analysis[17].

based on a three dimensional static model. In the 90's tire FEM's were developed for analysis of tire foot print under rolling conditions[23]–[27]. FEM's were also developed for tire force and moment predictions[28]–[38], which were later combined with theoretical models for the development of analytical vehicle models. In the recent years tire FEM's have been developed using a close to accurate material model, which considers viscoelasticty, hyperelasticity, etc. These models have accurate geometry with well defined tread patterns and also consider the tire model with the metal rim and pressurized air. These models also have the capability to model accurate loading conditions, which are based on a tire service matrix that can be used inside the tire simulation[39]–[43].

In addition to FEM's there are models such as the tire brush model[44] and semi-empirical tire model(also known as the Pacejka model[45]) are in place for modeling tire behavior under various loading conditions. Pure slip and combined slip conditions can also be modeled by prescribing the necessary input conditions. The Pacejka model is a dynamic

model comprised of equations for lateral force and longitudinal force. These equations are obtained by fitting curves to experimental data for a specific tire. Although it has come to be common practice to use these models in tire analysis, the inherent problem is tire specificity. This implies one global equation cannot be used as the equations pertain to a specific tire whose design parameters are taken into consideration. The most famous among the semi-empirical models is the Pacejka[45] model, from which the *magic formula* is derived. The general form of this formula for known values of vertical loads and camber angles is given by,

$$y = D \sin \left[C \arctan \left\{ Bx - E \left(Bx - \arctan Bx \right) \right\} \right] \tag{1.1}$$

with

$$Y(X) = y(x) + S_V \tag{1.2}$$

$$x = X + S_H \tag{1.3}$$

where Y: output variable F_x, F_y or M_z , X: input variable $\tan \alpha$ or κ, B is the stiffness factor, C is the shape factor, D is the peak value, E is the curvature factor, S_H is the horizontal shift, and S_V is the vertical shift.

The *Magic Formula* $y(x)$ will produce an asymptotic curve when it passes through the origin, typically after attaining a maximum peak value. If the necessary coefficients B, C, D, and E are known and input into Eq. 1.1, a non-symmetric curve about the abscissa is obtained with respect to the origin. The parameters S_H, and S_V are introduced into Eq. 1.1, to account for the shifts in the curve that are an inherent tire characteristic depending on the tire loading condition. An example of such a curve which incorporates all the parameters of the *Magic Formula*, is shown in Fig. 1.3. The *Magic Formula* has been shown to provide tire characteristics, which closely follow data obtained through experiments.

The parameters in the *Magic Formula* are inferred graphically from Fig. 1.3. The parameter D is the most obvious as it simply corresponds to the peak value of the curve, the

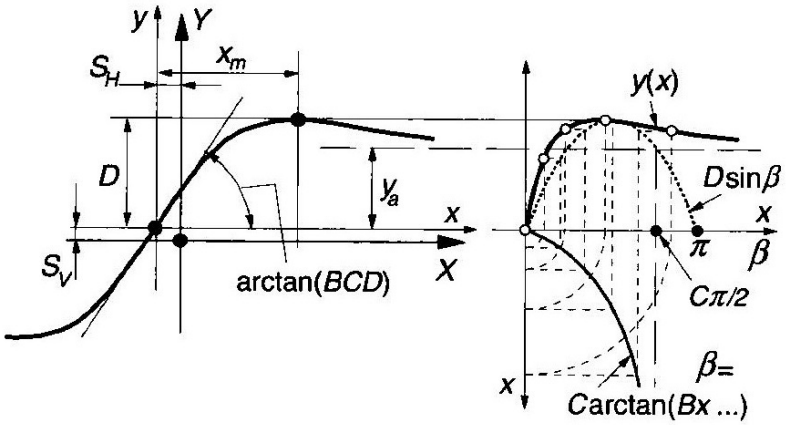

Figure 1.3: Graphical representation of the magic formula[45].

product BCD is claimed to be the value of the slope of the curve at the origin. The shape factor of the curve C, controls the range of the sine function that will appear in Eq. 1.1. Knowing the peak and the horizontal asymptote, C is computed as follows,

$$C = 1 \pm \left(1 - \frac{2}{\pi} \arcsin \frac{y_a}{D}\right) \tag{1.4}$$

The parameters B and C are necessary in computing the parameter E. This allows one to estimate the occurrence of the peak at say x_m and then E is estimated as,

$$E = \frac{Bx_m - \tan\{\pi/(2C)\}}{Bx_m - \arctan\{Bx_m\}} \tag{1.5}$$

Transient tire models are one option for estimating the relaxation length of a tire under lateral and longitudinal slip. The relaxation length (σ_k) of a tire is defined as the ratio of the lateral stiffness to the cornering stiffness of the tire, assuming an elliptical contact patch. The relaxation length is given by,

$$\sigma_k = \frac{1}{(\sigma + a)} \tag{1.6}$$

The transient models can be divided into two categories: 1)Linear model (see Fig. 1.4) and 2) Fully Non-linear model (see Fig. 1.5). In the linear model the slip characteristics are restricted to the linear portion of the lateral force versus slip angle curve.

In these models the contact patch is treated as a single point that is simply suspended from the wheel rim by springs in the lateral and the longitudinal directions. The springs are assumed to represent the tire carcass. With the introduction of tire movement, the contact patch (point) can have deflections in either the lateral or the longitudinal direction. Based on the relative motion introduced, lateral force, longitudinal force and the self aligning torque value is estimated. The forces and moments are estimated by introducing lateral slip and longitudinal slip parameters. These parameters can then be used in *Magic Formula* as well to estimate transient variation from the steady state condition that may exist in the contact patch.

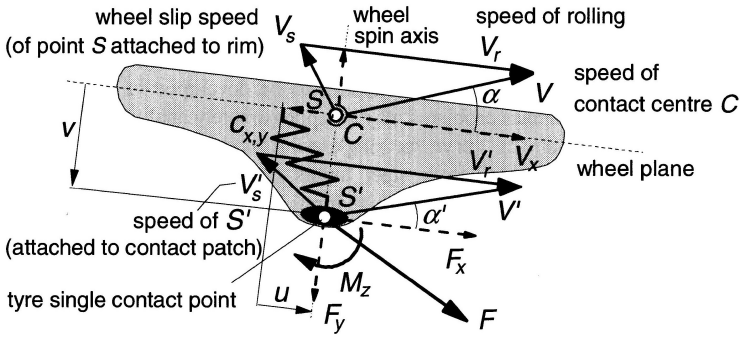

Figure 1.4: Linear model of a single contact point tire model[45].

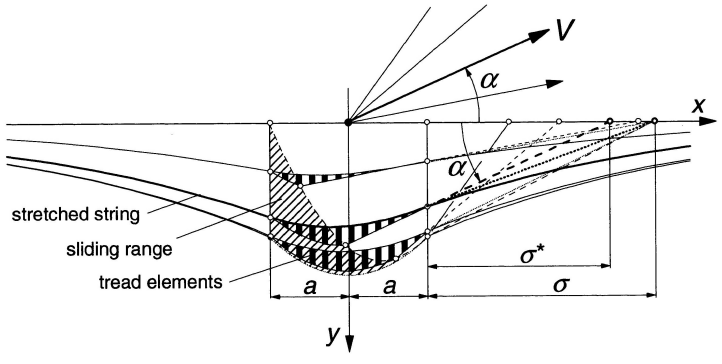

Figure 1.5: Fully non-linear string tire model[45].

1.3 Types of Tire Sensors

The current tire sensor technology can be broadly classified into two categories: I)sensors embedded in the tire(direct method also noted in Tab. **??**) and II)sensors mounted on the wheel(indirect method).

Table 1.1: Tire embedded sensors (Type I)

Capacitance	**Magnetic field**	**Acoustic wave**	**Polymer**
Sergio (2003)	Side wall torsion (1999)	Surface acoustic wave (1998)	PVDF (2008)
Matuzaki (2007)	Darmstadt sensor (2000)	Ultrasonic sensor (1998)	MetalRubber (2008)

The most commonly used TPMS employs a indirect measurement method, where a wheel-speed based sensor and the anti-lock braking systems (ABS) is used for pressure measurement. Persson et al.[46] proposed an indirect TPMS based on wheel radius and vibration analysis instead of a pressure sensor. A wheel speed sensor based TPMS was developed by Kojima et al.[47]. In their work the main focus is on estimating the tire stiffness based on the observed difference between the torsional tire stiffness and the tire pressure. Since, the changes in the road conditions affect the measured pressure indirectly, the accuracy of an indirect measurement based system is questionable.

In recent years, direct measurement methods have been developed for TPMS. These come either as clamp-on rim sensors or valve stem attached sensors for measurering pressure. The clamp-on type sensor developed by SmartTire System Inc. is simply fastened to the inner side of the wheel with the help of a clamp. On the other hand the valve-attached sensor casing is fixed to the valve stem. An innovative tire pressure sensor was developed by Arshak et al.[48]. In that work, a thick-film capacitor which has an oxide dielectric layer is used for measuring pressure based on capacitance change.

The operating time or the age of a direct measurement based sensor is an issue because power is supplied through a battery. In order to overcome this issue, battery-less TPMS's have been proposed[49]–[54]. In a battery-less system, energy is harvested from the vibrating

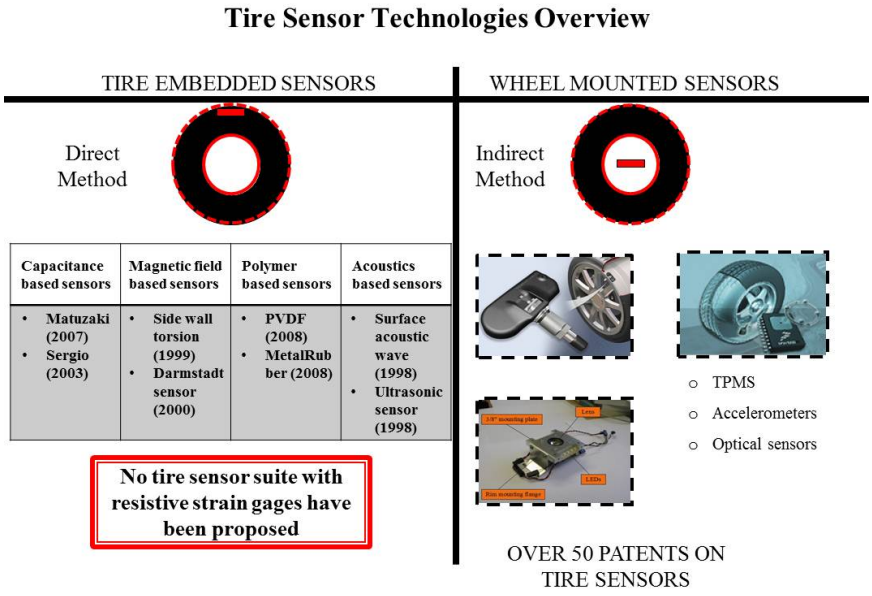

Figure 1.6: Types of tire sensors.

tire under operation. Some have used piezoelectric reeds in a tire to generate electricity. While others employ a transponder principle, where the necessary energy is obtained from a radio signal[55]. The electronic and mechanical robustness of a battery-less TPMS is still in the research phase. It is to be noted that insufficient energy could lead to shortened radio signal range.

The most extensive intelligent tire project ever pursued was the APOLLO tire project in the European Union. This was setup for the sole purpose of developing an advanced tire sensor system which can monitor tire deformations [56], temperature[57], etc. in addition to tire pressure, for occupant safety[57]. These mechatronic tires are commonly known as "intelligent tires". The strain monitoring in a tire enables one to predict the contact conditions at the tire-road interface. These predictions can be employed in advanced vehicle safety systems such as traction control units, vehicle stability assist (VSA), anti-lock braking system (ABS), etc.

For example, an intelligent tire which employs the indirect method, the road friction is predicted based on the estimated tire force from the difference in velocities of the driven and non-driven wheels[58]. Prediction of friction has been shown to improve[59, 60] the efficiency of the ABS, by reducing the system response time. Bevly et al. [61] have employed GPS to estimate wheel-slip, yaw and tire sideslip angle. Control systems based on fuzzy logic[62]–[64] which use data from conventional measurements such as velocity, angular speed and vertical load on the tire have been shown to correlate to road conditions. Accelerometers mounted on the tire axle have been used to predict the tire forces. Although many working sensors are in place, the degree of accuracy based on indirect measurements is questionable.

Figure 1.7: Continental's[56] side wall torsion sensor. (1) Magnetic field sensors. (2) Tire with two magnetized strips on the side wall

In contrast, an intelligent tire which employs the direct method, we can expect to make more precise measurements of tire operating conditions. The sensors used in the direct estimation[56] method are either embedded inside the tire or use the tire itself as a sensor to make precise measurements. The sensing concepts that have been explored are the change in capacitance, the change in the magnetic field or the acoustics of the tire.

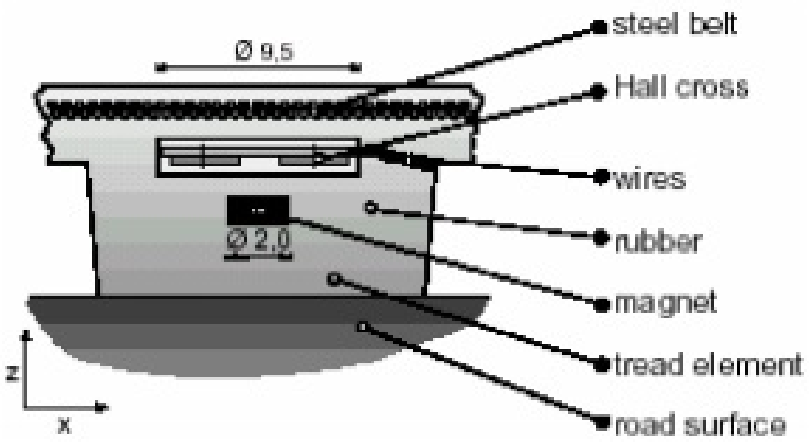

Figure 1.8: Darmstadt tire sensor[56]: Magnet and Hall sensor.

Matsuzaki et al.[65] use a capacitance based method (see Figs. 1.9 and 1.10) to estimate deformations in a tire. In principle the tire deformation causes a temporary change in the spacing of the steel wires inside the tread or the carcass causing a change in the measured impedance or capacitance which can then be related to the desired output quantities. A flexible capacitance change sensor is also proposed, which is of lower stiffness than a typical strain gage, and is analyzed under only static loading condition (see Fig. 1.11). This leaves room for the study of inexpensive and reliable resistive strain gages for further exploration. The array of sensors which are basically magnetic material based sensors, are either embedded in the tire side wall (see Fig. 1.7) or the tread (see Fig. 1.8). In the case of side wall embedded sensors, the magnetic field of the individual poles(North and South) are measured. Whereas, the sensing method for material embedded in the tread works on the Hall-effect, where the movement is monitored by a Hall-effect based sensor[56].

In addition, polymer based sensors have also found a place in characterizing the tire behavior. Yi et al.[68] propose a polyvinylidene fluoride (PVDF) (see Fig. 1.12) based micro-sensor embedded on the tire sidewall to measure the tread deformation. The PVDF sensor sits on the base of a flexible polyamide substrates and ultra-flexible epoxy resin. This epoxy makes the sensor low in stiffness and high in elongation as a whole structure.

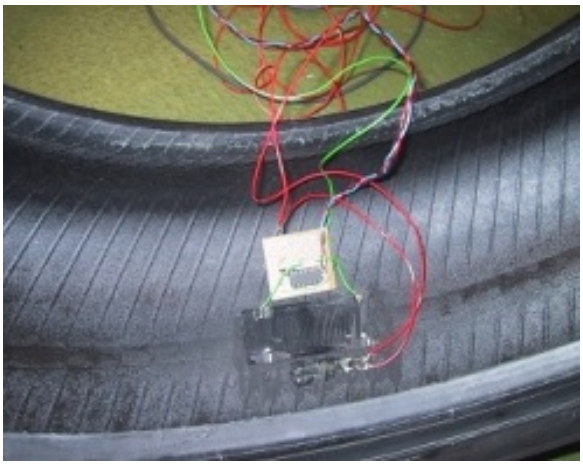

Figure 1.9: Oscillating circuit based wireless strain monitoring[66].

Figure 1.10: Capacitance change based wireless strain monitoring[66].

Gondal et al.[69] use a sensor called MetalRubber (see Fig. 1.13). The MetalRubber sensor has properties that resemble metal (for electrical conductivity) and rubber (for mechanical flexibility). This sensor works very much like a strain gage, where a change in sensor output voltage can be related to the strains.

A commonly used acoustics based sensor is a surface acoustic wave (SAW) sensor[70]–[75]. A SAW sensor (see Fig. 1.14) uses metallic structures such as interdigital transducers(IDT) arranged on the surface of a piezoelectric substrate. This then facilitates the

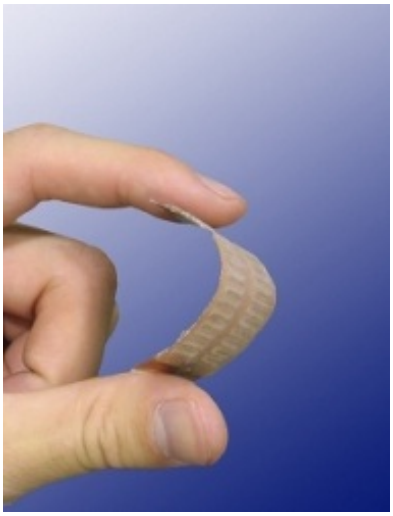

Figure 1.11: Flexible capacitance change based wireless strain monitoring[67].

propagation of the SAW over the substrate's surface. When used in conjunction with a second set of IDT's, the SAW (which is a mechanical signal) can then be converted back into an electric signal.

Based on the review of the literature on the currently available sensor technologies for characterizing tire behavior, no resistive strain gage based sensor suites have been proposed which will be the focus of the current work. A technology road map of the sensor technology is shown in Fig. 1.15. An array of sensor systems have been proposed in the past. The stark difference in making a passive and active smart tire lies in the instrumentation of the tire itself. Strain measurements form the basis for a passive smart tire and using more advanced sensor systems with the focus on non contact methods, transient conditions can be predicted.

1.4 Intelligent Tires in the Future

The technology has improved since the first generation tire monitoring systems (Fig. 1.15). This generation of tire monitoring systems had a pressure sensor. Termed Tire Pressure Monitoring System(TPMS) and was a unique solution for monitoring tire in real time. This TPMS although did not provide the actual pressure instead had a warning signal if the tire

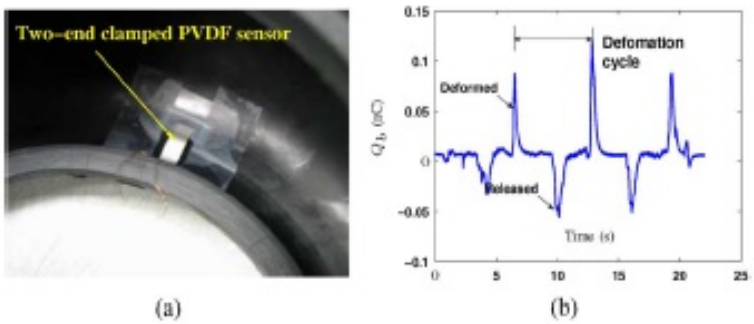

Figure 1.12: PVDF-based tire tread deformation sensor[68].(a)Sensor on the side wall. (b) Output for a periodically applied vertical load

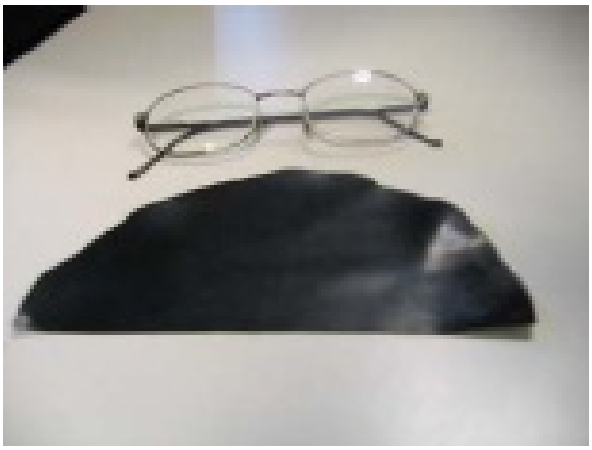

Figure 1.13: Rubber sensor[69] (also called MetalRubber) by NanoSonic Inc..

was either under inflated or over inflated. The packaging was a multi module package with an average lifespan of 15 years. The power source is a battery.

The second generation of tire monitoring systems has improved accuracy and a system level package module. This led to placement issues which were addressed by two methods. The first was a valve stem type of arrangement where the pressure sensor was mounted on to the tire air inlet valve and the pressure transducer had wireless communication enabled. In the second arrangement the pressure sensor was placed on wheel/hub with a belt type fastening. This arrangement has a range of 0-70 psi. The current TPMS system is a quad flat pack type of package module.

Figure 1.14: Seimens's[56] SAW sensor with energy generating piezoelectric crystals.

The improvement over the previous array of tire monitoring systems is the shift to employing low power sensor suites. Wireless communication was integrated with the onboard sensors thus making this a system on a chip. Although this technology is far better than the previous one in place, it has its own shortfalls. In future sensor suites should not be limited by the measurement capability. These sensor suites need to characterize tire in real time. Major parameters that define tire behavior under various conditions are camber, slip, tread wear, tire pressure and temperature. These sensors may also be extended to predict road conditions. Current research in this area is led by Pirelli, with a tire integrating bi-axial accelerometers along with a TPMS.

1.5 Objectives

The purpose of this research is to investigate the feasibility of a resistive strain gage based sensor suite for tire. Based on the literature concerning development of intelligent tire sensors, the objectives of this research are:

1. Development of a tire deformation model for static and steady state finite element analysis.

2. Development of a direct strain based measurement system with wireless data transfer capability.

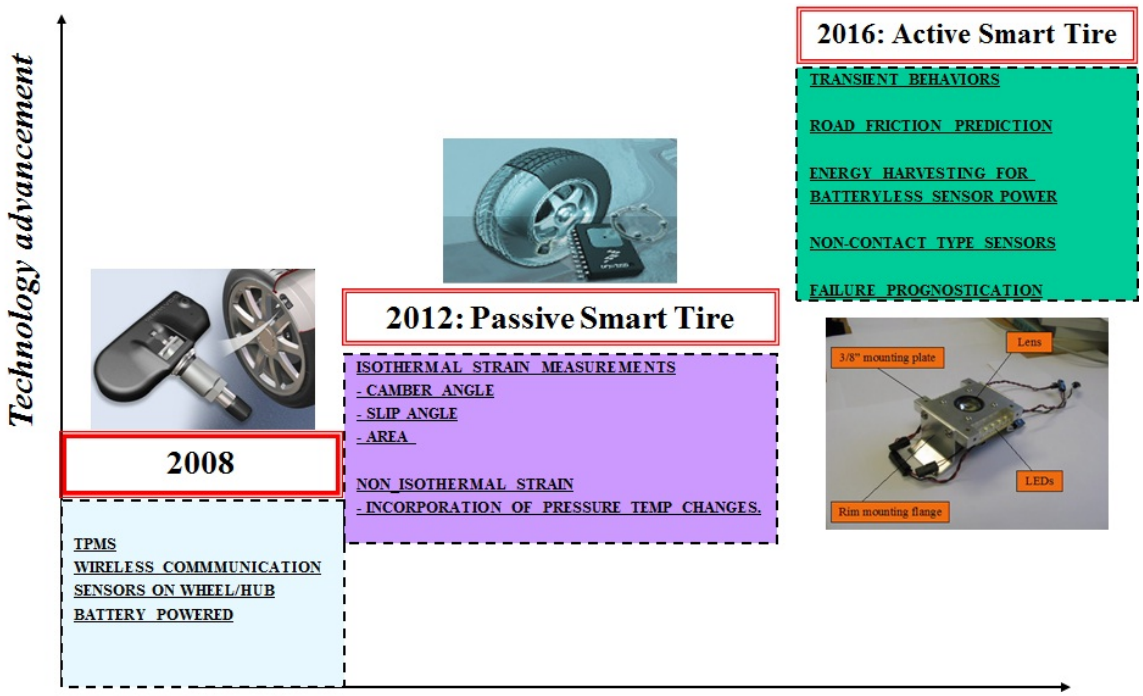

Figure 1.15: Sensor technology road map.

3. Demonstrate the use of measured strain data in predicting the operating conditions on the tire.

1.6 Dissertation Organization

This dissertation proposes a theoretical and experimental analysis of strain in a tire under various operating conditions. A wireless strain monitoring sensor suite based on resistance changes is proposed. The primary advantage of this sensor suite is the simplicity of integrating sensors with a tire. The theoretical aspect of this work focuses on developing a FEM for tire simulation. The dissertation is divided into ten chapters the first being this introductory chapter.

Chapter 2 presents the finite element tire deformation model. The tire cross-section with the various material layers are discussed in this chapter. The underlying assumptions, the material model, the types of elements used and how a 3D model is developed is also

discussed. This 3D model is then verified for accuracy based on comparison to experimental data available in the literature. The finite element model of the tire is fully developed and the necessary boundary conditions are enforced. The discussion then focuses on reducing the computational time by performing a mesh convergence.

Chapter 3 presents the results and discussion based on the finite element analysis of the tire under static loading conditions. The strain profile under the static loading condition is investigated. The circumferential strains from FEM are plotted versus the radial node position and an approximate contact region is estimated from the results.

Chapter 4 presents the experimental setup and the sensor suite used for experimental validation of the finite element model. The custom built test stand used for running the experiments is also discussed.

Chapter 5 presents the results and discussion based on experimental analysis of the tire under static loading conditions. A 235/70 R16 tire is considered in the experiments for the sole purpose of capturing the strain profile and in a way validating the finite element model.

Chapter 6 presents the finite element analysis (FEA) for the steady-state free-rolling condition. Simulations for braking and traction condition are presented. Free-rolling angular velocity is estimated. Based on the free-rolling angular velocity, parametric cases of slip angle are considered. An analysis is setup to capture the strain profile under the steady-state free-rolling condition.

Chapter 7 presents the strain analysis from the FEM results by various numerical techniques, namely, Fourier Analysis, Weibull Curve Fitting, and Slope Curve Method. Based on these techniques, the slip angle is estimated. Equations that predict the normal load, slip angle and lateral force are also presented in this chapter.

Chapter 8 presents the experimental methods for measuring tire strain under the free-rolling condition. The testing conditions considered are the exactly the same as what were used in the FEM.

Chapter 9 presents an analysis of the experimentally measured strain using the various techniques (also mentioned in Chapter 7). The validity of each of the techniques is presented. A quantitative analysis of effectiveness of each of the numerical techniques is also presented.

Chapter 10 presents the FEA for the steady-state rolling condition. Simulations for the traction condition are presented. Parametric cases of the slip ratio are considered. An analysis is setup to capture the strain profile under the steady-state rolling condition.

Chapter 11 presents the strain analysis from the FEM results by the Slope Curve Method. Based on this the slip ratio is estimated. Equations that predict the slip ratio and longitudinal force are also presented in this chapter.

Chapter 12 concludes the dissertation with inferences from the research on the analysis of strains in a tire and relating them to tire conditions. A suggestion for future work and improvements for the current sensor technology is also presented.

Chapter 2

Static Loading Finite Element Tire Model

The modern tire geometry is a complex structure to model. The complexity arises from the various sections making up the composite structure of the tire. A typical tire section (shown in Fig. 2.1)has in all about sixteen sections composing of different materials. From this, it is clear that a close to accurate model is essential to analyze the tire deformation.

Figure 2.1: Typical components of a passenger car radial tire.

Following are the assumptions made in the current tire finite element model:

1. Simplified tire cross-section(only Tread, Side wall, Innerliner, Bead filler, Carcass, Steelbelt and Cord plies are modeled).

2. Combination of elastic and hyperelastic material models.

3. Modeled under isothermal and isobaric conditions.

4. Only static and steady state free-rolling conditions are analyzed.

5. FEM nodal outputs assumed to be same as sensor outputs from the experiments.

2.1 Tire Cross-Section

In the current work the cross-section (see Fig. 2.2) of a Standard Reference Test Tire (SRTT) is modeled. A digital profile of the tire is imported into SolidEdge for developing the 2D solid model. The surfacing option in SolidEdge is used to smooth out rough edges in the digital profile. This profile is then imported into ABAQUS(Ver.6.7.1) for developing the FEM by defining the sections associated with the SRTT. As mentioned in the assumptions before, this is a simplified tire cross-section and only important sections are modeled. These

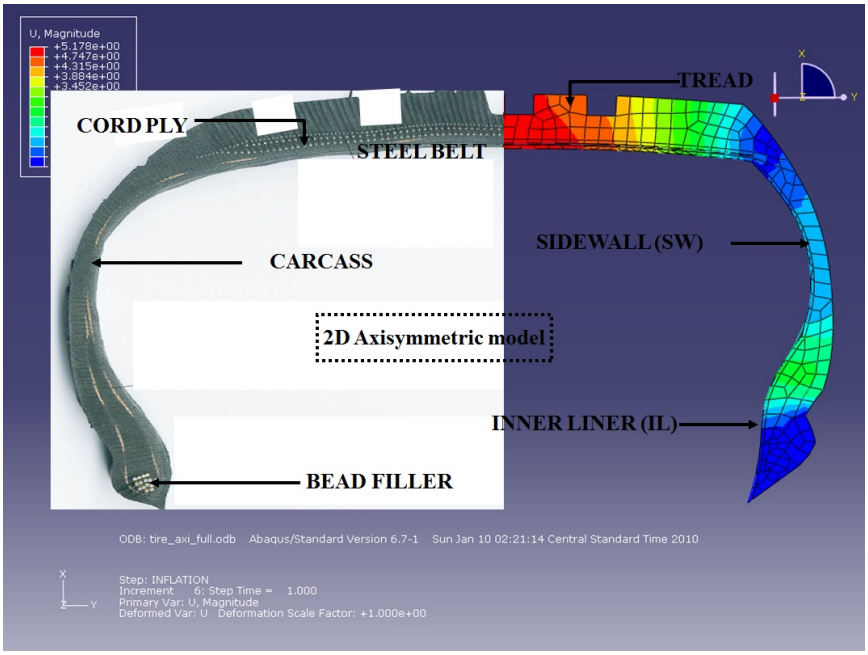

Figure 2.2: Tire cross-section.

sections can be divided into solid and surface type sections. The tread, sidewall, innerliner and bead filler form the solid sections. Whereas the cord ply, steelbelt and carcass which have elastic properties are modeled as surface sections with the rebar option. The rebar option in ABAQUS provides for a way to add to structural rigidity to the material model. The material properties of these sections are discussed in the following section.

2.2 Material Model

It has been shown in the past (see Fig. 2.3), based on tensile test data, that the stress-strain relationship of tire rubber compounds is non-linear but still elastic. The rubber compounds used in a SRTT exhibits hyperelastcity. A hyperelastic material is defined as a material, which derives the stress-strain relationships from a strain energy density function.

In the area of tire research it has become a common practise to employ Mooney[76]-Rivlin[77] for modeling tire rubber compounds. The strain energy density function for a Mooney-Rivlin type of material is

$$W = C_{01}\left(\bar{I}_1 - 3\right) + C_{10}\left(\bar{I}_2 - 3\right) + D_1\left(\bar{I}_3 - 1\right)^2 \tag{2.1}$$

where C_{01} and C_{10} are empirically determined material constants, D_1 is a material constant related to the volumetric response, and $\bar{I}_1$, $\bar{I}_2$, $\bar{I}_3$ are the first, second and third invariants of the strain tensor. The first invariant which is the dilation, and is also known as the trace of the strain tensor invariant, is given by,

$$\bar{I}_1 = \varepsilon_{11} + \varepsilon_{22} + \varepsilon_{33} \tag{2.2}$$

The second invariant which is magnitude of the strain tensor is given by,

$$\bar{I}_2 = \varepsilon_{11} \cdot \varepsilon_{22+}\varepsilon_{22} \cdot \varepsilon_{33} + \varepsilon_{11} \cdot \varepsilon_{33} - \varepsilon_{12}^2 - \varepsilon_{23}^2 - \varepsilon_{13}^2 \tag{2.3}$$

The third invariant is the determinant value of the strain tensor and is given by,

$$\bar{I}_3 = det(\epsilon) \tag{2.4}$$

For this constitutive material model to be consistent with linear elasticity in the region where small strains are most important, constraints are applied to the value of the empirical constants as,

$$\kappa = 2 \cdot D_1 \tag{2.5}$$

and

$$\mu = 2 \cdot (C_{01} + C_{10}) \tag{2.6}$$

where κ is the bulk modulus and μ is the shear modulus.

In Fig. 2.3 a stress-strain curve is shown for a rubber compound typically used in automobile tires. It can be seen that a linear Hooke's law based material model does not fit well to the tensile test data. The Mooney-Rivlin material model is a better fit to the data. A Neo-Hookian material model, which is also a material model sometimes used for tires, is a special case of the Mooney-Rivlin model, (it is obtained by setting the C_{01} constant to zero).

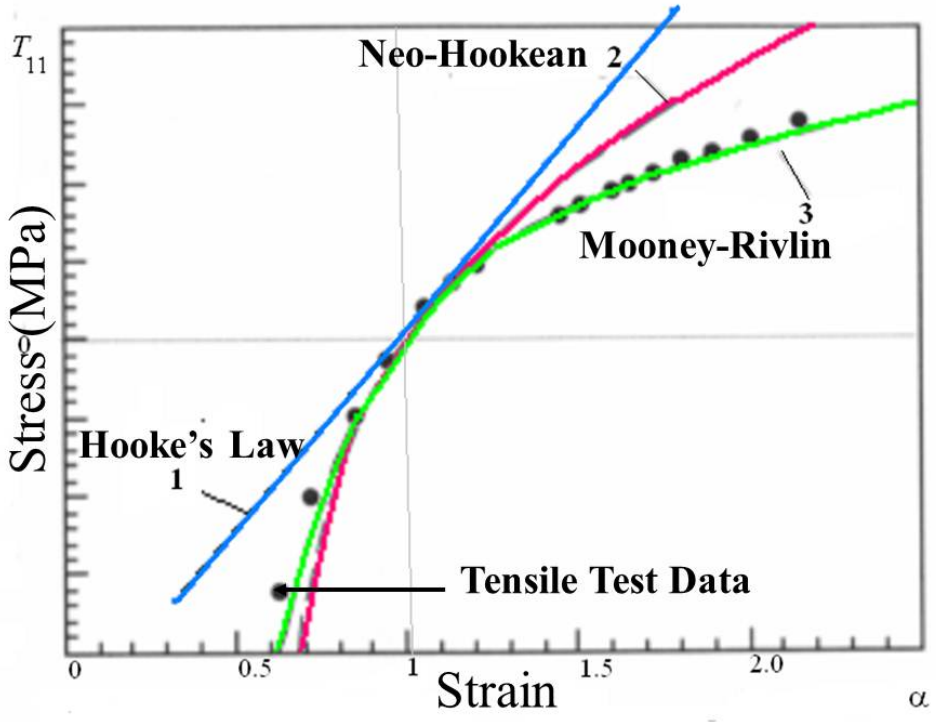

Figure 2.3: Constitutive material models[79].

The material properties of the tire sections modeled are tabulated in Tables 2.1 and 2.2. These material properties are available in the tire literature[30]. The Mooney-Rivlin constants used in the current work are that of a rubber compound commonly used in automobile tires.

Table 2.1: Tire section hyperelastic material properties[30].

Tire sections	Mooney-Rivlin constants (MPa)		
	C_{10}	C_{01}	D_1
Tread	0.8061	1.8050	0.0191
Sidewall	0.1718	0.8303	0.0498
Inner liner	0.1404	0.4270	0.0881
Bead filler	14.140	21.260	0.0014

The cord plies, steel belt and the carcass sections of the tire are the anisotropic section composites made up of mostly steel, rubber and fiber reinforcements. The primary composition of the tire carcass varies with each tire, but for the most part the carcass can be assumed to be made of rubber and organic fibers like nylon, polyester etc. The belt sections of the tire (some parts included in the carcass) also has rubber for the most part and steel wires in a meshed fashion are embedded in the rubber compound. The anisotropy nature of the steel wires and organic fibers is introduced due to the rebar orientation angle that is specified as an input option while defining the material model in ABAQUS. The steel orientations were set at 118^o while the cord ply orientations were set at 70^o. The coulomb friction between the tire and the road is modeled as frictionless for the static finite element model and is later changed t0 μ=0.85 for the steady state free-rolling finite element model.

Table 2.2: Tire section elastic material properties.

Tire sections	Area (mm^2)	Poisson's ratio	Young's Modulus (GPa)
Cord ply	0.28	0.25	3.97
Steel belt	0.30	0.33	200
Carcass	0.30	0.30	2.48

2.3 Three-Dimensional Tire Model

The three-dimensional tire model is obtained by revolving the two-dimensional cross section area about the tire axis of rotation. The symmetric model generation technique, which is a convenient technique available in ABAQUS[78], is utilized to generate the symmetric tire deformation model. The types of elements (see Fig. 2.4) used in the finite element model are as follows,

1. The solid sections are modeled as a combination of 8-node brick elements and 6-node triangular prism elements.

2. The embedded sections (carcass, steel belt and cord ply) are modeled using special elements in ABAQUS. One such special element available in ABAQUS is called the surface element. This is simply a 4-node membrane element with zero thickness. These surface elements also come with a rebar option, which can be specified to add structural rigidity to the model.

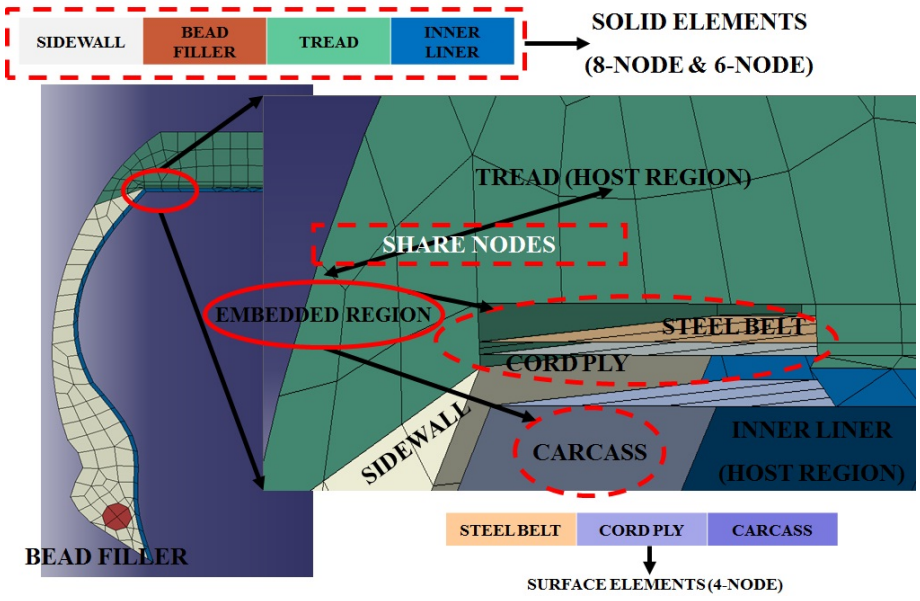

Figure 2.4: Element types used.

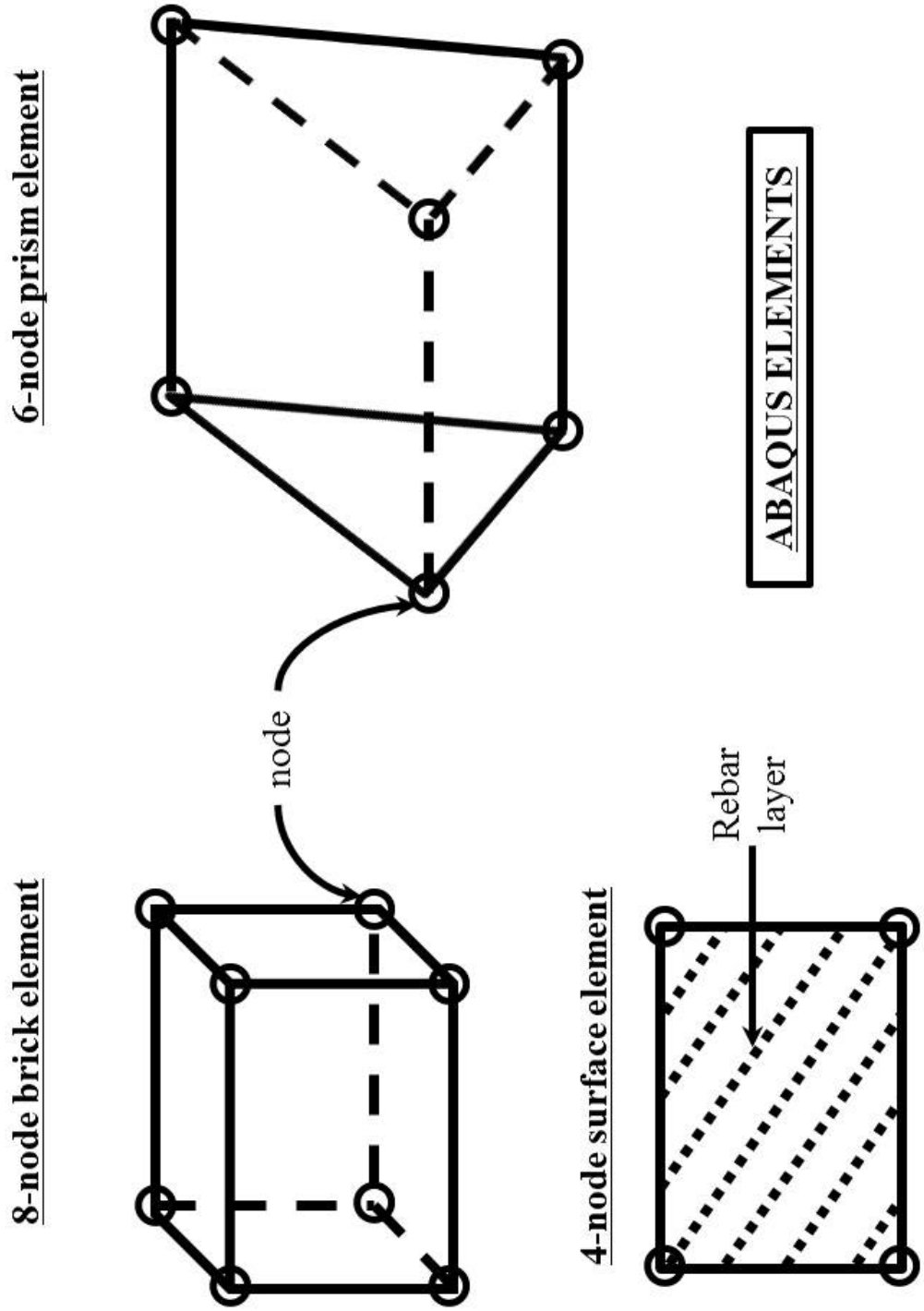

Figure 2.5: Enlarged view of ABAQUS elements used in the FEM.

2.4 Finite Element Analysis

2.4.1 Boundary Conditions

The boundary conditions for the normal load case that were enforced on the tire are depicted in Fig. 2.6. The hub is constrained in all directions throughout the length of the simulation. Contact interaction property is specified at the tire/rigid surface interface. The Lagrange multiplier algorithm is used in the contact property definition. Interference is applied to the rigid surface (in the z-direction) and the reaction force obtained at the hub is equal to the normal load that is acting on the tire. This method is employed because there is a considerable reduction in the simulation time and it converges more easily than other methods. In addition, the tangential behavior on the rigid surface is modeled as frictionless (this is changed later). The inflation pressure is set to 0.2 MPa (29 psi) for all cases.

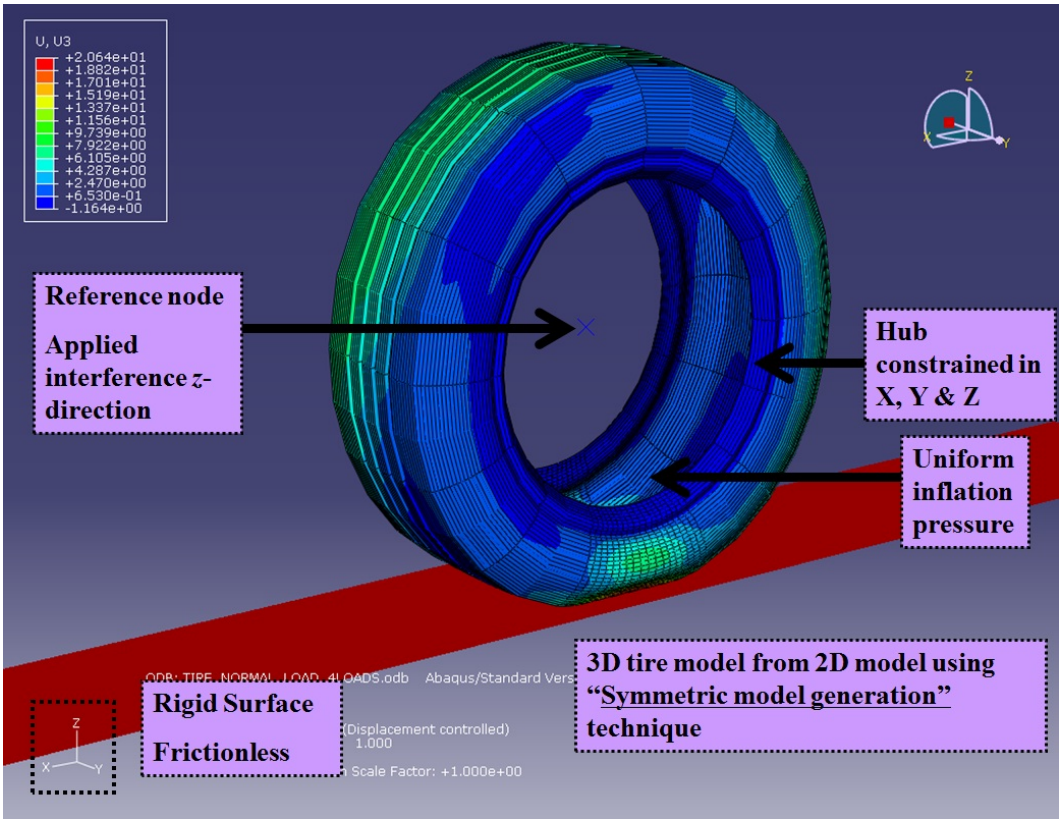

Figure 2.6: Three dimensional tire model.

2.4.2 Mesh Convergence and Verification of Model Accuracy

The next step is to perform a mesh convergence for the finite element model developed from the three-dimensional solid model of the tire. The final mesh is chosen by comparing the highest nodal stress at a particular node to the stress value at the integration point (some times referred to as a Gauss point). This also serves as a way to reduce the computational effort by reducing the number of elements (see Fig. 2.7) used in a simulation.

The mesh convergence and element reduction technique is applied to the current model by reaching an optimal value of the tire stiffness. The stiffness of a SRTT is about 240 Nmm^{-1}[39]. The stiffness value of the tire modeled in the current work is obtained from the ratio of the reaction force on the hub to the applied interference. The model accuracy is then verified by plotting the FEM results against standard ASTM test data (Fig. 2.8). It can be seen that the FEM predictions are fairly close to the test data, showing reasonable accuracy.

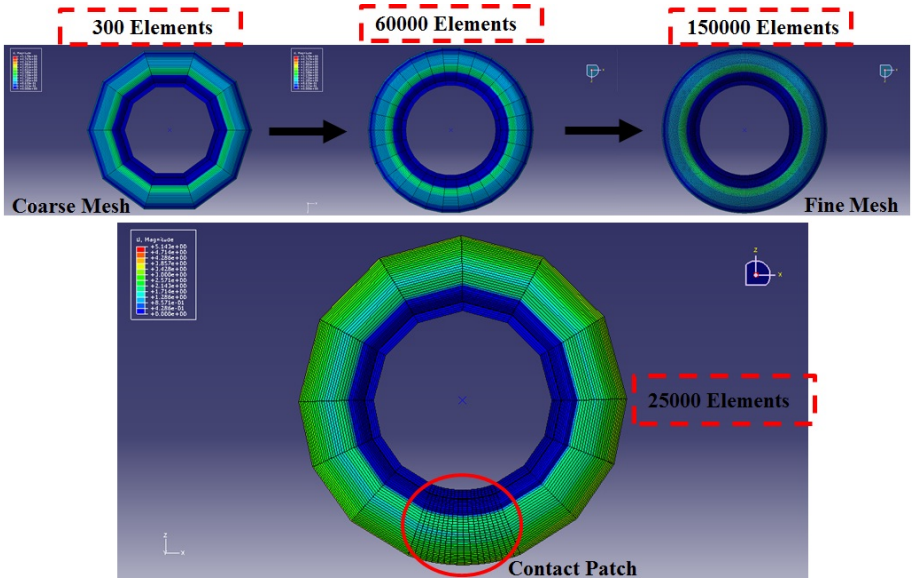

Figure 2.7: Mesh convergence and reduction in computational effort for coarse mesh optimization.

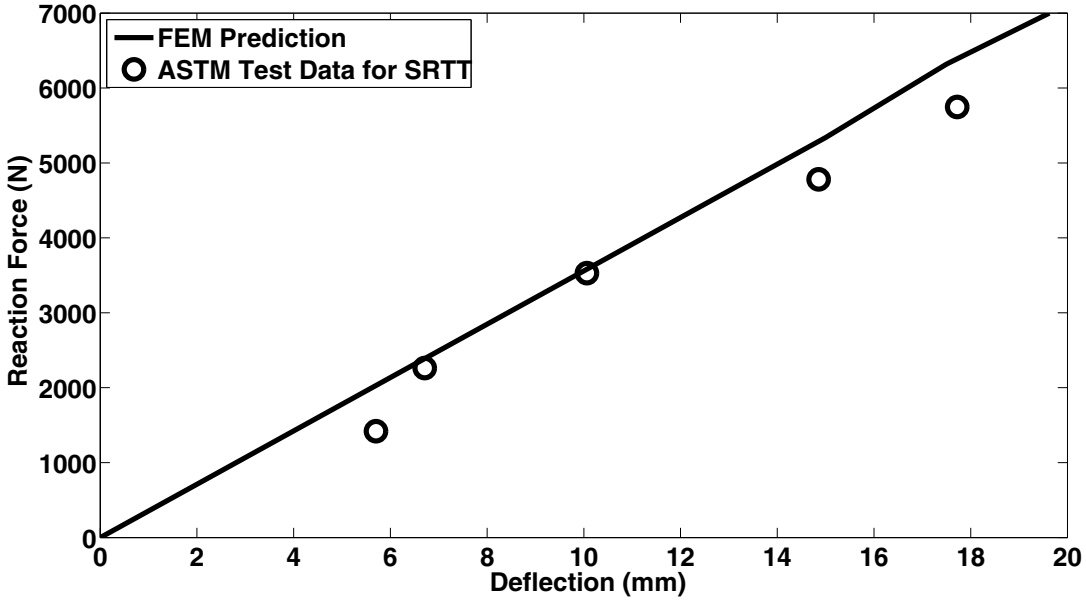

Figure 2.8: FEM results compared to ASTM test data for a SRTT.

2.5 Preliminary FEA Results

2.5.1 FEM Prediction of Contact Patch Area

The preliminary FEA results in this section pertain to the contact patch region. In order to develop theoretical models, which will predict the contact patch area, it is important to analyze how the contact patch dimensions vary with the normal load.

Figure 2.9 shows the contour results for the displacement in the normal direction, which is the same direction in which the load of 1000lbs is applied as deflection on the tire control node. The parametric cases performed have the same boundary conditions as mentioned before in section 2.4.1. It can be seen that for this static condition the contact patch width (simply the tread width) and the length appear to be straight lines. Hence the contact area would simply be the product of the tread width and the contact length.

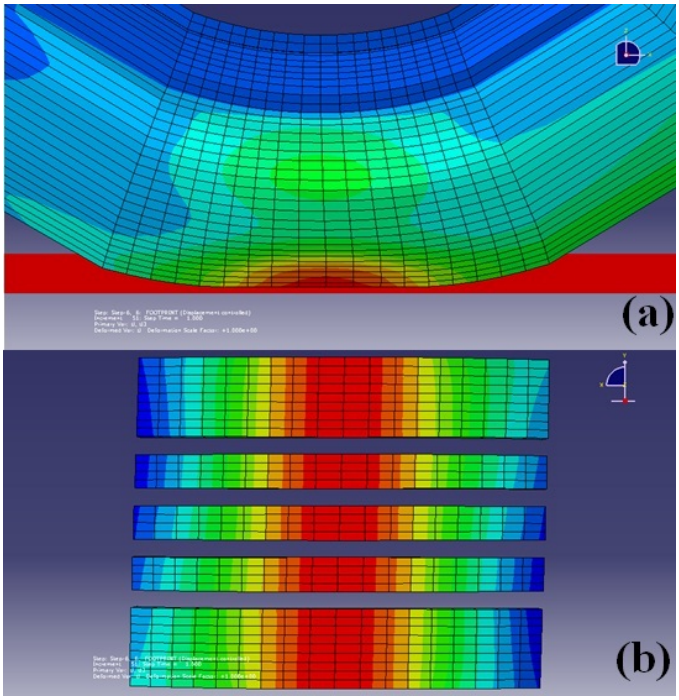

Figure 2.9: Contour plot of displacement in the z-direction (a)1000lbs Normal load;(b)Contact patch at 1000lbs.

Next the load is increased to 1200lbs(equivalent to approximately 15mm deflection), the contour results of the z-direction displacements results are shown in Fig. 2.10. As expected the contact patch area still appears to be a rectangle. This means that the contact patch length for the most part can be assumed to be invariant of the axial location. The load is then increased to 1400lbs(equivalent to approximately 17.5mm deflection). The displacement results is shown in Fig. 2.11. The contact patch at this load predicted by the FEM is similar to the earlier loads that were considered. Therefore the contact patch area can be easily predicted by multiplying the width times the contact length. This will be used later when correlating strains to normal load.

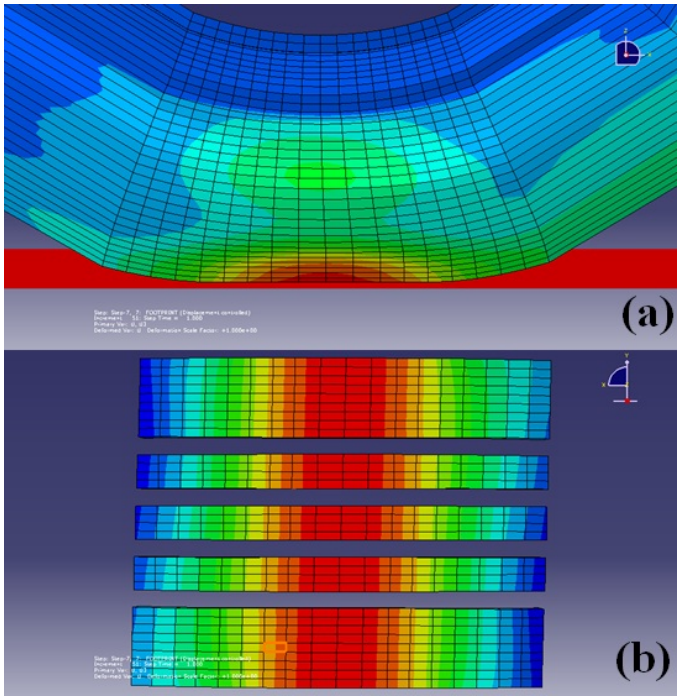

Figure 2.10: Contour plot of displacement in the z-direction (a)1200lbs Normal load;(b)Contact patch at 1200lbs.

The load is then increased to 1600lbs(equivalent to approximately 20mm deflection). This load is also very close to the maximum load rating of a SRTT(which is about 1653lbs). At this load the contact patch under static loading still resembles a rectangle. The contour plot of displacement results is shown in Fig. 2.12.

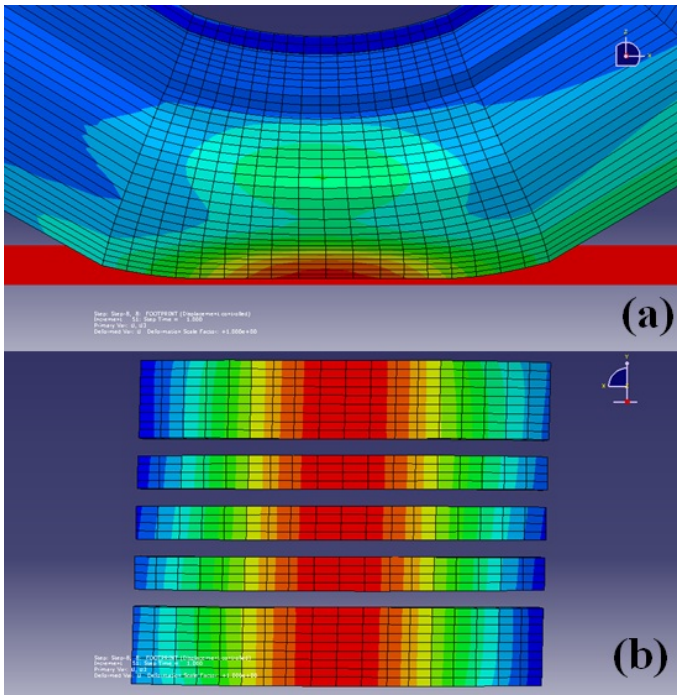

Figure 2.11: Contour plot of displacement in the z-direction (a)1400lbs Normal load;(b)Contact patch at 1400lbs.

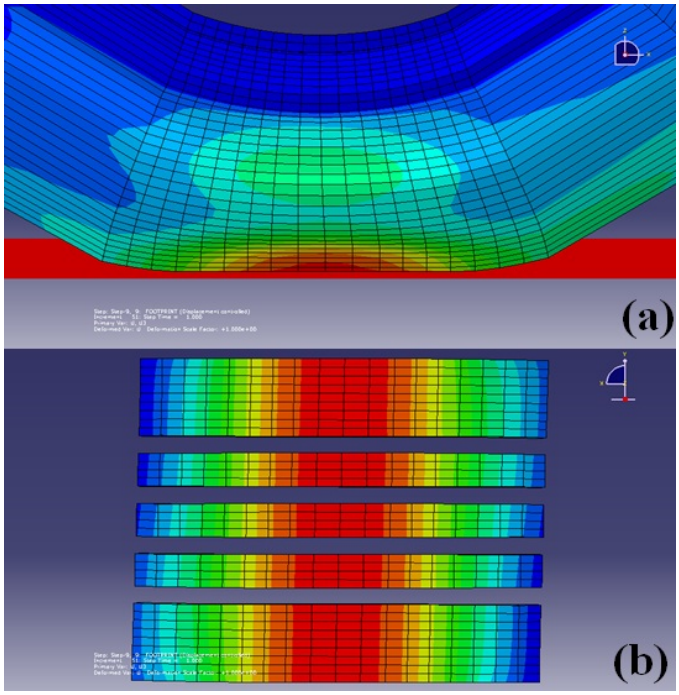

Figure 2.12: Contour plot of displacement in the z-direction (a)1600lbs Normal load;(b)Contact patch at 1600lbs.

2.5.2 FEM Prediction of Strain on the Tire Innerliner and Footprint

The strain predictions from the finite element model is analyzed in this section, with special focus on the tire innerliner and the tire rigid surface contact interface, sometimes referred to as the tire footprint or contact patch.

The strains (ϵ_{xx}) along the longitudinal direction (x-direction) is shown in Fig. 2.13. For the sake of consistency, strain predictions from only the 1600lbs normal loading condition are considered. In Fig. 2.13(a), the paths connecting the nodes from which the strain values are extracted, in the contact region, are illustrated by dotted lines. The footprint strains in the contact patch region are shown in Fig. 2.13(b). The strains on the inside and the outside of a tire are studied in order to understand which strain tensor component or combination of components correlates with the applied load. As expected, the strains in the footprint have higher values compared to strains in the innerliner. From the contour plot, it becomes clear

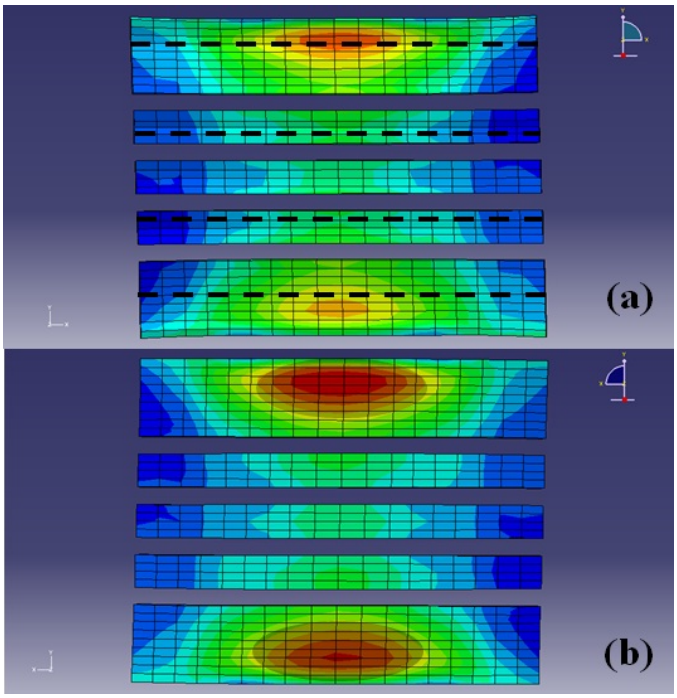

Figure 2.13: Strain prediction ϵ_{xx} for 1600lbs normal load;(a)Innerliner;(b)Contact patch.

that the strains along paths (illustrated by dotted lines) vary significantly with applied load. The outer nodal path predicts same trends but is significantly different from what nodes along the inner nodal paths predict. One reason for this behavior arises from the anisotropy of the steel belts and cord plies. Upon inflation the tire expands asymmetrically about the plane on which the rigid surface is created. This leads to an edge effect where the tire bends along this plane causing a difference in trend prediction by the outer and the inner nodal paths.

The strains along the lateral direction (ϵ_{yy}) are shown in Fig. 2.14. This component of strain is believed to have little to no effect on the circumferential strains that will eventually be measured on the surface of the tire innerliner. Even though the strain predictions appear to be significant in this contour plots, the actual values from the FEM are fairly low on the contact patch region and the tire innerliner itself. The reason being when the hoop is decomposed into its necessary components, there is no lateral component of the strain

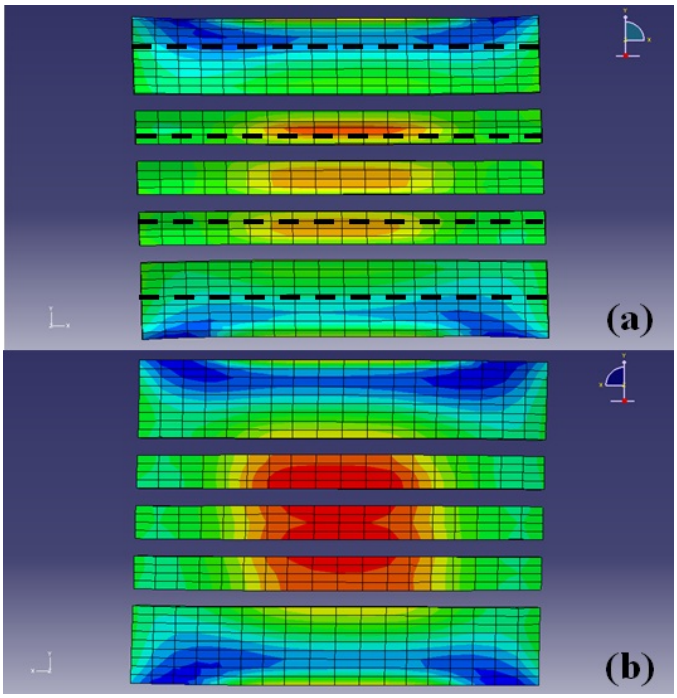

Figure 2.14: Strain prediction ϵ_{yy} for 1600lbs normal load;(a)Innerliner;(b)Contact patch.

tensor. A qualitative comparison is presented in the following section where circumferential strains are compared to the lateral strains.

The strains along the normal load or z-direction are shown in Fig. 2.15. The strains on the innerliner (Fig. 2.14(a)) and the strains in the contact patch region (Fig. 2.14(b)) show a significant value change in the normal direction. This is the same direction in which the normal load (an equivalent interference of 20mm) is applied on the tire control node. At this load it can be seen that all four nodal paths (illustrated by dotted lines) show significant variation in their trends in response to the applied load. The edge effect due to sidewalls is evident from the trends predicted by the nodal paths on the inside and outside. This also causes uneven deformation along the longitudinal direction. This is one reason (addressed in chapter 4) why the nodal paths on the outside predict similar trends and the nodal paths on the inside predict similar trends.

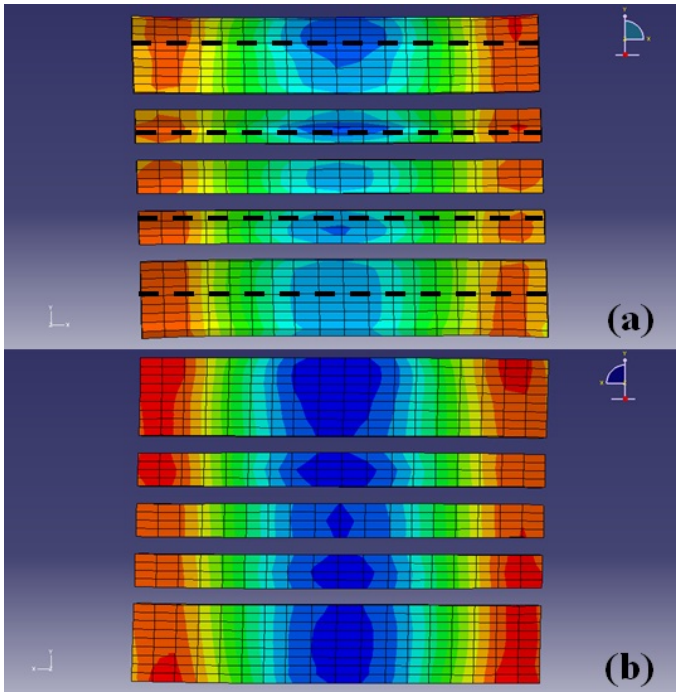

Figure 2.15: Strain prediction ϵ_{zz} for 1600lbs normal load;(a)Innerliner;(b)Contact patch.

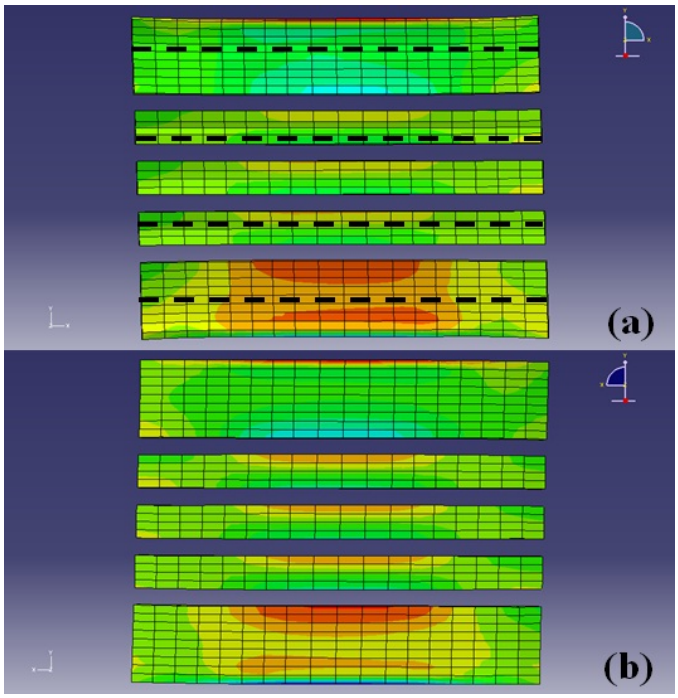

Figure 2.16: Strain prediction ϵ_{xy} for 1600lbs normal load;(a)Innerliner;(b)Contact patch.

The static finite element model does not account for friction behavior (this changed later in the steady state model) since the tangential direction material behavior is modeled as frictionless. The strains in the xy-direction is shown in Fig. 2.16. Nothing significant to be noted occurs in this direction and hence the strains along this direction is ignored as it does not form part the hoop direction. The same is also true for the strains in the yz-direction as it as no influence in the hoop direction. The strains from the finite element model for the yz-direction is shown in Fig. 2.17.

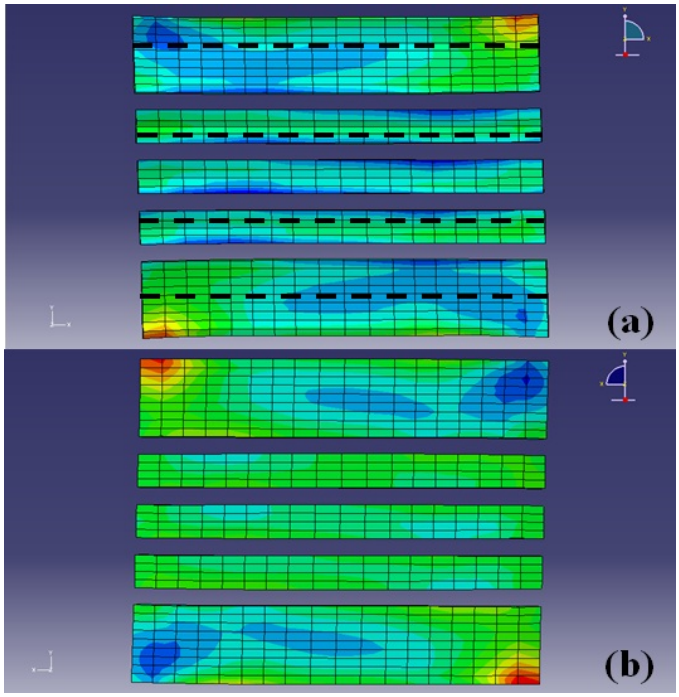

Figure 2.17: Strain prediction ϵ_{yz} for 1600lbs normal load;(a)Innerliner;(b)Contact patch.

The strain in the xz-direction is not dependent on the friction behavior in the tangential behavior but should be accounted for in the strains in the hoop direction. The contour plot of strains in the xz-direction is shown in Fig. 2.18. In effect of this component of strain can be visualized by assuming a mid-line that separates the footprint (Fig. 2.18(b)) into two. From the contour it is evident that the strains in this direction varies significantly along each of the nodal paths from the inside to the outside along the lateral direction. The

influence of each of the strain tensor component is crucial in establishing the strain along the circumferential direction.

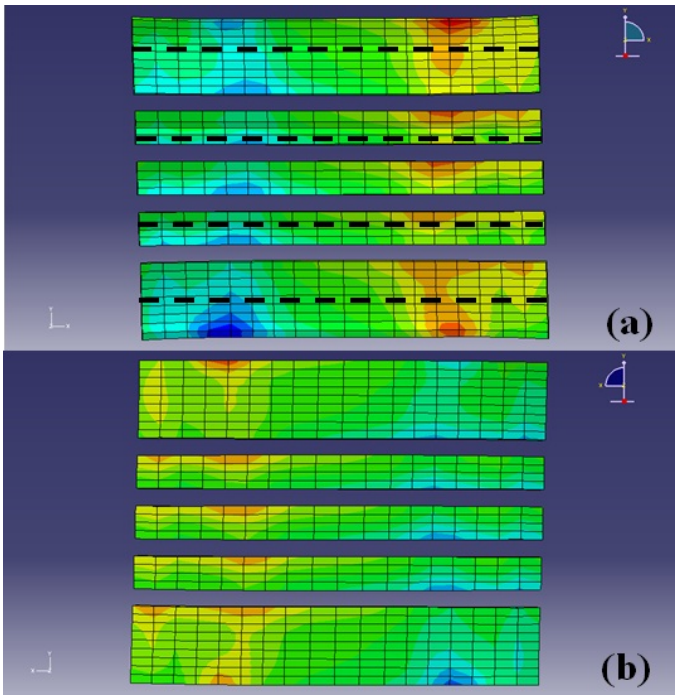

Figure 2.18: Strain prediction ϵ_{zx} for 1600lbs normal load;(a)Innerliner;(b)Contact patch.

2.5.3 Comparison Between Circumferential Strains and Lateral Strains

When a tire is loaded in the direction normal to the rigid surface at the rigid surface/tire interface, a tensile strain distribution occurs on the innerliner of the tire in the hoop direction (see Fig. 2.19), and the region outside the contact patch experiences a compressive strain distribution.

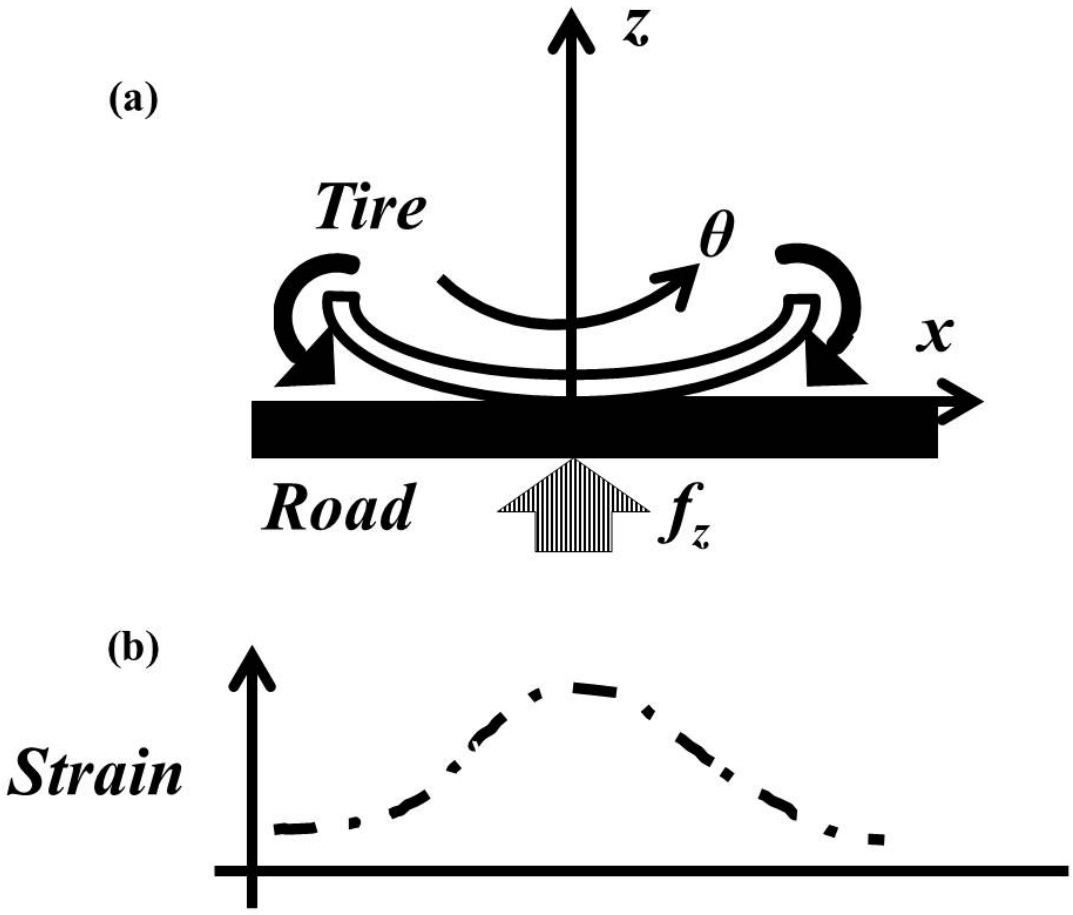

Figure 2.19: Tire deformation and strain prediction $\epsilon_{\theta\theta}$ due to a normal load:(a) Normal load;(b)Strain profile

When only the normal load acts on the tire and the rigid surface is assumed to be frictionless, a symmetric strain distribution (Fig.. 2.19(b)) appears about the abscissa.

It is now clear that if strain sensors were to be mounted on the innerliner of the tire, the strain sensed would be the circumferential or the hoop strains. In order to make the case for the choice of hoop strain, a comparison between the hoop strain $\epsilon_{\theta\theta}$ and lateral strain ϵ_{yy} is shown in Fig. 2.20. The FEM results from the 1600lbs normal load case is considered in this example. Now it becomes clear that the hoop strains predict a trend which is consistent with the strain distribution that will occur when a symmetric elastic member is deformed about the axis of symmetry. Despite the deformation that occurs in the lateral direction, lateral strains (ϵ_{yy}) show no clear trend with the applied load. For this simple reason, trends based on the circumferential strains is adopted for developing empirical models for slip angle and normal load in the later chapters of this dissertation.

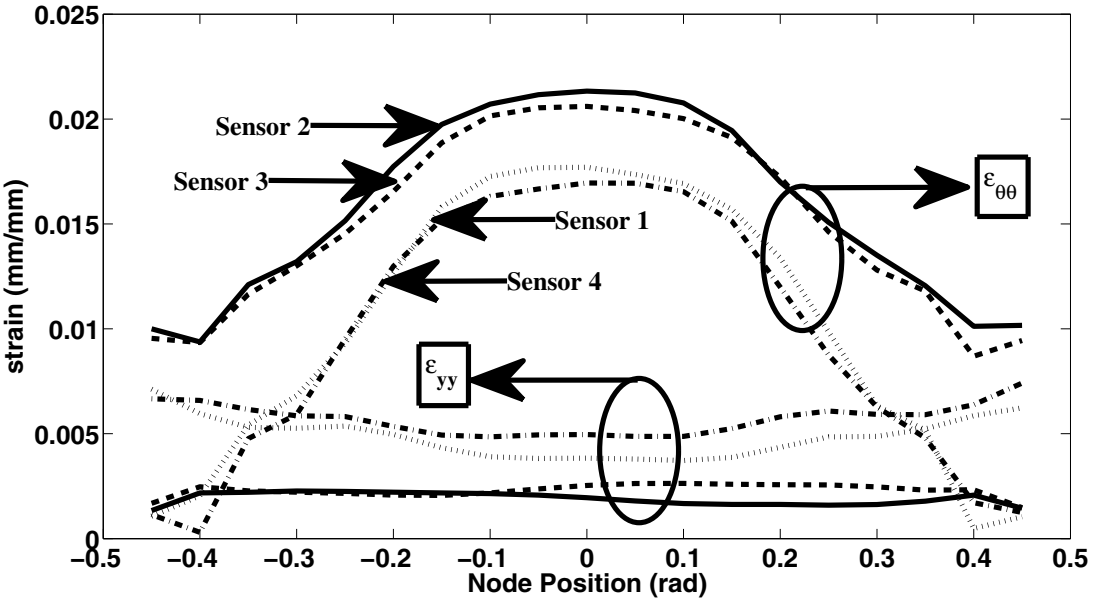

Figure 2.20: Strain prediction $\epsilon_{\theta\theta}$ and ϵ_{yy} comparison at 1600lbs normal load.

Chapter 3

Strain Analysis Based on Static Loading Finite Element Prediction

The location of strain gages is crucial with respect to capturing the contact patch dimensions. In this work the nodal solutions of the finite element model used approximately to predict the circumferential strains that will be measured from experiments. The sensor location (shown in Fig. 3.1) correspond to the nodes that equidistant are from each other and run circularly around the tire. From here on forth sensors 1 through 4 will represent node paths from the finite element model. The node path comprises of nodes which contain strain results from the integration points approximated at nodes, and extracted to make the necessary predictions.

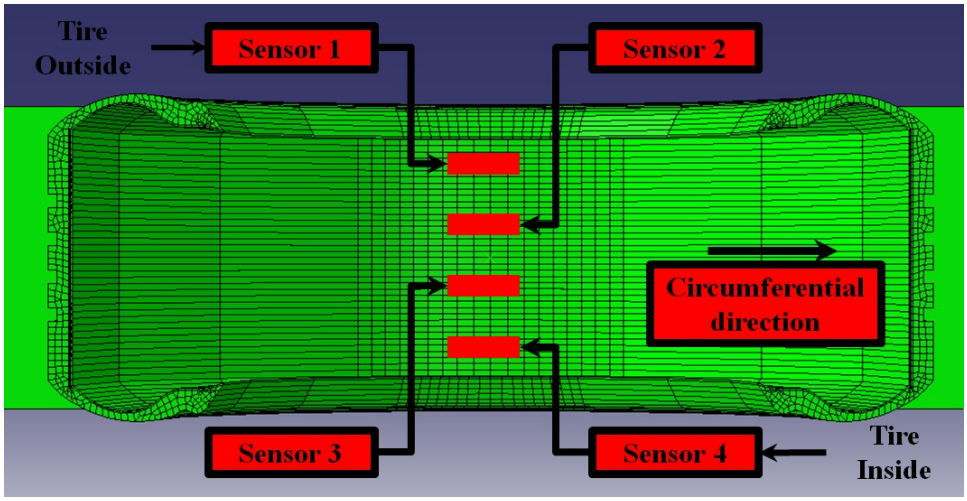

Figure 3.1: Sensor locations approximated to nodal solutions.

The nodal solutions correlate to sensors as the following:

1. All sensors are equidistant from each other

2. Sensor 1 is on the edge of contact patch (tire outside)

3. Sensors 2 and 3 are on the mid region

4. Sensor 4 is on the edge of contact patch (tire inside)

3.1 Results and Discussion

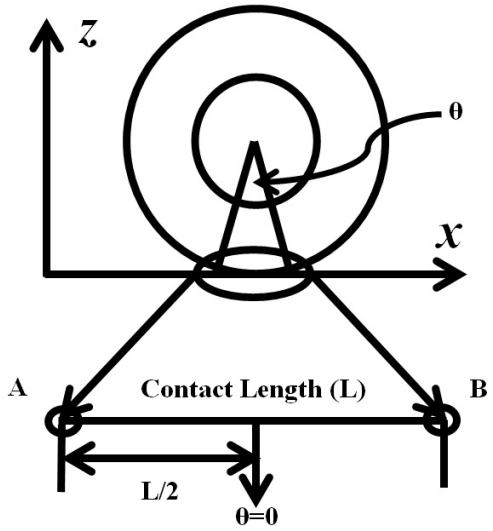

Figure 3.2: Schematic showing the θ=0 rad node position.

The hoop strains predicted from the FEM are plotted versus the radial node position (see schematic shown in Fig. 3.2) around the tire for parametrically varied cases of normal load. The strain predictions from this analysis are an approximate indicator of the contact patch length for a given case of normal load. In Fig. 3.3, the strain profile for the normal load case of 1000lbs is shown. The nodes that go in and out of contact experience a gradual increase and decrease in strain. A maximum strain of approximately 2.25% strain occurs at the edges of contact and is almost the same value throughout the contact.

When the normal load is increased to 1200lbs (Fig. 3.4) it can be seen that more nodes enter the contact patch zone. This is an indicator that the contact patch length increases with the applied load. When the nodes enter and exit the contact patch, the strain at these two extremities are in compression. The compressive strains are in reality realized as the

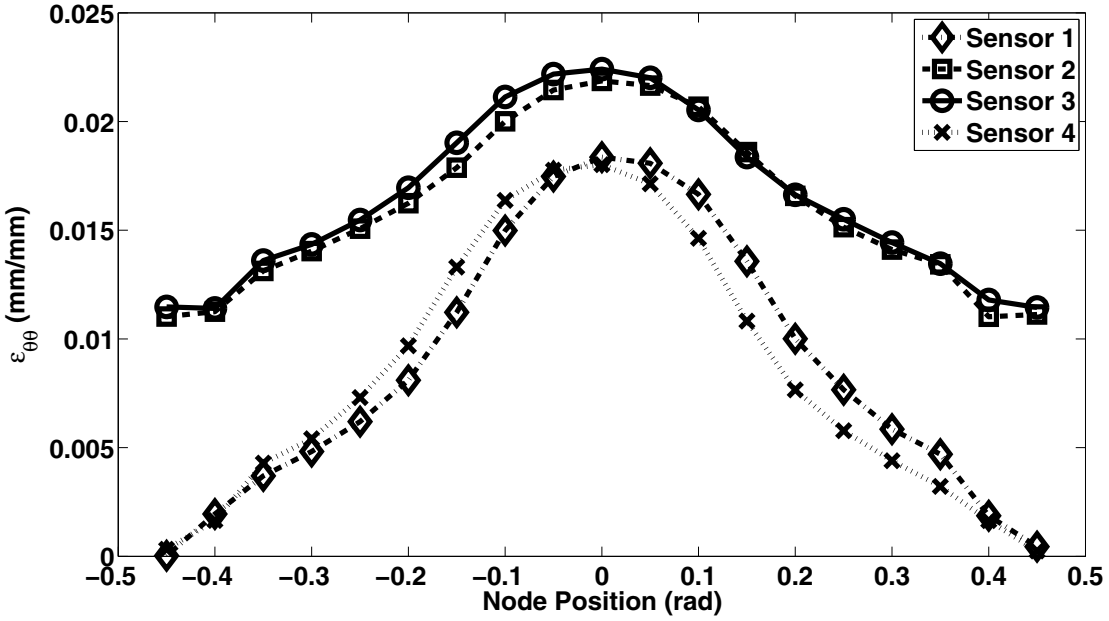

Figure 3.3: Strain prediction at 1000lbs normal load.

strains in the circumferential or the hoop direction. A similar observation can be be made from the 1400lbs(Fig. 3.5) and the 1600lbs(Fig. 3.6) load cases.

It is interesting to notice that sensors 1 and 4 and sensors 2 and 3 predict very similar trends but middle gages produce smaller magnitudes than the outer gages. The reason for the non-uniform behavior could be attributed to some sort of an edge effect[17] that comes into play when the tire is loaded in the normal direction. In Fig. 3.7, the contact length progression along sensor 1 for all loads considered in the FEM is shown. It can be seen that the contact length increases with an increase in the normal load. This is a direct indication that the contact patch area (which is simply the product of contact length and the tread width) increases as well.

Since the model in the current work approximates the tire geometry by considering a reduced number of tire sections, the predicted trends need to be validated experimentally. In order to validate the the finite element model, experiments with very similar loading

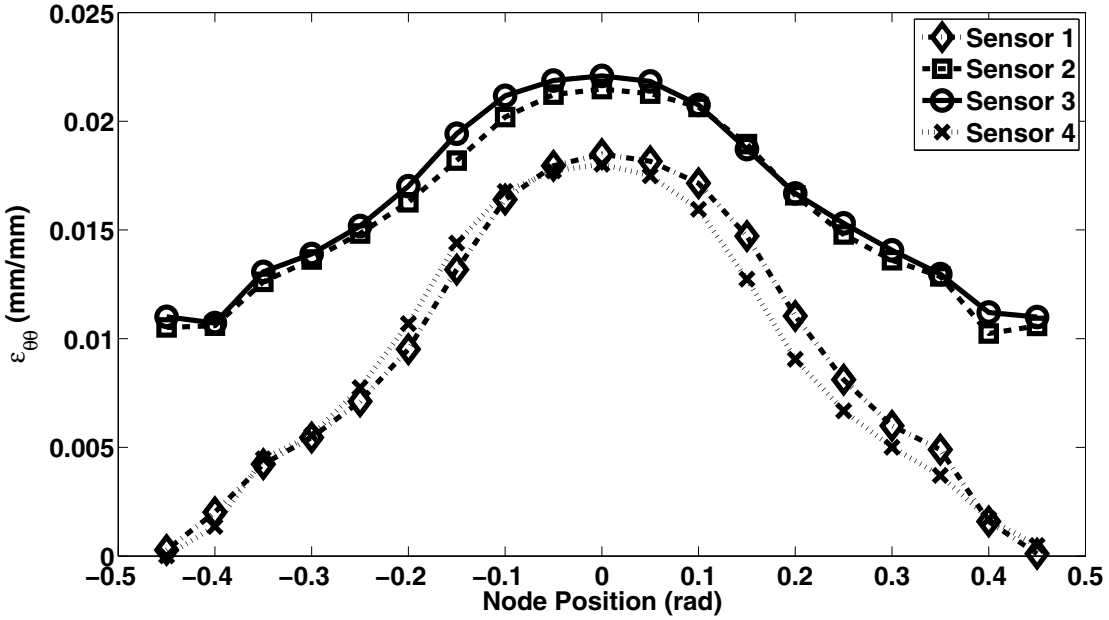

Figure 3.4: Strain prediction at 1200lbs normal load.

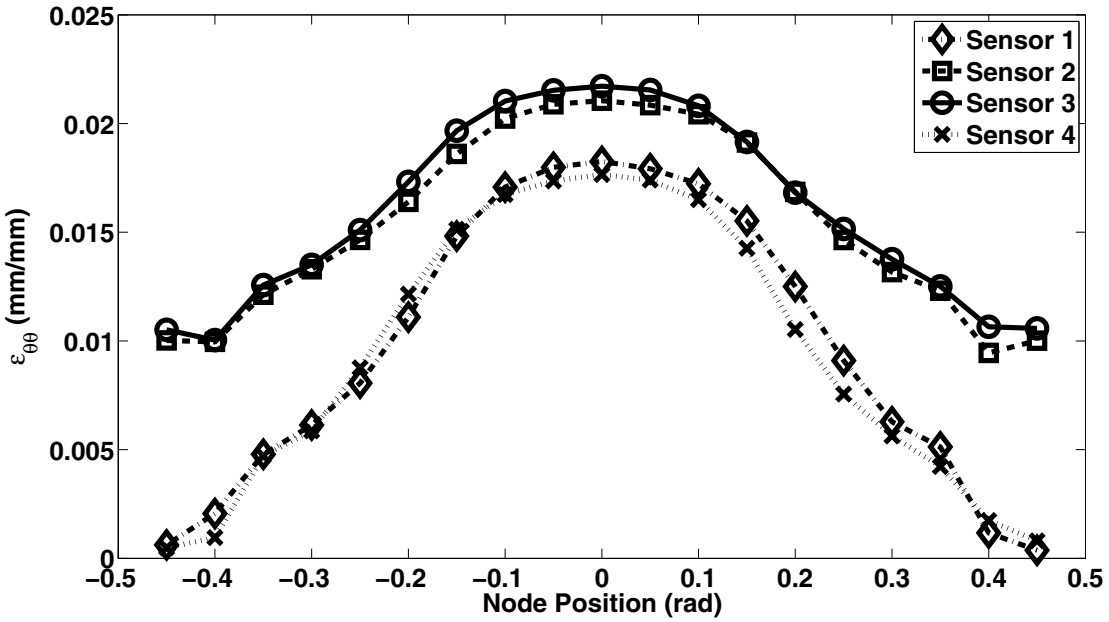

Figure 3.5: Strain prediction at 1400lbs normal load.

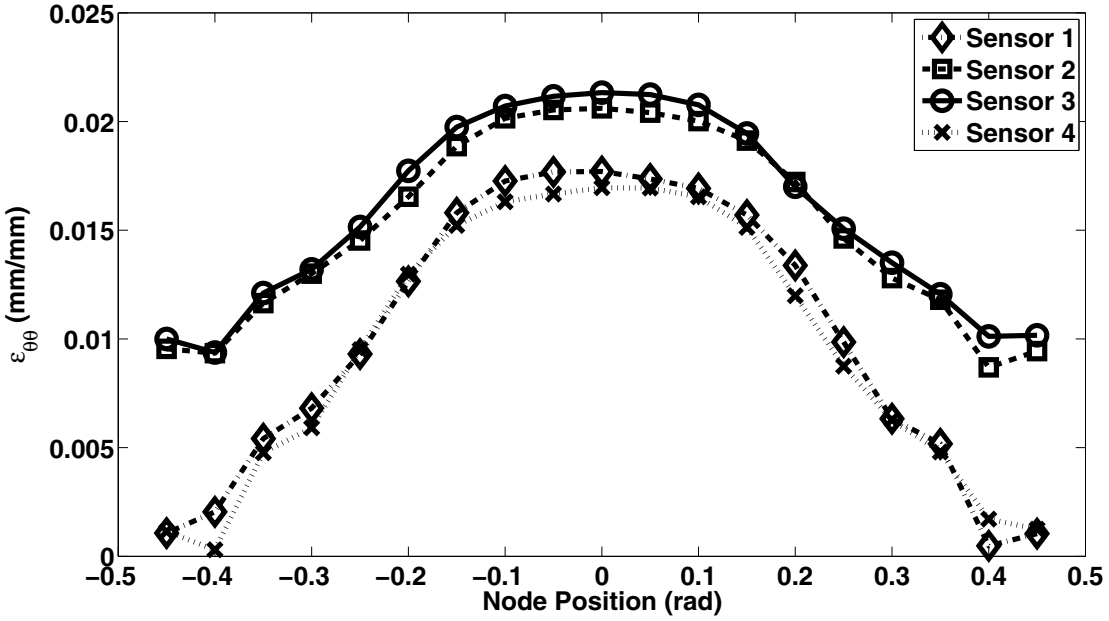

Figure 3.6: Strain prediction at 1600lbs normal load.

conditions have to conducted, to try and see if similar trends are captured. This forms the primary discussion in the next chapter.

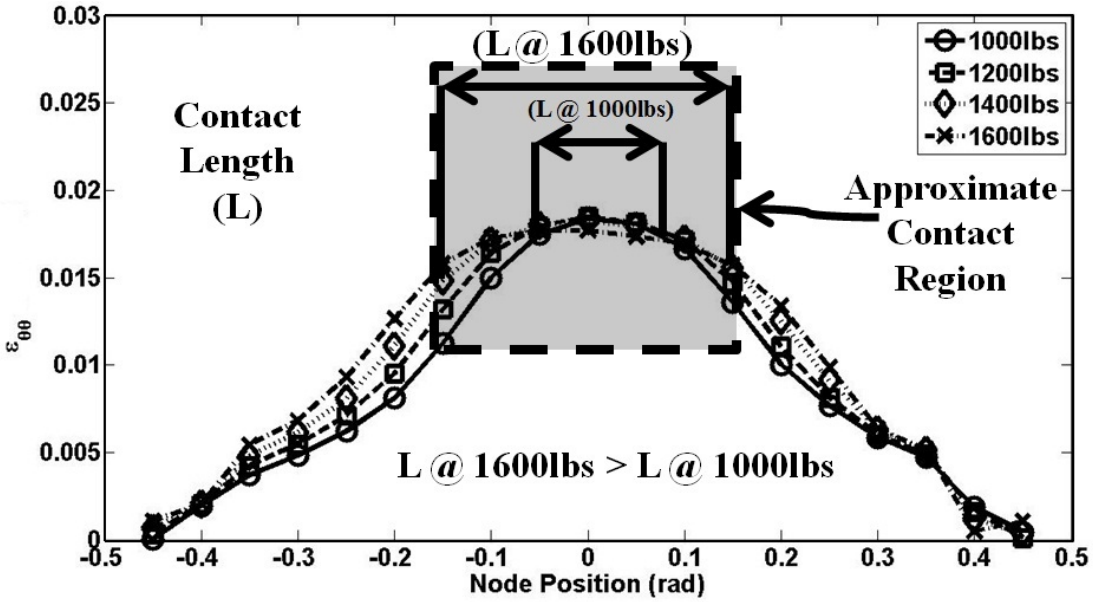

Figure 3.7: Strain prediction along sensor 1 for normal loads 1000lbs-1600lbs.

Chapter 4

Static Loading Experimental Set-up

4.1 Tire Test Stand for Experimental Validation

Experiments for the validation of the finite element model and evaluation of the new sensor suite and resulting strain/condition relations under static loading condition (also discussed in the previous chapter) are performed on a custom built test stand at the Advanced Propulsion Research Laboratory, Auburn University, Auburn. The tire test stand has two important features that is used to replicate the static loading condition used in the finite element model. The first feature is the rigid flat surface that is restrained in all directions and which also acts as the tire-road interface. The second feature is the capability of varying the normal load exerted on the tire. This is achieved by simply changing the air pressure of a pneumatic cylinder (see Fig. 4.1), which is mounted inline with the tire's rotational axis. A load cell is also mounted inline with the cylinder so that the load on the tire can be measured accurately. This fairly simple test setup (see Fig. 4.2) replicates the normal loading condition modeled using finite elements.

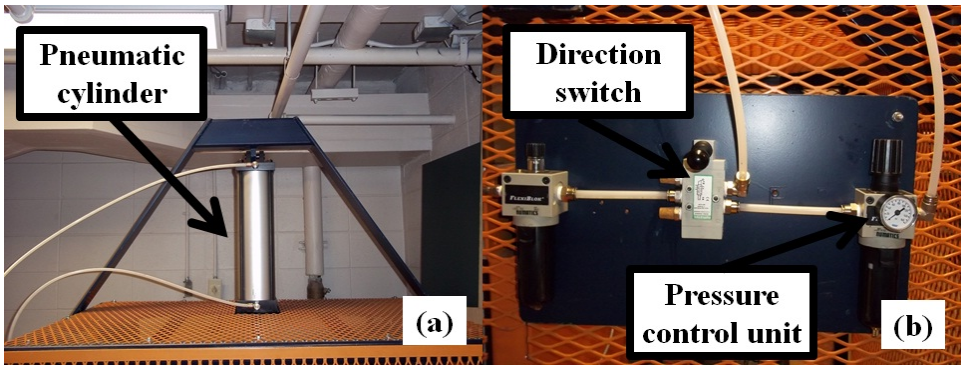

Figure 4.1: AU test stand (a) Pneumatic cylinder; (b) Pressure control unit.

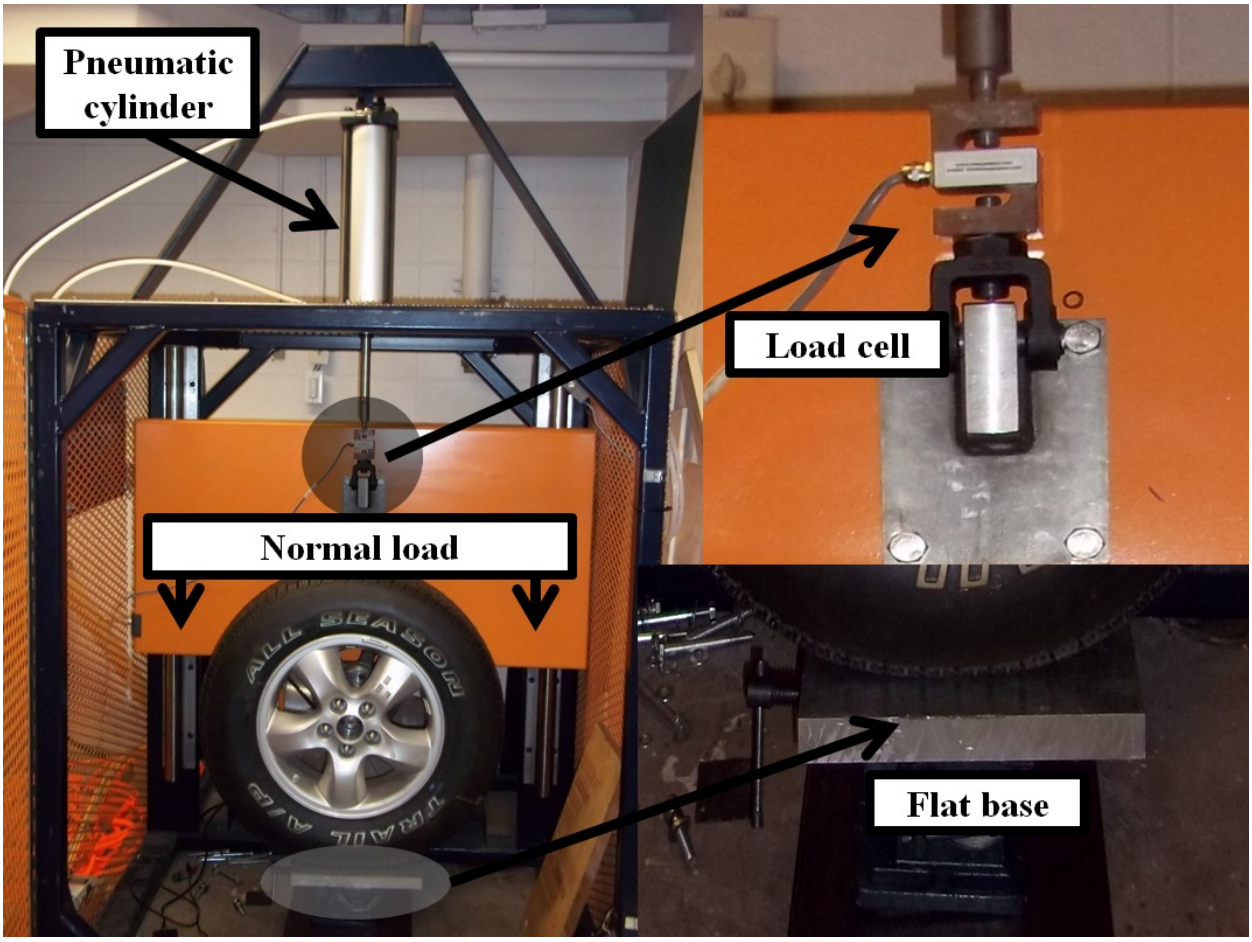

Figure 4.2: Custom built tire test stand for static loading condition.

4.2 Mechanical Layout of Hardware

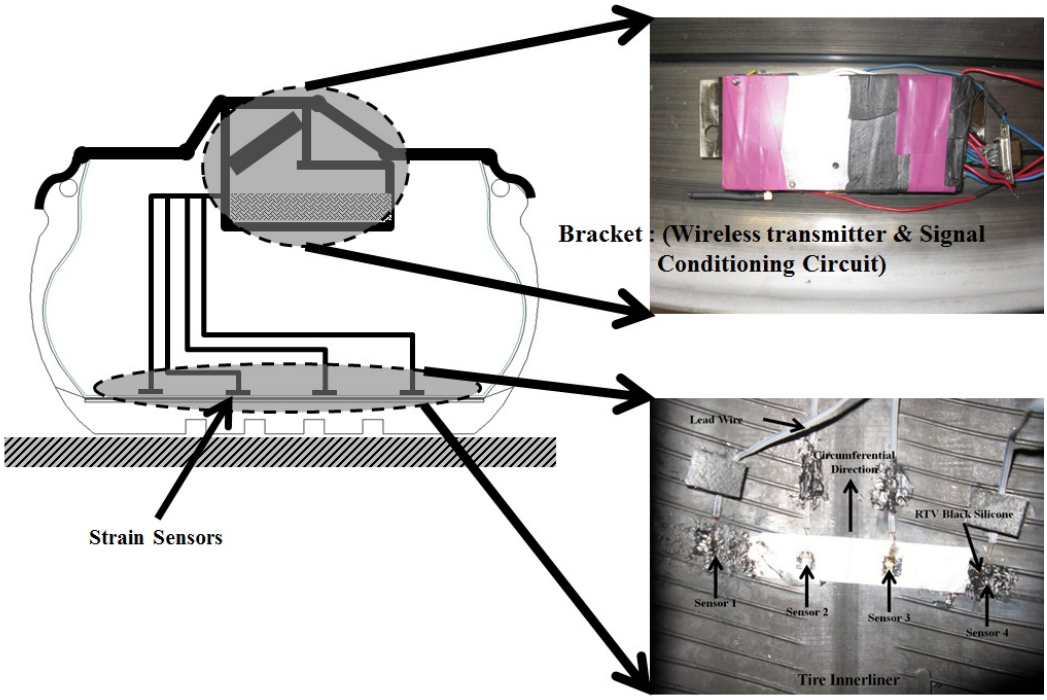

Figure 4.3: Schematic of the hardware arrangement.

The strain sensors are mounted on the innerliner of the tire as shown in Fig. 4.4. The sensors are placed equidistant from each other (similar to the placement mentioned in chapter 3). Sensor 1 is on the edge of contact patch (tire outside). Sensors 2 and 3 are mounted in the mid region over the width of the tread. Sensor 4 is on the edge of contact patch (tire inside). The sensor suite for the current work is packaged onto an aluminum bracket specifically built for holding all the necessary components. The mechanical components in the layout are,

1. Aluminum bracket (see Fig. 4.5) for holding the wireless transmitter and the signal conditioning circuit.

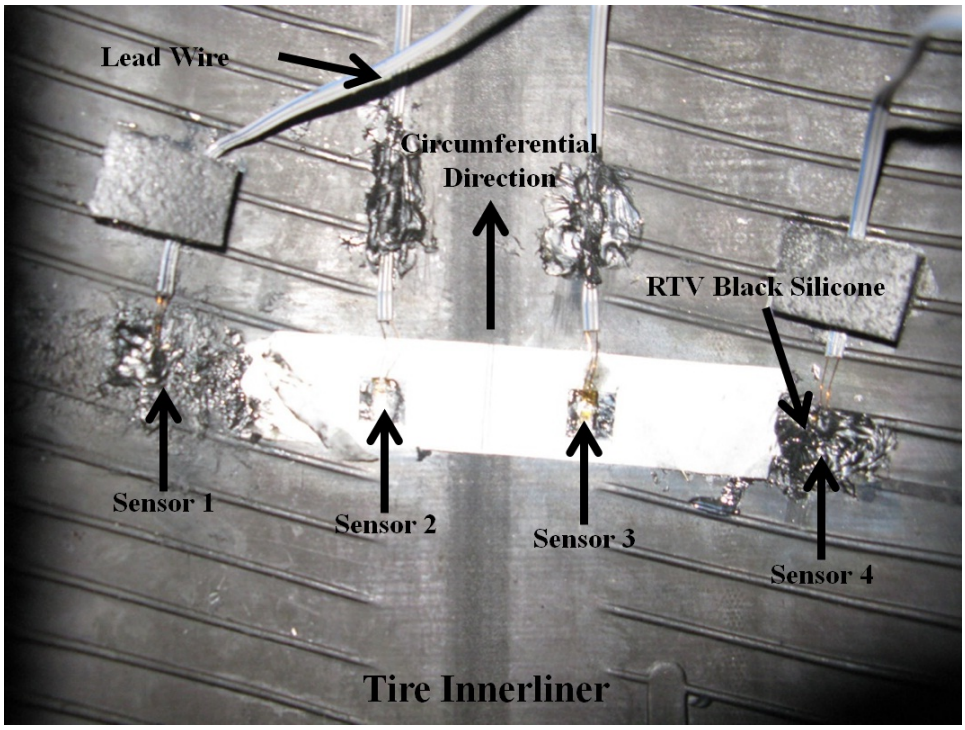

Figure 4.4: Strain sensor placement on the innerLiner of the tire.

2. A single array of strain sensors (see Fig. 4.4) are placed equidistant from each other, while covering the entire span of the tread width. This is done so in hopes that for every revolution of the tire the entire contact patch strains are captured.

3. A three-piece wheel (see Fig. 4.6) is used for reducing tire mounting effort once the sensor suite is secured to the wheel.

4. The final arrangement of the sensor suite before the tire is mounting the tire is shown in Fig. 4.7.

5. A CN strain gage adhesive and RTV black silicone is used for securing the strain gages to the innerliner of the tire.

6. A printed circuit board of the signal conditioning circuit is also built to considering various issues pertaining to tire mounting.

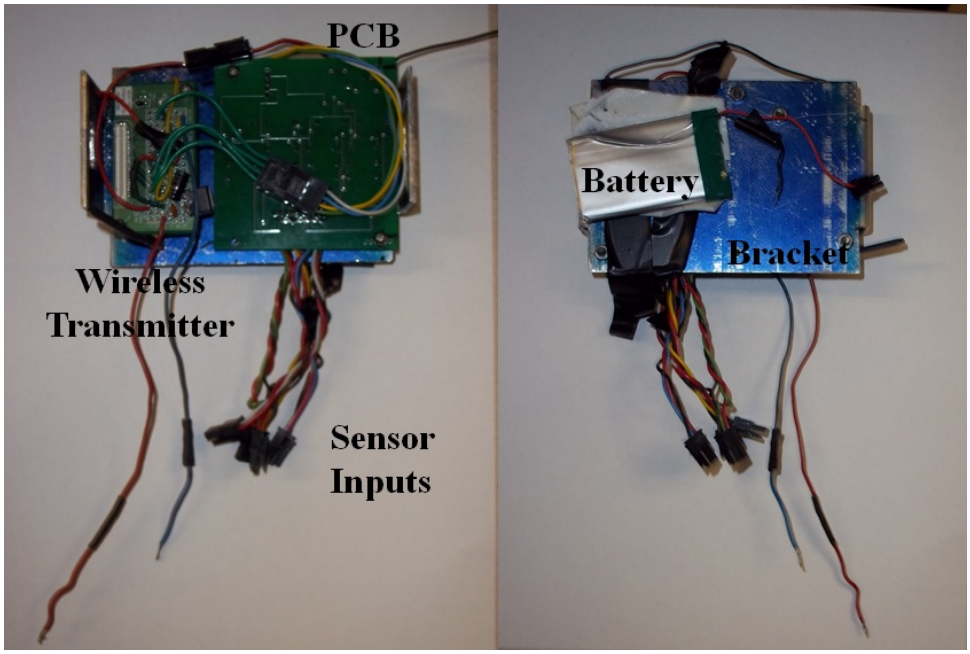

Figure 4.5: Wireless transmitter and signal conditioning circuit arrangement on a bracket.

Figure 4.6: Three-Piece Wheel.

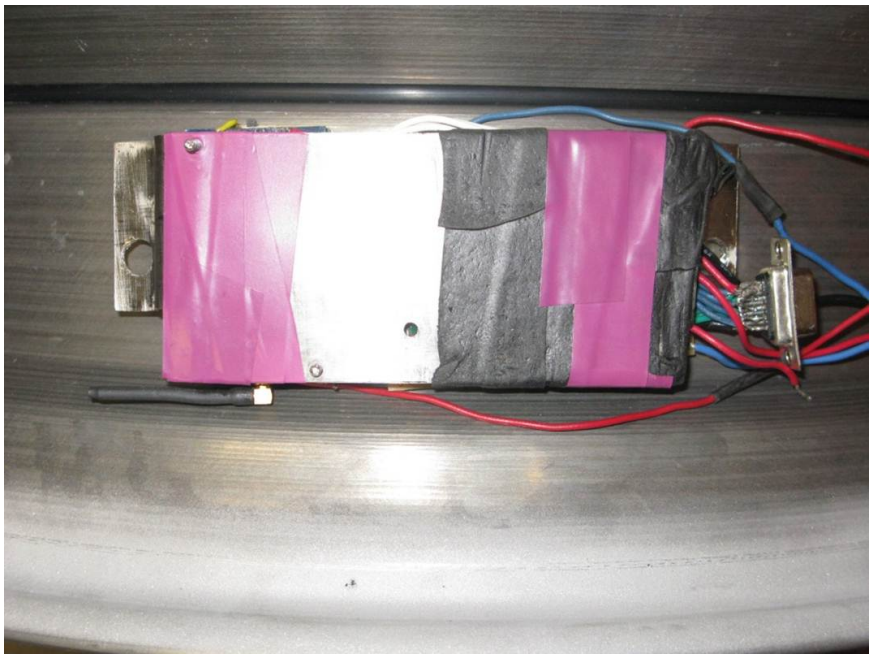

Figure 4.7: Final arrangement of bracket on the wheel.

4.3 Electrical Layout of Hardware

The predesign of the electrical circuit used as a signal conditioning circuit is shown in Fig.4.8. A quarter wheatstone bridge is employed in the current work. The bridge has a nominal resistance of 120Ω and an excitation voltage of 3.3 V. The strain gage acts as the variable resistor in the quarter bridge wheatstone network, as shown in Fig. 4.9. The measured strains is in μv, this small voltage measured is amplified with the help of a signal conditioning circuit. The signal conditioning circuit has a instrumentation amplifier. The gain resistor in the instrumentation amplifier is modified accordingly to amplify the measured voltage.

The output from the quarter bridge, where one of the member is a strain gage, is related to the measured strain. This change in output from when the bridge is balanced is related to the resistance change of the strain gage. A resolution of .05% can be achieved with the current amplifying circuit. Knowing the gage factor of the strain gage, the measured output

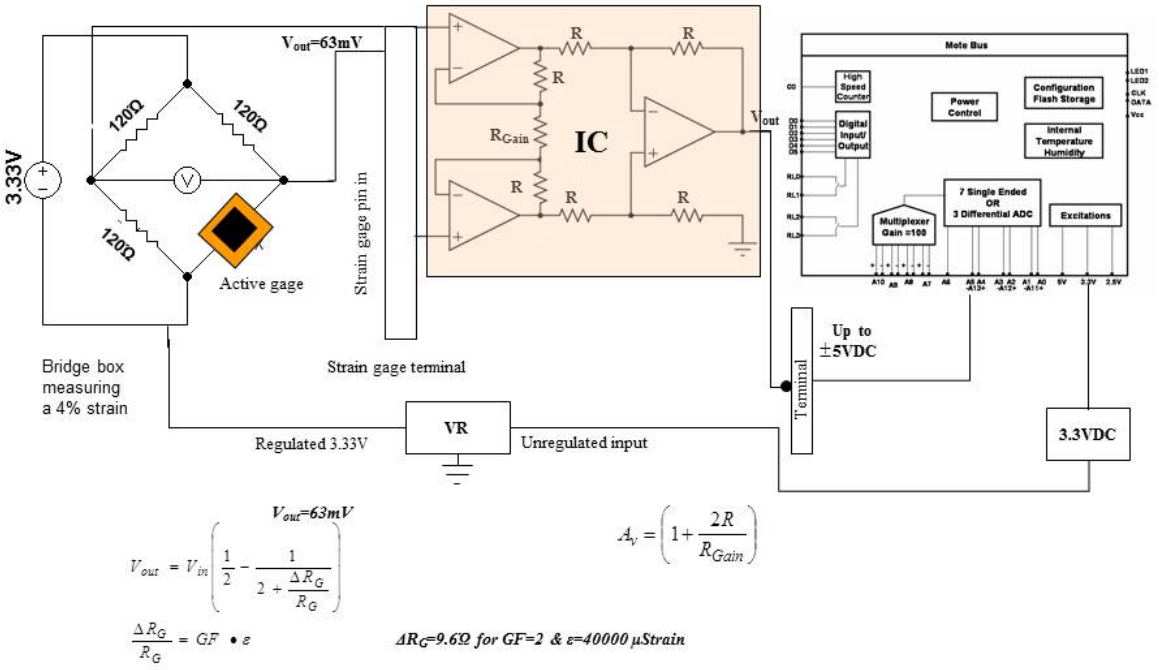

Figure 4.8: Pre-design of signal conditioning circuit for strain measurements.

voltage is converted to the strain ϵ by using the following equation:

$$\frac{V_{out}}{E_{ext}} = \frac{G_f \cdot \varepsilon \times 10^{-3}}{(4 + 2 \cdot G_f \cdot \varepsilon \times 10^{-6})} \tag{4.1}$$

where V_{out} is measured output voltage, E_{ext} is the bridge excitation voltage, ϵ is the strain and G_f is the gage factor, typically found to be 2.1. The gage factor is given by the following equation:

$$G_f = \frac{\Delta R/R}{\Delta L/L} \tag{4.2}$$

A CrossBow XDA100 wireless/MICA2 DAQ(Fig. 4.10) system is used in the current work for wireless data transmission and collection. The wireless data transmitter used in

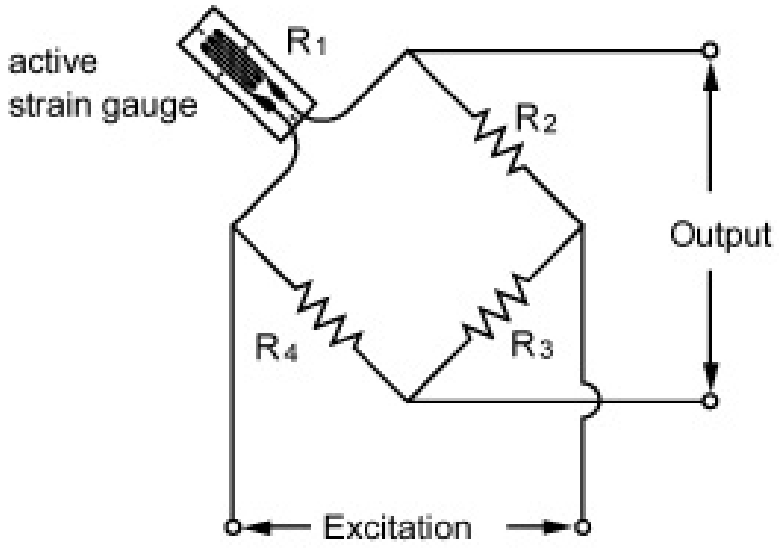

Figure 4.9: Quarter bridge wheatstone network.

the current work has a sampling time of 0.1 s (f_s=10Hz). The XDA100 has a 51-pin programmable prototyping area and comes with an onboard temperature sensor. The electrical layout (Fig. 4.11) is comprised of the wireless transmitter/receiver, signal conditioning for voltage amplification of outputs from strain sensors. The size of this circuit is significantly reduced by building a PCB. The size reduction helped reduce the mechanical effort in mounting the tire onto the wheel. The reduced effort in turn helps avoid damage to the strain gages as a result of the tire mounting process. The custom built sensor suite in it's current form is not ready for industrial use. A higher sampling frequency, smaller package size of the sensing module, and the over all integration with the wheel needs to be addressed before this sensor suite can become commercially available.

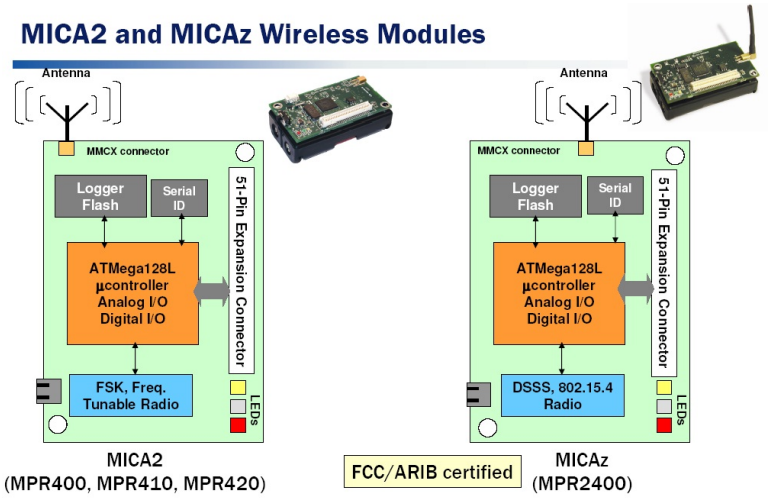

Figure 4.10: XDA100 and MICA2 wireless module[80].

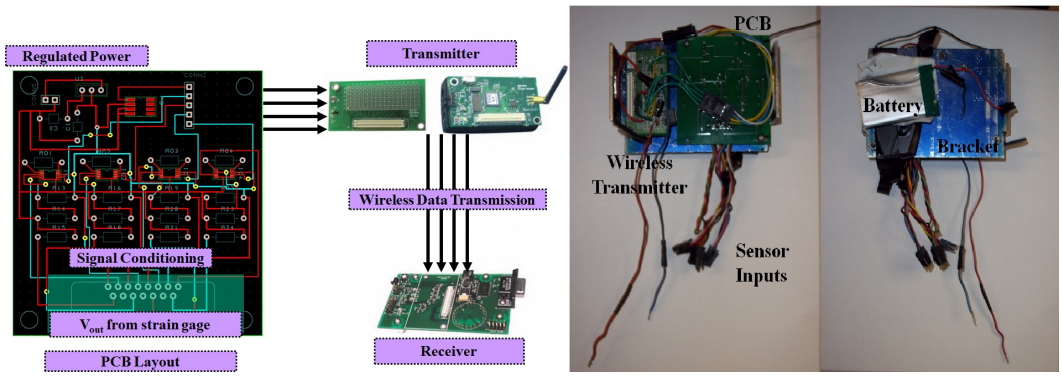

Figure 4.11: Electrical layout.

Chapter 5

Strain Analysis Based on Static Loading Experimental Data

An approach similar to the one discussed in the previous chapter is adopted in experiments for static loading cases. The strain gages are placed (see Fig. 4.4) along the lateral direction capturing the width of the tread. A 235/70 R16 (different from FEM tire) is considered in experiments. The goal of the experiments for the static loading condition is to validate the trends predicted by the FEM, demonstrate the created hardware and to develop relationships between normal load and strain. A SRTT does not have to be necessarily used for this purpose since the analysis is qualitative in nature.

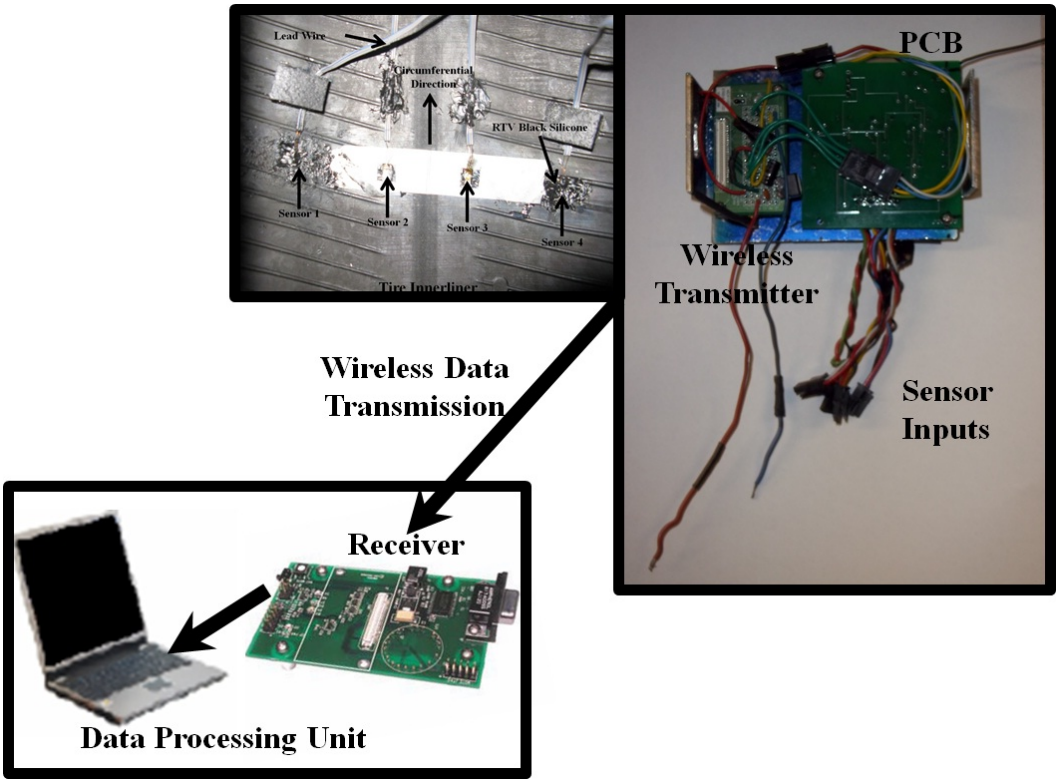

Figure 5.1: Data transmission from sensor to data processing unit.

5.1 Results and Discussion

The strains from the normal load case of 800lbs are shown in Fig. 5.2. A maximum strain of approximately 2% strain is measured for this load case. The strains vary gradually as the strain gages go in and out of contact and remain fairly constant outside the contact patch region. A similar trend is noticed for the higher load case of 1300lbs (see Fig. 5.3). In this load case a maximum value of 2.5% strain is reached. It can also be seen that the contact patch length increases with an increase in load. The trends from the experiments match fairly close to the trends predicted by the FEM. A similar conclusion can be made about the edge effect. It can be seen that sensors 1 and 4 measure approximately the same magnitude of strains. Sensors 2 and 3 behave in a similar fashion.

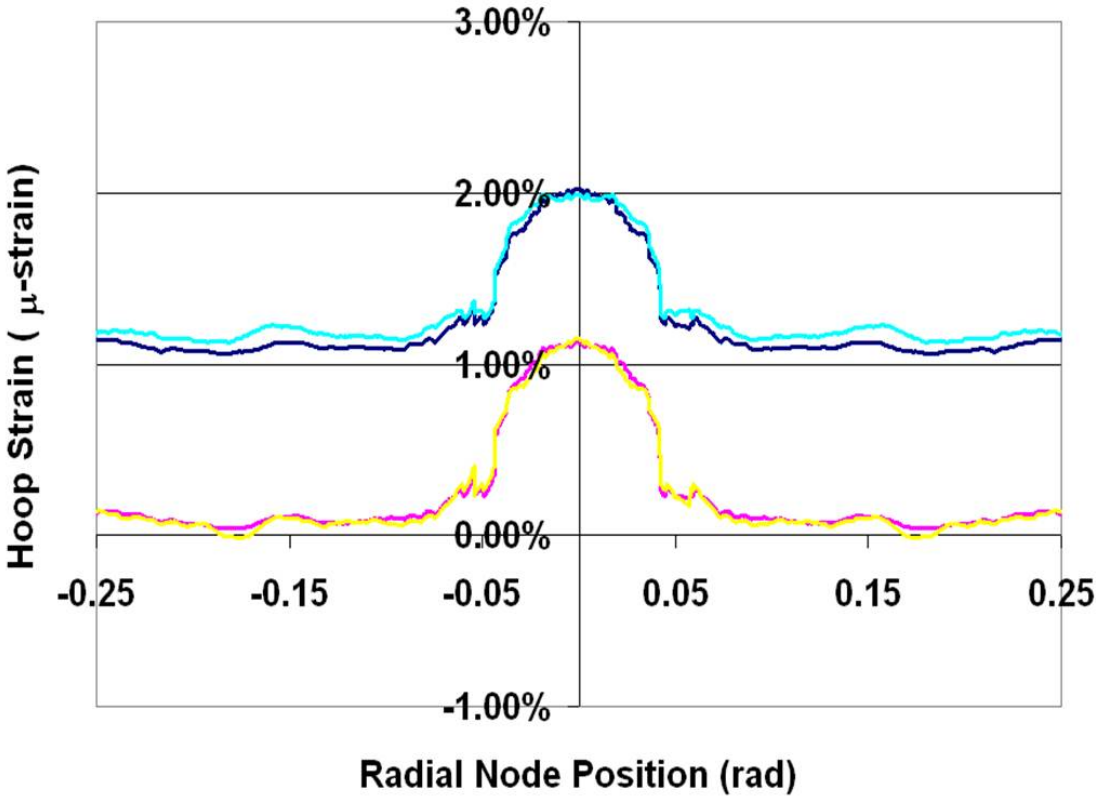

Figure 5.2: Strain measurements for 800lbs normal load.

The load on the tire is then increased to 1300lbs and the circumferential strain profile is shown in Fig. 5.3. As expected at this load the maximum strain value in the contact patch is more than what was measured from the 800lbs normal load case. This simply means that the applied load is directly proportional to tire deflection in the normal direction. The same trend is observed in the FEM where the simulation is displacement controlled and the reaction force at the wheel hub is the same as the normal load.

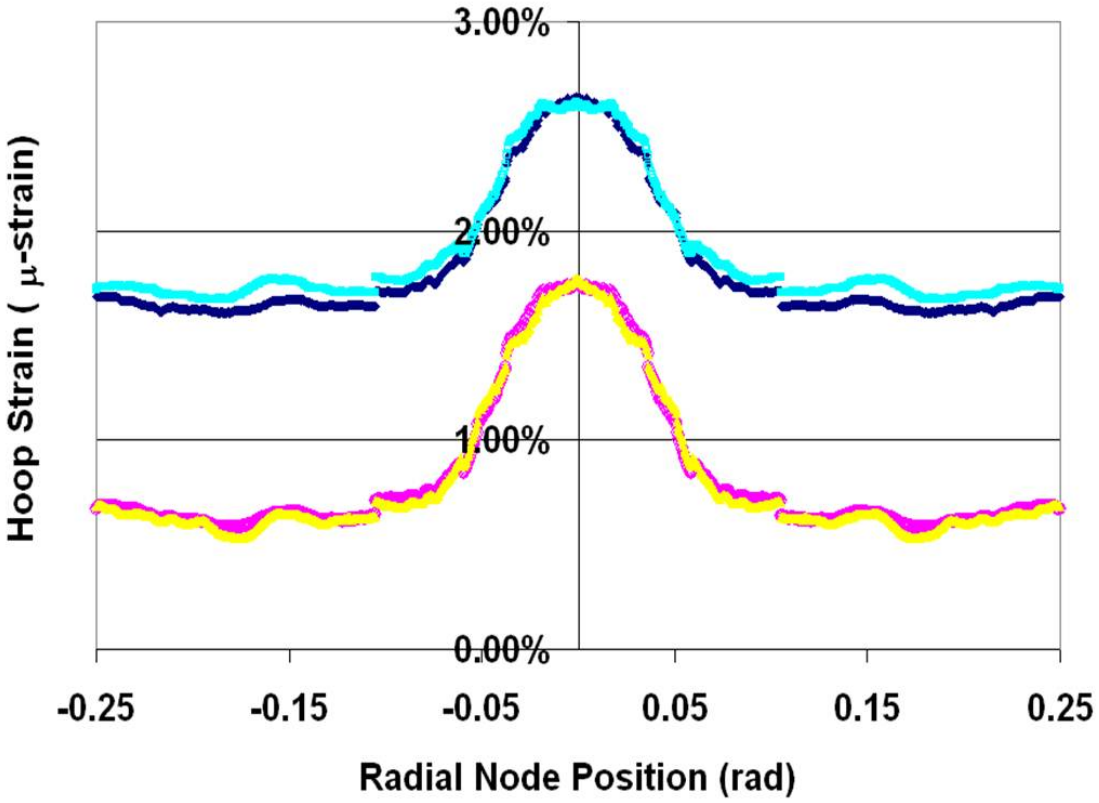

Figure 5.3: Strain measurements for 1300lbs normal load.

A comparison can be made between the trends predicted by the FEM and the experiments. In Fig. 5.4, for the normal load case of 1000lbs, strain predictions from the FEM is compared to the strains from the experiments. It can be seen that trends are similar although quantitatively different. Although a different tire is considered in the experiments, the strain profile, which is of importance in this exercise, seems to qualitatively follow closely with the

FEM predictions. The experimental comparison is simply used to validate the FEM before more complicated conditions involving slip and surface friction are modeled. The reasons for difference in magnitude of strains between FEM and experiments are as follows:

1. Different tires are considered (the tire size in FEM is 225/60 R16 & the tire size in the experiments is 235/70 R16).

2. Model inaccuracies due to different material compounds in the tire structure.

3. Neglected tire sections in the FEM.

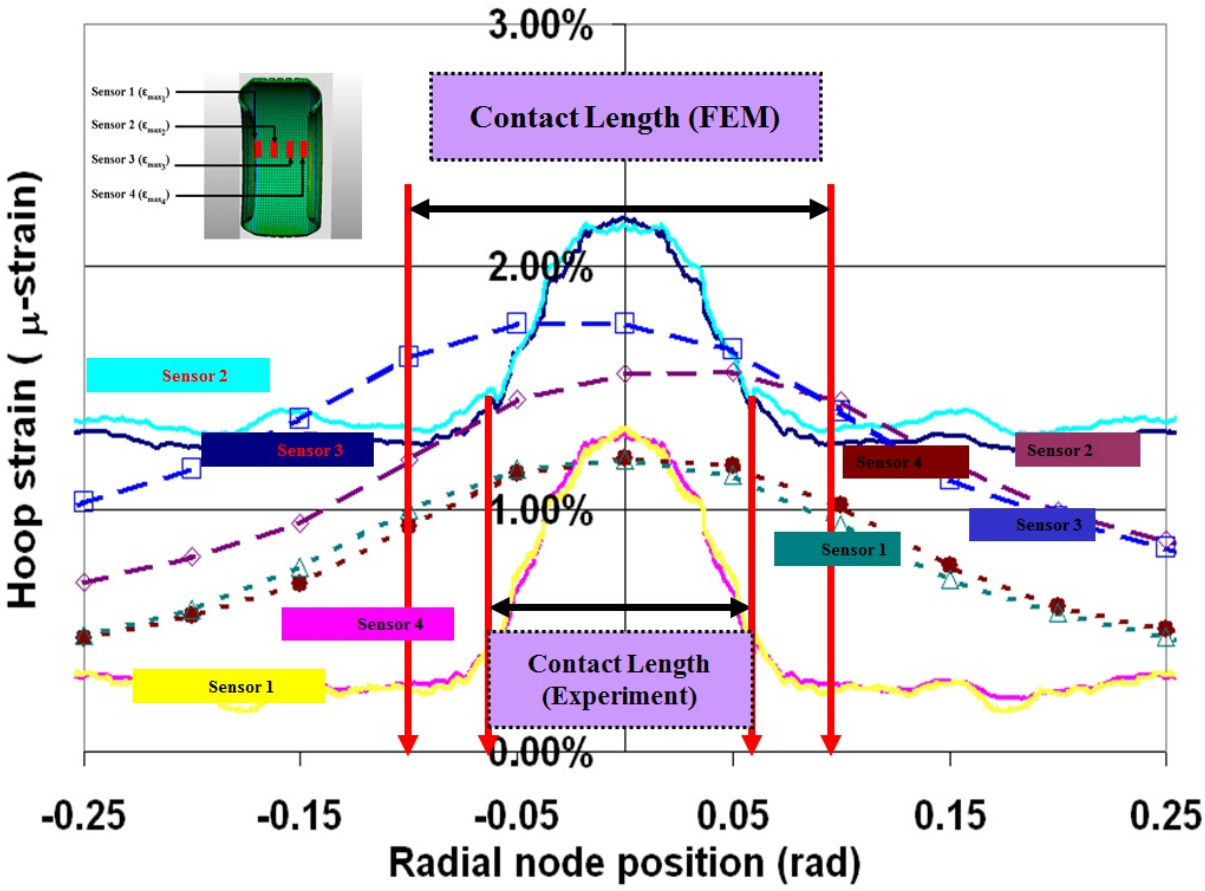

Figure 5.4: FEM results compared to 235/70 R16 tire at 1025lbs.

Chapter 6

Steady-State Free Rolling Finite Element Model

6.1 Straight Line Rolling

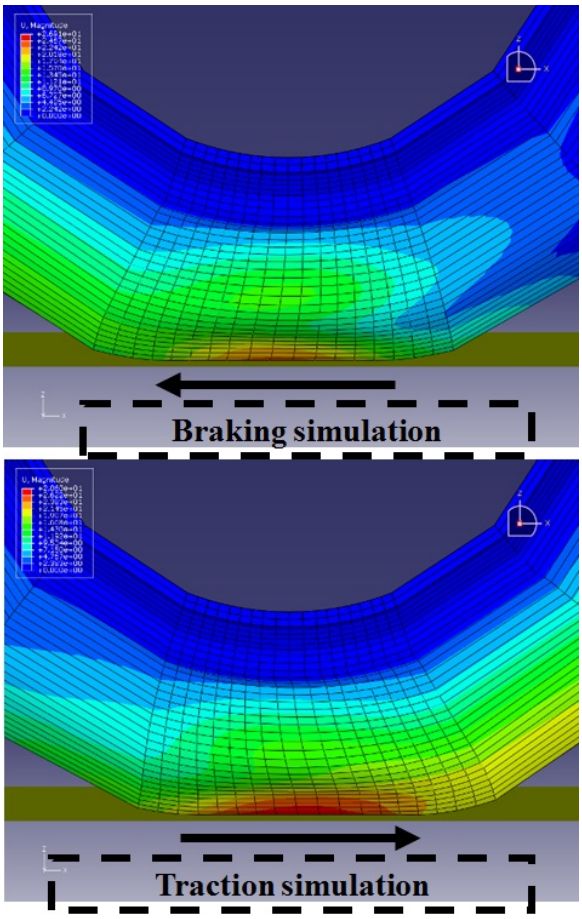

Figure 6.1: Braking and Traction simulation for free-rolling angular velocity (ω) extraction.

A straight line rolling analysis is a combination of a braking and traction simulation (see Fig. 6.1). The purpose of this analysis is to obtain the free rolling equilibrium solution (that is the torque on the axle is zero) for a velocity of 10 kph on a rigid flat surface. To achieve

this equilibrium condition a full braking and full traction condition is required. In the first step for the full braking condition the corresponding angular velocity is estimated as follows. A free rolling tire will travel farther in one revolution than determined by the loaded tire radius, but less than determined by the unloaded tire radius. The unloaded tire radius is 339.38 mm and for a maximum vertical deflection of 20 mm, the wheel center height=319.38 mm. Now using the unloaded radius and applied deflection, it is estimated that free rolling occurs somewhere between an angular velocity ω=8.18 rad/s and 8.69 rad/s. It is clear that smaller angular velocities will result in braking and larger angular velocities would result in traction. Hence an angular velocity ω=8.0 rad/s is used to run the braking simulation to ensure a steady-state solution is in the braking condition region.

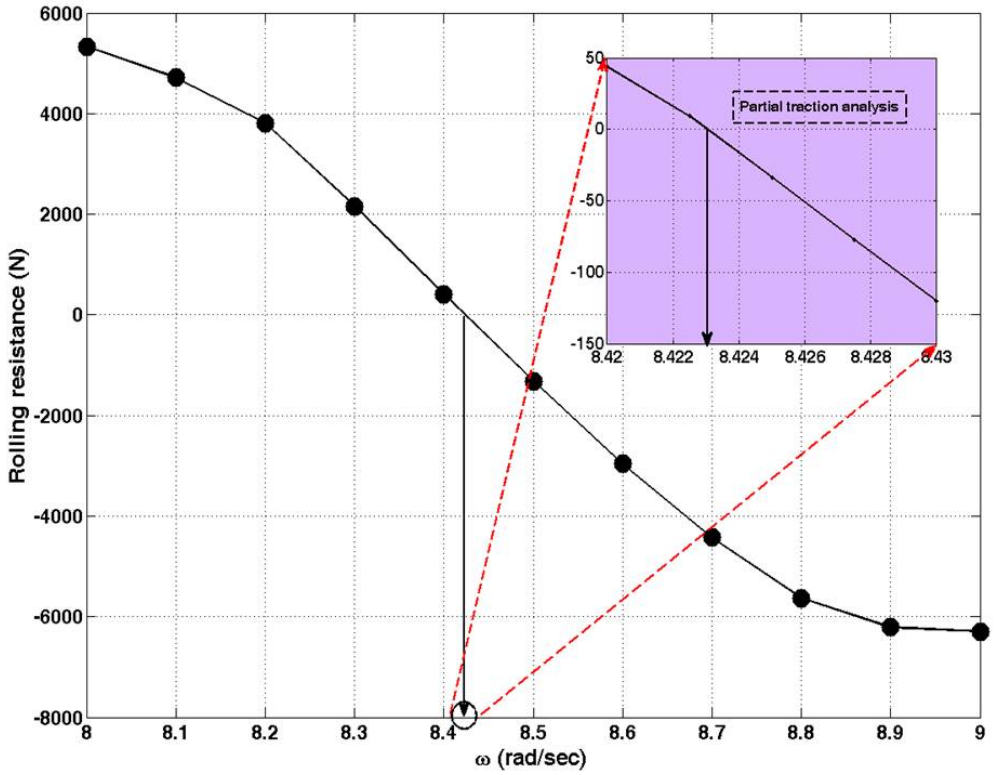

Figure 6.2: Rolling resistance versus angular velocity for free-rolling angular velocity (ω) extraction.

In the next step the angular velocity is gradually increased to ω=9.0 rad/s while keeping the wheel velocity constant. Since the solution at the end of each time step is a steady-state solution each of the time step would correspond to a steady state solution under the full braking and traction condition.

To better understand when free-rolling occurs, rolling resistance is plotted (Fig. 6.2) versus the angular velocity. From Fig. 6.2, it can be seen that free rolling occurs when the torque on the axle is zero and thus providing an estimate of the free rolling angular velocity. A partial traction analysis (see inset Fig. 6.2), which is performed in the neighborhood of the estimated angular velocity, is next performed to obtain a more refined solution of the free rolling angular velocity.

6.2 Steady-State Free-Rolling at Various Slip Angles

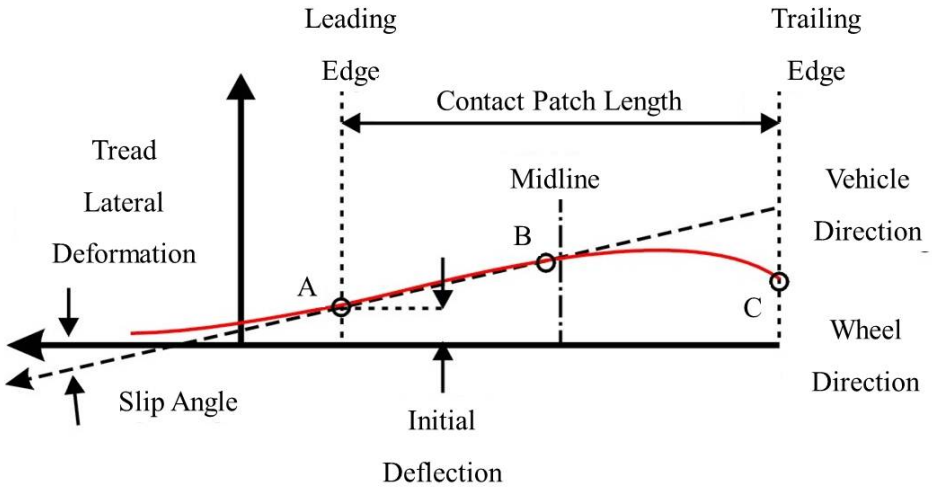

Figure 6.3: Lateral tread deformation under steady state cornering.

Once the free-rolling angular velocity is estimated it is used in all the steady state simulations involving various slip angles. By definition, slip angle is the angle between the vehicle heading direction and the tire heading direction. Slip generally occurs while the vehicle is negotiating a corner or turn. This is oftentimes referred to as cornering. The effect of cornering induces a force in the lateral direction. The lateral force is self induced by the tire in response to the direction in which the tire is being steered. The lateral tread deformation that occurs while cornering is pictorially depicted in Fig. 6.3.

The boundary conditions for the slip angle simulation are shown in Fig. 6.4. For this simulation it is required that both the translational and rotational velocities be supplied. The translation velocity, which in the free-rolling case is the wheel velocity, is decomposed into longitudinal and lateral components. And the rotational velocity is the free-rolling angular velocity estimated in the braking and traction simulations. To incorporate slip angles from 0^o to 6^o, the longitudinal and lateral components of the vehicle velocity are supplied to the FEA code as,

$$v_x = v_0 cos(\theta) \quad v_y = v_0 sin(\theta) \tag{6.1}$$

where v_0 is the vehicle velocity and v_x and v_y are longitudinal and lateral components respectively.

All other boundary conditions are kept intact for the parametric normal load(1000lbs, 1200lbs, 1400lbs and 1600lbs) cases. Each case simply involves restarting the whole simulation for a particular load that needs to be modeled. The simulation time for each the cases considered varies. The low normal load (1000 lbs) cases have a shorter simulation time while the high normal loads (1600lbs) have a longer simulation times. The average time to completion of each simulation varies from 20 mins to 2 hrs on a computer with 4 GB RAM and 3 GHz speed.

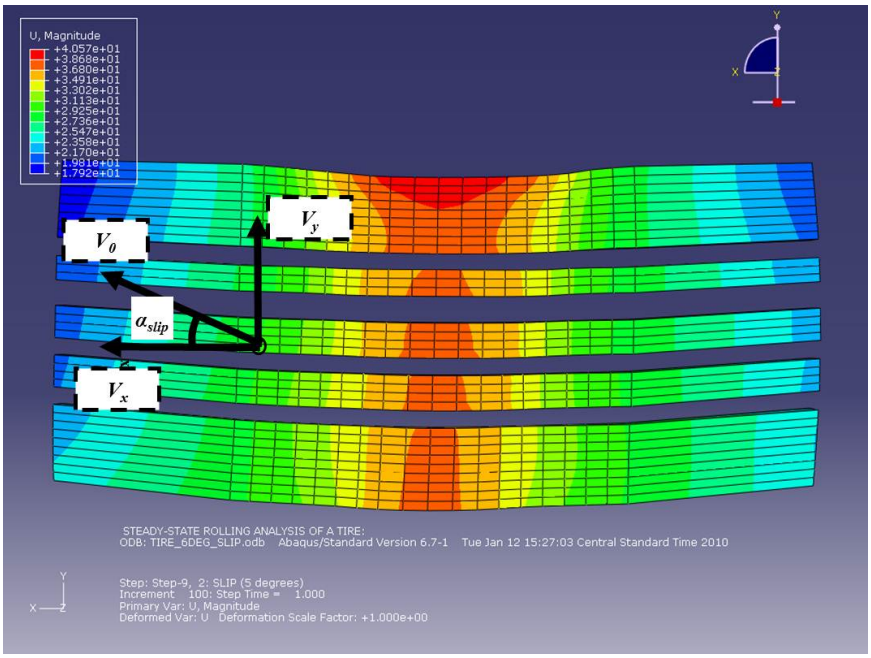

Figure 6.4: Boundary condition for free-rolling at various slip angles.

6.3 Strain Profile Under Steady-State Free-Rolling

In Fig. 6.5, the strains predicted along the path of sensor 1 for the 1000lbs normal load and all the slip angles modeled ($0^o - 6^o$) is shown. Fig. 6.5 shows that with an increase in slip angle the predicted strains around the tire decreases. At 0^o slip angle, which is also the straight line rolling condition, the strains around the tire are symmetric about the abscissa. The strains predicted from the 1.5^o slip angle case, as can be seen, are also asymmetric about the x-axis. The asymmetry becomes more pronounced with an increase in the slip angle for a given normal loading condition. From this unsymmetrical strain prediction it can been seen that a set of leading and trailing edges are formed. The tread deforms more in the lateral direction in the leading edge region caused by the tire induced lateral force. The region in which the tread does not deform as much, leads to the formation of the trailing edge. From this Fig. 6.5 it can also be seen that contact duration, which is an indicator of the contact length, remains practically constant with change in slip angle for a given particular load.

In the first set of figures (see Fig. 6.6), the strain profiles of normal loads from 1000lbs to 1600lbs in increments of 200lbs and 0^o slip angle are shown. When the nodes go in and out of contact, depending on the tire headed direction, a leading and trailing edge is formed (see Fig. 6.3). For this particular case where a slip angle of 0^o exists, the strain distribution is fairly symmetric about the x-axis. This is consistent with the fact that tire is not cornering and hence a lateral force will not be generated.

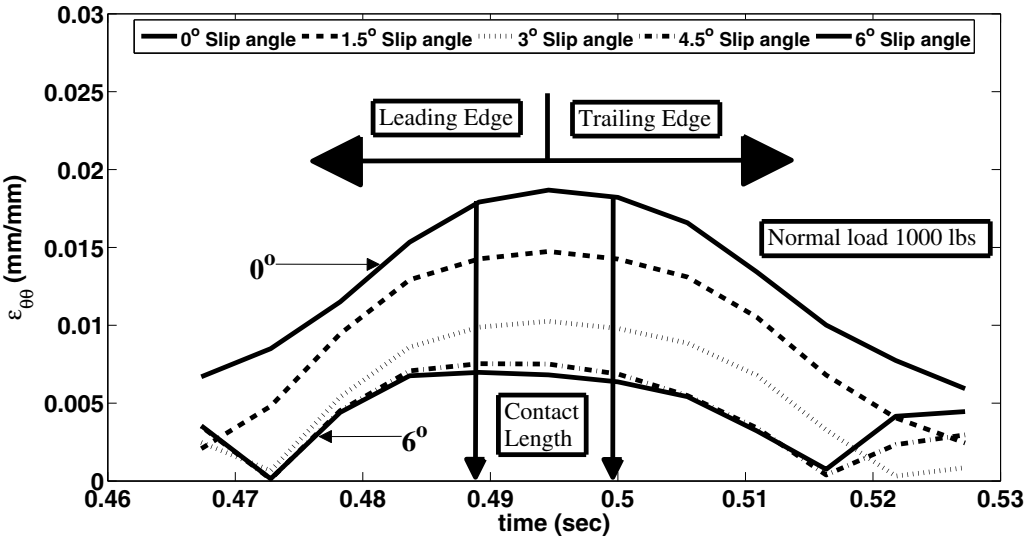

Figure 6.5: Strain profile $0^o - 6^o$ slip angle sensor 1; Normal load 1000lbs.

When tire starts to undergo cornering (ie. $\alpha_{slip} > 0^o$), like in Fig. 6.7, it can be seen that the leading and trailing edges start to differ and the strain profile is not symmetric about the x-axis anymore. This is because the tire induces a force in the lateral direction to counter the effect of slip angle. In doing so the tread deforms in the lateral direction. This phenomenon becomes fairly clear when the slip angle is further increased. It is interesting to note that the average contact duration of these sensors is not a function of slip angle. It appears to be dependent only on the load carried by the tire.

With a sufficient increase in the slip angle, the cornering force produced by the tire tends to dominate the tire deformation. At a slip angle of 3^o (see Fig. 6.8) it should be

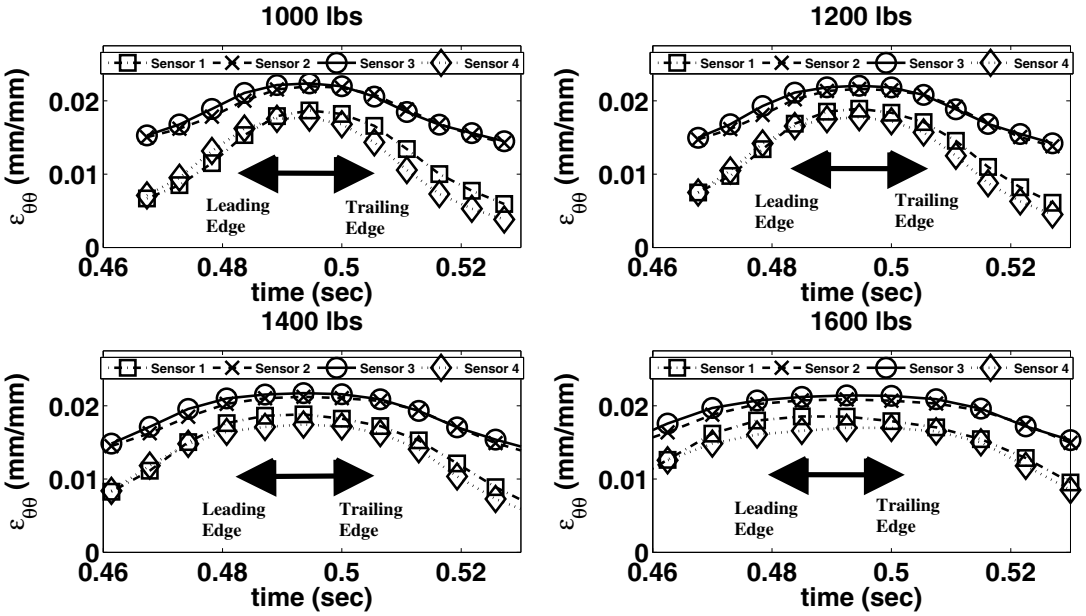

Figure 6.6: Strain profile 0^o slip angle sensors 1, 2, 3,and 4; Loads 1000lbs, 1200lbs, 1400lbs, and 1600lbs.

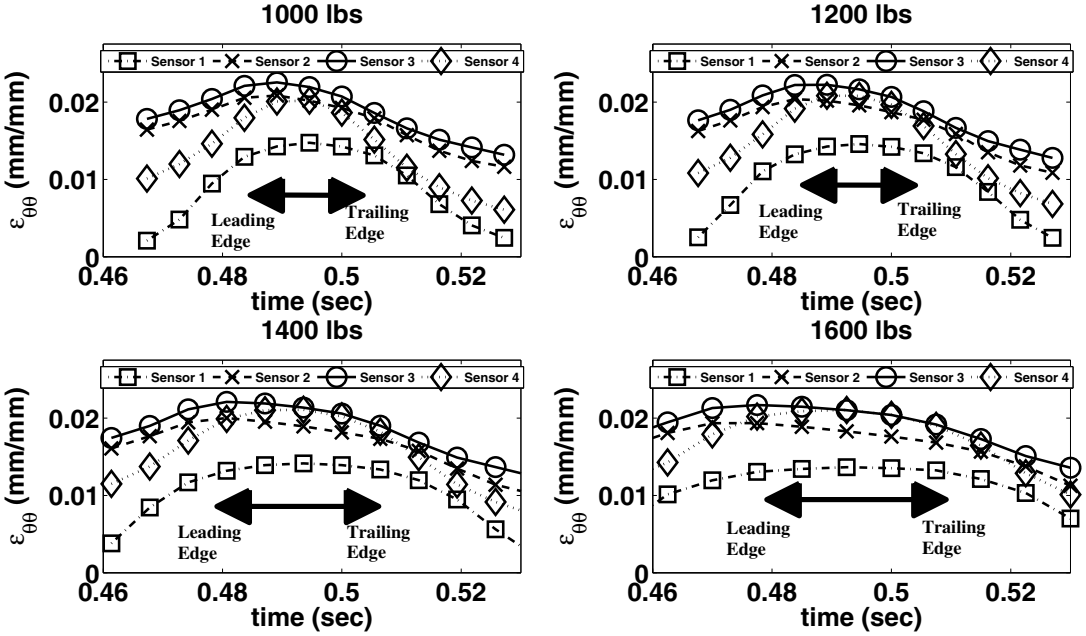

Figure 6.7: Strain profile 1.5^o slip angle sensors 1, 2, 3,and 4; Loads 1000lbs, 1200lbs, 1400lbs, and 1600lbs.

noted that the circumferential strains measured on the tire innerliner become the same for all values of normal load. At this slip angle the lateral deformation seems to be dominating. This can be seen from how the strain curves for sensors 2-4 shift in the direction of lateral deformation. To a certain extent the same effect can be seen for the slip angle case of 4.5^o (Fig. 6.9 for normal loads of 1000lbs-1400lbs for all the sensors and then when the normal load is increased to 1600lbs sensor 2 suddenly drops while sensors 3 and 4 still deform in the lateral direction.

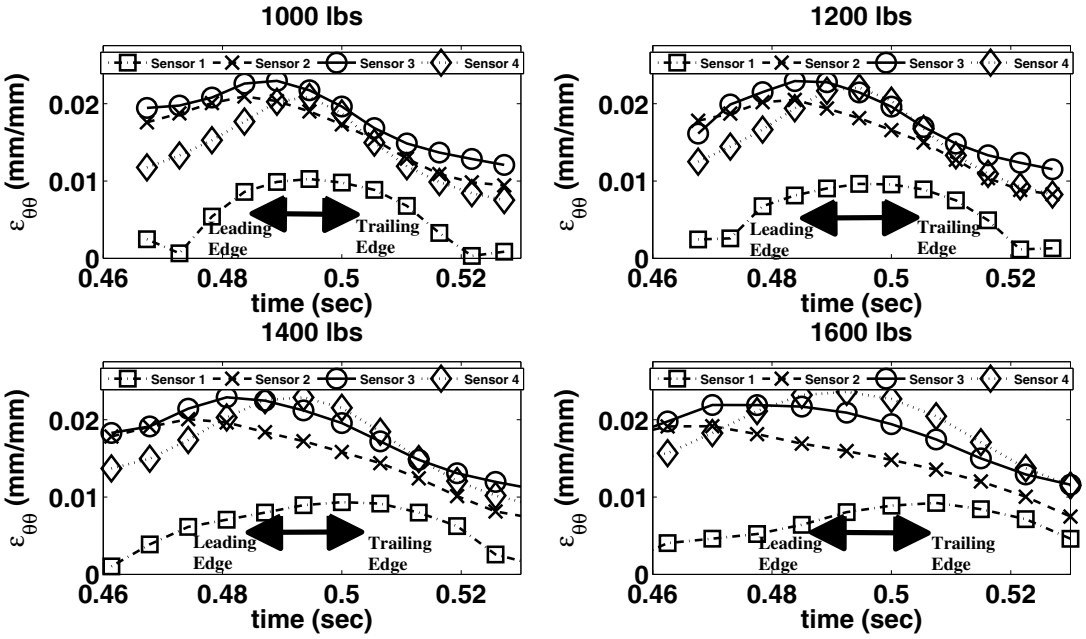

Figure 6.8: Strain profile 3^o slip angle sensors 1, 2, 3,and 4; Loads 1000lbs, 1200lbs, 1400lbs, and 1600lbs.

The lateral tread deformation peaks for the 6^o slip angle (see Fig. 6.10) relative to the lower slip angle values. Once this value of slip angle is reached it can be seen that there is not much difference between the 4.5^o slip angle case and the 6^o slip angle case (Also shown in Fig. 6.5). This is because once the peak value of lateral force is attained (as limited by the friction coefficient), a force saturation occurs and the force no longer increases with slip

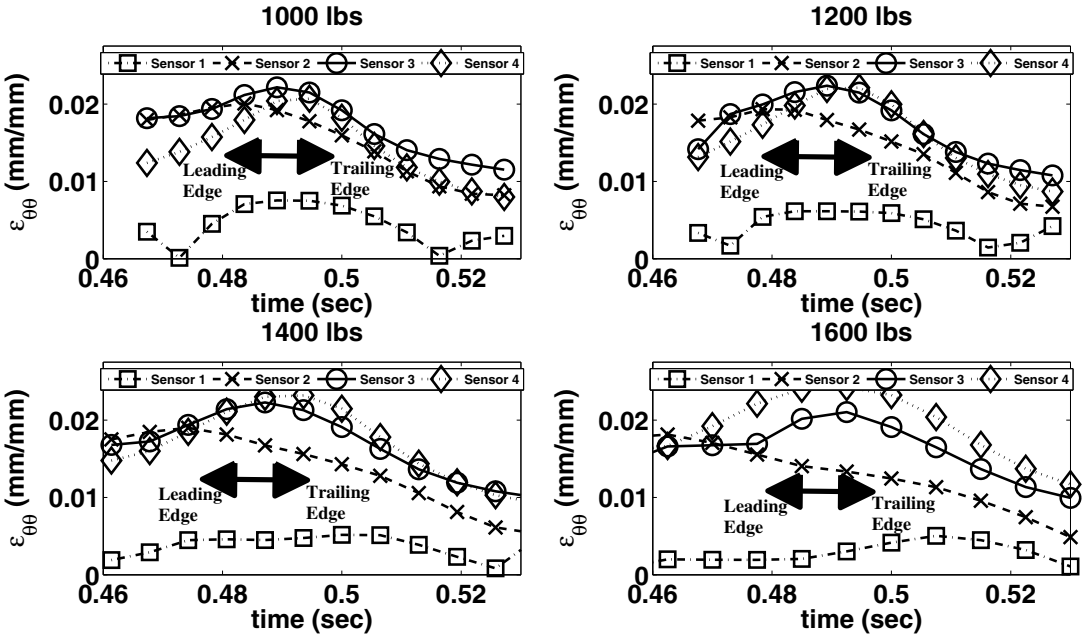

Figure 6.9: Strain profile 4.5^o slip angle sensors 1, 2, 3,and 4; Loads 1000lbs, 1200lbs, 1400lbs, and 1600lbs.

angle. This would mean the tread can deform no more in the direction in which the lateral force is acting.

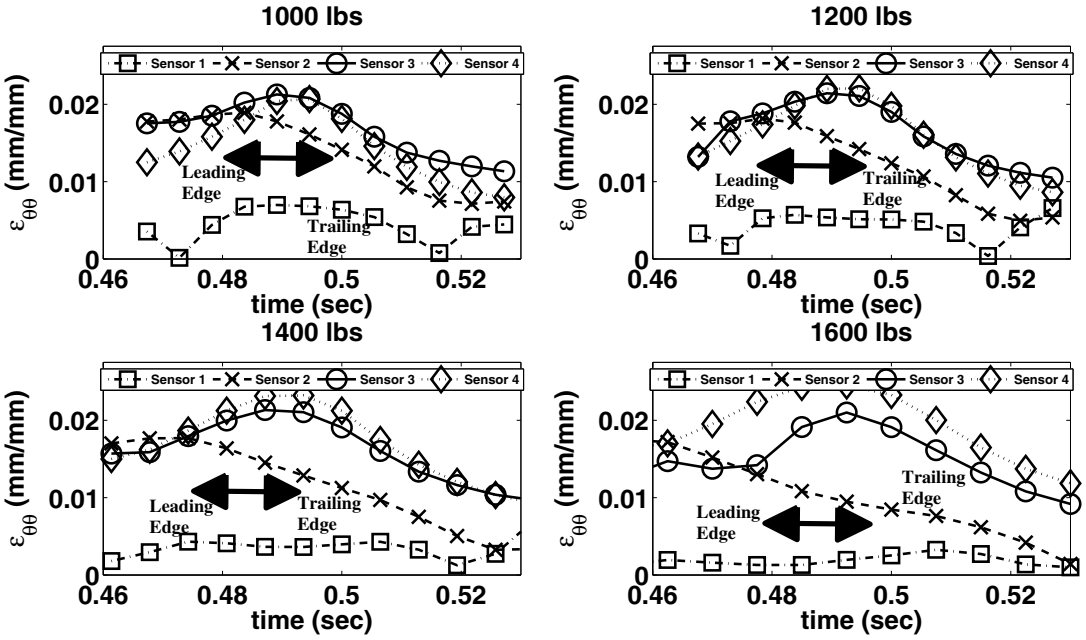

Figure 6.10: Strain profile 6^o slip angle sensors 1, 2, 3,and 4; Loads 1000lbs, 1200lbs, 1400lbs, and 1600lbs.

Chapter 7

Strain Analysis Based on Steady-State Free-Rolling Finite Element Prediction

The strain predictions from the FEM are analyzed using various numerical techniques. The biggest challenge lies in developing relationships between tire operating conditions and the measured or the predicted strain. Hence this chapter evaluates several of different methods that might be used.

7.1 Fourier Analysis

The Fourier analysis is a subject area in mathematics which came into existence from analyzing a Fourier series. The Fourier formula of a typical Fourier series involving 2π-periodic functions with sines and cosines for a function $f(x)$ that is integratable over the the period $[-\pi, \pi]$ is given by,

$$F(s) = \frac{a_0}{2} + \sum_{n=1}^{N} \left[a_n \cos(nx) + b_n \sin(nx)\right] \tag{7.1}$$

where,

$$a_0 = \frac{1}{\pi} \int_{-\pi}^{\pi} f(x)\, dx \tag{7.2}$$

$$a_n = \frac{1}{\pi} \int_{-\pi}^{\pi} f(x) \cos(nx)\, dx \tag{7.3}$$

$$b_n = \frac{1}{\pi} \int_{-\pi}^{\pi} f(x) \sin(nx)\, dx \tag{7.4}$$

The Fourier transform, is a technique that involves transforming the data from the time domain to the frequency domain. One way to efficiently implement this technique is to use Fast Fourier Transform (FFT) to compute the fourier transform. This method is

implemented in the current work by taking the FFT of the strain data over the contact patch region. The FFT of the strain data yields (see Fig. 7.1) the frequency spectrum. In Fig. 7.1 the strain data from sensor 1 is considered for the Fourier analysis for various slip angles and a normal load of 1200lbs. It can be seen that the amplitude changes occur with different slip angles, but remain fairly constant for upto 100Hz.

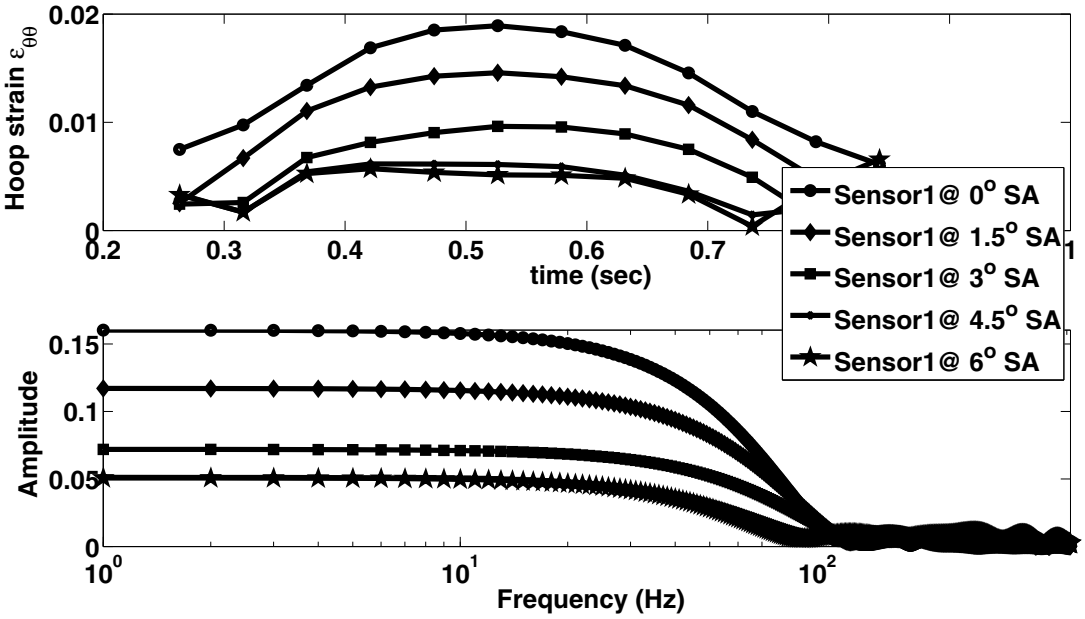

Figure 7.1: Fast Fourier Transform of the strain data (Sensor 1; 1200lbs normal load).

Fig. 7.2 shows the strain profile along the path of sensor 2 and the FFT of the strain data. It can be seen that the frequencies from 1 to 20 or so all contribute to the entire spectrum. An FFT of sensor 3 (see Fig. 7.3) and sensor 4 (see Fig. 7.4) show no variation with normal load. Amplitude change alone is not sufficient to quantify the necessary parameters.

The strain profile and the FFT over the data from sensors 3 is shown in Fig. 7.3. For the first few frequencies the amplitude change is noticed when the slip angle is varied. The amplitude change is maximum for the 0^o slip angle case and with changes in the slip the amplitude too changes. The length of contact however is not captured even though the strain data is for the contact patch region. This missing information can be a factor that is

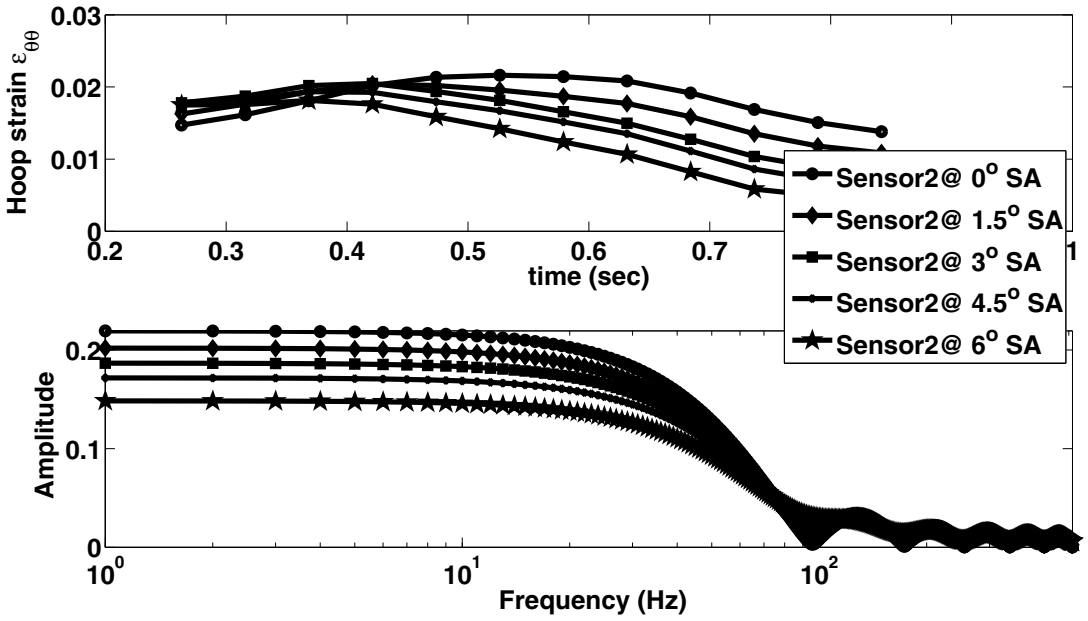

Figure 7.2: Fast Fourier Transform of the strain data (Sensor 2; 1200lbs normal load).

influenced by the resolution, in this case the number of elements, being insufficient for this method to work. Next the strains along sensor 4 (see Fig. 7.4) is analyzed. The same trend as seen with strains along the other sensors is realized. The amplitude change is noticed when the slip angle varies, but the contact length is not to be noticed with change in the normal load. This issue is further analyzed by extracting the first few frequencies and then all the parameters necessary, which are the normal load and slip angle, are plotted in uniform three dimensional array.

An FFT is then performed over the parametric loading cases. The amplitudes from the first few frequencies is then analyzed. Figs. 7.5– 7.8 are the plots of the parametric cases of normal load and slip angles. Normal load of 1000lbs, 1200lbs, 1400lbs and 1600lbs and slip angles of 0^o-6^o are considered. It can be seen that the extracted amplitude changes with slip angle but does not exhibit any significant change with the normal load. From this method only slip angle can be predicted from all the contributing frequencies, the other parameter (normal load) cannot be estimated from this method.

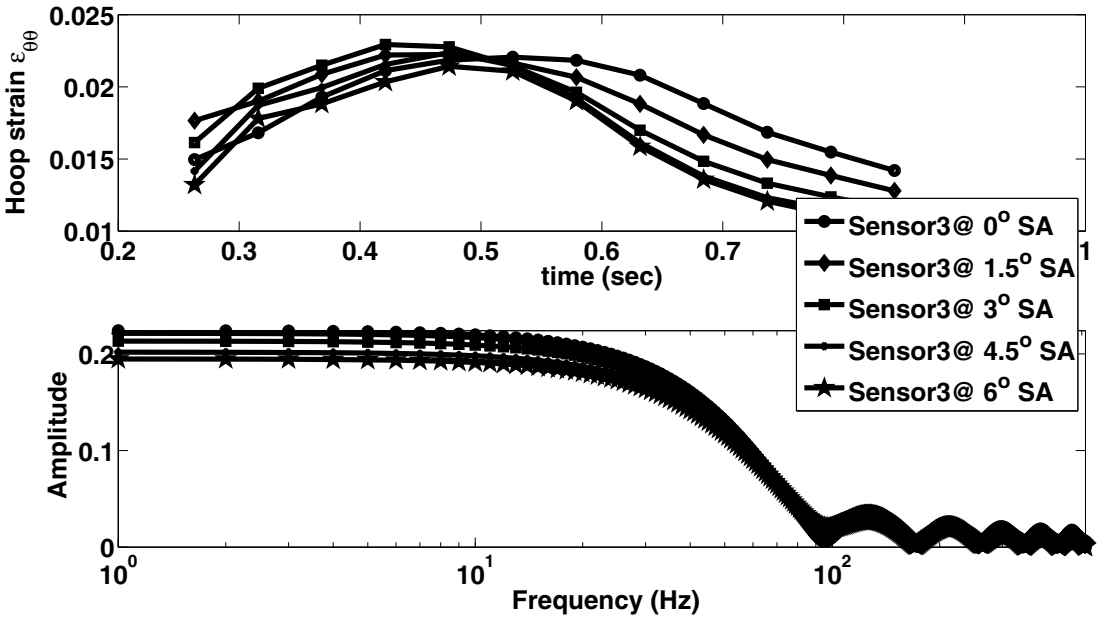

Figure 7.3: Fast Fourier Transform of the strain data (Sensor 3; 1200lbs normal load).

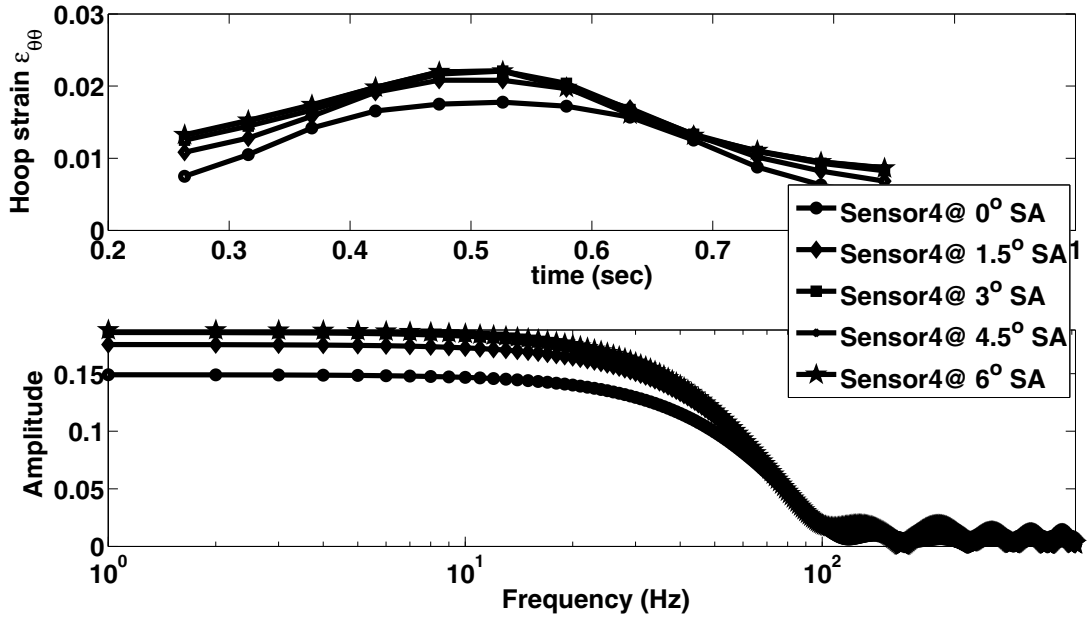

Figure 7.4: Fast Fourier Transform of the strain data (Sensor 4; 1200lbs normal load).

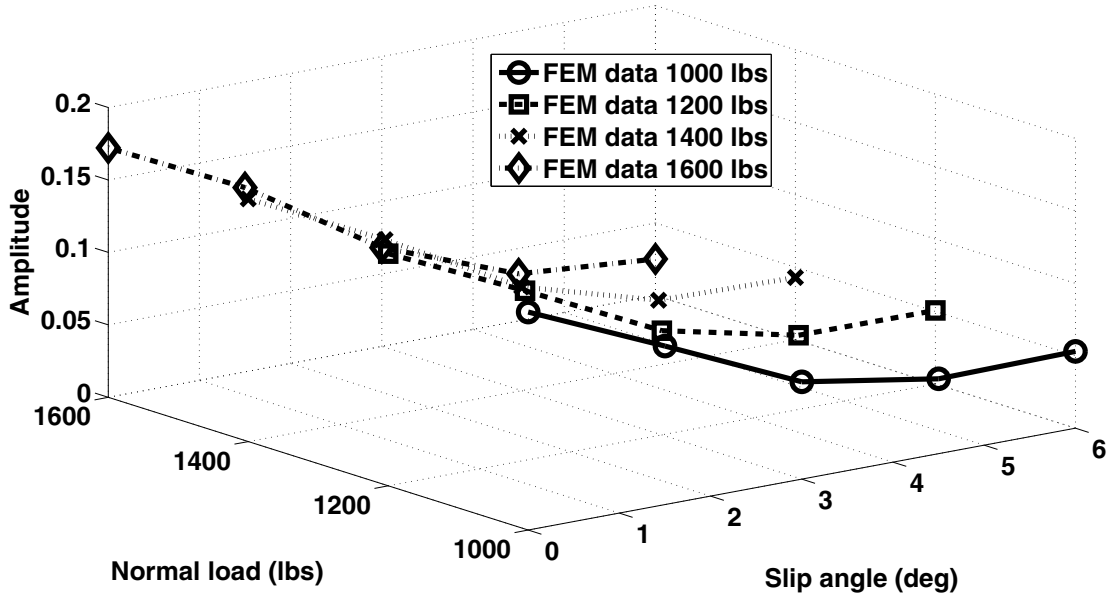

Figure 7.5: Relating amp. changes to normal load and slip angle 2^{nd} frequency (sensor 1).

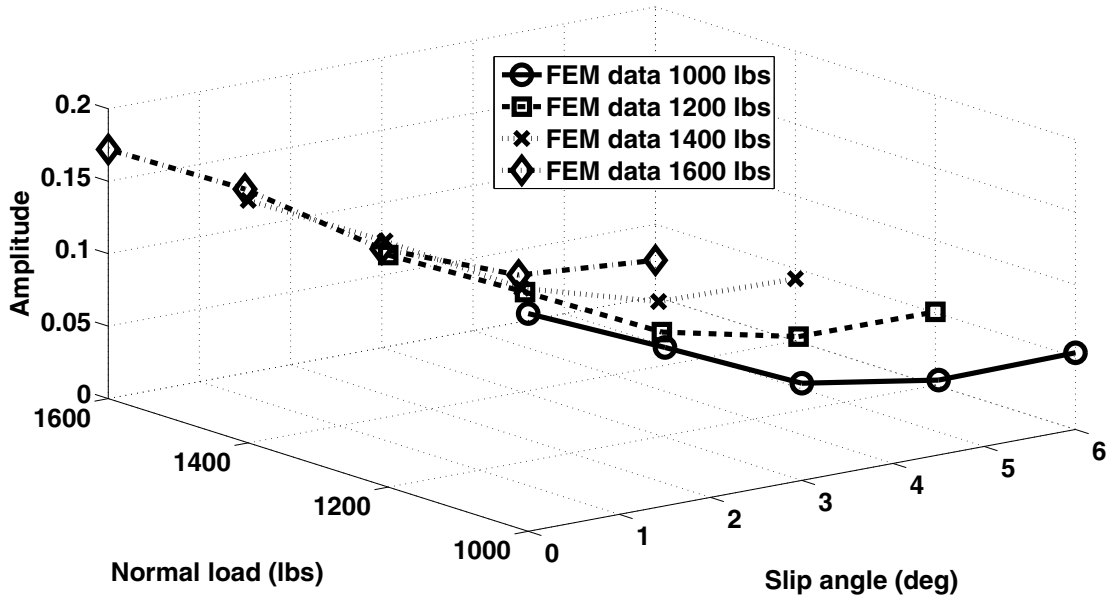

Figure 7.6: Relating amp. changes to normal load and slip angle 3^{rd} frequency (sensor 1).

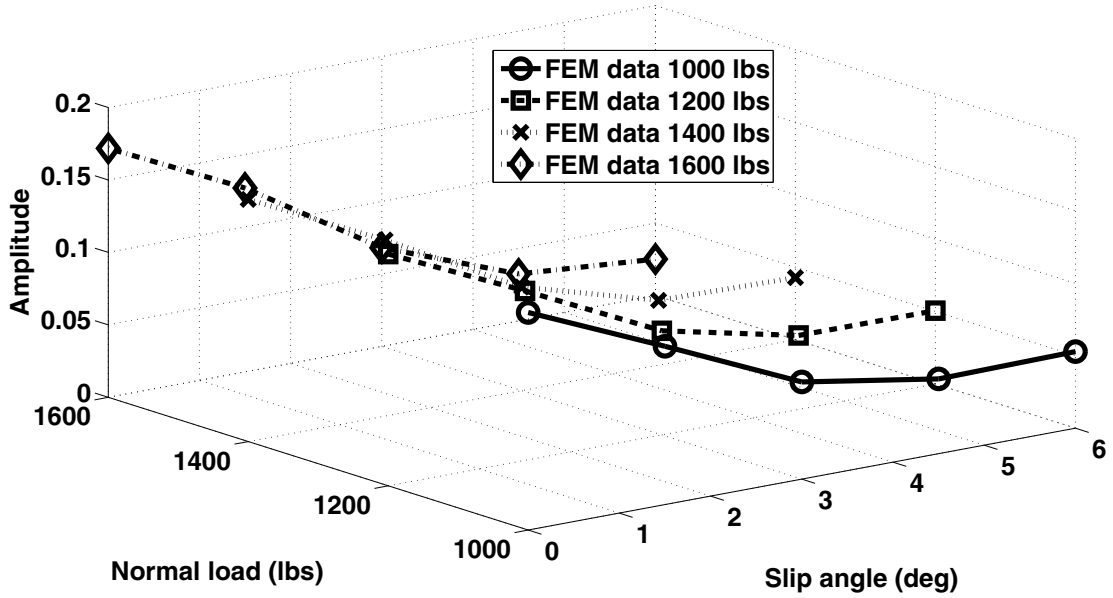

Figure 7.7: Relating amp. changes to normal load and slip angle 4^{th} frequency (sensor 1).

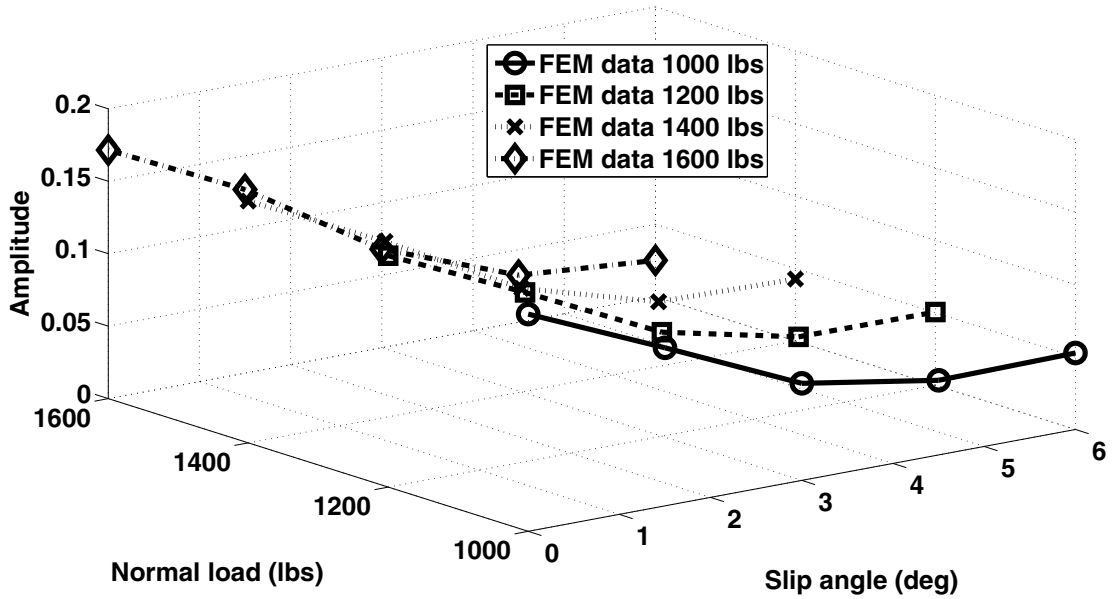

Figure 7.8: Relating amp. changes to normal load and slip angle 5^{th} frequency (sensor 1).

7.2 Weibull Curve Fitting

The Weibull distribution is typically used in reliability studies where life cycle predictions are made based on the data distribution. It is a versatile and easy to use distribution which can take the characteristics of other distributions, simply based on the shape parameter β. An example of Weibull distribution is shown in Fig. 7.9. A function that is used for making predictions is as follows,

$$f(x) = \begin{cases} \frac{\beta}{\lambda}\left(\frac{x}{\lambda}\right)^{\beta-1} e^{-\left(\frac{x}{\lambda}\right)^{\beta}} & \text{x>=0} \\ 0 & \text{x<0} \end{cases} \tag{7.5}$$

where β is the shape parameter and λ is the scale parameter. And as the name suggest the way the shape and scale of the curve changes, the parameters that influence these changes can be predicted.

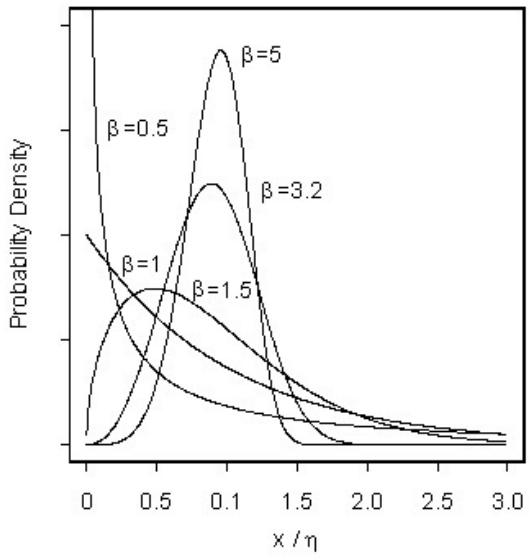

Figure 7.9: Weibull distribution for life cycle prediction[81].

The strain data from the FEM predictions appears to follow the shape of a Weibull type function. Therefore one might be able to fit to the data in order to relate strain to normal load and slip angle. In Fig. 7.10, which is the strain profile for varying slip angles

from sensor 1 for 1200lbs normal load, a Weibull type function is fit to the strain data. This function is given by,

$$\varepsilon_{\theta\theta} = \left(\frac{c}{a}\right)^{\left(\frac{1}{a}\right)} \left(\frac{x}{a}\right)^{\left(\frac{b}{a}-1\right)} \frac{e^{\left(\frac{-x}{a}\right)^{b}}}{c} \tag{7.6}$$

where a is the scale parameter, b is the shape parameter and c is the height parameter. Now, this method simply involves fitting this equation to all the strain data and then relating the function parameters to the loading conditions. The biggest drawback of this method is that it involves fitting too many constants. Also multiple fits are possible for the same strain data and so the Weibull parameters then do not relate directly to changes in load conditions. Hence the prediction model will become highly tire specific. Weibull curve fits to sensors 2, 3, and 4 are shown in Figs. 7.11– 7.13 respectively. It is clear that good fits can be generated for observed strains in a tire but the underlying fact is that this is a very cumbersome process and the number of constants involved is too many.

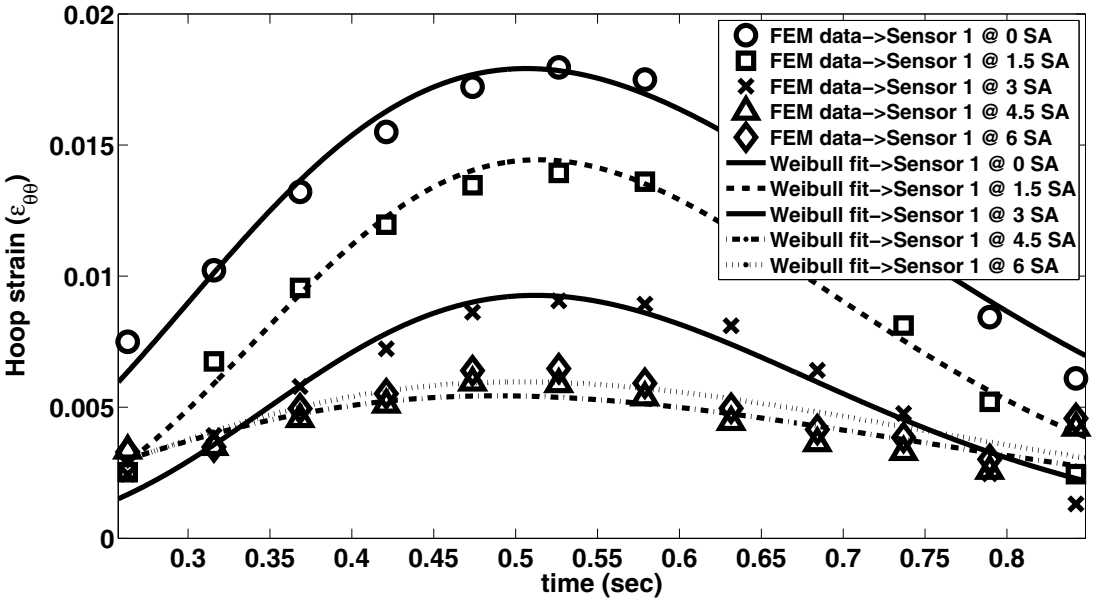

Figure 7.10: Weibull type function fit to strain data (sensor 1).

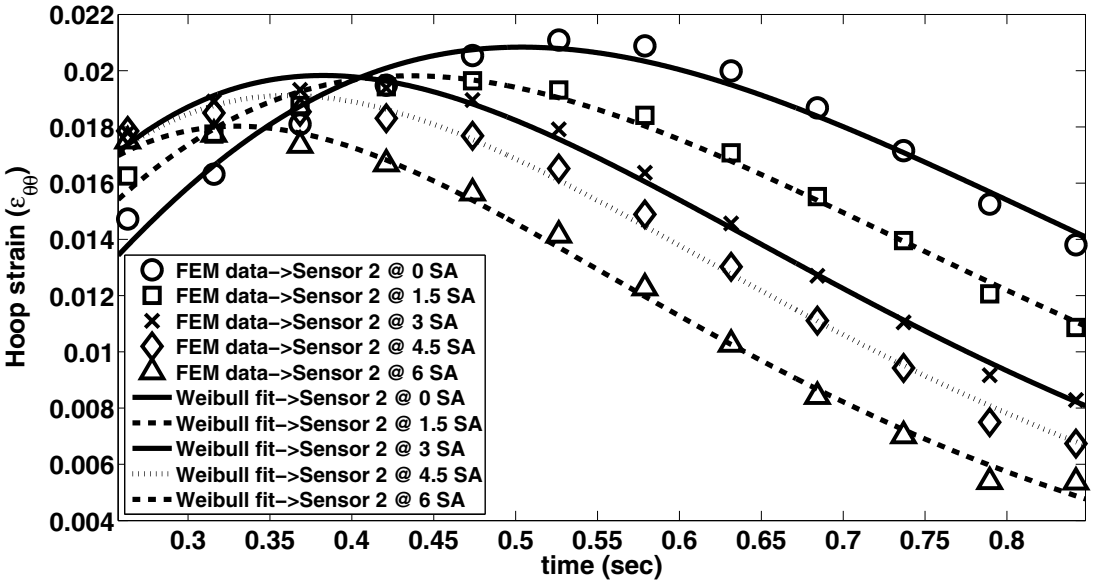

Figure 7.11: Weibull type function fit to strain data (sensor 2).

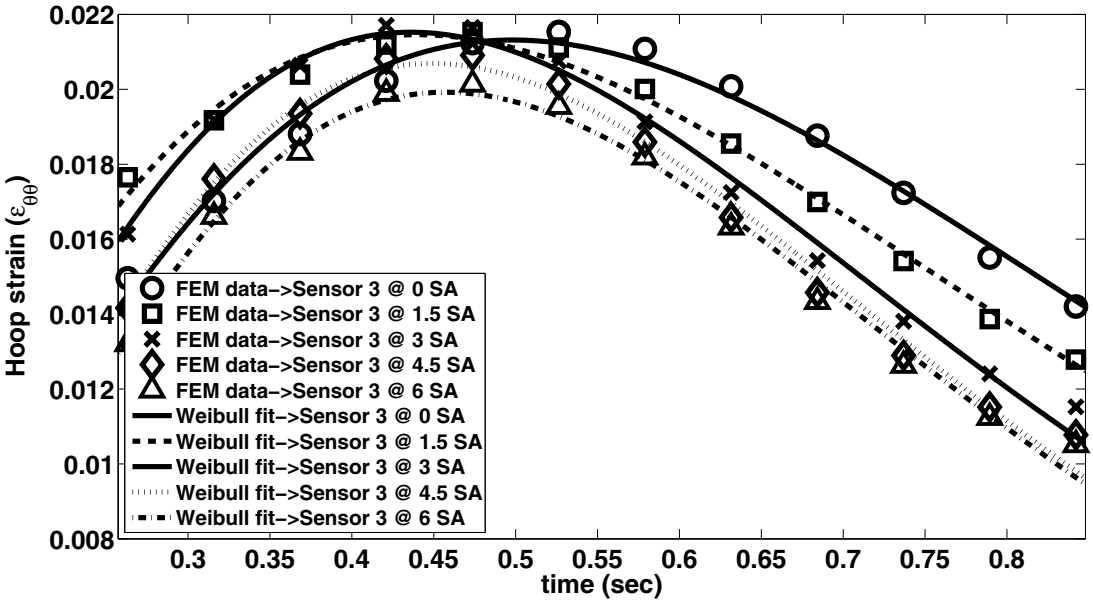

Figure 7.12: Weibull type function fit to strain data (sensor 3).

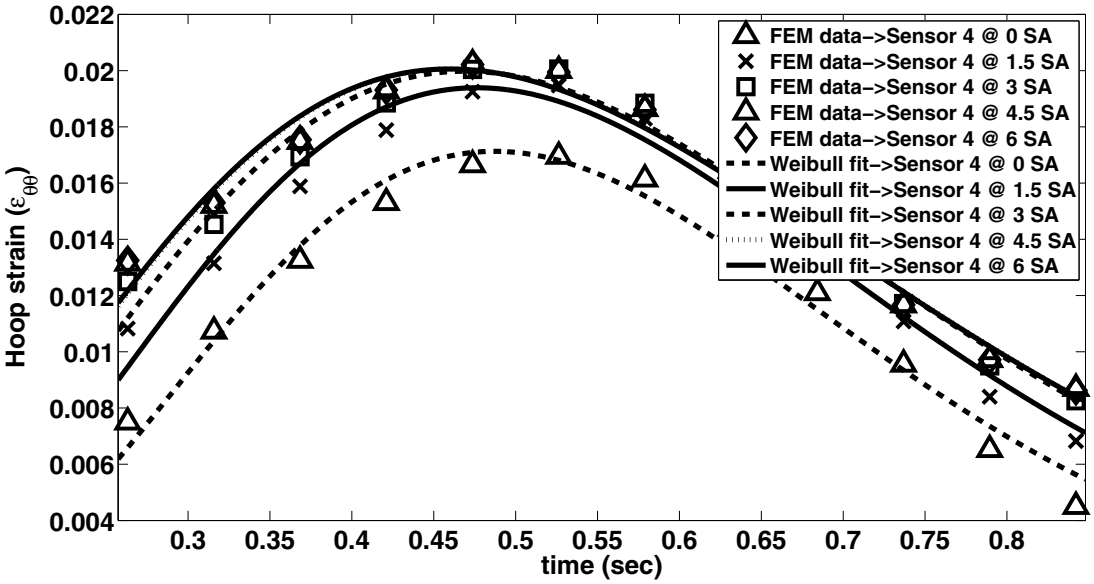

Figure 7.13: Weibull type function fit to strain data (sensor 4).

7.3 Slope Curve Method

In the slope curve method the slope or gradient of the data is predicted by the change in the strain between two consecutive nodes. The basic idea behind this method is that maxima and minima of slope changes would typically occur at the edges of contact. This is because when the sensors go in and out of the contact patch, they will sense maximum strains at the entry and exit points of the patch. And so this would then correspond to two spikes in the slope change profile, one each for a maxima and a minima. The contact duration which is the time difference between the instances of these spikes can then be estimated. The slope change is calculated using the center difference method which is done iteratively over all the nodes under consideration. The center difference for slope change calculation is as follows,

$$\left(\frac{\Delta\varepsilon_{\theta\theta}}{\Delta t}\right)_i = \frac{(\varepsilon_{i+1} - \varepsilon_{i-1})}{(t_{i+1} - t_{i-1})} \tag{7.7}$$

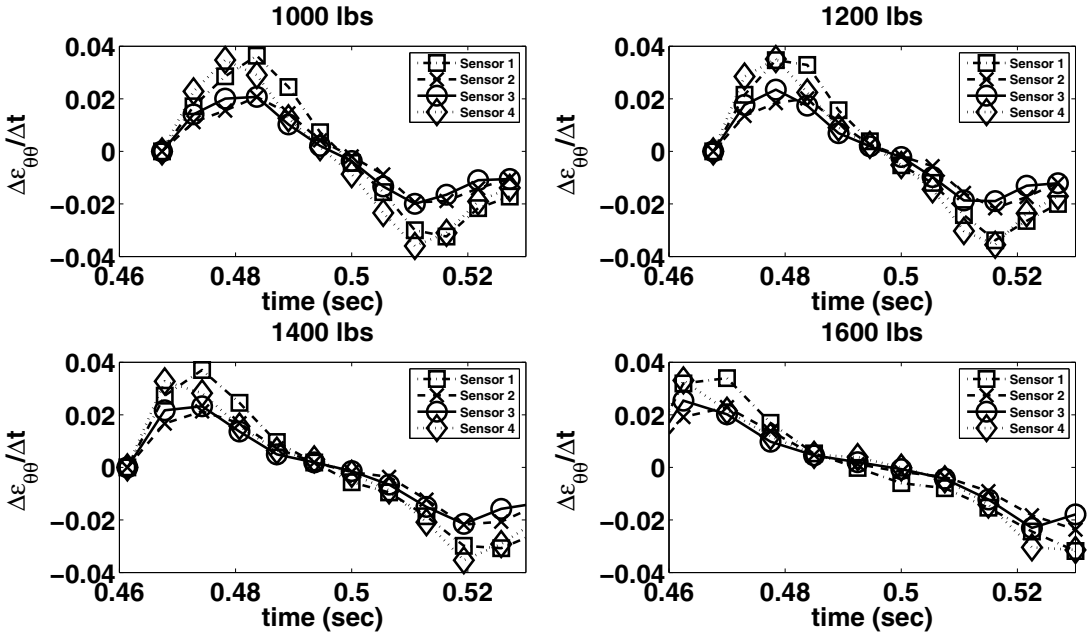

Figure 7.14: Slope change 0^o slip angle (4 sensors and 4 loads).

In order to estimate the contact area under the cornering condition (ie. $\alpha_{slip} > 0^o$), it is imperative to know if the contact patch area changes with slip angle. Intuitively speaking, for a given normal load without any cornering, if the load is symmetric and the tread and road are flat, then the entire width of the tread should be in contact with road. To better understand the effect of cornering on a contact patch area, the slope change method is applied to parametric cases of slip angle and normal load. The free-rolling condition with 0^o slip angle (see Fig. 7.14) is a good starting point to see how the slope change method can be used effectively. For the 0^o slip angle case the slope change prediction is shown in Fig. 7.14. It can be seen that every sensor as it goes in and out of contact generates two peaks which correspond to a maxima and a minima. The difference in time between the occurrences of a maxima and a minima is simply the contact duration.

Next, the slope change for the 1.5^o slip angle case is shown in Fig. 7.15. From this figure it can be seen that the spikes corresponding to the maximum and minimum change in the

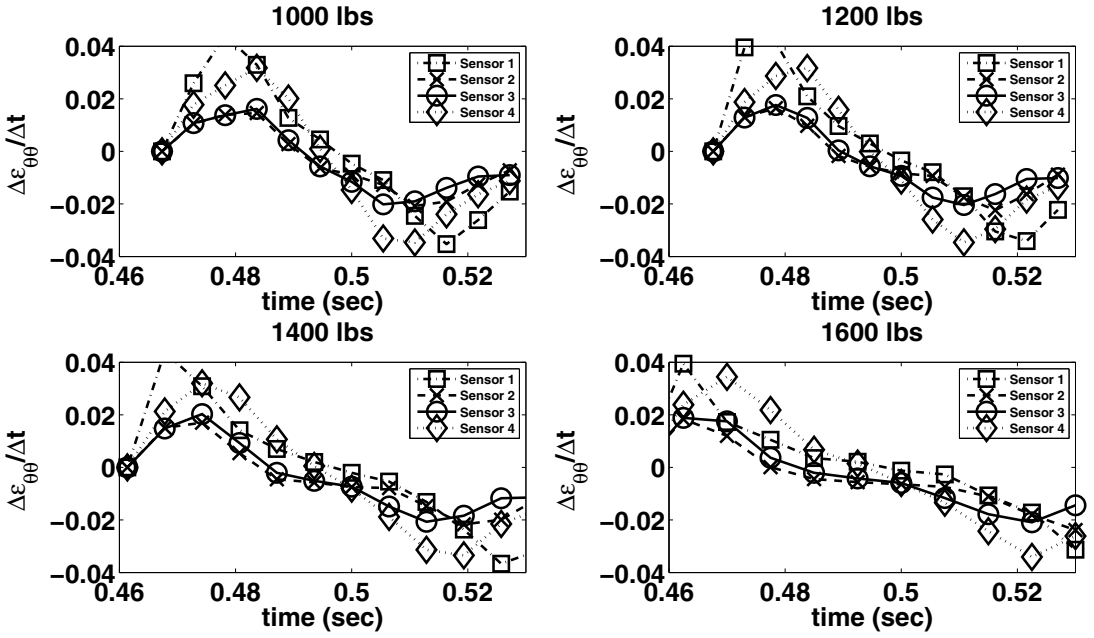

Figure 7.15: Slope change 1.5^o slip angle (4 sensors and 4 loads).

slope with respect to time remains constant with the change in slip angle and only changes when the normal load is varied.

The 3^o slip angle case shown in Fig. 7.16, also exhibits a similar trend, where the peaks (for a particular case of normal load) occur at the same time indicating that the maximum strain values are realized at the edges of the contact. It should be noted that the magnitude of the maximum and minimum slope change decreases with increases in slip angle. A possible reason for this occurrence at higher slip angles could be attributed to high values of the lateral force which could cause the lateral tread deformation making it slightly more pronounced than when there is no slip angle. An interesting thing to note from the slope curve method is the prediction of the contact duration. It is clear that contact duration, which the time difference between the maximum and minimum values of the slope change, remains a constant with change in slip angle. The contact duration appears to be only a function of the load on the tire. This suggests that the average of the contact duration predicted by all four sensors can be used to predict the load on the tire.

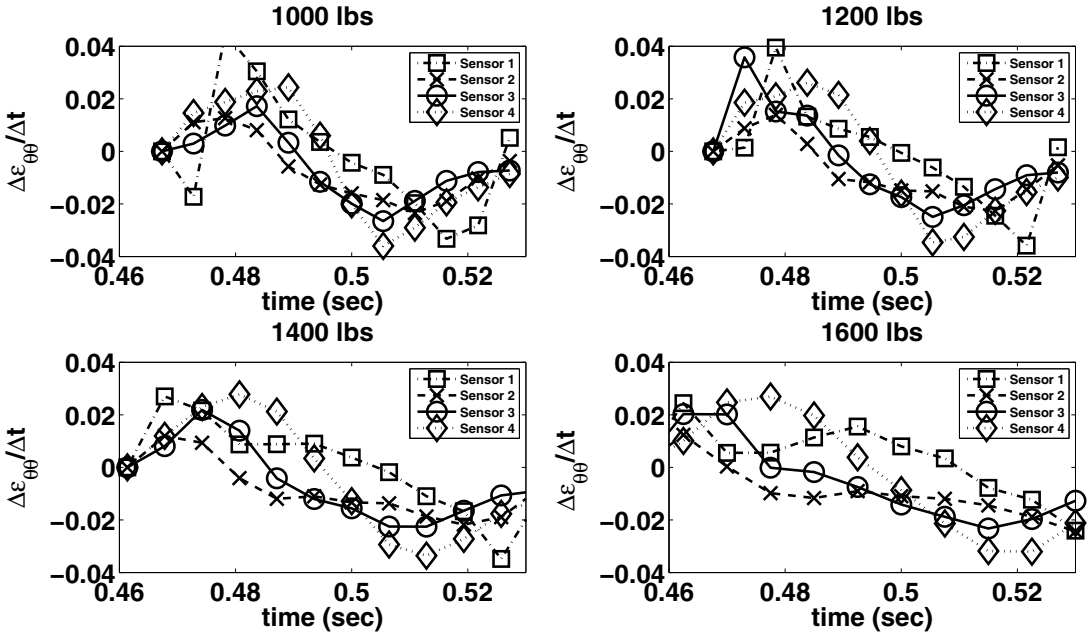

Figure 7.16: Slope change 3^o slip angle (4 sensors and 4 loads).

7.4 Evaluation of Methods for Strain Analysis

The various methods for strain analysis mentioned in the previous sections have their own advantages and disadvantages. To help one narrow down on using the above mentioned techniques, the following observations might prove useful,

Notes on the Fourier analysis are

1. Is a powerful tool, but requires a high sampling frequency to effectively capture trends.
2. Fairly simple procedure once the amplitudes and frequency are extracted from the data.
3. Computationally expensive method.
4. May not be feasible for real-time data processing.

Notes on the Weibull curve fitting are

1. Multiple functions can be made to follow strain data.
2. Too many constants involved, making the model very tire specific.
3. Weibull parameters don't relate to changes in load conditions.

Notes on slope curve method are

1. Fairly simple procedure for parameter estimation.
2. Does not require a high sampling frequency.
3. Slope change could be amplified if the data is noisy. As an alternative something like "total-variation regularization" technique (a method for derivative calculation of noisy data) could be used if the data appears too noisy.

These observations are purely based on the FEM, and since the slope change method works best with the strain data, it is further explored to relate the necessary parameters (normal load, slip angle and lateral force). The steps involved in predicting the necessary parameters based on slope change method are as follows:

1. Collect the strain data.
2. Employ slope curve method.
3. Determine the maximum and minimum change in slope
4. Determine the average contact duration over all four sensors (underlying assumption:contact patch area does not change with slip angle).
5. Estimate the contact area based on average contact duration (this would be a function of the vehicle speed).
6. Predict normal load based on estimated contact area.

Based on the methods explored using the FEM data the procedure shown in Fig. 7.17 will be adopted.

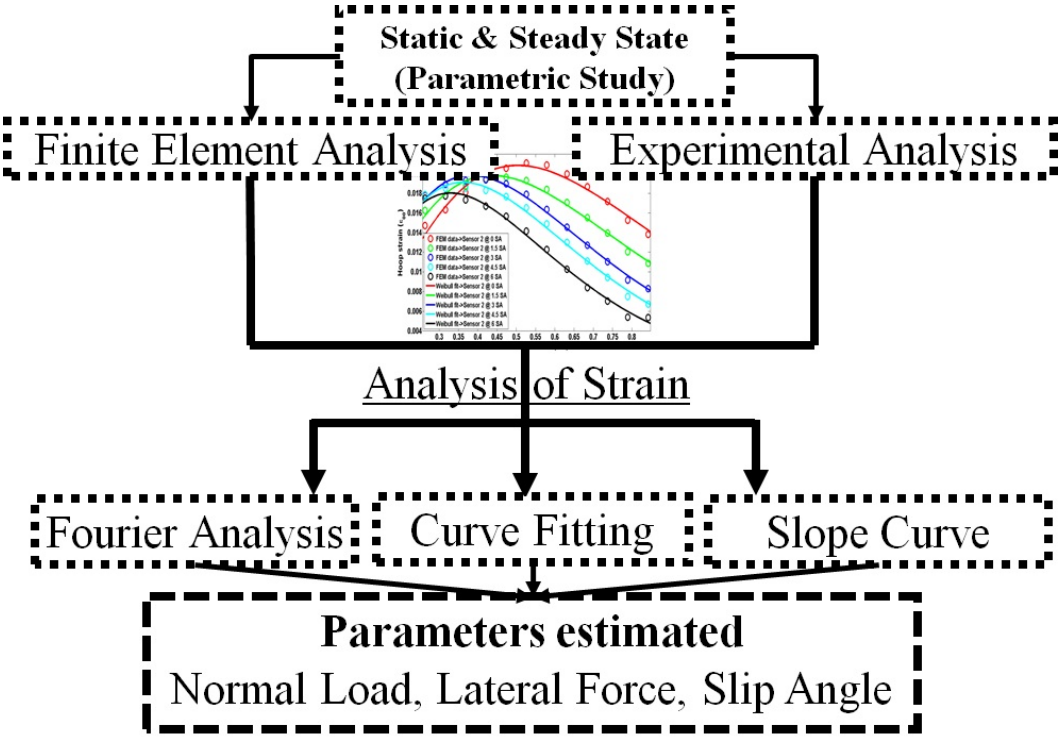

Figure 7.17: Procedure for parameter prediction based on methods explored.

7.5 Normal Load Estimation

The normal load estimation is based on the fundamental equation relating force and pressure when two objects are in contact. This stems primarily from the fact that the load is carried mostly by the inflation pressure rather than the structure of the tire carcass[17]. The equation is given below,

$$f_z = p_{inf} \cdot A_{contact} \tag{7.8}$$

where f_z is the normal load, p_{inf} is inflation pressure and $A_{contact}$ is the contact area. Eq. 7.8 is a fairly good estimate of the normal load on the tire. In practice the pressure term in the above equation needs an additional factor for the equation to work because some of the load is actually carried by the carcass.

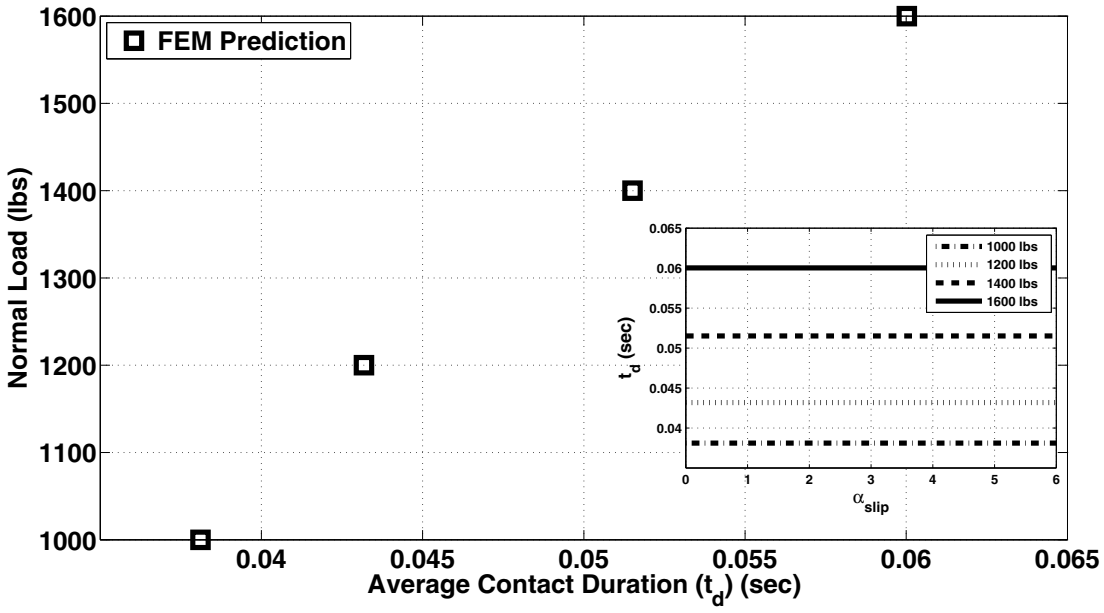

Figure 7.18: FEM prediction of average contact duration.

The predictions from the FEM show that contact area is independent of the slip angle and is only dependent on the normal load applied to the tire. This prediction is used to estimate the contact area, as it can be simply approximated as follows,

$$A_{contact} = v \cdot t_d \cdot w_{tread} \tag{7.9}$$

where v is the velocity of the vehicle, t_d is the average contact duration time and w_{tread} is the width of the tread. The above mentioned equation can also be inferred from Fig. 7.18. In this figure an FEM prediction of the average contact duration for varying normal loads is shown. Once the contact duration is known (this is also an indirect measure of the contact length), the contact area($A_{contact}$) can be quickly estimated with Eq. 7.9.

Now Eq. 7.8 can be modified to incorporate the inflation pressure factor by introducing a additional factor, and so,

$$f_z = f_{fem} \cdot (p_{inf}) \cdot A_{contact} \tag{7.10}$$

where the additional factor f_{fem} is fit to FEM data.

Next the normal load estimated from Eq. 7.10 is plotted (see Fig. 7.19 versus the true normal load (reaction force at the hub). A good correlation is present and the average error between the theoretical model and the finite element model is less than 5%.

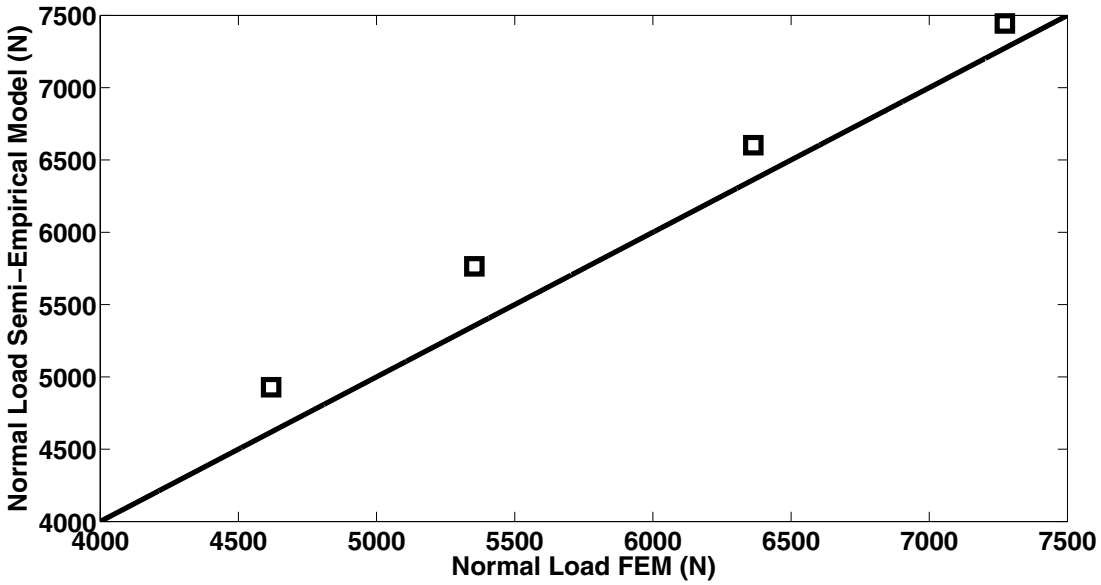

Figure 7.19: FEM versus semi-empirical model prediction of normal load.

7.6 Slip Angle Estimation

7.6.1 Innerliner Deformation Due to Slip Angle

The tire innerliner deformation ideally should follow the tread deformation while the vehicle is cornering. If this is true, then a strain sensor mounted on the innerliner will measure the lateral tread deformation for a given normal load. The relationship that might exist between slip angle and the deformation (which is nothing but the strain) becomes fairly simple to develop.

The top-down view of a tire contact patch is shown in Fig. 7.20. For the sake of visualization, sensors are represented as S_1, S_2, S_3, and S_4. In the current work these labels refer to strain gages. Under the straight line rolling condition, the tread deforms only in

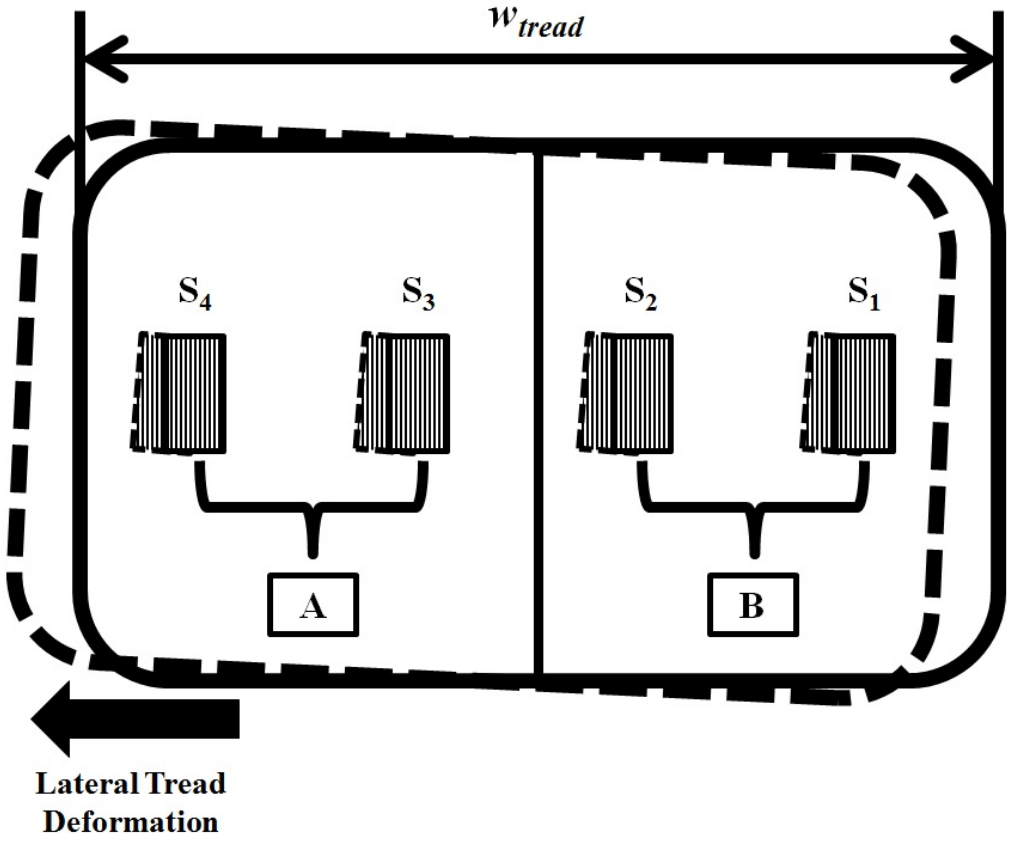

Figure 7.20: Relating lateral tread deformation to the slip angle.

the longitudinal direction. And since it is assumed that the tread and the innerliner deform simultaneously, the sensors should measure the same strains. When cornering occurs, the tread will deform in the direction in which lateral force acts. The sensors on the innerliner now measure the lateral deformation as strains due to the slip angle. The contact patch can be divided into two sections (see Fig. 7.20), section A and section B, in order to relate the lateral deformation to the slip angle. Section A consists of sensors 1 and 2 and section B consists of sensors 3 and 4. The relationship between slip angle and the lateral deformation can be mathematically expressed as a sum of the differences of the strains in section A and section B. This is as follows,

$$\alpha_{slip} = (\varepsilon_4 + \varepsilon_3) - (\varepsilon_2 + \varepsilon_1) \tag{7.11}$$

The physical meaning behind Eq. 7.11 can be inferred by analyzing the changes in the stress distribution in the innerliner due to slip angle. The von-Mises stress from the 0^o slip angle and 1200 lbs normal load (this normal load case, for the sake of argument is used in the rest of this section) condition, which is the straight line rolling condition, is shown in Fig. 7.21. The stress distribution about the xz plane is symmetric as predicted by the FEM. This means that when the sensors go in and out of the contact patch, the lateral deformation is not sensed, as there is only deformation along the longitudinal direction. From Eq. 7.11 it can be quickly concluded that the sum of strain difference between section A and section B is zero.

The stress distribution for the 1.5^o slip angle case is shown in Fig. 7.22. It can be seen that when the slip angle is enforced, that the stress distribution is no longer symmetric about the xz plane. The stresses in section B are more than in section A. This difference is a result of the lateral deformation in response to the slip angle. So when the strain sensors go in and out of contact, depending on the direction in which the tread is deforming, a difference in deformation is sensed by all the sensors. Going back to the section assignment it can be seen that the difference of the sum of strains in each section is simply a function of the slip angle and Eq. 7.11 is just one way to understand the relationship.

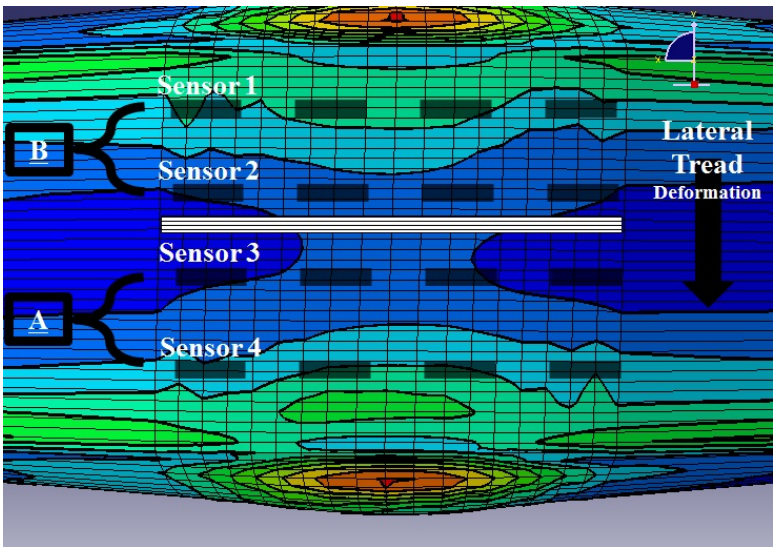

Figure 7.21: von-Mises stress distribution on the innerliner 0^o slip angle and 1200 lbs normal load.

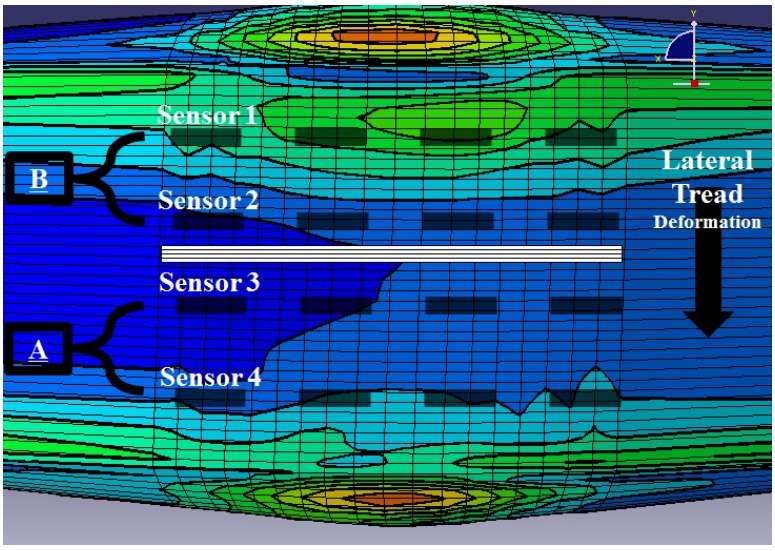

Figure 7.22: von-Mises stress distribution on the innerliner 1.5^o slip angle and 1200 lbs normal load.

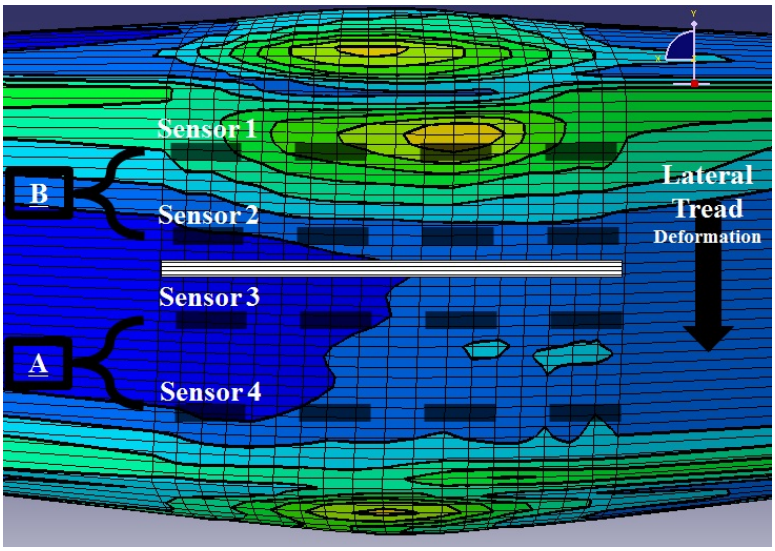

Figure 7.23: von-Mises stress distribution on the innerliner 3^o slip angle and 1200 lbs normal load.

Next the stress distribution for the 3^o slip angle case is analyzed. The von-Mises stress distribution is shown in Fig. 7.23. With the increase in slip angle, the stresses in the tire increase as well. As the slip angle increases a significant amount of stress is developed in section B due to the lateral tread deformation. Again when the sensors trace the contact patch, a difference in the measured strain can be related to the slip angle. As this slip angle the difference in stress values between each individual sensor itself appears to be significant. Since the strains are of more importance to this work, the stress distribution is simply looked at as realizing a physical significance to the proposed Eq. 7.11.

The von-Mises stress distribution for the 4.5^o slip angle case is shown in Fig. 7.24. At this slip angle condition the intensity of the stress distribution in section B becomes more pronounced. The intense distribution extends almost over the entire contact length in section B. Sensors 1 and 2 for every revolution of the tire will sense the strain in response to the lateral deformation. This is also an implication that the strain difference between section B and section A can be related to the slip angle itself for a given load. To put things in perspective, what is important to note is that even though the circumferential strains

predicted by the FEM show an asymmetric trend, the stress distribution appears to be fairly symmetric.

The effect of the friction at the tire road interface also has to be accounted for, as shear stress is induced in the contact patch region. The stress values predicted by the FEM is slightly larger in magnitude than one might expect. The reason for the elevated values is due to the μ=0.85 value used. This affects the lateral deformation as well.

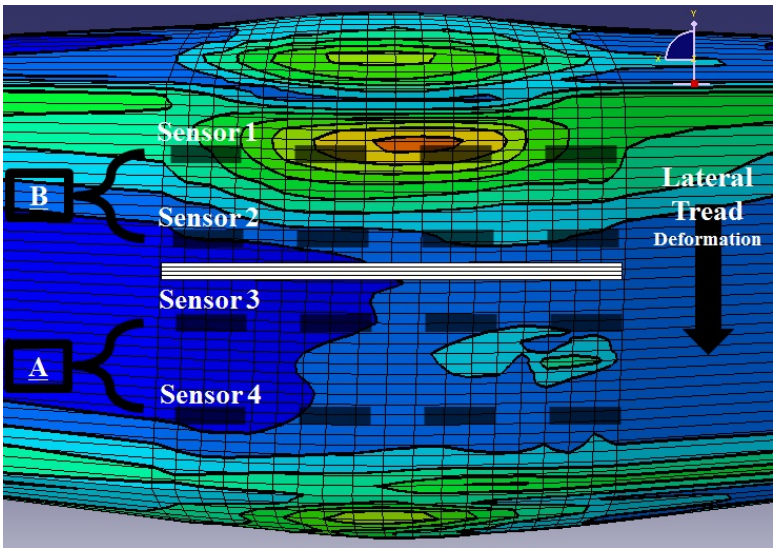

Figure 7.24: von-Mises stress distribution on the innerliner 4.5^o slip angle and 1200 lbs normal load.

In Fig. 7.25, the von-Mises stress distribution for the 6^o slip angle is shown. At this slip angle it can be seen that there is a significant distribution of stress is over the entire contact length in section B. This is an indication that the strains in the innerliner are affected as a result of the slip angle. This simply means that the difference in strains between section A and section B enlarges with increase in slip angle. The variations that may exist even under controlled conditions can be easily accounted for by simply averaging the strains over the entire contact patch. These average values of strains can then be used to develop the necessary equations that relate the tire strains to the slip angle.

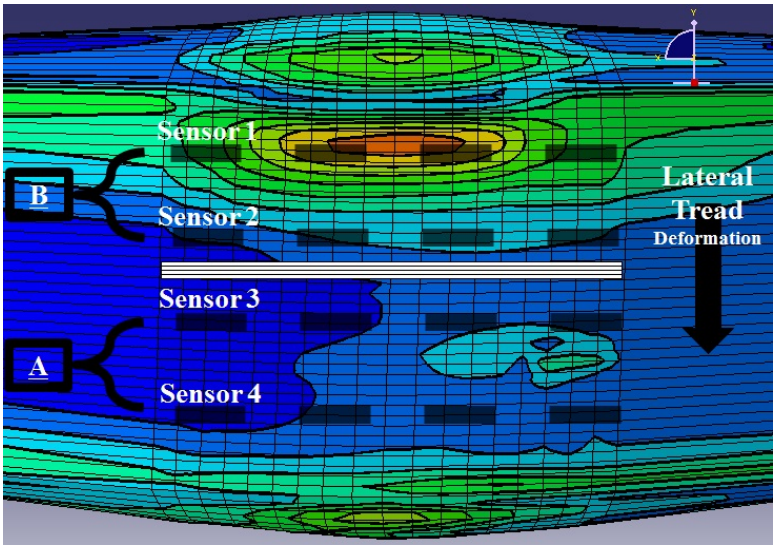

Figure 7.25: von-Mises stress distribution on the innerliner 6^o slip angle and 1200 lbs normal load.

7.6.2 Analytical Relationship Between Strain and Slip Angle

In this section an analytical relationship between the strain and the slip angle is presented. The lateral deformation of the tire innerliner practically follows the lateral tread deformation under the steady state free-rolling condition. The geometry of the contact patch (see Fig. 7.26) can be used to derive an analytical expression which will be used to support the claims in the previous section. The contact patch can be divided into two sections A and B (this is also discussed in the previous section). The outer and the middle edges and the middle and inner edges as shown in Fig. 7.26 form sections A and B respectively. Assuming an original length L, the strains along the outer edge L_{outer} and the inner edge L_{inner} can be analytically expressed as follows,

$$\epsilon_{outer} = \frac{L_{outer}}{L}; \epsilon_{inner} = \frac{L_{inner}}{L} \tag{7.12}$$

Where the outer edge L_{outer} is given by,

$$L_{outer} = \left[R_{ave} + \frac{w_{tread}}{2}\right] \cdot \theta_{patch} \tag{7.13}$$

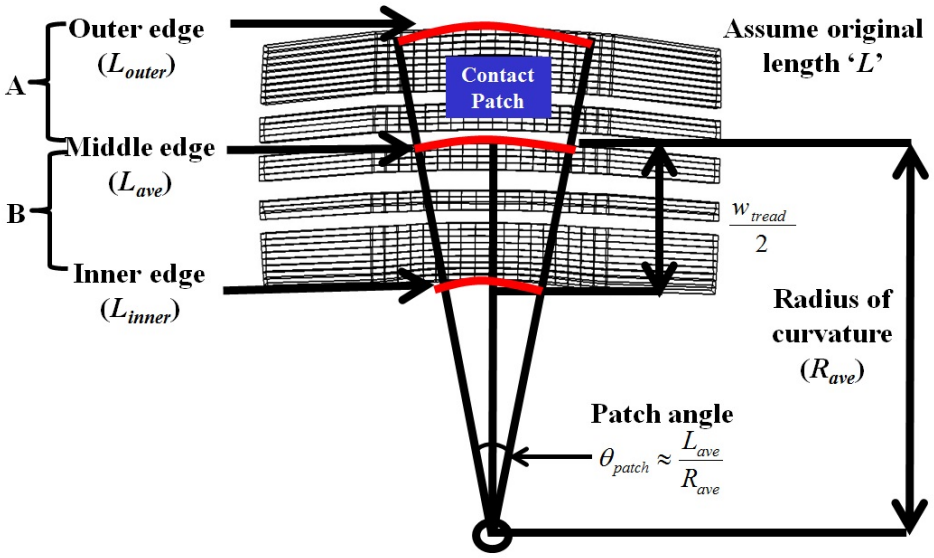

Figure 7.26: Analytical relationship between slip angle and strain.

and the inner edge L_{inner} is given by,

$$L_{outer} = \left[R_{ave} - \frac{w_{tread}}{2}\right] \cdot \theta_{patch} \tag{7.14}$$

In the above mentioned equations (Eq. 7.13 and Eq. 7.14), w_{tread} is the width of the tread, R_{ave} is the radius of curvature given by,

$$R_{ave} = \frac{|1 + (x')^2|^{\frac{3}{2}}}{|x''|} \tag{7.15}$$

and θ_{patch} is the contact patch angle given by,

$$\theta_{patch} \approx \frac{L_{ave}}{R_{ave}} \tag{7.16}$$

Now, from Eqs. 7.13, 7.14 and 7.12 the following conclusion is attained,

$$\epsilon_{outer} > \epsilon_{inner} \tag{7.17}$$

It is clear from the above relationship that the strains measured in section A will be greater than that of the strains measured in section B (this is also consistent with the claims made in section 7.6.1).

7.6.3 Relating Strain to the Slip Angle

The estimation of the slip angle under steady state free-rolling condition will be discussed in this section. It is a fact that load distribution occurs between the tires on a vehicle when negotiating a turn. For example, when a car with front wheel drive is negotiating a turn (see Fig. 7.27), the front tires and the rear tires react from cornering in a different fashion. The front wheels (because of the steering angle), tend to have a larger value of slip angle(α_{slip}) than the rear wheels. An equilibrium is then reached by simply redistributing the normal load, which occurs instantaneously as a reaction to the lateral force. This is one reason why lateral force induced under such a scenario is termed as a self-induced tire force.

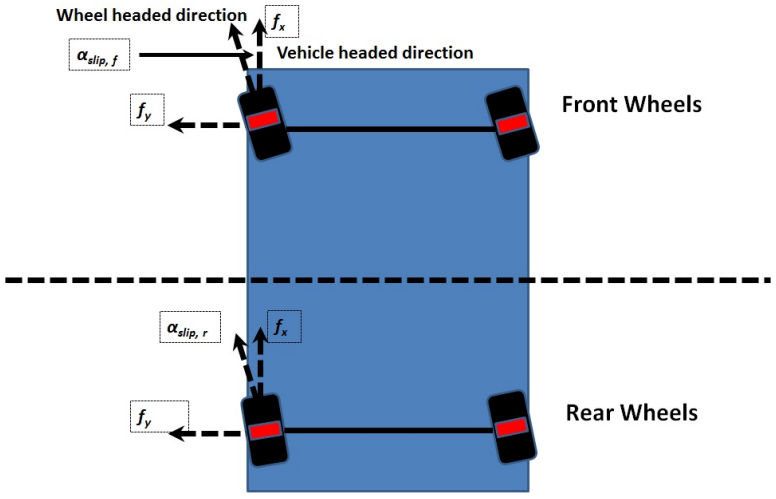

Figure 7.27: Normal load distribution while cornering.

The estimation of slip angle based on the strain becomes rather straight forward once the load on the tire is estimated. The slip angle can be related to the strains by the following variable, $delta_{\alpha_{slip}}$

$$\delta_{\alpha_{slip}} = ((\varepsilon_{ave_4} + \varepsilon_{ave_3}) - (\varepsilon_{ave_2} + \varepsilon_{ave_1})) \tag{7.18}$$

where ϵ_{ave_1}, ϵ_{ave_2}, ϵ_{ave_3} and ϵ_{ave_4} are the average value of the strains in the contact patch. This average value is calculated from knowing the average contact duration, which indirectly gives

an estimate of the contact length. And, $\delta_{\alpha_{slip}}$ is a new term introduced in this estimation process and is referred to as the slip angle strain indicator.

Next, the slip angle is plotted versus $\delta_{\alpha_{slip}}$ (see Fig. 7.28)to obtain an equation relating the slip angle to the measured strain. The fit to the strain data results in an equation, which is of the form,

$$\alpha_{slip} = A_{fem} e^{B_{fem} \cdot \delta_{\alpha_{slip}}} + C_{fem} \tag{7.19}$$

where A_{fem}, B_{fem}, and C_{fem} are load dependent constants fit to the FEM data, H_s is tire section height, W_s is section width and S_{cv} is the suspension comfort value. The estimation of the constants from the resulting fits is discussed in section 7.8.1. It is to be noted that these equations serve as a tool for initial starting point while analyzing the experimental data.

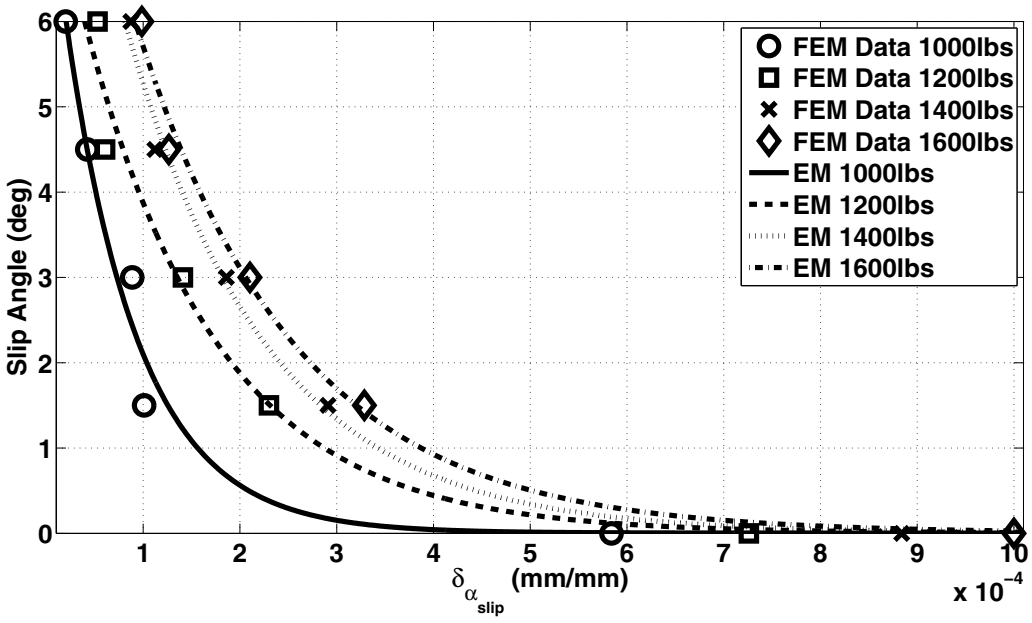

Figure 7.28: Slip angle estimation from FEM.

7.7 Lateral Force Estimation

The tire forces and moments in reality are a complex non-linear function of tire variables which are established based on inputs and vehicle output responses. The primary focus of this work is to establish a relationship between slip angle and cornering force under steady state free-rolling condition. The SAE tire axis system shown in Fig. 7.29 is used in defining the necessary parameters. According to the SAE definition, the cornering force is simply the lateral force when a side slip in the form of slip angle exists. For the sake of consistency lateral force will be used and the condition of steady state free-rolling under various slip angles will be referred to as cornering.

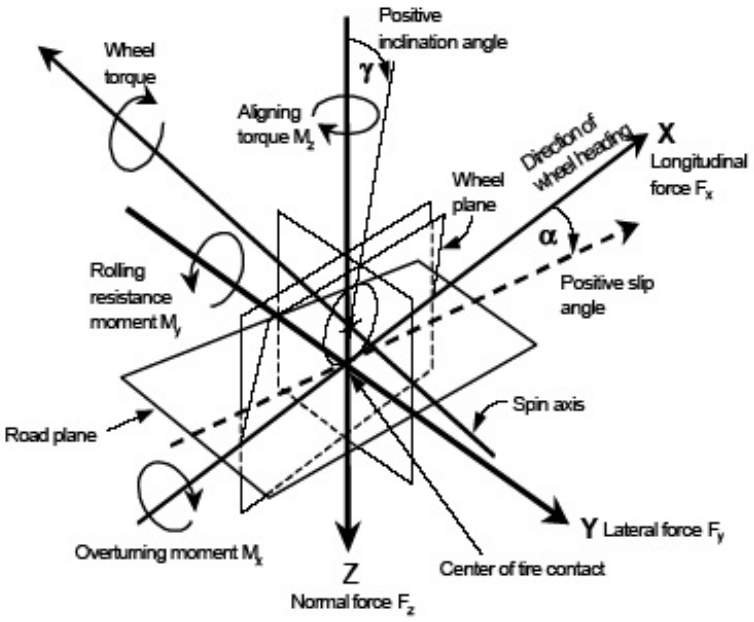

Figure 7.29: The SAE tire axis system[82].

The lateral force for all the normal load slip angle cases considered is shown in Fig. 7.30. Since every load step in the FEM corresponds to a steady state solution, the lateral force for a particular slip angle of interest is extracted from the FEM. It can be seen that with the increase in load the slip at which the peak force occurs also changes accordingly. For example the 1000lbs normal load case when considered, the lateral force peaks out at about

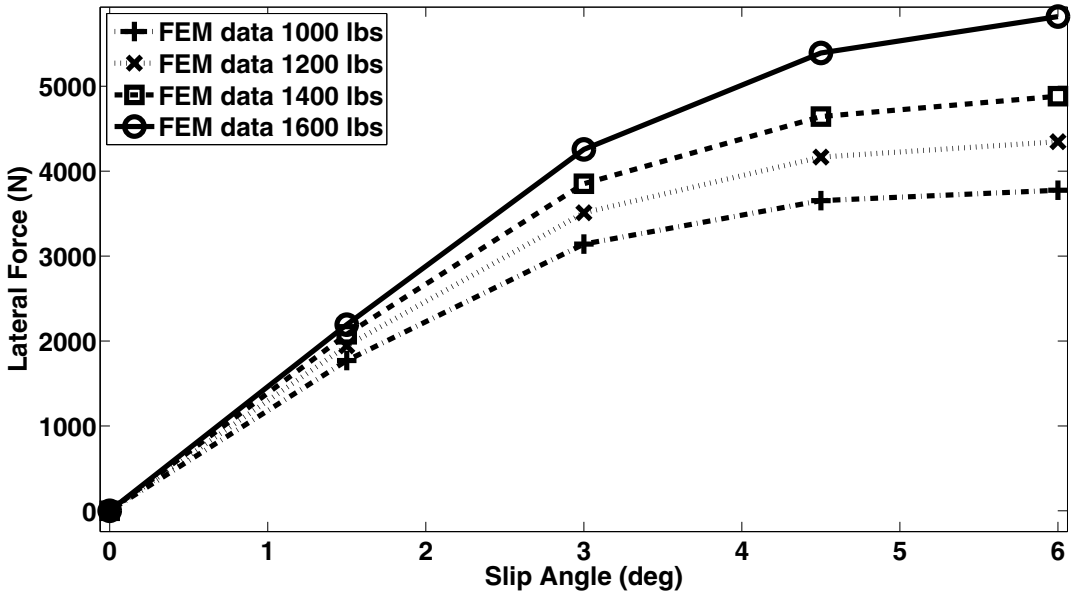

Figure 7.30: Lateral force prediction from FEM.

4.5^o of slip angle and tends to remain until a peak value corresponding to 6^o slip angle is attained.

The lateral force acting on a tire is a function of the slip angle (α_{slip}). The FEM prediction of lateral force versus slip angle is shown in Fig. 7.31. The current model predicts a peak lateral force at 6^o slip angle. This suggests that a non-linear polynomial would be sufficient to develop an empirical model. A quadratic polynomial function is then fit to the FEM data. The resulting equation is as follows,

$$f_y = C_\alpha \cdot (\alpha_{slip})^2 + D_\alpha \cdot (\alpha_{slip}) + E_\alpha \tag{7.20}$$

where C_α, D_α, E_α are load dependent constants fit to the FEM data. Equations relating the FEM constants to the normal load are shown in section 7.8.2. Eq. 7.20 should not used outside the range of the data considered here.

In Fig. 7.32, the lateral force estimated from the semi-empirical model versus the lateral force measured through experiments is shown. An average error of 5% error exists between the predicted and the measured values of the lateral force.

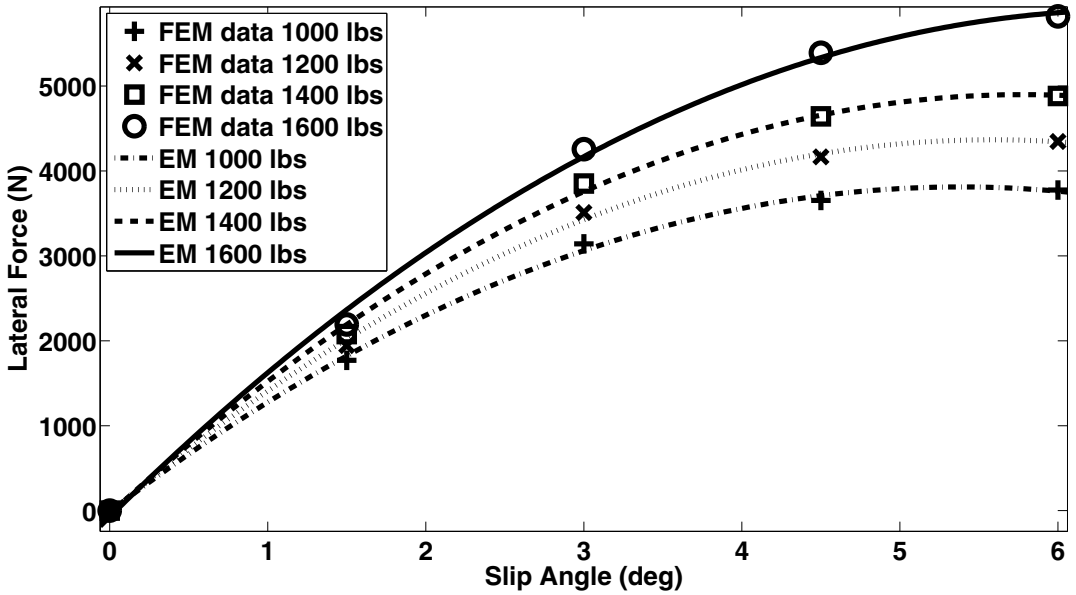

Figure 7.31: Lateral force estimation from FEM.

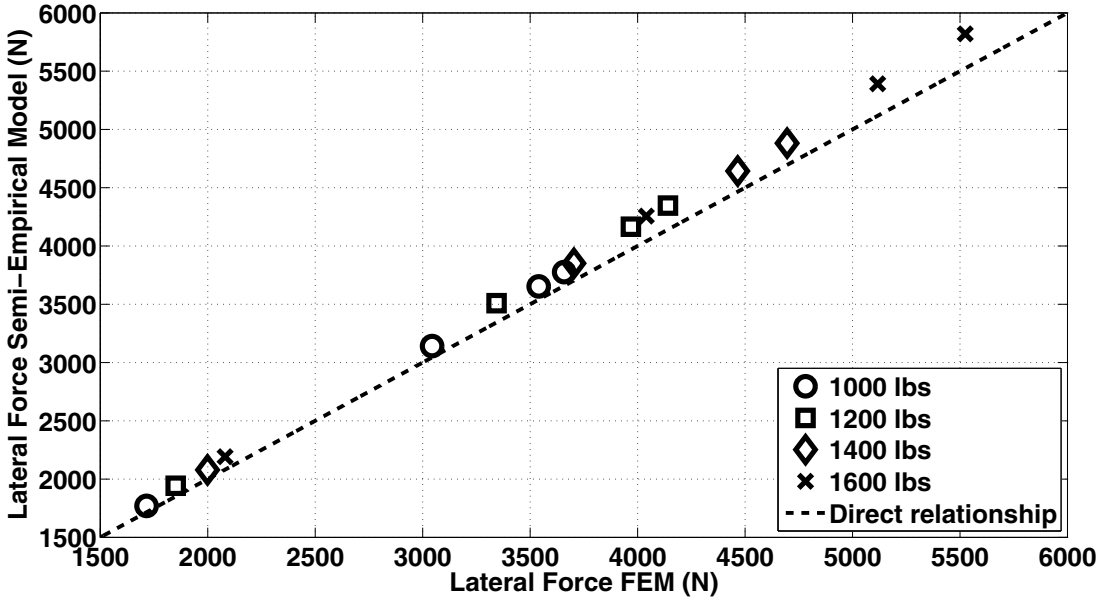

Figure 7.32: Lateral force comparison between the semi-empirical model prediction and the FEM prediction.

7.8 Estimating Constants of the Semi-Empirical Model Based on FEM Results

7.8.1 Constants in the Slip Angle Empirical Model

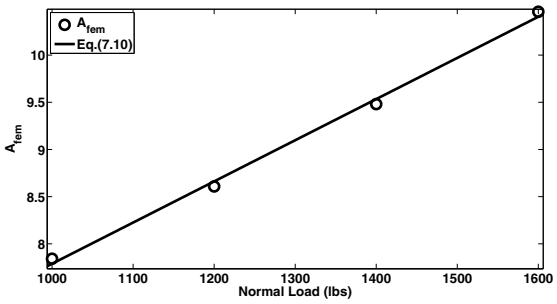

Figure 7.33: Load dependent constant A_{fem} estimated from normal load.

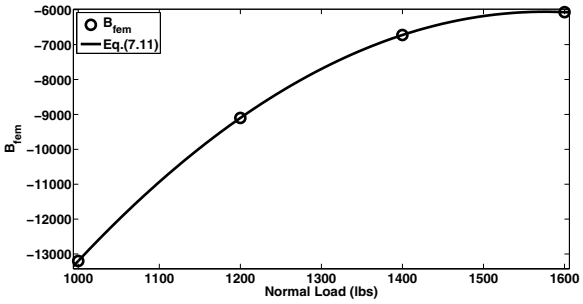

Figure 7.34: Load dependent constant B_{fem} estimated from normal load

Constants (A_{fem}) (also shown in Fig. 7.33) obtained from the slip angle empirical model for the parametric normal loading cases follows a linear relationship with the load and is estimated graphically by fitting an equation. A linear function fit to the A_{fem} values results in Eq.7.21.

$$A_{fem} = 0.004363 \cdot (f_z) + 3.425 \tag{7.21}$$

Next the constant terms B_{fem} are plotted versus the normal load and is shown in Fig. 7.34. These values are also only functions of the normal load. A quadratic equation is fit to the B_{fem} values and this results in Eq. refeq711.

$$B_{fem} = -0.02153 \cdot (f_z)^2 + 67.86 \cdot (f_z) - 5.953e^4 \tag{7.22}$$

7.8.2 Constants in the Lateral Force Empirical Model

The next load dependent constant term C_α, is estimated for the lateral force empirical model (Eq. 7.20). C_α is first plotted versus the load (see Fig. 7.35) and an equation is fit. The resulting equation is a quadratic equation of the form,

$$C_\alpha = 3.313 \cdot 10^{-5} \cdot (f_z)^2 + 0.1191 \cdot (f_z) - 45.86 \tag{7.23}$$

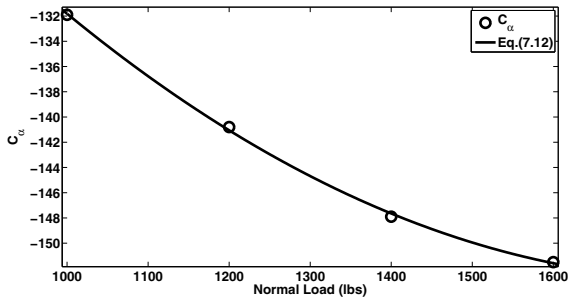

Figure 7.35: Load dependent constant C_α estimated from normal load.

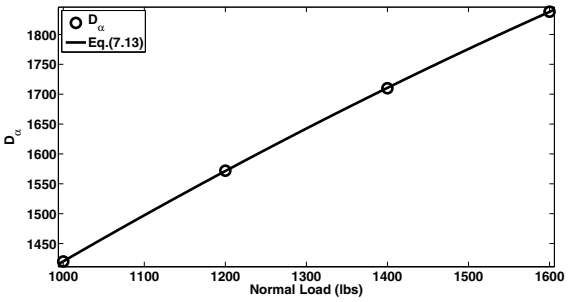

Figure 7.36: Load dependent constant D_α estimated from normal load.

The D_α constant term from Eq. 7.20 is plotted versus the normal load. This is shown in Fig. 7.36. A quadratic polynomial is fit to the data and the resulting equation is of the form,

$$D_\alpha = -0.00015 \cdot (f_z)^2 + 1.086 \cdot (f_z) + 48.42 \tag{7.24}$$

The last set of constant terms E_α from Eq. reflafeq for the parametric normal load case

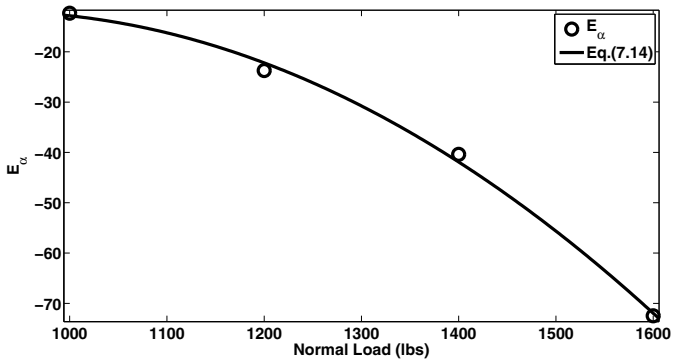

Figure 7.37: Load dependent constant E_α estimated from normal load.

is shown in Fig. 7.37. This constant term follows a quadratic trend and hence a quadratic polynomial it fit to the data. The resulting equation is of the form,

$$E_\alpha = -0.0001294 \cdot (f_z)^2 + 0.2378 \cdot (f_z) - 121.3 \tag{7.25}$$

Chapter 8

Steady-State Free Rolling Experimental Methodology

8.1 Test Bed for Experimental Validation

The steady-state free-rolling experiments were conducted on a MTS FlatTrac test bed (see Fig. 8.1). The important features of the FlatTrac test bed are as follows,

1. Actuating pneumatic cylinders that can apply a vertical load of up to 5000lbs.
2. Uniform belt speed of 7kph.
3. Capability of incremental testing, where slip angle and normal load can be varied in increments independently.
4. Sweep testing where normal load increases incrementally and then sweeps slip angle from negative to positive.
5. Lateral tread movement through laser based optical sensor.
6. External force sensors on the wheel unit.
7. Fully automated system with high speed DAQ boards.

The same hardware used in the static loading experimental study to measure strain in the tire is used here. Following is the list of components:

1. Crossbow wireless DAQ: Mica2 reciever & XDA100 wireless transmitter.
2. PCB of signal conditioning circuit.
3. Strain sensors mounted on the tire innerliner.

Figure 8.1: MTS FlatTrac®test bed courtesy: General Motors.

8.2 Steady-State Rolling at Various Slip Angles

The steady state response to slip angle can be carried out by free-rolling cornering with an incremental test. In this test (which was conducted on the FlatTrac test bed(see Fig. 8.3)) the slip angle (α_{slip}) is increased incrementally and then the normal load is also increased, to create the necessary test conditions that were considered in the FEM. The following are the specific test conditions used,

1. Both slip angles and normal loads have fixed values at every test condition.
2. Ample rolling distance is given to tire at each test point once slip angle and normal load reach the specified value.
3. Ample rolling distance to ensure attainment of steady state equilibrium condition.
4. Uniform belt speed of 7kph.
5. Force data averaged to suppress tire non-uniformity.

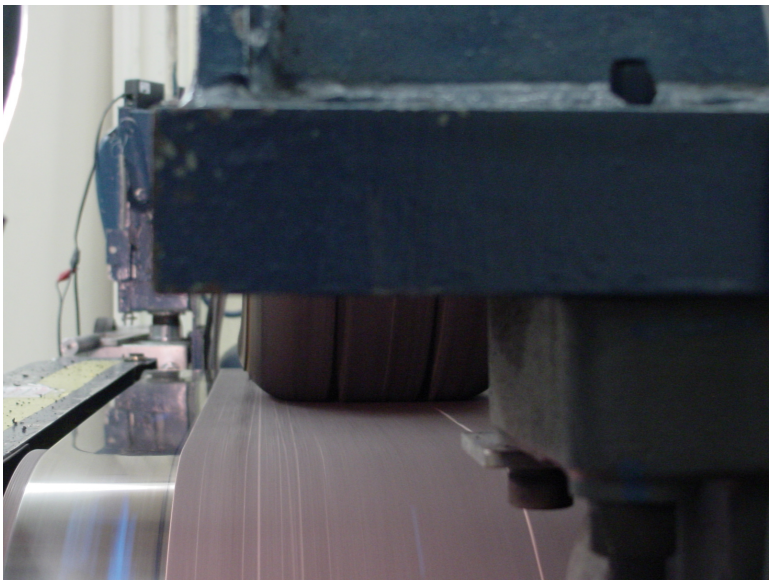

Figure 8.2: Sideview of tread on the belt: MTS FlatTrac®test bed courtesy General Motors.

Figure 8.3: MTS FlatTrac®test bed courtesy: General Motors.

8.3 Strain Profile Under Steady-State Free-Rolling

The steady state free rolling experiments were performed at a belt speed of 7kph. For this belt speed, the strain measurements around the tire for one revolution per second is considered. Normal loads were varied from 1000lbs to 1600lbs in increments of 200lbs and slip angles from 0^o-6^odeg. Due to limitations in the sampling rate of the wireless transmitter (10Hz), only a few data points could be taken during each revolution. The initial position of the tire (from 0^o phase with respect to the tire axis) is incremented by 1^o in each test to map the strain at a higher resolution around the tire. Each of the test was run over a period of 20 seconds. Thus allowing to capture 360 data points over 36 tests by superimposing the results. The method adopted for taking the data is pictorially shown in Fig. 8.4. The hoop strain predictions from experiments does not show a gradual strain profile as seen in the predictions from the FEM. Notes on possible reasons that might be responsible for this behavior is listed at the end of this section.

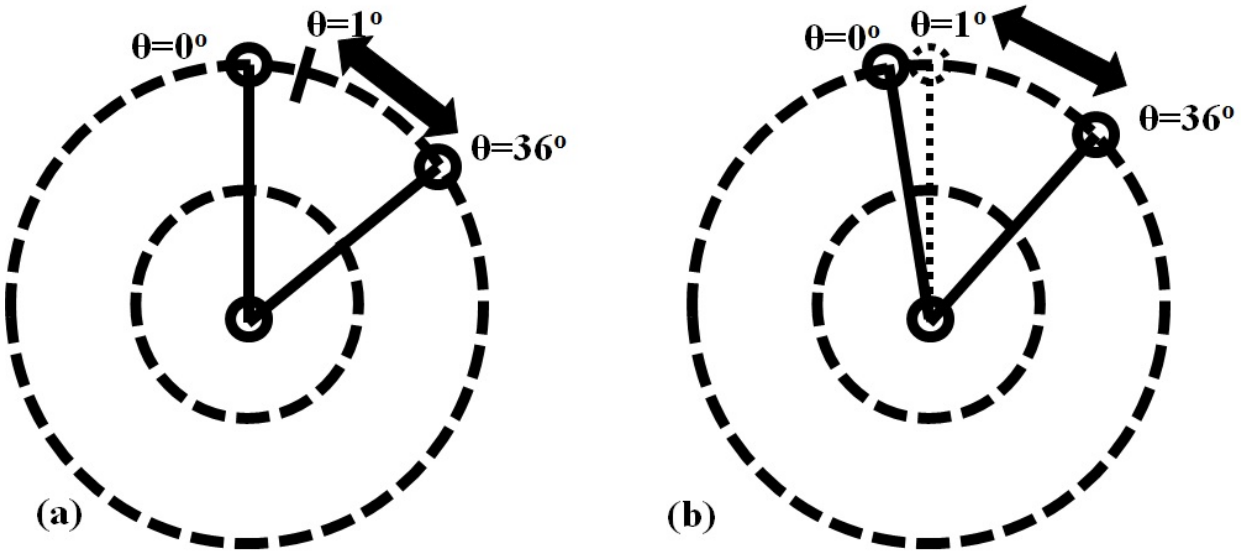

Figure 8.4: Schematic for acquiring test data:(a) 0^o phase; (b) 1^o phase.

Figure 8.5 shows the hoop strain prediction for all the strain gages under the pure rolling condition with varying normal load. It can be seen that the contact duration predicted by

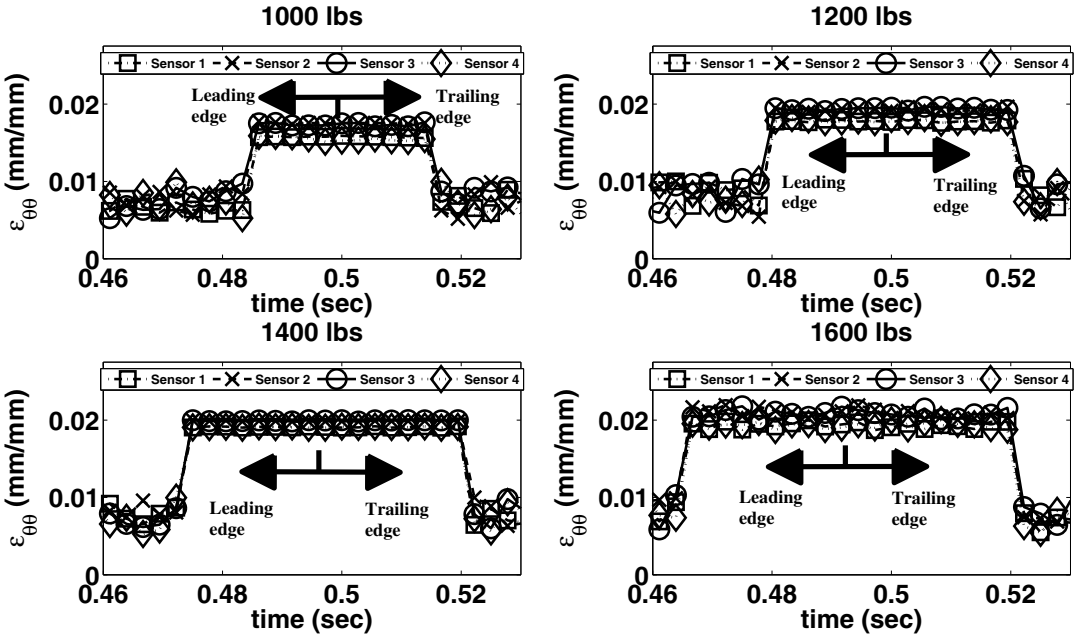

Figure 8.5: Strain profile 0^o slip angle sensors 1, 2, 3,and 4; Loads 1000lbs, 1200lbs, 1400lbs, and 1600lbs.

all the sensors is the same for a given load. And the contact duration increases with an increase in normal load. The strains seem to jump to a maximum value of about .022μstrain while in contact and fall down to a smaller value when out of contact. This happens over all the loads for which the testing was done.

In the next test case the slip angle is incremented to 1.5^o and the normal loads are varied from 1000lbs to 1600lbs with gradual increments of 200lbs. The strain profile of this test case is shown in Fig. 8.6. At 1000lbs and 1.5^o slip angle a gradual formation of the leading and trailing edges can be noticed (also see Fig. 6.3). The cornering effect is more pronounced in the FEM as compared to experiments because the tire used in experiments could be slightly stiffer. This however cannot be verified because the exact rubber compounds of the test tire is not known and at this time only a hypothesis can be made to understand the experimental results. The same trend appears to be occurring with the increase in load and when a normal load value of 1600lbs is reached the trends momentarily disappear. One

reason could be because the maximum load rating of the test tire is 1653lbs and at such high loads the tire might be experiencing bending and compression and not exactly undergoing cornering.

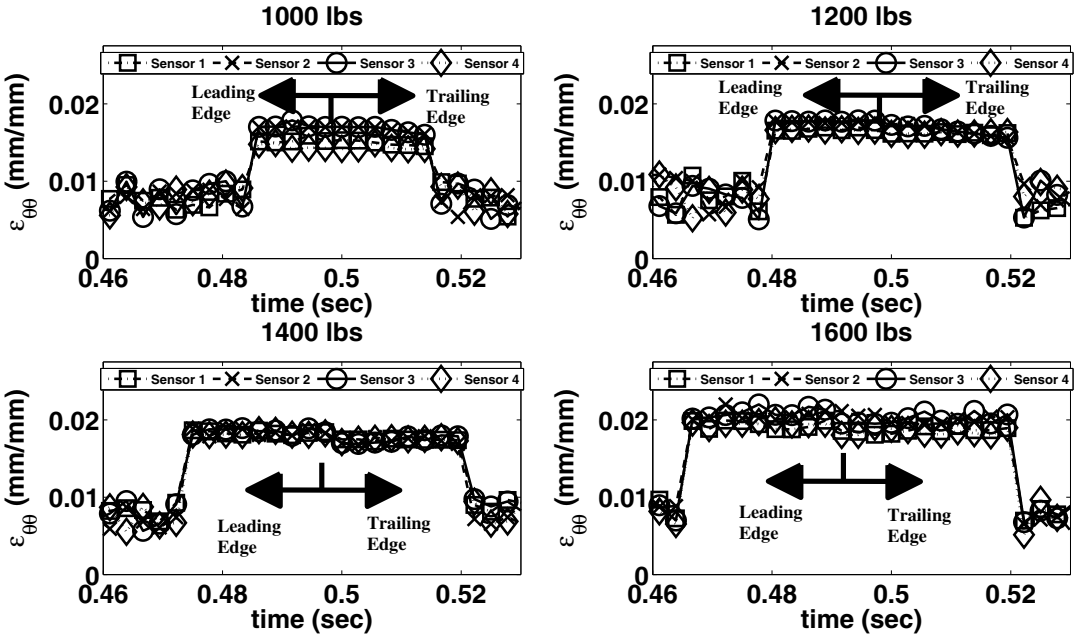

Figure 8.6: Strain profile 1.5^o slip angle sensors 1, 2, 3,and 4; Loads 1000lbs, 1200lbs, 1400lbs, and 1600lbs.

In the third test case the slip angle is increased to 3^o and the testing is carried out for all the normal loads which are of interest. The strains from this test are shown in Fig. 8.7. From the figure it can be seen that the effect of cornering is captured to a reasonable level. All the sensors tend to exhibit a strain profile which can be deduced into a leading and trailing edge. A 225/60 R16 (SRTT) tire is a popular choice for an sport's utility vehicle who's curb weight is in the neighborhood of 1200lbs. At this load and a 3^o slip angle a clear shift in the curve is produced indicating cornering under the steady state free rolling condition. The lateral force generated by the tire at this slip angle starts to dominate the tire deformation by deflecting the tread in the lateral direction. Surprisingly, at this slip angle and a normal

load of 1600lbs it can be seen that a trailing and leading edge in fact is formed, another indication that the generated lateral force tends to deform the tread laterally.

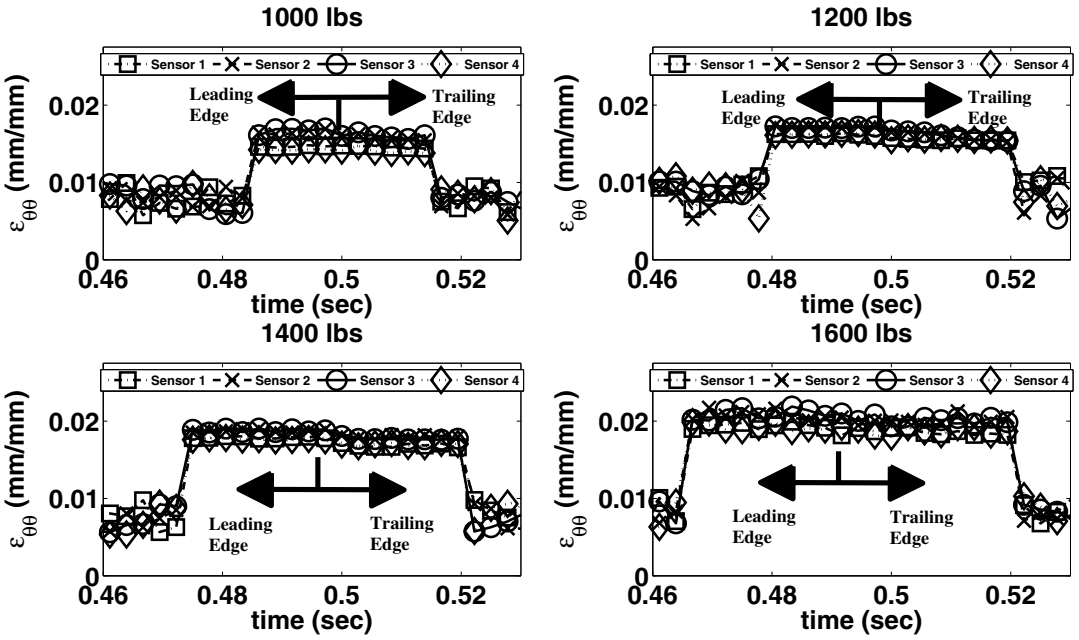

Figure 8.7: Strain profile 3^o slip angle sensors 1, 2, 3,and 4; Loads 1000lbs, 1200lbs, 1400lbs, and 1600lbs.

The slip angle is then increased to 4.5^o and a parametric variation of the normal loading is performed over this case. The strain profile is shown in Fig. 8.8. In this test case scenario the tire is nearing its peak saturation point in terms of the lateral force. It is interesting to note that the lower normal load at this slip angle barely forms a leading and a trailing edge and is more prevalent when the normal is at higher values of 1200lbs, 1400lbs and 1600lbs. This occurs primarily due to the lateral force domination at higher slip angles until a peak value of lateral force is reached as limited by the friction coefficient.

The last test case scenario of 6^o slip angle and the parametric variation of normal loads is performed to capture the lateral force saturation effects on the lateral tread deformation. The strains from this test case are shown in Fig. 8.9. The 1000lbs normal load case at 6^o predicts a strain profile from which neither the leading edge nor the trailing edge can be

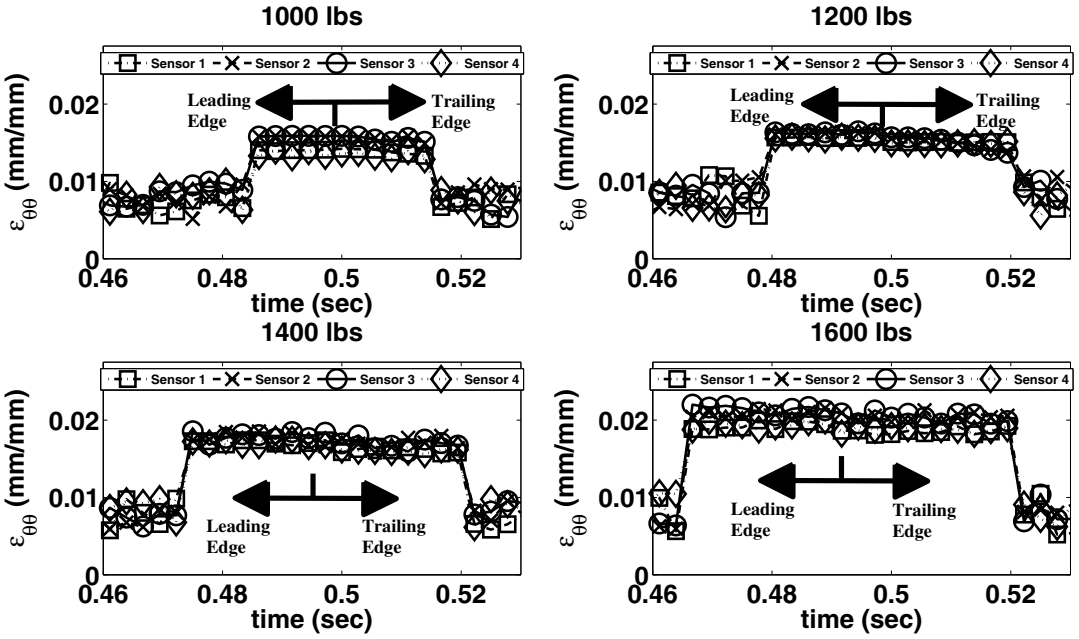

Figure 8.8: Strain profile 4.5^o slip angle sensors 1, 2, 3,and 4; Loads 1000lbs, 1200lbs, 1400lbs, and 1600lbs.

noticed. This is an indication that the lateral force generated by the tire has most certainly reached a peak value and the hence the lateral tread deformation is almost absent. The same conclusion cannot be reached for the higher loads at this slip angle because the strain profile predict that some amount of lateral tread deformation still exists at this slip angle. This drastic shift in the trend raises a question. Has the lateral force really reached its peak value? Since this current work was focused on developing models for the linear portion of the side force versus slip angle curve, higher slip angles were not considered to quantify the conditions beyond the peak force value.

Some notes on the strain profile from the steady state free rolling experiments:

1. A higher or matching resolution than the FEM could not be achieved.

2. Lesser than 1^o angular position could not be achieved as this is limited by the test machine and the sampling rate or wireless transmitter.

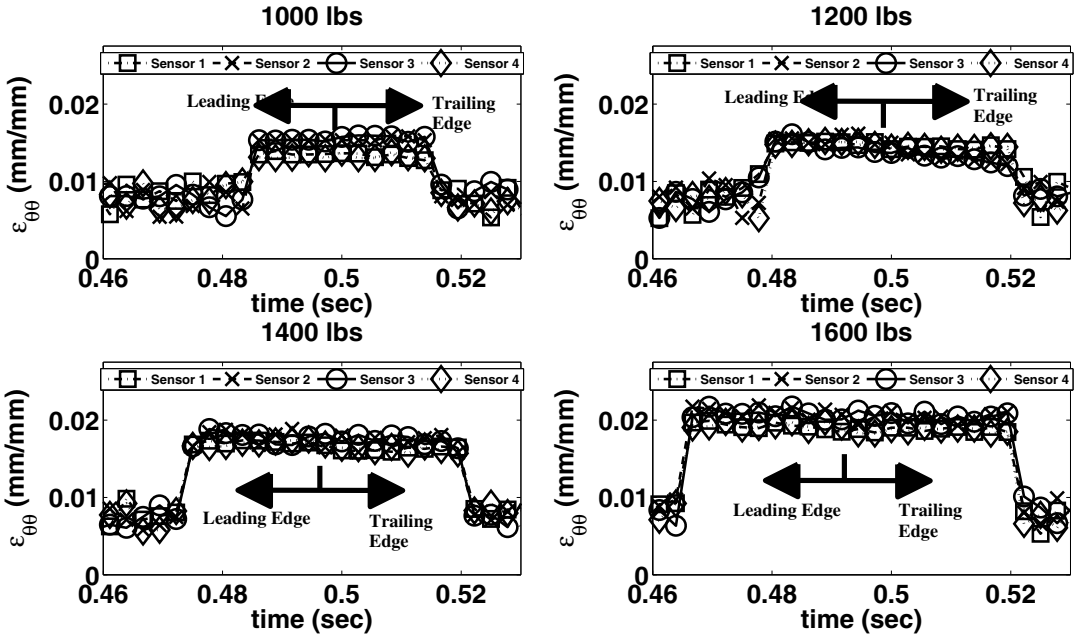

Figure 8.9: Strain profile 6^o slip angle sensors 1, 2, 3,and 4; Loads 1000lbs, 1200lbs, 1400lbs, and 1600lbs.

3. Based on the experimental data it can be concluded that this method is capturing only the contact patch conditions.

4. The adhesives used in this current work might be restraining the strain gages more than they should and result in possible stiffening.

5. The strain gages themselves are much more stiffer than the tire, Matsuzaki et al.[67] have shown that an ultra flexible strain sensor works better with tire strain monitoring.

Chapter 9

Strain Analysis Based on Steady-State Free-Rolling Experimental Data

9.1 Slope Curve Method

The slope curve method discussed in Chapter 7(section 7.3), is used to analyze the experimental data of free-rolling from Chapter 8 to estimate the contact duration. The slope change is estimated from Eq. 9.1. In order to validate the slope curve method explored in Chapter 7, figures similar to Fig. 7.14, Fig. 7.15, Fig. 7.16 are generated using the experimental data. The center difference for slope change calculation is as follows,

$$\left(\frac{\Delta\varepsilon_{\theta\theta}}{\Delta t}\right)_i = \frac{(\varepsilon_{i+1} - \varepsilon_{i-1})}{(t_{i+1} - t_{i-1})} \tag{9.1}$$

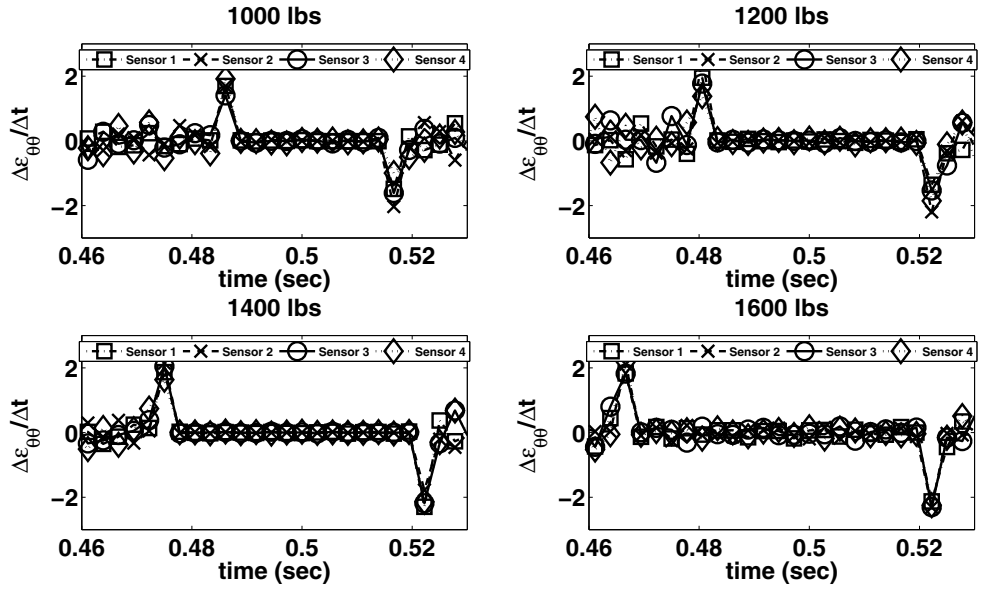

Figure 9.1: Slope change 0^o slip angle (4 sensors and 4 loads).

The analysis process starts with the 0^o slip angle case(i.e the tire is freely rolling) while the load on the tire is varied from 1000lbs to 1600lbs. The slope change for this test condition is shown in Fig. 9.1. The curve shows two distinct peaks that occur over all the 4 sensors. As expected the time between the occurrences of the two peaks increases as the normal load is increased on the tire. This can also be clearly seen from the slope change plot in Fig. 9.2. Later, this observation could be used to relate strain to normal load measurement.

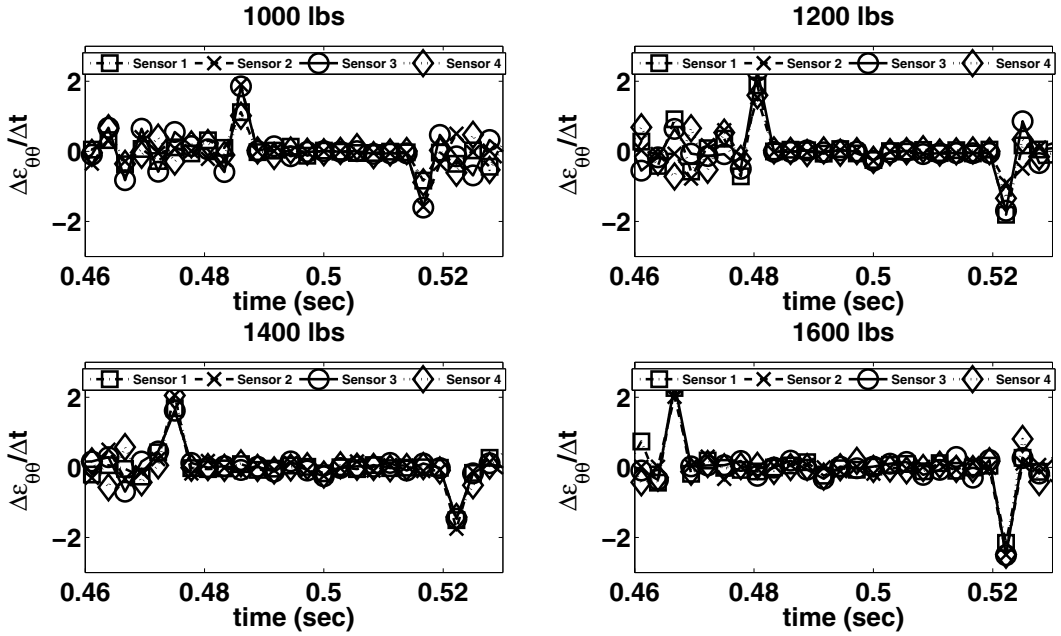

Figure 9.2: Slope change 1.5^o slip angle (4 sensors and 4 loads).

In the next test condition a slip angle of 1.5^o is applied. The slope change plot when the slip angle is held constant and the normal load is varied is shown in Fig. 9.2. As shown, the contact length does not change significantly with slip angle.

The 3^o slip angle test is next considered. The slope change with respect to time is shown in Fig. 9.3. It can be seen that all 4 sensors predict the exact same time of occurrence of peak values corresponding to maximum sensed strain by the strain gages. Note that there might be a change too small to recognize with the current resolution. A thing to be noted here is that the magnitude change of the slope with respect to time is not as pronounced as

the magnitude change predictions by the FEM. However as long as the predictions are within the region of maximum allowable error, the experimental predictions should be acceptable.

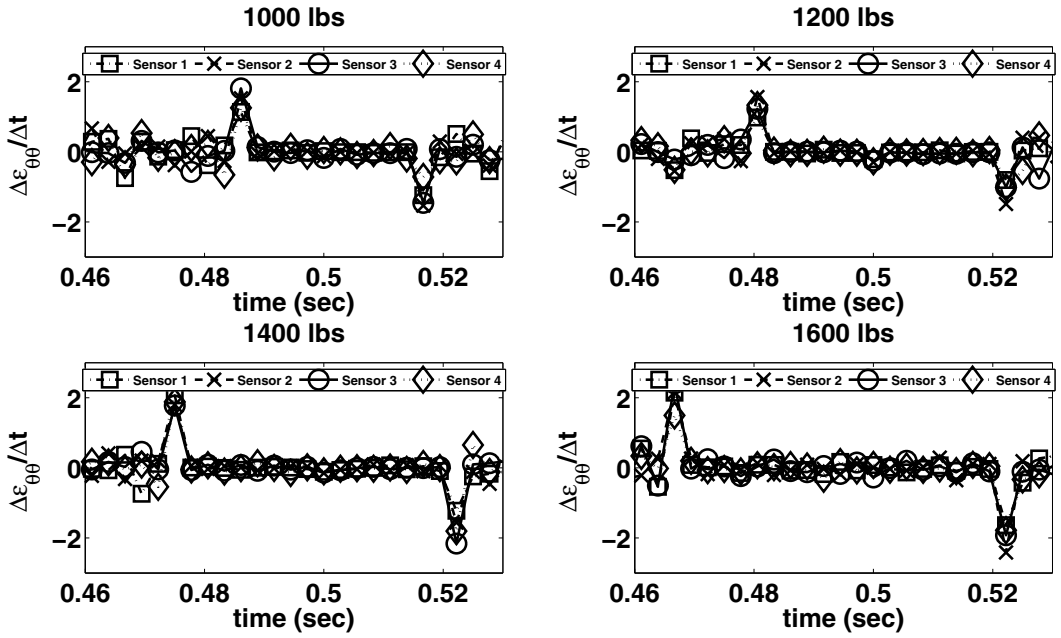

Figure 9.3: Slope change 3^o slip angle (4 sensors and 4 loads).

9.2 Normal Load Estimation

Now Eq. 7.8 (same method was adopted in chapter 7) is modified to incorporate the inflation pressure factor by introducing an additional factor, and so Eq. 7.8 becomes,

$$f_z = f_{exp} \cdot (p_{inf}) \cdot A_{contact} \tag{9.2}$$

where the additional factor f_{exp} is constant fit to the experimental data.

The above developed model (also discussed in Chapter 7) in an ideal case scenario of FEM should work with the experimental results. The average contact duration, which is also an indicator of the contact length, is practically a function of the load and the vehicle speed and not the slip angle experienced by a tire while cornering. Fig. 9.4 is a verification of this claim. In this figure the normal load on the tire is plotted versus the average contact

duration and it can bee seen that slip angle has little to no influence on the contact duration.

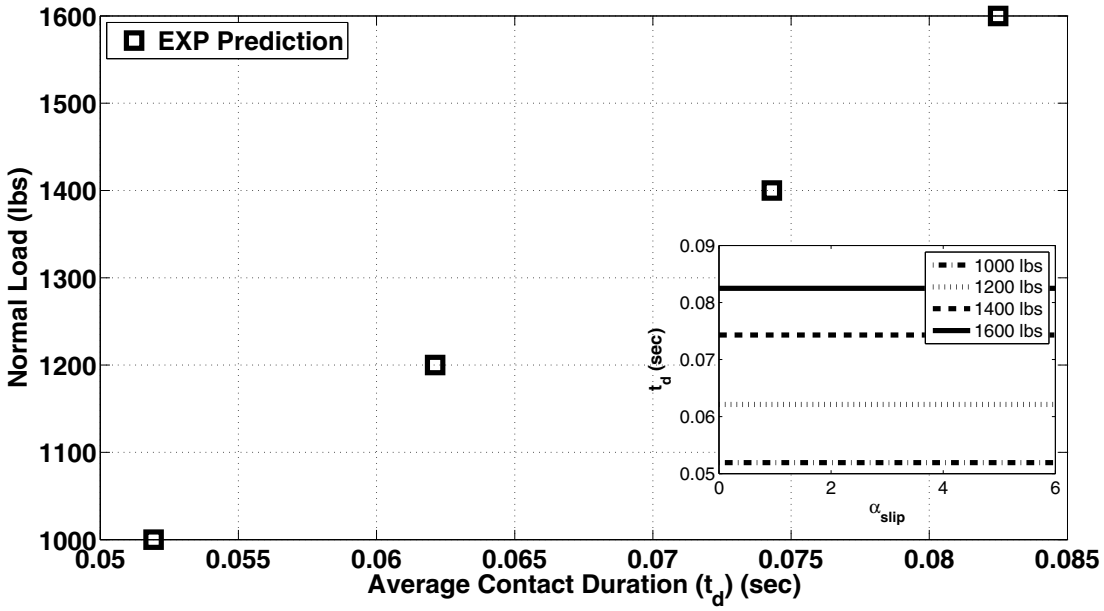

Figure 9.4: Experimental prediction of average contact duration.

Once the average contact duration is verified to be not significantly influenced by the slip angle, Eq. 9.2 can be used to estimate the normal load from the experimental data. The estimated normal load from Eq. 9.2 is then plotted versus the normal load from the experiments, which is shown in Fig. 9.5. An average error of less than 2% exists between the theoretical model and experimental results, which is a promising result and suggests that the fits are well within an acceptable margin of error. Finally, a comparison between the FEM prediction of the normal load and the experimental measurement of the normal load is shown in Fig. 9.6. From this it can been seen that the FEM predictions and the experimental measurements are in good agreement. The average error is less than 5%.

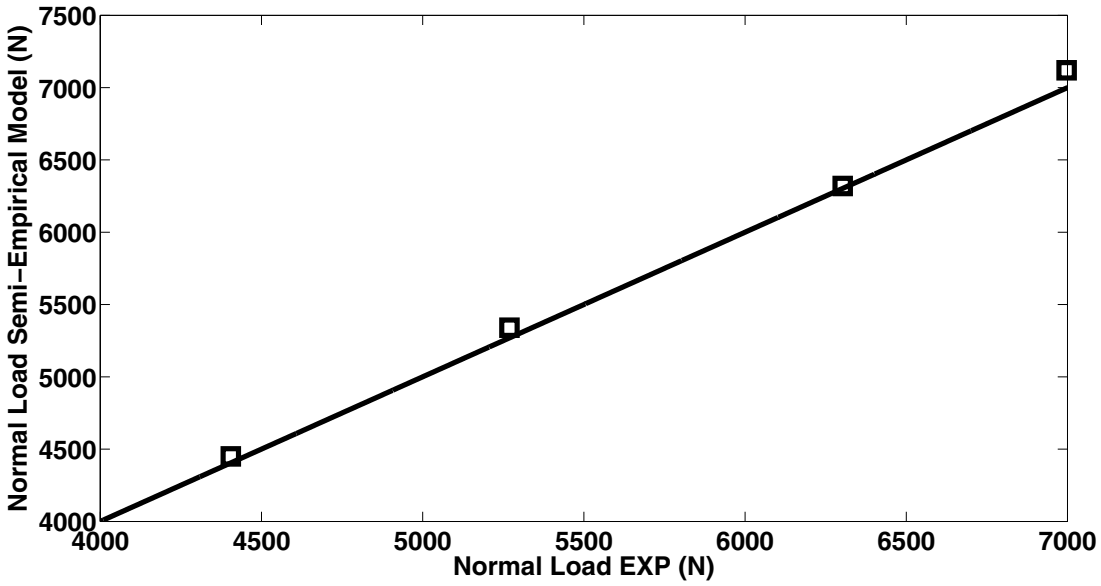

Figure 9.5: Experimental data versus semi-empirical model prediction of normal load.

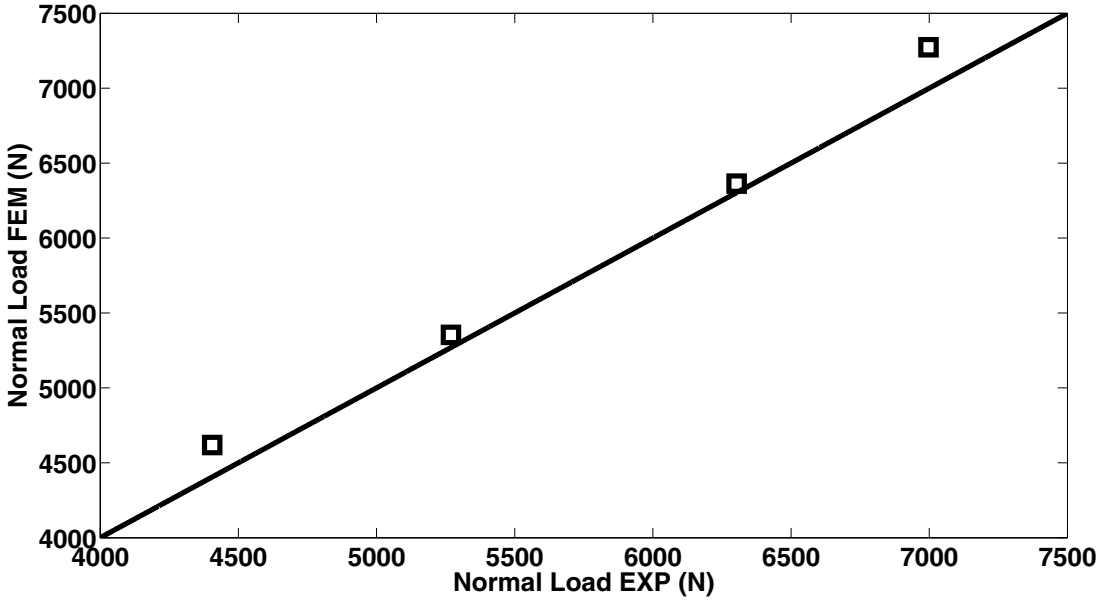

Figure 9.6: Normal load comparison between FEM results and experimental data.

9.3 Slip Angle Estimation

In order to validate the slip angle/strain relationship developed in section 7.6, a similar approach is taken to estimate the slip angle from the average of the strains from all the sensors in the contact patch region. The average contact duration, which is an indicator of the contact length, is used for the purpose of collecting all the strains in the contact patch region. Now, a relationship (similar to Eq. 7.18) between slip angle and measured strains is developed from the following,

$$\delta_{\alpha_{slip}} = ((\varepsilon_{ave_4} + \varepsilon_{ave_3}) - (\varepsilon_{ave_2} + \varepsilon_{ave_1})) \tag{9.3}$$

where ϵ_{ave_1}, ϵ_{ave_2}, ϵ_{ave_3} and ϵ_{ave_4} are the average value of the maximum strains in the contact patch.

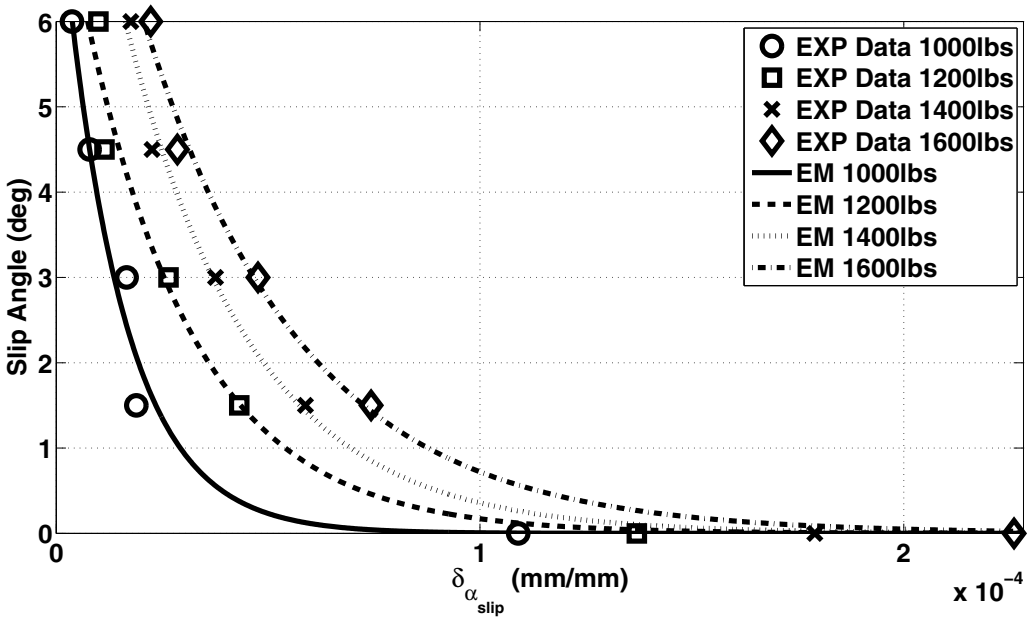

Figure 9.7: Slip angle estimation from experimental data.

The slip angle is plotted versus $\delta_{\alpha_{slip}}$ (see Fig. 9.7) and a curve is experimentally fit to obtain an equation relating the slip angle to measured strain. The equation is of the form

(the same as the FEM),

$$\alpha_{slip} = A_{exp} e^{B_{exp} \cdot \delta_{\alpha_{slip}}} \tag{9.4}$$

where A_{exp} and B_{exp} are load dependent constants fit to the experimental data. The only difference between Eq.(9.2) and Eq.(7.7) is the additional constant term that was used while fitting an equation to FEM data is ignored and still a good fit to experimental data is obtained (average error less than 5%). From Fig. 9.7 it can be seen that the $\delta_{\alpha_{slip}}$ value decreases with an increase in the slip angle and reaches a saturation point at the highest slip angle considered. This trend is very similar to what can be seen in Fig. 9.10, where a lateral force saturation occurs at higher values of slip angle.

A comparison between the $\delta_{\alpha_{slip}}$, based on FEM results, and the $\delta_{\alpha_{slip}}$, based on experimental data is shown in Fig. 9.8. The comparison pertains to all the normal load cases that were considered. From this it can be seen that the FEM predictions are almost an order of magnitude different from the experimental data. One reason could be that the FEM tire is less stiff than the tire used in experiments. This would simply mean that the lateral tread deformation in the FEM is significantly more than the experiments. Friction coefficient could also be responsible for the mismatch between FEM strains and the experimental strains. As is shown, later, it could also be due to the lateral force in the FEM being higher than the experiments.

The estimation of the constants A_{exp} and B_{exp}, which independent of the slip angle and only a function of the normal load, by fitting equations is shown in section 9.5.1.

9.4 Lateral Force Estimation

The tire forces and moments in reality are a complex non-linear function of tire variables which are established based on inputs and vehicle output responses. The primary focus of this work is to establish a relationship between slip angle and cornering force under steady state free-rolling condition. The SAE tire axis system shown in Fig. 7.29 is used in defining

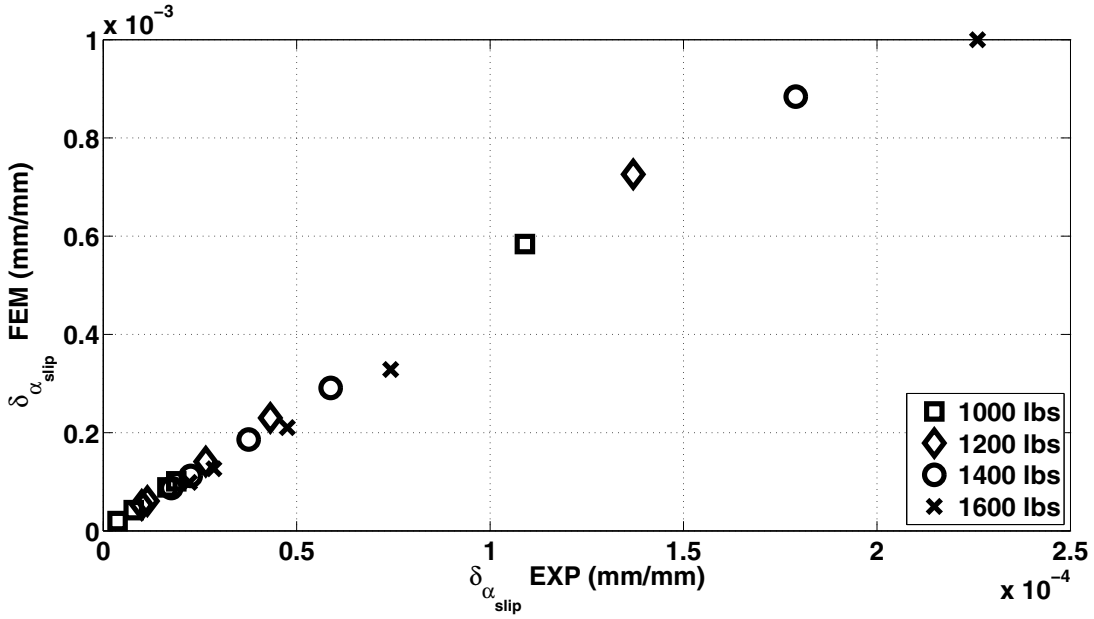

Figure 9.8: $\delta_{\alpha_{slip}}$ comparison between FEM results and experimental data.

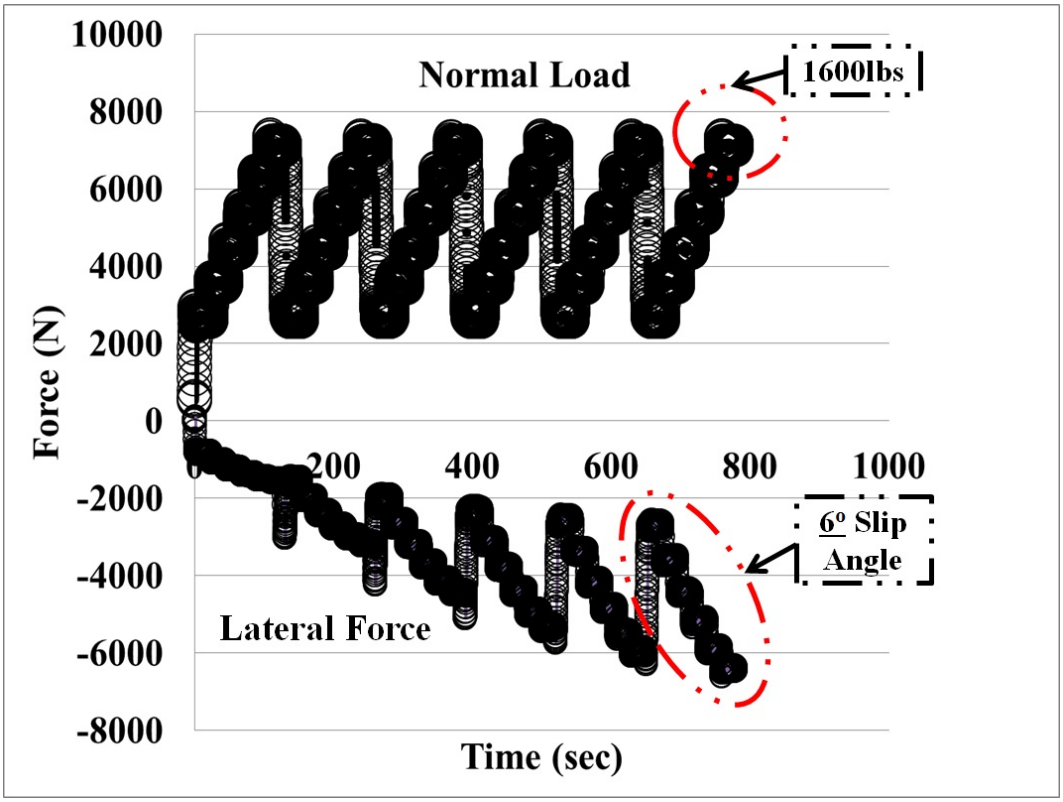

Figure 9.9: Measured lateral force for all normal loads and slip angle cases.

the necessary parameters. According to the SAE definition, the cornering force is simply the lateral force when a side slip in the form of slip angle exist. For the sake of consistency lateral force will be used and the condition of steady state free-rolling under various slip angles will be referred to as cornering.

The raw data of the lateral force from the experiments is shown in Fig. 9.9. The test was conducted in such a way that that the normal load cases loop within the slip angle cases. For example say for 3^o slip angle case, the load was varied while keeping the slip angle constant. This method is employed while keeping in mind the amount of time required to complete all the testing. From Fig. 9.9, the necessary lateral forces for the slip angles considered is extracted and this is shown in Fig. 9.10.

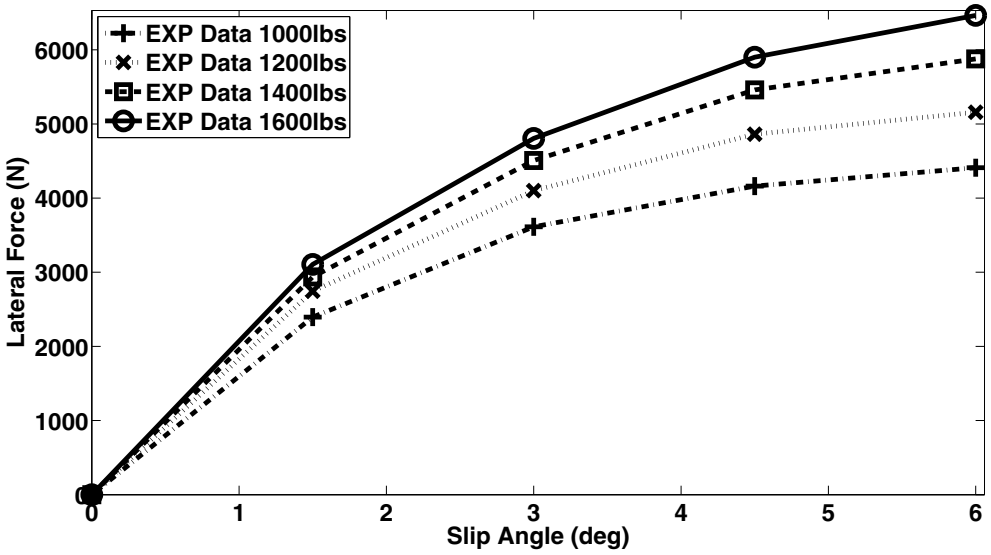

Figure 9.10: Averaged lateral force for cases considered.

The lateral force acting on a tire is a function of the slip angle (α_{slip}). The experimental prediction of lateral force versus slip angle is shown in Fig. 9.11. The current model predicts a peak lateral force at 6^odeg slip angle. A quadratic polynomial function is then fit to the experimental data. The resulting equation that is fit to the experimental data is as follows,

$$f_y = F_\alpha \cdot (\alpha_{slip})^2 + G_\alpha \cdot (\alpha_{slip}) + H_\alpha \tag{9.5}$$

where F_α, G_α, H_α are load dependent constants fit to the experimental data. The estimation of the constants F_α, G_α and H_α, which are independent of the slip angle and only a function of the slip, is shown in section 9.5.2.

In Fig. 9.12, the lateral force estimated from the semi-empirical model versus the lateral force measured through experiments is shown. An average error of 4% error exists between the predicted and the measured values of the lateral force. Finally, the lateral force from the FEM results is compared to the lateral force from the experimental data for all the normal load cases that were considered are shown in Fig. 9.13. From this it can be seen that the FEM predictions of the lateral forces are higher in comparison to the experimentally measured lateral forces. The average error between the FEM prediction and the experimental data is about 12%. One reason for this mismatch could be due to the stiffness of the tire. The tire stiffness directly affects the cornering stiffness, which is the ratio of cornering (or lateral) force to the slip angle. This simply means that a tire with low vertical stiffness (as witnessed by the FEM tire), produces a high force in the lateral direction. The mismatch could also be due to the friction coefficient used in the FEM (μ=0.85) which is different than the friction coefficient of the FlatTrac tire testing machine's belt (μ=0.63). The boundary conditions that are used in the FEM and experiments are not exactly the same, this could also be a reason for the mismatch.

9.5 Estimating Constants of the Semi-Empirical Model Based on Experimental Results

9.5.1 Constants in the Slip Angle Empirical Model

The A_{exp} constant terms from all the normal load cases that were considered in developing Eq. 9.5 is collected and plotted versus the normal load. This results in a linear relationship between A_{exp} and the normal load (shown in Fig. 9.14). A linear polynomial is

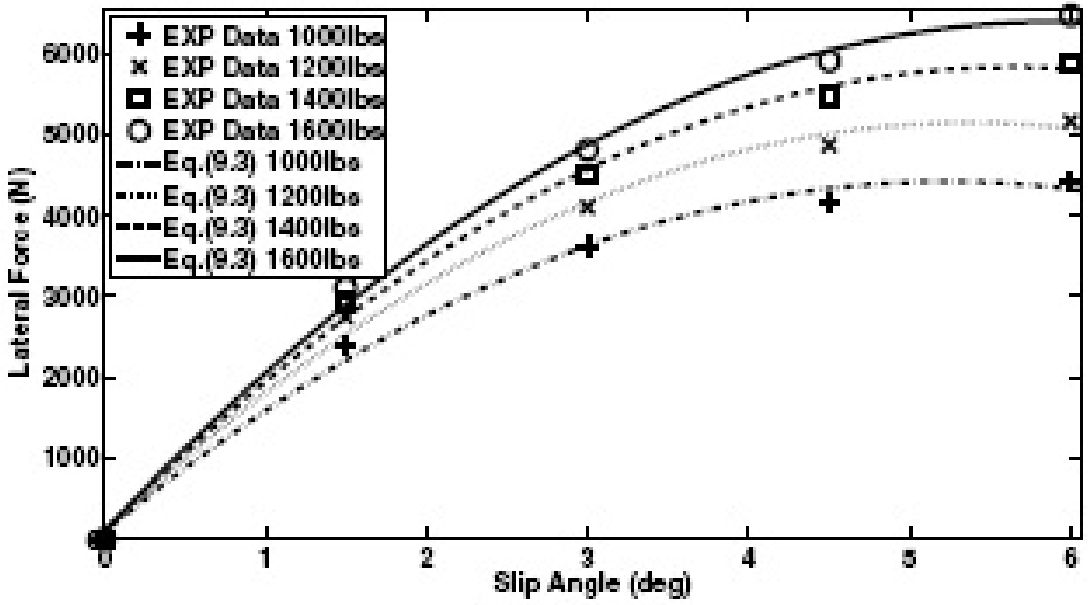

Figure 9.11: Lateral force estimation from experiments.

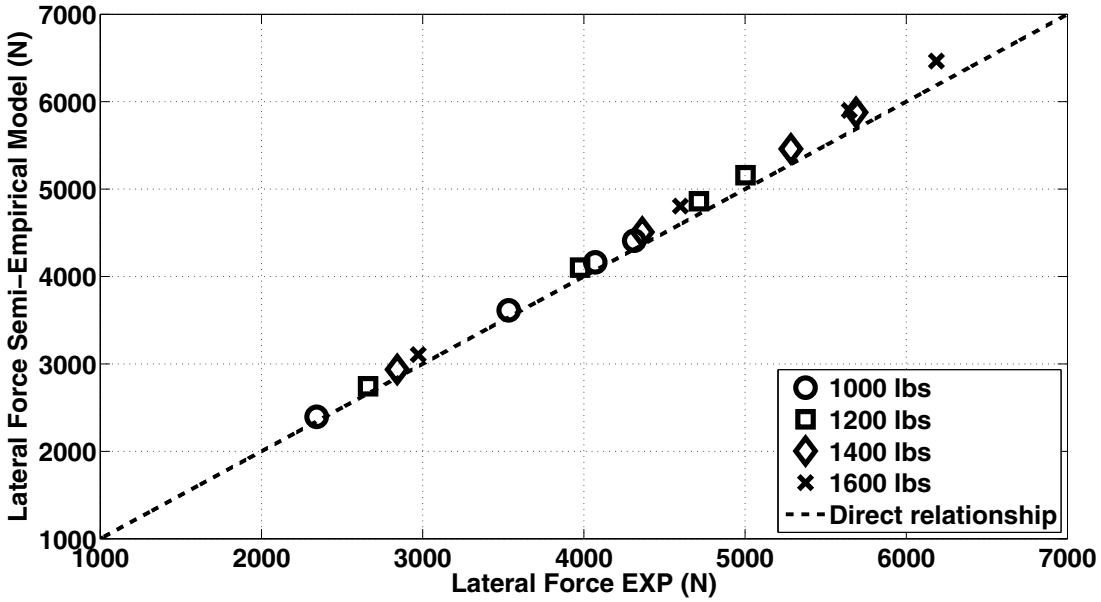

Figure 9.12: Lateral force comparison between semi-empirical model prediction and experimental measurement.

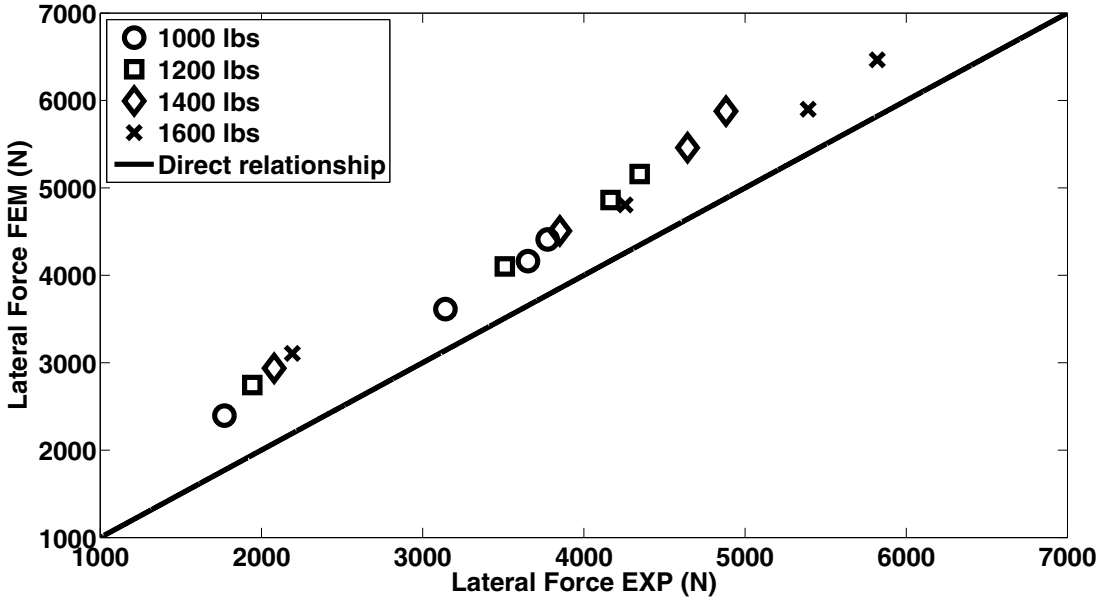

Figure 9.13: Lateral force comparison between FEM results and experimental measurement.

then fit to the data and the resulting equation is given by,

$$A_{exp} = 0.004343 \cdot (f_z) + 3.505 \tag{9.6}$$

Fig. 9.15 shows the plot of B_{exp} (a constant term in Eq. 9.5) versus the normal load. A non-linear tread is observed and hence a quadratic polynomial is fit to the data. The resulting equation is given by,

$$B_{exp} = 0.03181 \cdot (f_z)^2 - 60.02 \cdot (f_z) - 1.211e^4 \tag{9.7}$$

9.5.2 Constants in the Lateral Force Empirical Model

The first constant term in Eq. 9.5, F_α, is plotted versus the normal load and is shown in Fig. 9.16. A polynomial of order three best fits to the data. The resulting cubic equation is given by,

$$F_\alpha = -1.479 \cdot 10^{-7} \cdot (f_z)^3 + 0.000675 \cdot (f_z)^2 - 1.03 \cdot (f_z) + 345.4 \tag{9.8}$$

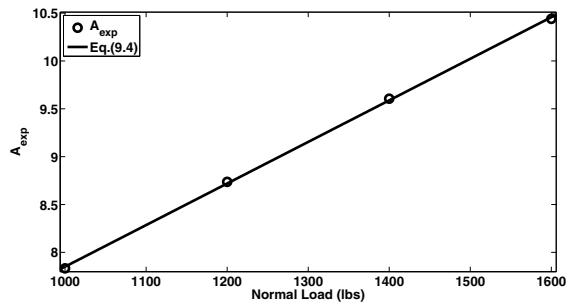

Figure 9.14: Load dependent constant A_{exp} estimated from normal load.

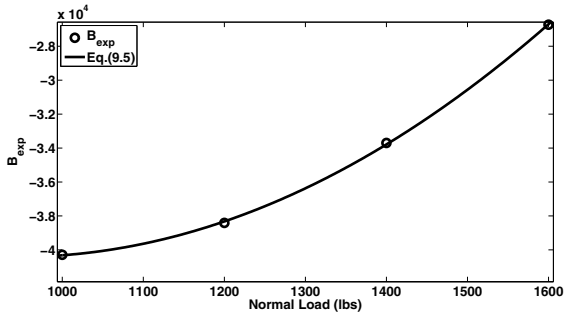

Figure 9.15: Load dependent constant B_{exp} estimated from normal load

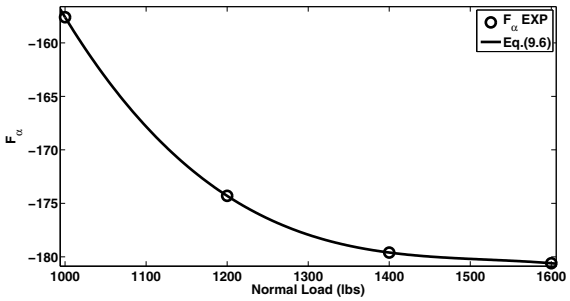

Figure 9.16: Load dependent constant F_α estimated from normal load.

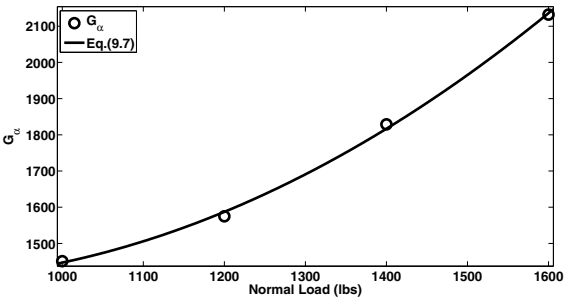

Figure 9.17: Load dependent constant G_α estimated from normal load.

Fig. 9.17 shows the second term in Eq. 9.5, G_α, plotted versus the normal load. A quadratic polynomial best fits to the data. The resulting equation is given by,

$$G_\alpha = 0.001119 \cdot (f_z)^2 - 1.76 \cdot (f_z) + 2088 \tag{9.9}$$

Fig. 9.18 shows the second term in Eq. 9.5, H_α, plotted versus the normal load. A cubic polynomial best fits to the data. The resulting equation is given by,

$$H_\alpha = 2.708 \cdot 10^{-8} \cdot (f_z)^3 - 7.65e^{-5} \cdot (f_z)^2 + 0.0734 \cdot (f_z) + 65.4 \tag{9.10}$$

Table 9.1: Slip angle constants

Type	**A**	**B**
FEM	$A_{fem} = 0.004363 \cdot (f_z) + 3.425$	$B_{fem} = -0.02153 \cdot (f_z)^2 + 67.86 \cdot (f_z) - 5.953e^4$
EXP	$A_{exp} = 0.004343 \cdot (f_z) + 3.505$	$B_{exp} = 0.03181 \cdot (f_z)^2 - 60.02 \cdot (f_z) - 1.211e^4$

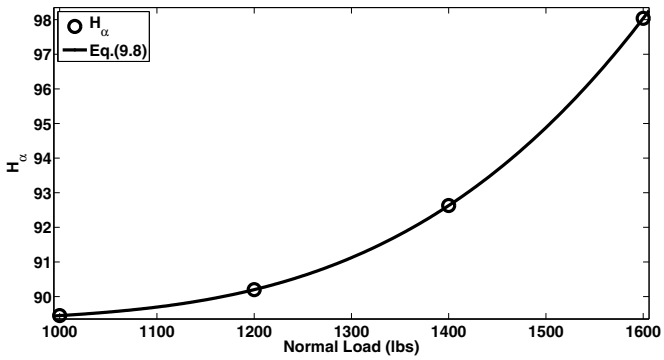

Figure 9.18: Load dependent constant H_α estimated from normal load.

Table 9.2: Lateral force constants (1^{st} constant term)

Type	1^{st} **constant term**
FEM	$C_\alpha = 3.313 \cdot 10^{-5} \cdot (f_z)^2 + 0.1191 \cdot (f_z) - 45.86$
EXP	$F_\alpha = -1.479 \cdot 10^{-7} \cdot (f_z)^3 + 0.000675 \cdot (f_z)^2 - 1.03 \cdot (f_z) + 345.4$

Table 9.3: Lateral force constants (2^{nd} constant term)

Type	2^{nd} **constant term**
FEM	$D_\alpha = -0.00015 \cdot (f_z)^2 + 1.086 \cdot (f_z) + 48.42$
EXP	$G_\alpha = 0.001119 \cdot (f_z)^2 - 1.76 \cdot (f_z) + 2088$

Table 9.4: Lateral force constants (3^{rd} constant term)

Type	3^{rd} **constant term**
FEM	$E_\alpha = -0.0001294 \cdot (f_z)^2 + 0.2378 \cdot (f_z) - 121.3$
EXP	$H_\alpha = 2.708 \cdot 10^{-8} \cdot (f_z)^3 - 7.65 \cdot 10^{-5} \cdot (f_z)^2 + 0.0734 \cdot (f_z) + 65.4$

Chapter 10

Steady-State Rolling Finite Element Model

10.1 Steady-State Rolling at Various Slip Ratios

In this section the steady-state rolling finite element model is developed to estimate the slip ratio (also known as the longitudinal slip). The slip ratio (according to the SAE convention) is defined as a difference between the tire speed in the longitudinal direction and the axle speed relative to the road. This is represented by the following equation.

$$\Omega_{SR} = \begin{cases} \frac{V_o - R\omega}{V_o} \cdot 100\% & \text{if } V_o > R\omega \\ \frac{R\omega - V_o}{R\omega} \cdot 100\% & \text{if } R\omega > V_o \end{cases} \tag{10.1}$$

where Ω_{SR} is the slip ratio, R is the radius of the wheel, ω is the angular velocity (rad/s), and V_o is the axle speed relative to the road (illustrated in Fig. 10.2). The slip ratio is expressed as a % and is limited as such by $|\Omega_{SR}| <= 100\%$. For full-braking (sometime referred to as a locked wheel), the axle speed (V_o) is used in the denominator so that the slip ratio is 1 when ω is zero. The slip ratio has the opposite sign for the full-traction when tractive force is generated.

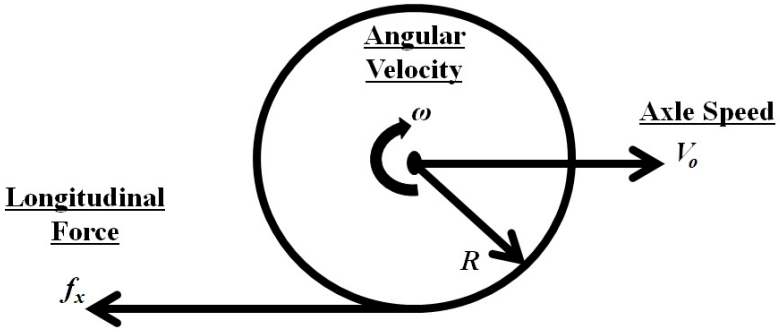

Figure 10.1: Basic variables of tire under steady-state rolling

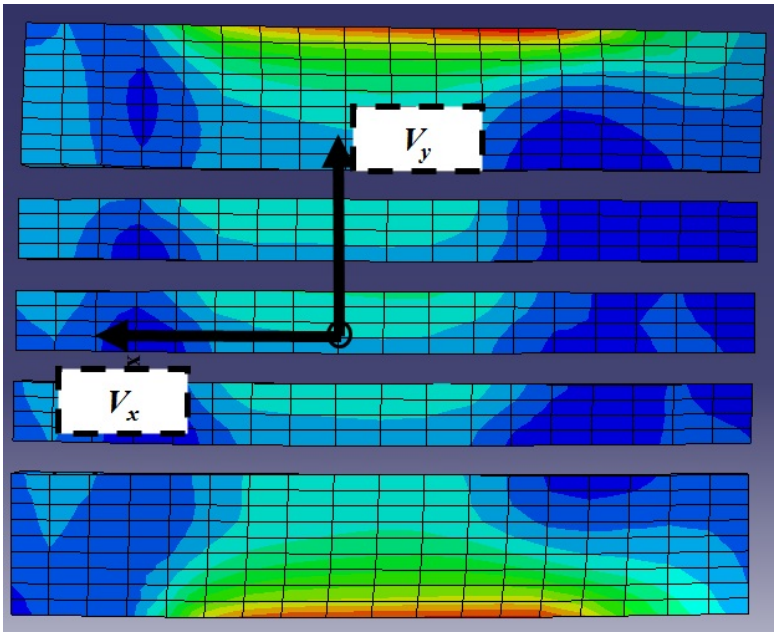

Figure 10.2: Boundary condition for the steady-state rolling condition

The simulation methodology described in Chapter 6 (section 6.1) for the straight line rolling condition is used to develop the steady-state rolling finite element model. The straight line rolling simulation involves obtaining solutions for the braking and the traction conditions. The free-rolling angular velocity is estimated from the straight line rolling simulation and is braking and traction simulations. The braking simulation results are obtained at a rotational velocity (ω) of 8 rad/sec (starting from the free-rolling angular velocity) and a translational velocity (u_o) of 10 kph. The traction simulation results are obtained at a rotational velocity (ω) of 9 rad/sec (starting from the free-rolling angular velocity) and a translational velocity (u_o) of 10 kph. The velocities considered in this Chapter are the same as what was considered in Chapter 6 (section 6.1) while estimating the free-rolling angular velocity. A coefficient of friction of μ=0.85 is used in the steady-state rolling FEM. The constraints set on the hub are the same as those used in Chapter 6.

The SAE tire conventions are used in this work. The traction slip ratio is negative and the corresponding longitudinal force is positive and vice-versa for braking. The longitudinal

forces from the FEM results from the braking and traction simulations for various normal load cases is shown in Fig. 10.3. From this it can be seen that the force curves are symmetric about the x-axis. Owing to the symmetry, it is sufficient to consider either traction or braking for analysis purposes. Hence, only the results from the traction simulations are considered.

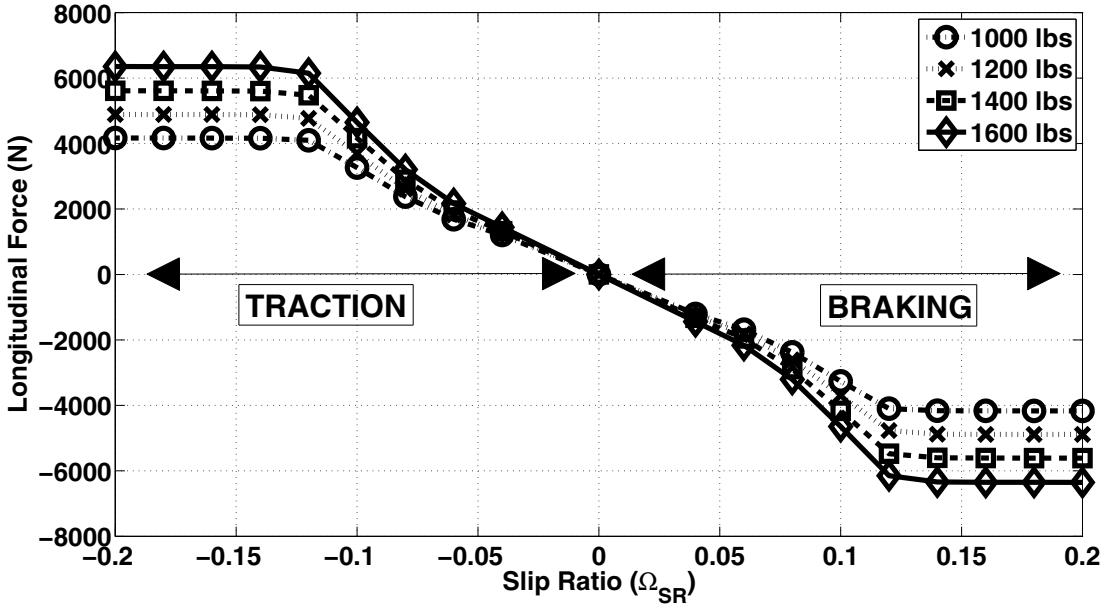

Figure 10.3: Longitudinal force under braking and traction.

10.2 Strain Profile Under Steady-State Rolling

The strains in the contact patch under traction for the various cases of the normal load and the slip ratio (longitudinal slip) are analyzed in this section.

In the first set of figures (see Fig. 10.4), the circumferential strains ($\epsilon_{\theta\theta}$ as predicted by the FEM along sensors 1-4) when a normal load of 1000 lbs is applied are shown. From this, it can be seen that sensors 2 and 3 show no variations with increases in slip ratio from 0-20%. In contrast, sensors 1 and 4 exhibit variations with the increases in the slip ratio. The strain distribution starts as symmetrical about the center of contact, but asymmetry can be observed along all the four sensors with increases in the slip ratio up to 20%. However, the

asymmetric strain distribution is absent when the slip ratio is 0% and no driving torque is applied on the wheel. It is also evident from the strain predictions (especially sensors 1 and 4) that the force saturation that occurs beyond the 10% slip ratio limits the longitudinal tread deformation. This is the reason that the strain curves to fall on top of each other beyond a 10% slip ratio. i.e. no change in the strains for slip ratio's >10%. But, the saturation limit at 10% might change if a different coeffcient of friction value is used. Next the normal load is increased to 1200 lbs and the FEM strain predictions are shown in Fig. 10.5. From this it can be quickly concluded that the strain predictions are similar to the 1000 lbs normal load case.

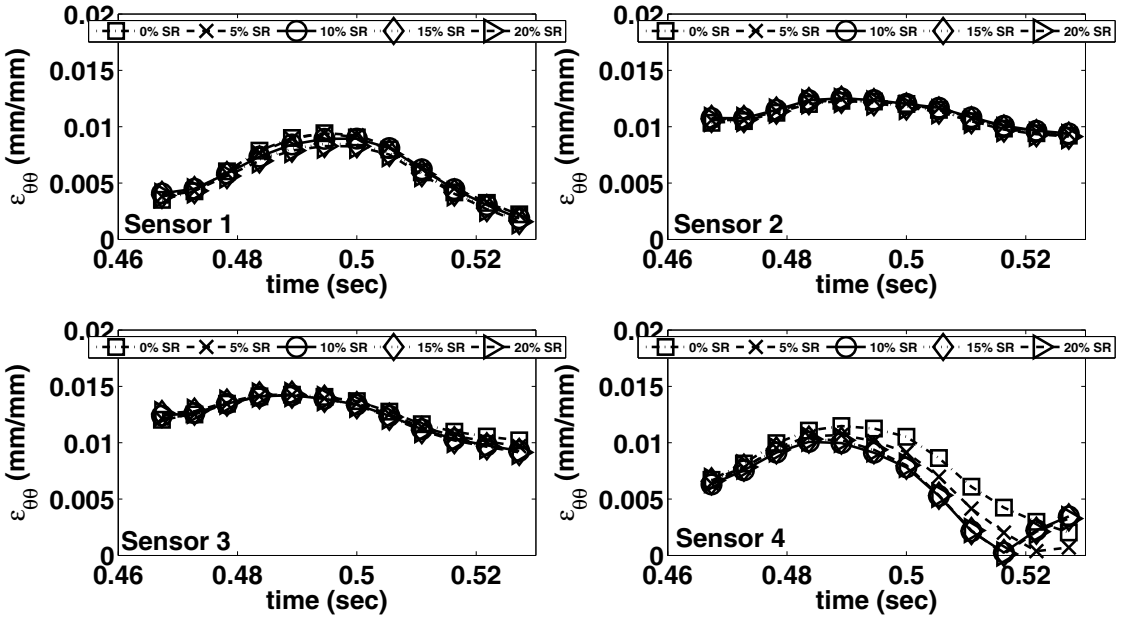

Figure 10.4: Strain profile under steady-state rolling 0-20% slip ratio; Normal load 1000lbs (Sensors 1-4).

The strain profile for the 1400 lbs normal load case of the sensors 1-4 is shown in Fig. 10.6. From this, it can be seen that the trailing edge, which is under tension for the traction case, deforms asymmetrically about the x-axis (sensors 1 and 4 clearly exhibit this trend). The sensors 2 and 3 on the other hand show no variation with the increases in the slip

ratio. However, it is interesting to note that the sensor 2 and 3 strain curves almost flatten out while going in and out of contact. At the edges of contact, the strains predicted by sensors 1 and 4 clearly exhibit a dependency on slip ratio (up to 10%). A similar conclusion can be obtained for the 1600 lbs normal load case (see Fig. 10.7). Further, from all the normal load cases that were considered, it can be concluded that the time of contact is only a function of the applied normal load. This simply implies that the equation developed in Chapter 7, for predicting the normal load should work for the steady-state rolling condition. (However this needs to be confirmed with additional tests).

In conclusion, it is evident from the strain profiles that the strains at the edges of contact can be used when developing equations for the slip ratio. The symmetric and the asymmetric strain distribution should provide a way for relating the strains to the slip ratio. Therefore the focus of the next Chapter will be on deriving an analytical relationship between the slip ratio and the strain due to the frictional load (longitudinal slip).

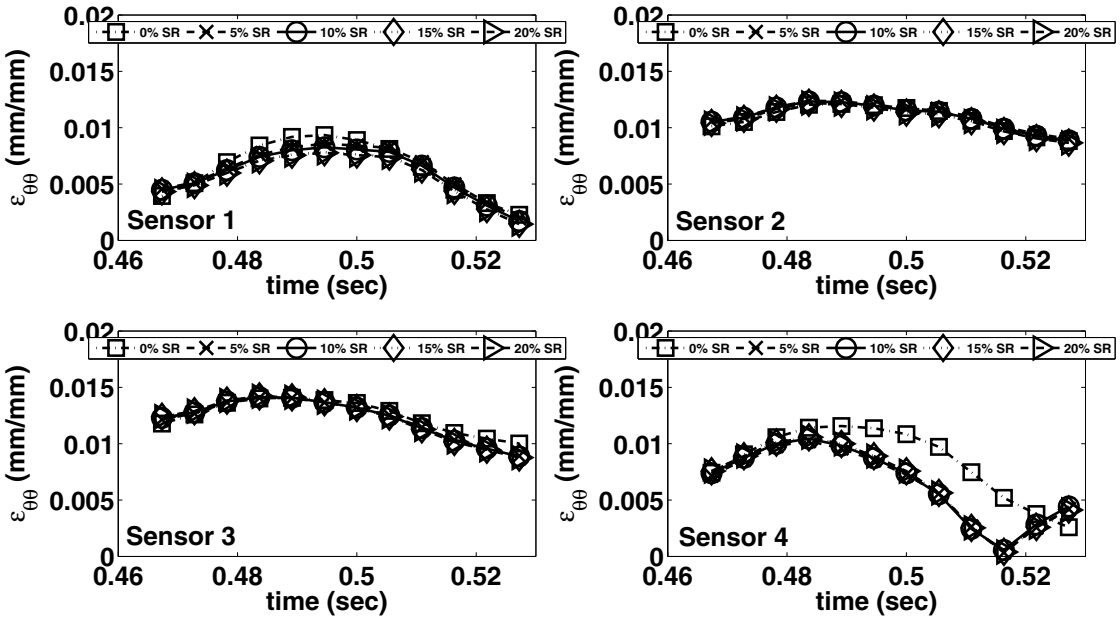

Figure 10.5: Strain profile under steady-state rolling 0-20% slip ratio; Normal load 1200lbs (Sensors 1-4).

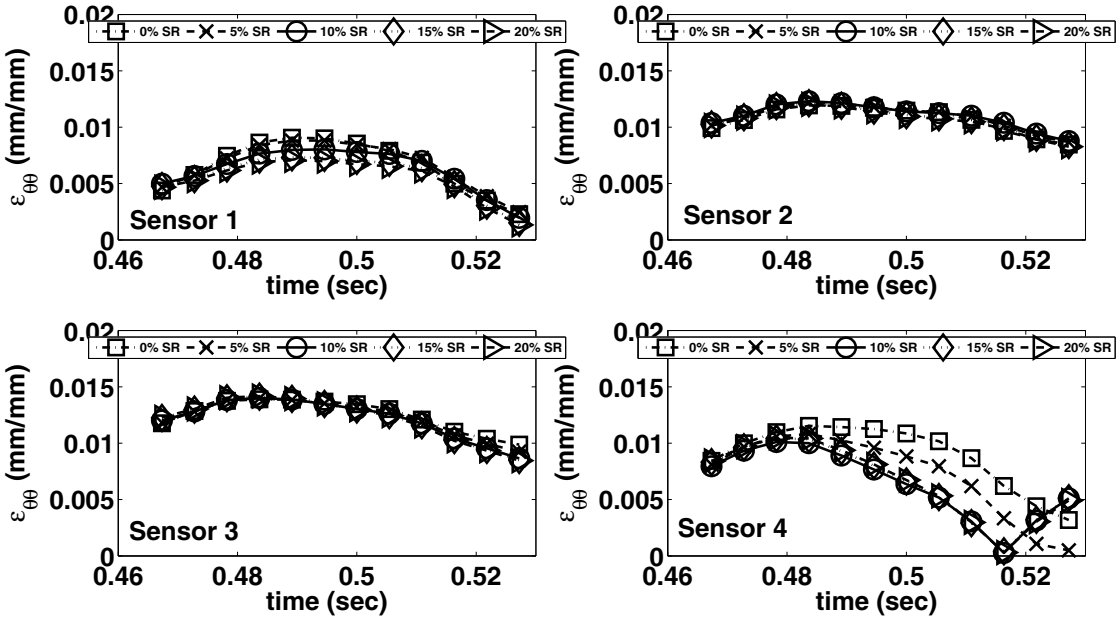

Figure 10.6: Strain profile under steady-state rolling 0-20% slip ratio; Normal load 1400lbs (Sensors 1-4).

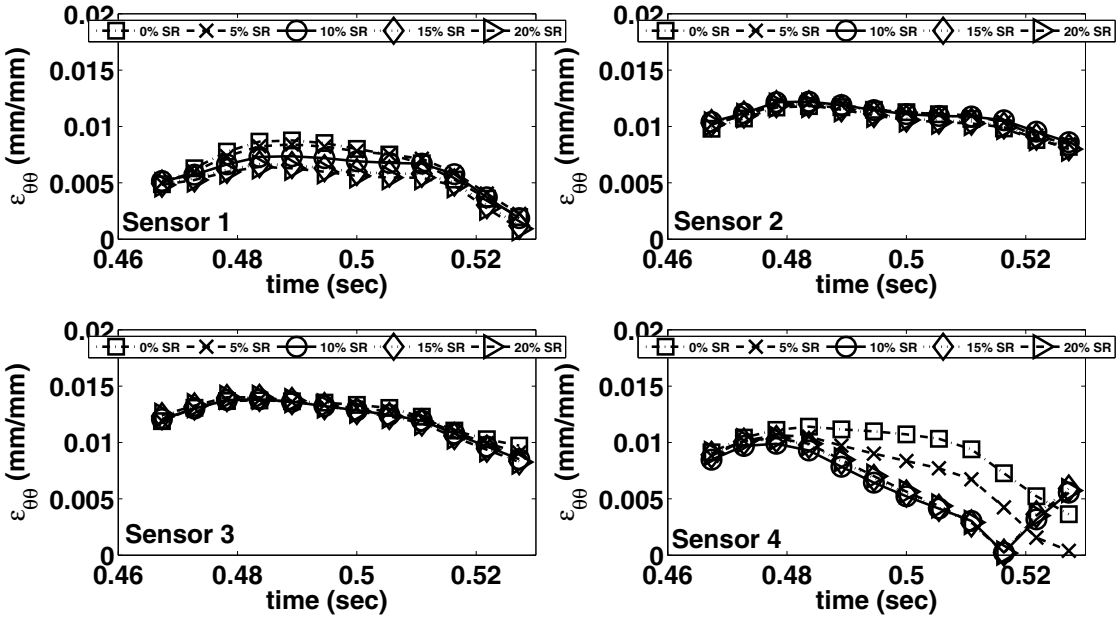

Figure 10.7: Strain profile under steady-state rolling 0-20% slip ratio; Normal load 1600lbs (Sensors 1-4).

Chapter 11

Strain Analysis Based on Steady-State Rolling Finite Element Prediction

In this chapter the strain results from the steady-state rolling finite element model are analyzed. Owing to the symmetric longitudinal force as a function of slip ratio about the free-rolling case results from the braking and traction simulations, the strain results from either the braking or the traction FEM is sufficient to predict the slip ratio and the longitudinal force. In this work only the traction simulation results are considered for analysis purposes but can then be 'reversed' to obtain the braking results. The slope curve method is used to estimate the contact duration from the FEM results (see section 7.3). A relationship between the strains predicted from the FEM and the slip ratio is developed. An empirical equation relating the slip ratio to the longitudinal force is also developed. The longitudinal force predictions from the FEM is then compared to the predictions from the empirical model.

11.1 Slope Curve Method

The slope curve method developed in Chapter 7 is used to analyze the strain data from the FEM. In this method the slope change is calculated by employing the center difference method. The equation for slope change based on center difference method is as follows,

$$\left(\frac{\Delta\varepsilon_{\theta\theta}}{\Delta t}\right)_i = \frac{(\varepsilon_{i+1} - \varepsilon_{i-1})}{(t_{i+1} - t_{i-1})} \tag{11.1}$$

The slope change curves for the steady-state rolling without longitudinal slip (0% slip ratio) as a function of time is shown in Fig. 11.1. It can be seen that the time of contact along the paths of the four sensors increases with increases in the normal load. It can also be seen that every sensor as it goes in and out of contact generates two peaks which correspond to a

maxima and a minima slope and approximately make the edge of contact. The difference in the time between the occurrences of a maxima and a minima slope is the contact duration.

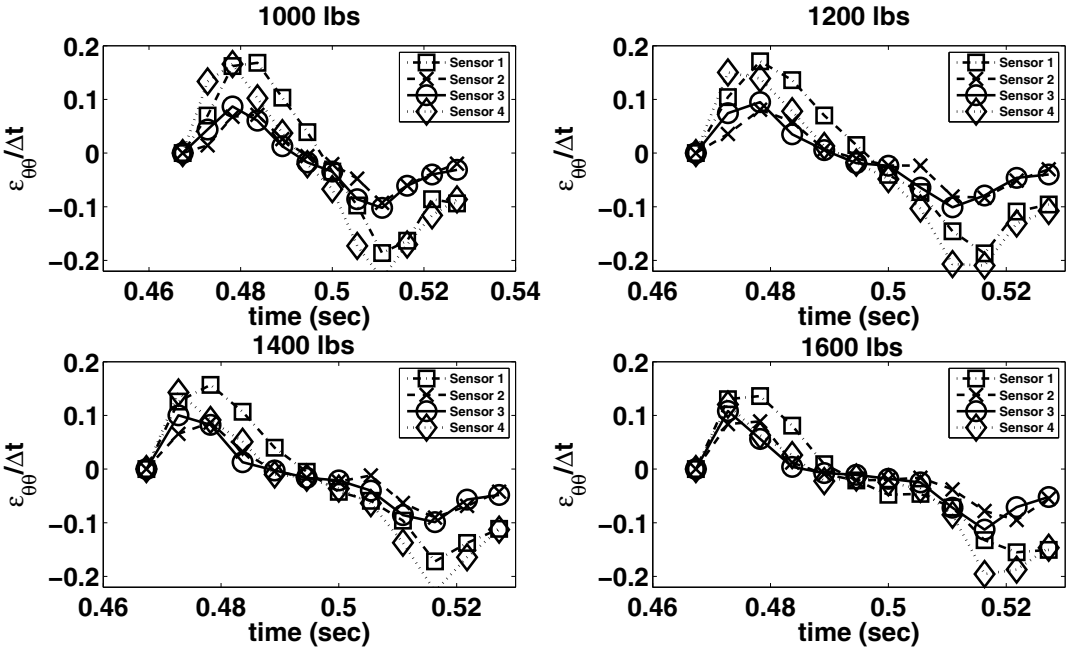

Figure 11.1: Slope change 0% slip ratio; Normal loads 1000lbs, 1200lbs, 1400lbs and 1600lbs.

Next, the slope change for the 5% slip ratio is shown in Fig. 11.2. From this figure it can be seen that the maximum and minimum changes in slope with respect to slip ratio remains constant with the change in slip ratio and only changes when the normal load on the tire is varied.

The 10% slip ratio case shown in Fig. 11.3, also exhibits a similar trend, where a maxima and a minima occur at the same time indicating that the maximum strain values are realized at the edges of the contact. It is interesting to note that the magnitude of the maximum and minimum changes in the slope remain almost constant with further increase in slip ratio (this can be clearly seen in Fig. 11.4). A possible reason could be that the longitudinal force reaches saturation for a given load as limited by the friction coefficient. It is clear that the contact duration, which is the difference in time between the occurrence of a maxima and a minima, is practically a function of normal load only. This implies that the magnitude

of the strain due to friction is predominant at the edges of the contact and the magnitude of the strains due to normal load almost vanish. This would then lead to an asymmetric strain distribution. Hence, at the edges of the contact, the slip ratio can be correlated to the frictional strains.

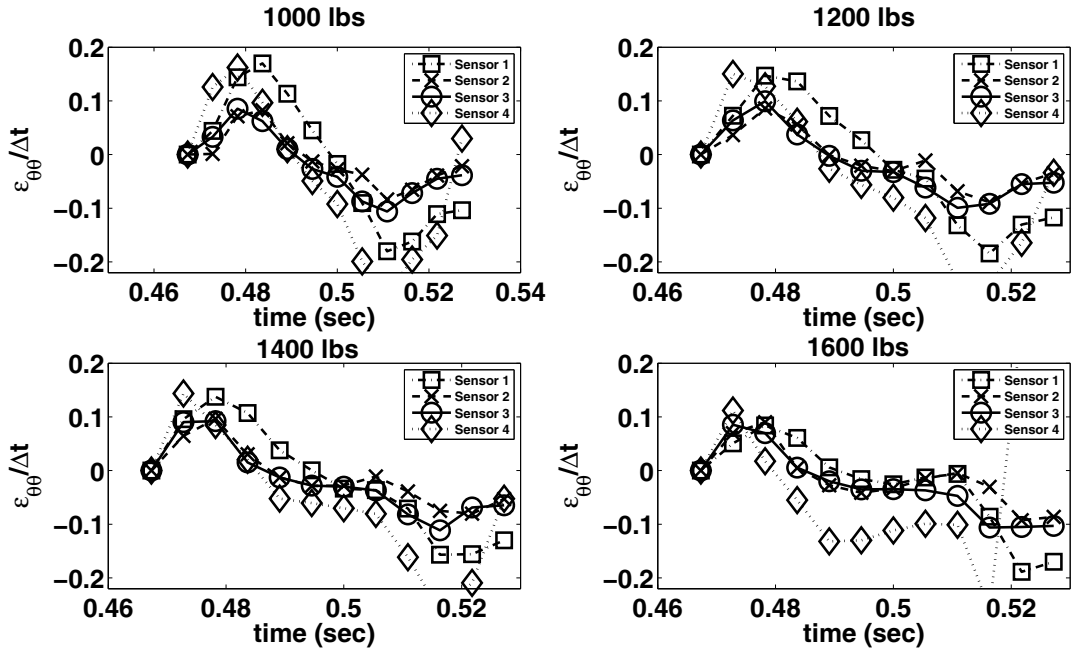

Figure 11.2: Slope change 5% slip ratio; Normal loads 1000lbs, 1200lbs, 1400lbs and 1600lbs.

11.2 Slip Ratio Estimation

The slip ratio estimation follows a rather straight forward approach with an underlying assumption that the tread deforms only in the longitudinal direction (see Fig. 11.5). Based on this assumption, it can be quickly concluded that the contact patch deforms in the direction in which the tire rotates (clockwise for traction). When the tire rotates in the clockwise direction and a driving torque is applied on the wheel, a shear deformation of the tread occurs. This shear deformation creates an asymmetric strain distribution about the center point of contact. In other words, an additional tensile strain results on one side of the contact

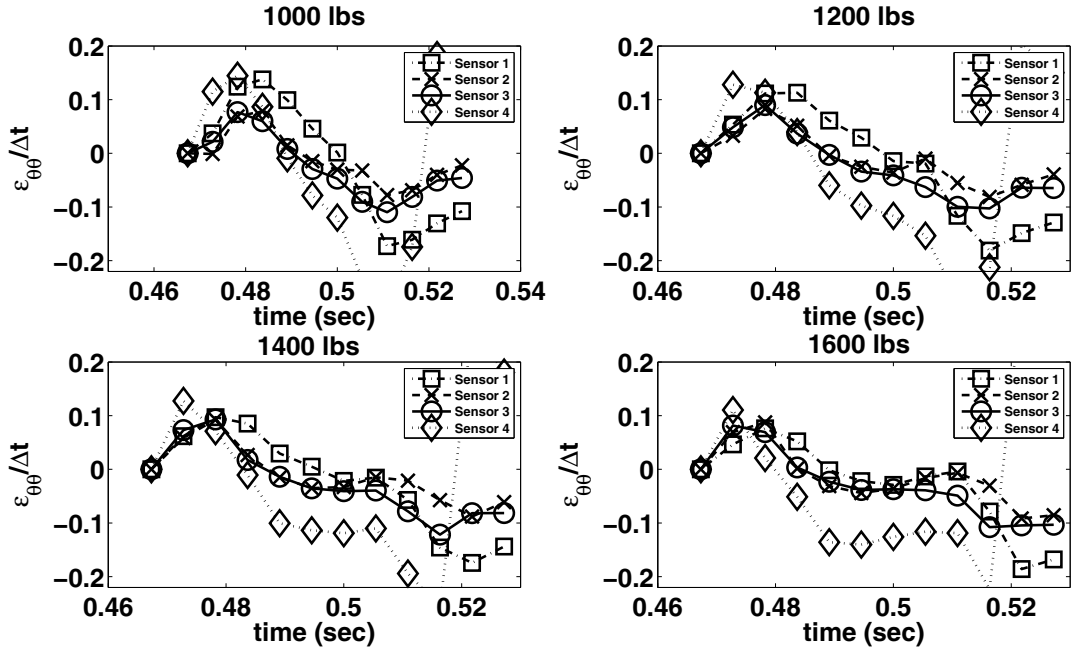

Figure 11.3: Slope change 10% slip ratio; Normal loads 1000lbs, 1200lbs, 1400lbs and 1600lbs.

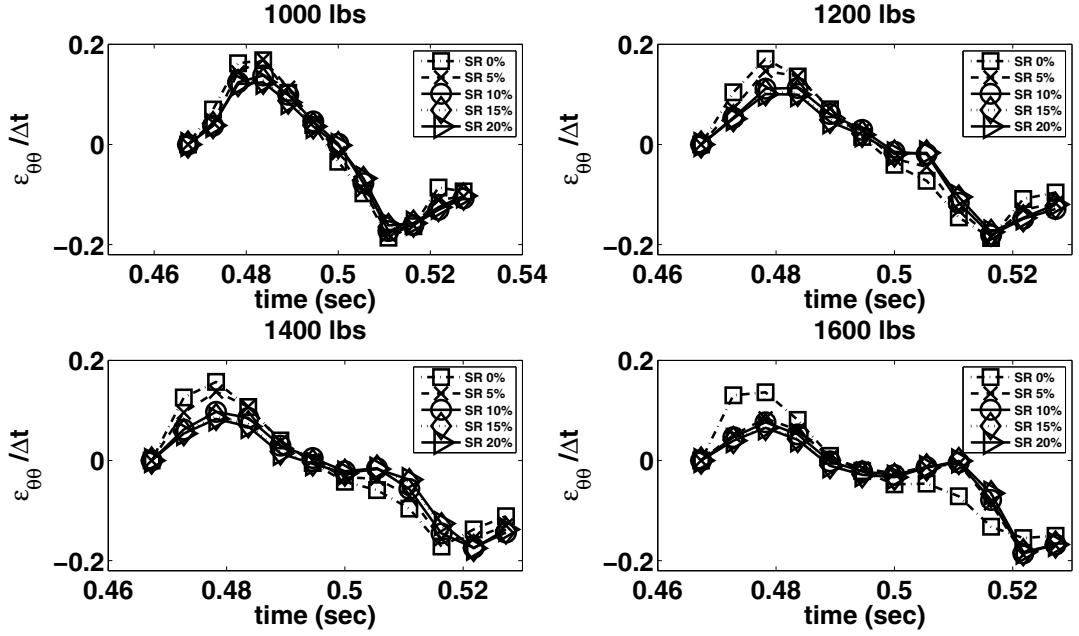

Figure 11.4: Slope change 0%-20% slip ratio; Normal loads 1000lbs, 1200lbs, 1400lbs and 1600lbs along sensor 1.

and a compressive on the other. Which is on the leading or the trailing edge depending on if it is braking or traction. When the sensors go in and out of contact (as shown in Fig. 11.5), the longitudinal slip for a particular load can be estimated.

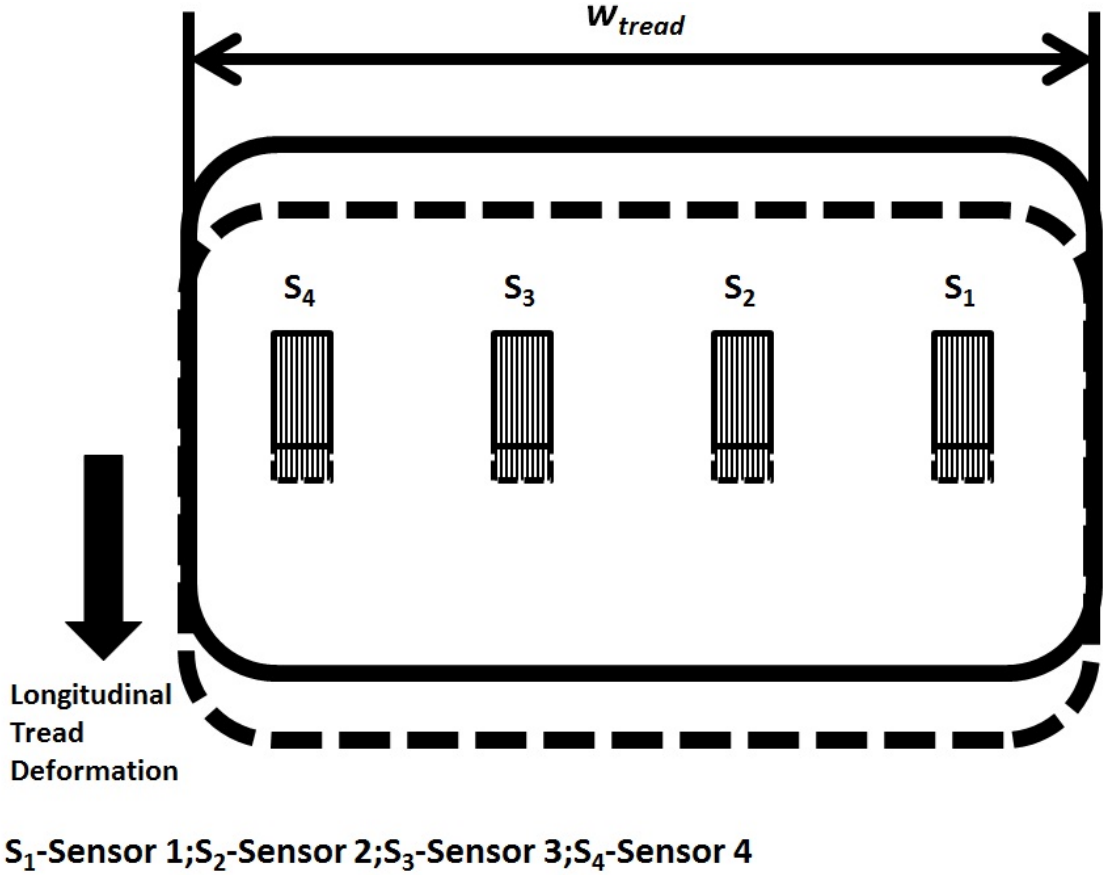

Figure 11.5: Relating strain to the slip ratio.

In order to theoretically explain this change in strain at the leading and the trailing edge the following analysis is provided. The circumferential strain in the tire can be expressed as follows,

$$\epsilon_{\theta\theta} = \epsilon_{norm} + \epsilon_{fric} \tag{11.2}$$

where ϵ_{norm} is the strain due to the normal load and ϵ_{norm} is the strain due the frictional load on the tire. At the edges of contact, points A and B (see Fig. 11.6) respectively, the

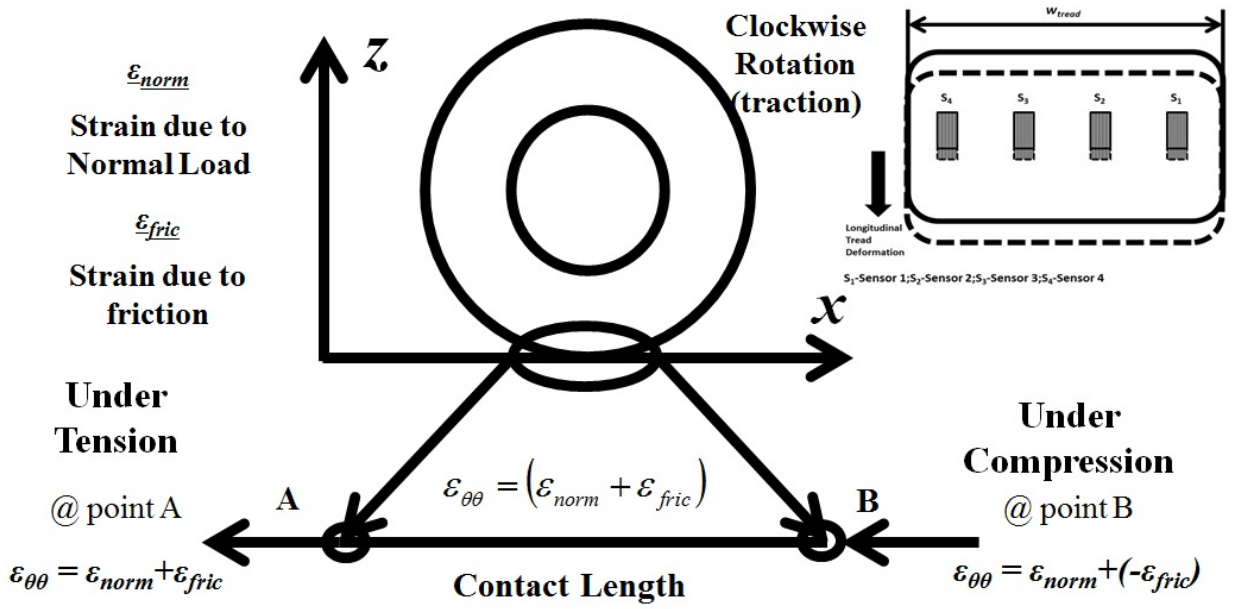

Figure 11.6: Analytical relationship between strain and slip ratio.

circumferential strain is given as follows,

$$\varepsilon_{\theta\theta_A} = \varepsilon_{norm} + \varepsilon_{fric}; \varepsilon_{\theta\theta_B} = \varepsilon_{norm} + (-\varepsilon_{fric}) \tag{11.3}$$

The symmetric and asymmetric characteristics of the tire strains at the edges of contact can be exploited to obtain a relationship between frictional strain and the slip ratio. The primary reason for the asymmetry in frictional strain is because point A (for clockwise tire rotation) is in tension ('+') and point B is under compression ('-'). In short, the frictional strain is related to the circumferential strain as follows,

$$\varepsilon_{\theta\theta_A} - \varepsilon_{\theta\theta_B} = (\varepsilon_{norm} + \varepsilon_{fric}) - (\varepsilon_{norm} + (-\varepsilon_{fric})) \tag{11.4}$$

$$\varepsilon_{fric} = \frac{(\varepsilon_{\theta\theta_A} - \varepsilon_{\theta\theta_B})}{2} \tag{11.5}$$

Eq. 11.5 derived above will be a function of slip ratio (and longitudinal force). In Fig. 11.7, the slip ratio as a function of the frictional strain ϵ_{fric} from the FEM results for various

normal load cases considered, is shown. A linear polynomial is then fit to the FEM data and an empirical equation is obtained. The equation is given as follows,

$$\Omega_{SR} = A_{fem} \cdot (\varepsilon_{fric}) + B_{fem} \tag{11.6}$$

where A_{fem} and B_{fem} are load dependent constants. The equations for these two constants is given in section 11.4.1.

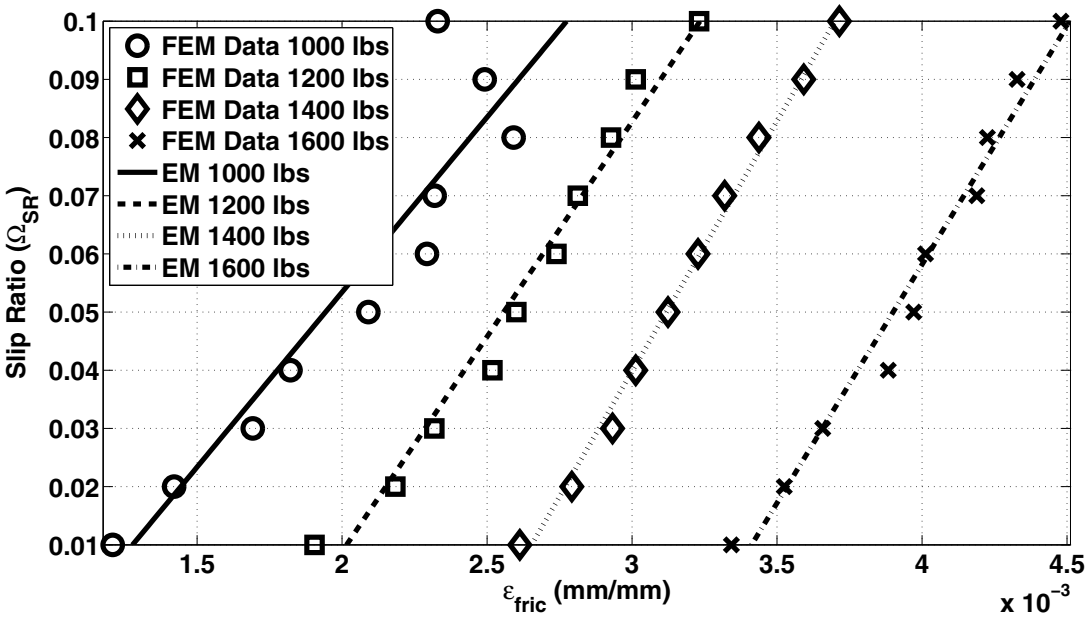

Figure 11.7: Slip ratio plotted as function of ϵ_{fric}.

11.3 Longitudinal Force Estimation

The steady-state rolling condition with a negative slip ratio will capture full-traction. The force exerted on the tire under such a condition is known as longitudinal force (also known as rolling resistance). According to the SAE definition, the longitudinal force is simply the force exerted on the tire by the road when a longitudinal slip as characterized by the slip ratio exists.

In Fig. 11.8, the longitudinal force versus the slip ratio (0-10%) from the FEM results is shown. It can be seen that for a given load the longitudinal force increases when the slip ratio increases. The longitudinal force is of course limited by the friction coefficient (μ=0.85 in this case). A quadratic polynomial of the form shown in Eq. 11.7 is fit to the FEM results. The curve fit to the FEM results is shown in Fig. 11.9.

$$f_x = c_\Omega \cdot (\Omega_{SR})^2 + d_\Omega \cdot (\Omega_{SR}) + e_\Omega \tag{11.7}$$

where c_Ω, d_Ω, and e_Ω are load dependent constants fit to the FEM results. The equations for these constants is given in the following section.

The strain based longitudinal force prediction labeled (EM) is shown in Fig. 11.10 in comparison to that predicted from the FEM. First, the slip ratio is estimated from the empirical model by Eq. 11.6. Then, the estimated slip ratio is input into Eq. 11.7 and the longitudinal force from the semi-empirical model is obtained. An average error less than 5% exists between the FEM results and the strain-based model (Eqs. 11.6 and 11.7).

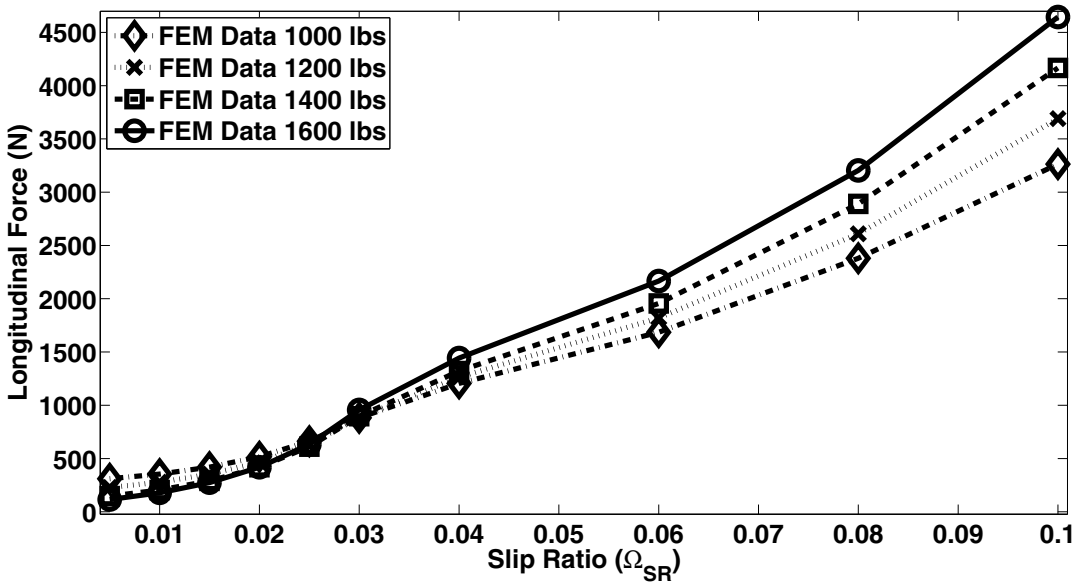

Figure 11.8: Longitudinal force under a driving torque for various normal loads.

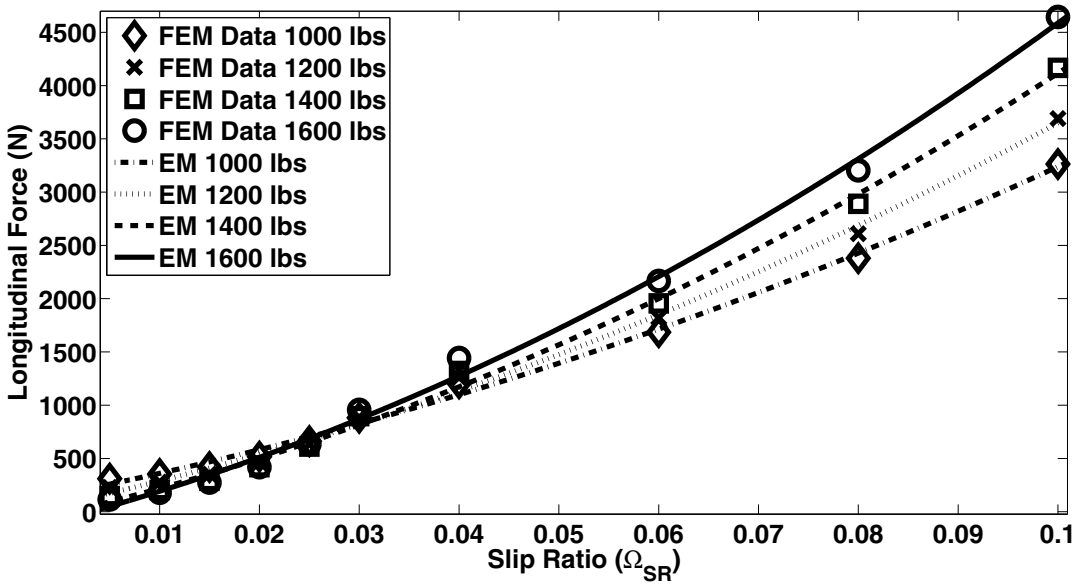

Figure 11.9: Longitudinal force estimated from the semi-empirical model versus the slip ratio.

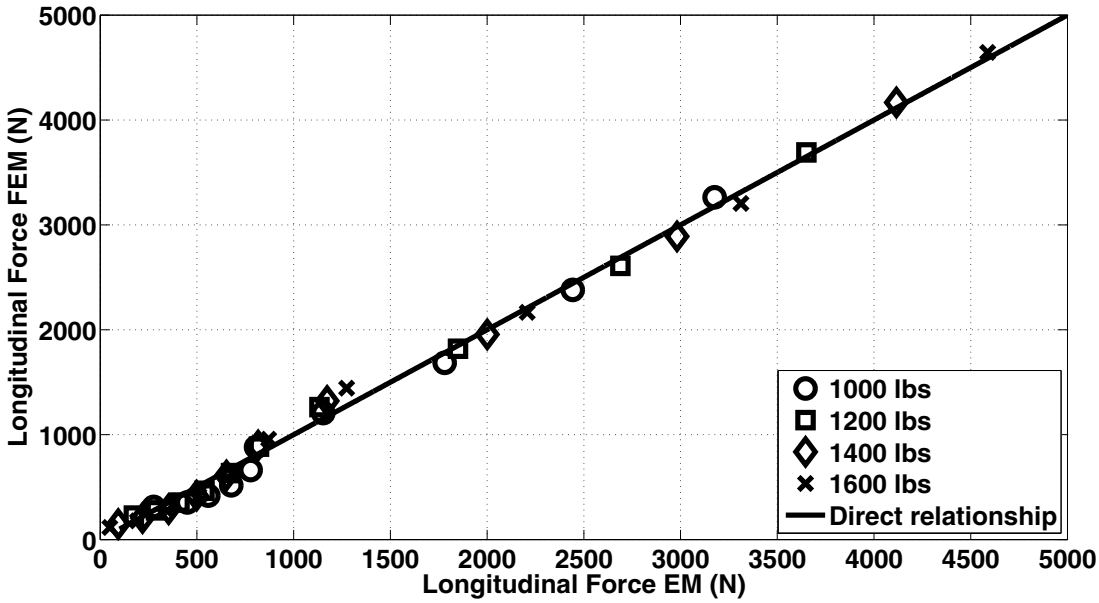

Figure 11.10: Longitudinal force estimated from the semi-empirical model compared to the FEM results.

11.4 Estimating Constants of Semi-Empirical Model based on FEM Results

11.4.1 Constants in the Slip Ratio Empirical Model

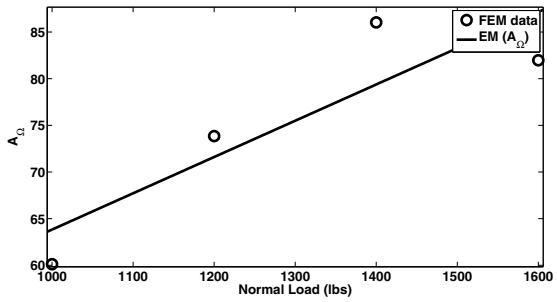

Figure 11.11: Load dependent constant A_{fem} estimated from normal load.

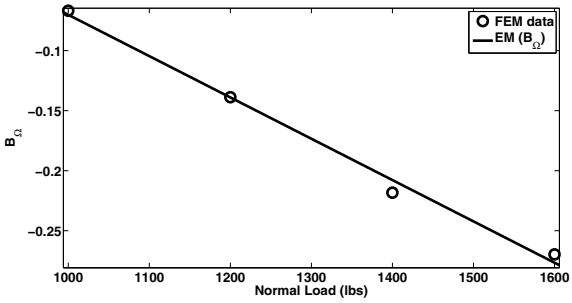

Figure 11.12: Load dependent constant B_{fem} estimated from normal load

The A_{fem} constant terms from all the normal load cases that were considered in developing Eq. 11.6 are collected and plotted versus the normal load. A curve is fit to obtain a relationship between A_{fem} and the normal load (shown in Fig. 11.11). The curve represents a linear polynomial and the resulting equation is given by,

$$A_{fem} = 0.03888 \cdot (f_z) + 24.95 \tag{11.8}$$

Figure 11.12 shows the plot of B_{fem} (a constant term in Eq. 11.6) versus the normal load. A non-linear tread is observed and hence a linear polynomial is fit to the data. The resulting equation is given by,

$$B_{fem} = -0.0003441 \cdot (f_z) + 0.2739 \tag{11.9}$$

11.4.2 Constants in the Longitudinal Force Empirical Model

The first constant term in Eq. 11.7, c_Ω, is plotted versus the normal load and is shown in Fig. 11.14. A polynomial of order one best fits to the data. The resulting linear equation is given by,

$$c_\Omega = 155 \cdot (f_z) - 31340 \tag{11.10}$$

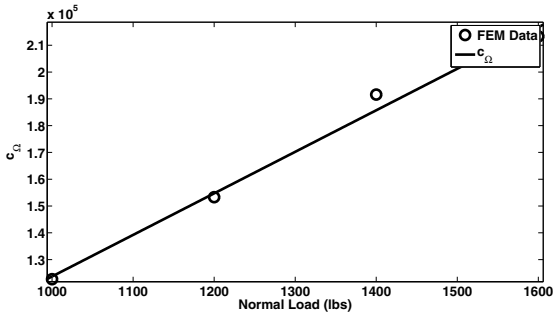

Figure 11.13: Load dependent constant c_Ω estimated from normal load.

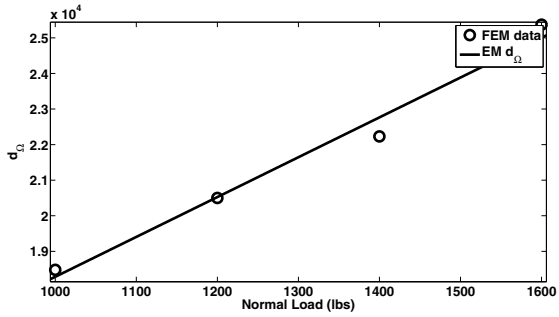

Figure 11.14: Load dependent constant d_Ω estimated from normal load.

Figure 11.14 shows the second term in Eq. 11.7, d_Ω, plotted versus the normal load. A linear polynomial best fits to the data. The resulting equation is given by,

$$d_\Omega = 11.2 \cdot (f_z) + 7085 \tag{11.11}$$

Figure 11.15 shows the third term in Eq. 11.7, e_Ω, plotted versus the normal load. A linear

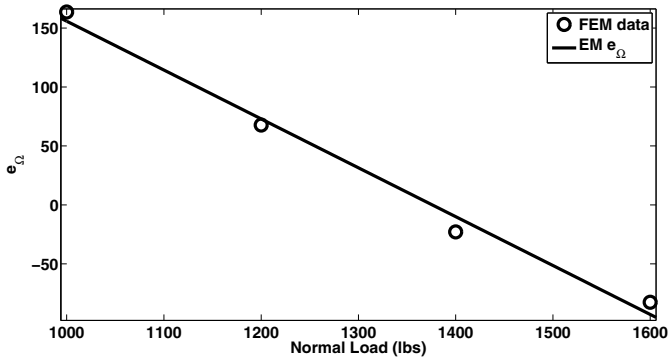

Figure 11.15: Load dependent constant e_Ω estimated from normal load.

polynomial best fits to the data. The resulting equation is given by,

$$e_\Omega = -0.4145 \cdot (f_z) + 570.4 \tag{11.12}$$

Chapter 12

Conclusions and Future Work

This dissertation contributes to the research in the area of advanced tire sensor technology using a finite element modeling technique for monitoring the state of the tire under various operating conditions. The deformation characteristics of a Standard Reference Test Tire under static loading and steady-state loading conditions are investigated. The numerical analysis techniques such as the Fourier analysis, the Weibull curve fitting and the slope curve method are explored to relate strains to the loads experienced by a tire under the static and steady-state rolling conditions. The various numerical analysis techniques explored have their own advantages and disadvantages. The Fourier analysis is a powerful tool, but requires a high sampling frequency to effectively capture the trends. This is a fairly simple procedure once the amplitudes and the frequencies are extracted from the data. Although, this is a computationally expensive method. Also, this method may not be feasible for real-time data processing. The Weibull curve fitting method is a simple method to generate good fits to the strain data. However, multiple functions can be fit to the same strain data. The number constants involved are too many, which would make this method very tire specific. Also, the Weibull parameters don't relate to changes in the load conditions. The slop curve method involves a simple procedure for parmeter estimation, which does not require a high sampling frequency. The notable problem with this method is the error amplification if the aquired data is noisy. However, this could be overcome by employing an alternative technique like the "total-variation regularization" technique (a method for derivative calculation of noisy data).

In summary the slope curve method appears to be the best method for estimating the necessary parameters. Hence, this method is used in this work. Based on the FEM results,

a semi-empirical model relating normal load to the strains is proposed. An empirical model relating the slip angle to the tire strains, based on the steady-state free-rolling FEM results, is also proposed. An empirical model relating the lateral force to the slip angle is proposed. The strain based prediction of the lateral force is then compared to the FEM results. An equation relating the slip ratio to the tire strains, based on the steady-state rolling FEM results, is proposed. An equation relating the longitudinal force to the slip ratio is also proposed. The strain based prediction of the longitudinal force is then compared to the FEM results. These models can be used in contact patch strain sensing modules.

This dissertation contributes to the research in the area of advanced tire sensor technology using an experimental technique for monitoring the state of the tire under various operating conditions. A wireless tire sensor suite is developed and it's use is demonstrated in aquiring the tire strains in real time. The tire sensor suite is comprised of strain sensors, a signal coditioning circuit and a wireless data transmitter/reciever. The test setup for the static loading and the steady state rolling are discussed in Chapter 3 and Chapter 8 respectively. A semi-empirical model for each of the tire loads considered above (only static and steady-state free- rolling) is developed based on the experimental data.

The FEM work serves as a template for the experimental work in relating the various tire operating conditions to the strains. The empirical model based on the FEM results for estimating the normal load on the tire is in good agreement with the empirical model based on the experimental data. An order of magnitude difference in the δ_{slip} values exists between the FEM results and the experimental data in the slip angle empirical model. Despite the difference, similar functions fit well to the FEM results and the experimental data. The FEM over predicts the lateral force in comparison to the experiments. The lateral force empirical model based on the FEM results is of the same order as that of the empirical model based on the experimental data. The resulting constants are a function of the normal load on the tire. The equations that relate the various constants to the load are of the same order, but the values of these constants are different. Since the FEM work is viewed more as a tool

for developing a template for the various tire operating conditions, a qualitative comparison between the models and the resulting load dependent constants may not be required.

In conclusion, the slope curve method used in the current work, is shown to work well with the FEM results and the experimental data under the steady-state free-rolling conditon. This method also works well with the FEM results for the steady-state rolling condition (for estimating slip ratio and longitudinal force). However, further testing is required to understand the implications of the slope curve method on the experimental data.

In the future, the FEM work can be extended by modeling all the sections of the tire for better predictions. The material dependent properties such as viscoelasticity and hysteresis can be included in the material model to better understand their influence on the tire deformation. An actual strain sensor can be modeled instead of depending on the nodal solution for strain measurement. The debonding effects can also be studied if an actual strain sensor were to be modeled. In addition, dynamic loading conditions such as tire vibration, impact loading etc. can be considered. These considerations will extend the validity of equations and models to the non steady-state conditions.

The experimental work can be extended by considering novel contact patch strain sensing modules, such as rubber based sensors or MEMS based devices or optical sensors. The driving and braking torque tests can be done to aquire wireless strain data. The experiemental data can be used to develop models relating the slip ratio to the tire strains and the longitudinal force to the slip ratio. The testing can also be extended by running the tire fitted on a real vehicle. A comprehensive set of components can be achieved by incorporating temperature sensors, pressure sensors, accelerometers etc., in the tire sensor suite.

Bibliography

[1] Title 49 United States Code 30101, *Transportation Recall Enhancement, Accountability, and Documentation (TREAD) Act*, 2000., **Public Law 106-414-nov.1**.

[2] Sensatec LLC, National Highway Traffic Safety Administration, *Tiresafe Product Overview*, 2000., **NHTSA-00-8572-1**.

[3] Grygier, P., Garrott, W. R., Mazzae, E. N., Hoover, R. L., Elsasser, D., and Ranney, T. A., *An Evaluation of Existing Tire Pressure Monitoring Systems*, NHTSA, 2001., **DOT 809 297**.

[4] Mazzae, E. N. and Ranney, T. A., *Development of an Automotive Icon for Indication of Significant Tire Under-Inflation*, HFES 45th Annual Meeting, 2001.

[5] MacIsacc, J. D. J. and Garrott, W. R., *Preliminary Findings of the Effect of Tire Inflation Pressure on the Peak and Slide Coefficients of Friction*, NHTSA , 2002., **DOT 809 428**.

[6] National Highway Traffics Safety Administration, *Federal Motor Vehicle Safety Standards; Tire Pressure Monitoring Systems; Control and Displays*, 2002., **NHTSA-2000-8572**.

[7] Persson, N., Ahlqvist, S., Forssell, U., and Gustafsson, F., *Low Tyre Pressure Warning System Using Sensor Fusion*, SAE Conf. Proc. on Automotive and Transportation Technology Congress Exposition, 2001., p. 77-79.

[8] Minf, K., *A Smart Tire Pressure Monitoring System*, Sensors, 2001., **18**11: p. 40-46.

[9] Umeno, T., Asano, K., Ohashi, H., Yotetani, M., Naitou, T., and Taguchi, T., *Observer Based Estimation of Parameter Variations and its Application to Tyre Pressure Diagnosis*, Control Engineering Practice, 2001., **9**: p. 639-645.

[10] Ymagiwa, T., Orita, M., and Harada, T., *Development of a Tire Pressure Monitoring System for Motorcycles*, JSAE Review, 2003., **23**: pp. 495-496.

[11] Cullen, J. D., Arvanitis, N., Lucas, J., and Al-Shamma'a, A. I., *In-field Trials of a Tyre Pressure Monitoring System Based on Segmented Capacitance Rings*, Measurements, 2002., **32**33: pp. 181-192.

[12] Halfmann, C., Ayoubi, M., and Holzmann, H., *Suspension of Vehicles' Tyre Pressures by Measurement of Body Accelerations*, Control Engineering Practice, 1997., **5**8: p. 1151-1159.

[13] Siddons, J., and Derbyshire, A., *Tyre Pressure Measurement Using Smart Low Power Microsystems*, Sensor Review, 1997., **17**2: pp. 126-130.

[14] Gustafsson, F., Drevo, M., Forssell, U., Lofgen, M., Persson, N., and Quiklund, H., *Virtual Sensors of Tire Pressure and Road Friction*, SAE Technical Papers, 2001., **2001-01-0796**.

[15] Kowalewski, M., *Monitoring and Managing Tire Pressure*, IEEE Potentials, 2004., **23**3: pp. 8-10.

[16] Garrott, W.R, and Forkenbrock, G.J, *Testing the Effects of Tire Pressure Monitoring System Minimum Activation Pressure on the Handling and Rollover Resistance of a 15-Passenger Van*, NHTSA, 2004., **DOT HS 809 701**.

[17] Clark, S.K., *Mechanics of Pneumatic Tires*, National Bureau of Standards, Monograpgh, 1971., **122**.

[18] Browne, A., Ludema, K.C., and Clark, S.K, *Mechanics of Pneumatic Tires*, National Bureau of Standards, Monograpgh, 1971., **122**.

[19] Patel, H.P, and Zorowski, C.F, *Deformation of the Pneumatic Tire*, Tire Science and Technology, 1978., **6**4: pp. 233-247.

[20] Noor, A. K., and Andersen, C. M., *Finite Element Modeling and Analysis of Tires*, Proceedings from NASA Tire Modeling Workshop, 1982., **2264**: pp. 1-33.

[21] Oden, J.T., Becker, E.B., Miller, T.H., Endo, T., and Pires, E.B., *Finite Element Method for Non-Linear Elastoplastic Problems in Rubber Elasticity*, Proceedings from NASA Tire Modeling Workshop, 1982., **2264**: pp. 39-70.

[22] Ridha, R.A., *Computation of Stresses, Strains, and Deformation of Tires*, Rubber Chemistry and technology, 1980., **53**4: pp. 849-902.

[23] Faria, L.O., Oden, J.T., Yavari, B., Tworzydlo, W.W., Bass, J.M., and Becker, E.B., *Tire Modeling by Finite Elements*, Tire Science and Technology, 1992., **20**1: pp. 33-56.

[24] Gall, R., Tabaddor, F., Robbins, D., Majors, P., Shepherd, W., and Johnson, S., *Some Notes on the Finite Element Analysis of Tires*, Tire Science and Technology, 1995., **23**3: pp. 175-188.

[25] Kagami, S., Akasaka, T., Shiobara, H., and Hasegawa, A., *Analysis of the Contact Deformation of Radial Tires with Camber Angle*, Tire Science and Technology, 1995., **23**1: pp. 26-51.

[26] Shida, Z., Koishi, M., Kogure, T., and Kabe, K., *A Rolling Resistance Simulation of Tires Using Static Finite Element Analysis*, Tire Science and Technology, 1999., **27**2: pp. 84-105.

[27] Fujikawa, T., Uchiyama, Y., and Yamaguchi, I., *Tire Model to Predict Treadwear*, Tire Science and Technology, 1999., **27**2: pp. 106-125.

[28] Chandra, S., *Challenges in the Finite Element Analysis of Tire Design using ABAQUS*, American Engineering Group, 2000.

[29] Kim, S. Kondo, K., and Akasaka, T. , *Contact Pressure Distribution of Radial Tire in Motion with Camber Angle*, Tire Science and Technology, 2000., **28**1: pp. 2-32.

[30] Holscher, H., Tewes, M., Botkin, N., Lohndrof, M., Hoffmann, K. H., and Quandt, E., *Modeling of Pneumatic Tires by a Finite Element Method for the Development of a Tire Friction Sensor*, Computers and Structures, 2004., pp. 1-17.

[31] Yan, X., *Finite Element Formulation of tire with Static Foundation Contact and its Application*, Journal of Reinforced Plastics and Composites, 2005., **24**16: pp. 1671-1696.

[32] Haney, P., *The Racing and High-Performance Tire*, Sports Car, February, 2004.

[33] Yanjin, G., and Guoqun, Z., *FEA and Testing Studies on Static Camber Performance of the Radial Tire*, Journal of Reinforced Plastics and Composites, 2007., **26**16: pp. 1921-1936.

[34] Sokolov, S. L., *Calculation of the Stress-Strain State of Pneumatic Tires by the Finite Element Method*, Calculation of the Stress-Strain State of Pneumatic Tires by the Finite Element Method, 2007., **36**1: pp. 45-49.

[35] Miyashita, N., and Kabe, K., *A New Analytical Tire Model for Cornering Simulation. Part II: Cornering Force and Self-aligning Torque*, Tire Science and Technology, 2006., **34**2: pp. 100-118.

[36] Bozdog, D. and Olson, W. W., *An Advanced Shell Theory Based Tire Model*, Tire Science and Technology, 2005., **33**4: pp. 227-238.

[37] Darnell, I., Mousseau, R., and Hulbert, G., *Analysis of Tire Force and Moment Response During Side Slip Using an Efficient Finite Element Model,*, Tire Science and Technology, 2002., **30**2: pp. 66-82.

[38] Salaani, M.K., *Analytical Tire Forces and Moments with Physical Parameters*, Tire Science and Technology, 2008., **36**1: pp. 3-42.

[39] Rhyne, T. B., *Development of a Vertical Stiffness Relationship for Belted Radial Tires*, Tire Science and Technology, 2005., **33**3: pp. 136-155.

[40] Olatunbosun, O. A., Bolarinwa, O., *FE Simulation of the Effect of Tire Design Parameters on Lateral Forces and Moments*, Tire Science and Technology, 2004., **32**3: pp. 146-163.

[41] Zhang, X., Tamini, N., and Palmer, T., *Finite Element Tire Model Parameters for Road Load Predictions*, SAE International, 2004.

[42] Zheng, D., *"Prediction of Tire Tread Wear with FEM Steady State Rolling Contact Simulation*, Tire Science and Technology, 2002., **31**3: pp. 189-202.

[43] Hall, W., Mottram, J. T., and Jones, R. P., *Tire Modeling Methodology with the Explicit Finite Element Code LS-DYNA*, Tire Science and Technology, 2004., **32**4: pp. 236-261.

[44] Taheri, S., and, Ding, N., *A Modified Dugoff Tire Model for Combined-slip Forces*, Tire Science and Technology, 2010., **38**3: pp. 228-245.

[45] Pacejka, B.H., *Tire and Vehicle Dynamics*, SAE International, 2nd Edition, 2006.

[46] Persson, N., Gustafsson, F., and Drevo, M., *Indirect tire pressure monitoring using sensor fusion*, Proceedings of SAE, 2002.

[47] Kojima, H., Ohashi, H., Kubota, K., Fujiwara, K., Tomiita, K., and Umeno, T., *Development of tire pressure warning system using wheel speed sensor*, JSAE Review, 1998., **19**1: pp. 100-106.

[48] Arshak, K., Morris, D., Arshak, A., Korostynska, O., and Kaneswaran, K., *Developement of oxide thick film capacitors for a real time pressure monitoring system*, Materials Science and Engineering C, 2006.

[49] Synder, D.S., *Piezoelectric reed power supply for use in abnormal tire condition warning systems*, US-Patent, 1985., **510,484**.

[50] Zhihao, J., Huiwen, Y., Liji, W., Chen, J., Chun, Z., Zhihua, W., *Key Module Design of a Battery-less TPMS on Chip*, Proceedings of Solid-State and Integrated-Circuit Technology, 2008., **10**1109: pp. 1941-1944.

[51] Lange, T., and Kvisteroy, T., *Intelligent Low-Power Management and Concepts for Battery-less Direct Tire Pressure Monitoring Systems (TPMS)*, Advanced Microsystems for Automotive Applications, 2007., **5**: pp. 237-249.

[52] http://www.energyharvestingjournal.com, *Tyre Pressure Monitoring Systemsand Energy Harvesting*, January, 2011.

[53] I-Hsiu, H., Jia-min, C., Hsiao-Chin, C.,and, Hung-Wei, C., *A Battery-less Tire Pressure Monitoring System*, IEEE, 2009., **1**: pp. 978-983.

[54] Yong, L., Liji, W., Chun, Z.,and Zhihua, W., *Power Recovery circuit for Battery-less TPMS*, Proc.of International Conference on ASIC (ASICON), 2007., **1**: pp. 454-457.

[55] Qinglong, Z., Hongen, T., Aubry, A. and Yong, X., *Vibration Energy Harvesting Device based on Asymmetric Air-Spaced Cantilevers for Tire Pressure Monitoring System*, PowerMEMS, 2009., **5**1: pp. 403-406.

[56] Technical Research Centre of Finland (VTT), *Intelligent tyre systems - state of the art and potential technologies*, APOLLO **IST-2001-34372** Intelligent tyre for accident-free traffic, Deliverable D7, 2001.

[57] Yamamoto, S., Nakao, O., and Nishimura, H., *Touch mode capacitive pressure sensor for passive tire monitoring system*, IEEE Sensors, 2002., **2**: pp. 8-17.

[58] Nabipoor, M. and Majlis, B.Y, *A new passive telemetry LC pressure and temperature senosr optimized for TPMS*, Journal of Physics: Conference Series, 2006., **34**: pp. 770-775.

[59] Todoroki, A., Miyatani, S., and Shimamura, Y., *Wireless strain monitoring using electrical capacitance change of tire: part I - with oscillating circuit*, Smart Materials and Structures, 2003., **12**: pp. 403-409.

[60] Todoroki, A., Miyatani, S., and Shimamura, Y., *Wireless strain monitoring using electrical capacitance change of tire: II - passive*, Smart Materials and Structures, 2003., **12**: pp. 410-416.

[61] Bevly, D.M., Gerdes, J.C., Wilson, C., and Zhang, G., *The use of GPS based velocity measurements for improved vehicle state estimation*, Proceedings of the American Control Conference, 2000., pp. 2538-2542.

[62] Mauer, G.F., *A fuzzy logic controller for an ABS braking system*, IEEE Transactions on Fuzzy Systems, 1995., **3**4: pp. 381-388.

[63] Zhang, X., Wang, Z., Li, W., He, D., and Wang, F., *A fuzzy logic controller for an intelligent tires system*, Proceedings IEEE of Intelligent Vehicles Symposium, 2005., pp. 875-881.

[64] Lee, C., Hedrick, K., and Yi, K., *Real-time slip-based estimation of maximum tire-road friction coefficient*, IEEE/ASME Transactions on Mechatronics, 2004., **9**2: pp. 454-458.

[65] Matsuzaki, R., and Todoroki, A., *Wireless strain monitoring of tires using electrical capacitance changes with an oscillating circuit*, Sensors and Actuators A, 2005., **119**: pp. 323-331.

[66] Matsuzaki, R., and Todoroki, A., *Passive wireless strain monitoring of actual tire using capacitanceresistance change and multiple spectral features*, Sensors and Actuators A, 2006., **126**: pp. 277-286.

[67] Matsuzaki, R., and Todoroki, A., *Wireless flexible capacitive sensor based on ultra-flexible epoxy resin for intelligent tires*, Sensors and Actuators A: Physical, 2007., **140**1: pp. 32-42.

[68] Yi, J., and Liang, H., *A PVDF-Based Deformation and Motion Sensor: Modeling and Experiments*, IEEE Sensors, 2008., **8**4: pp. 384-391.

[69] Gondal, M.F., *Embedded Wireless Sensor Network for Aircraft/Automobile Tire Structural Health Monitoring*, MS thesis, Virginia Polytechnic Institute and State University, 2007.

[70] Sergio, M., Manaresi, N., Tartagni, M., Guerrieri, R., and Canegallo, R., *On road tire deformation measurement system using capacitive-resistive sensor*, IEEE Sensors, 2003., pp. 1059-1063.

[71] Magori, V., Magori, V.R, and Seitz, N., *On-line determination of tyre deformation, a novel sensor principle*, IEEE Proceedings of Ultrasonics Symposium, 1998., pp. 485-488.

[72] Schimetta, G., Dollinger, F., Scholl, G., and Weigel, R., *Wireless pressure and temperature measurement using SAW hybrid sensor*, IEEE Ultrasonics Symposium, 2000., pp. 445-448.

[73] Zhang, X., Wang, F., Wang, Z., Li, W., and He, D., *Intelligent tires based on wireless passive surface acoustic wave sensors*, IEEE Conference on Intelligent Transportation Systems, 2004., pp. 960-964.

[74] Pohl, A., and Seifert, F., *New applications of wirelessly interrogable passive SAW sensors*, IEEE Transactions on microwave theory and techniques, 1998., **46**12: pp. 2208-2212.

[75] Phol, A., *The "Intelligent Tire" utilizing passive SAW sensors - Measurement of tire friction*, IEEE Transactions of instrumentation and measurement, 1999., **48**6: pp. 1041-1046.

[76] Mooney, M., *A Theory of Large Elastic Deformation*, Journal of Applied Physics, 1940., **11**: pp. 582-592.

[77] Rivlin, R. S., *Large Elastic Deformations of Isotropic Materials*, Rheology Acta., 1983., **22**: pp. 160.

[78] *ABAQUS User Manual*, ABAQUS **VER. 6.7-1**, 2008.

[79] *www.en.wikipedia.org*, January, 2011.

[80] *Crossbow MoteView User's Manual* September, 2009.

[81] *www.weibull.com*, November, 2010.

[82] *Vehicle Dynamics Terminology*, Society of Automotive Engineers, SAE J670e, Warrendale, PA, 1978.

[83] Milliken, W. F. and Milliken, D. L., *Race Car Vehicle Dynamics*, SAE J670e, Warrendale, PA, 1995, pp. 39-40.

[84] *Tire Performance Terminology*, Society of Automotive Engineers, SAE J2047, Warrendale, PA, 1998.

[85] Gillespie, T. D., *Fundamentals of Vehicle Dynamics*, Society of Automotive Engineers, Warrendale, PA, 1992, pp. 351-360.

[86] Gough, V. F., Barson, C. W., Gough, S. W., and Bennett, W. D., *Tire Uniformity Grading Machine*, SAE 322A, Warrendale, PA, 1961.

[87] Pottinger, M. G.,*The Flat-Trac II®Machine, the State-of-the-Art in Tire Force and Moment Measurements*, Tire Science and Technology, 1992., **20**3: pp. 132-153.

[88] Pottinger, M. G., Tapia, G. A., Winkler, C. B., and Pelz, W., *A Straight-Line Braking Test for Truck Tires*, Rubber World, September 1996., pp. 2936.

[89] Pottinger, M. G., *Plysteer in Radial Carcass Tires*, Society of Automotive Engineers, SAE 760731, Warrendale, PA, 1976.

Appendices

Appendix A

ABAQUS FEA Code

Inflation analysis (2D axisymmetric model)

$*HEADING$
$*RESTART, WRITE, FREQ = 1$
$*NODE, NSET = TIRENODE, INPUT = TIRE_NODE.INP$
$*NODE, NSET = RIM$
$799, 0, 0, 0$
$*ELEMENT, TYPE = CGAX3, INPUT = TIRE_CGAX3.INP$
$*ELEMENT, TYPE = CGAX4RH, INPUT = TIRE_CGAX4RH.INP$
$*ELEMENT, TYPE = CGAX4R, INPUT = TIRE_CGAX4R.INP$
$*ELEMENT, TYPE = SFMGAX1, INPUT = SURF_ELEM.INP$
$*NSET, NSET = HUB$
$298, 297, 296, 295, 20, 294, 293, 292, 19, 51$
$221, 222, 223, 224, 12, 225, 226, 227, 13, 45$
$*ELSET, ELSET = CORDPLY, GENERATE$
$560, 598, 1$
$*ELSET, ELSET = STEELBELT, GENERATE$
$599, 637, 1$
$*ELSET, ELSET = MEM_CARCASS, GENERATE$
$638, 725, 1$
$*ELSET, ELSET = TREAD, GENERATE$
$1, 153, 1$
$291, 437, 1$
$*ELSET, ELSET = SW, GENERATE$
$154, 284, 1$
$*ELSET, ELSET = BEAD$
$285, 286, 287, 288, 289, 290, 438, 439, 440, 441$
$*ELSET, ELSET = IL, GENERATE$
$442, 559, 1$
$*ELSET, ELSET = CARCASS$
SW, IL
$*SURFACE, NAME = IP_IL$
IL
$**$
$*RIGIDBODY, TIENSET = HUB, REFNODE = RIM$
$**$
$**SECTION : TREAD$

$*SOLIDSECTION, ELSET = TREAD, MATERIAL = TREAD$
1.,
$**SECTION : SW$
$*SOLIDSECTION, ELSET = SW, MATERIAL = SIDEWALL$
1.,
$**SECTION : BEAD$
$*SOLIDSECTION, ELSET = BEAD, MATERIAL = BEAD$
1.,
$**SECTION : IL$
$*SOLIDSECTION, ELSET = IL, MATERIAL = UNDERTREAD$
1.,
$**SECTION : CORDPLY$
$*SURFACESECTION, ELSET = CORDPLY$
$*REBARLAYER$
$CP, 0.28, 1., , "CORDPLY", 70., 1$
$**SECTION : STEELBELT$
$*SURFACESECTION, ELSET = STEELBELT$
$*REBARLAYER$
$SB, 0.3, 1., , "STEELBELT", 118., 1$
$**SECTION : CARSCASS$
$*SURFACESECTION, ELSET = MEM_CARCASS$
$*REBARLAYER$
$CARCASS, 0.420835, 1., , CARCASS, 0., 1$
$*EMBEDDEDELEMENT, HOST = TREAD, ROUNDOFFTOL = 1.E-6$
$CORDPLY$
$*EMBEDDEDELEMENT, HOST = TREAD, ROUNDOFFTOL = 1.E-6$
$STEELBELT$
$*EMBEDDEDELEMENT, HOST = CARCASS, ROUNDOFFTOL = 1.E-6$
$MEM_CARCASS$
$**MATERIALS$
**
$*MATERIAL, NAME = BEAD$
$*HYPERELASTIC, MOONEY - RIVLIN$
$14.14, 21.26, 0.001412$
$*DENSITY$
1100000000000,
$*MATERIAL, NAME = "CORDPLY"$
$*ELASTIC, TYPE = ISO$
$3970., 0.3$
$*DENSITY$
1500000000000,
$*MATERIAL, NAME = SIDEWALL$
$*HYPERELASTIC, MOONEY - RIVLIN$
$0.1718, 0.8303, 0.0498$
$*DENSITY$

5900000000000,
$*MATERIAL, NAME = "STEELBELT"$
$*ELASTIC, TYPE = ISO$
200000., 0.3
$*DENSITY$
5900000000000,
$*MATERIAL, NAME = TREAD$
$*HYPERELASTIC, MOONEY - RIVLIN$
0.8061, 1.805, 0.0191
$*DENSITY$
1100000000000,
$*MATERIAL, NAME = UNDERTREAD$
$*HYPERELASTIC, MOONEY - RIVLIN$
V0.1404, 0.427, 0.0881
$*DENSITY$
1100000000000
$*MATERIAL, NAME = CARCASS$
$*ELASTIC, TYPE = ISO$
9870, 0.3
$*DENSITY$
1500000000000
**
$**----------$
$----------$
**
$**STEP : INFLATION$
**
$*STEP, NAME = INFLATION, NLGEOM = YES, INC = 10000$
$*STATIC$
.1, 1., .1, 1.
$*BOUNDARY$
RIM, 1, 2
RIM, 5, 6
**
$**LOADS$
**
$**NAME : INFLATIONTYPE : PRESSURE$
$*DSLOAD$
IP_IL, P, 0.2
**
$**OUTPUTREQUESTS$
**
$*RESTART, WRITE, FREQUENCY = 0$
**
$**FIELDOUTPUT : F - OUTPUT - 1$

**
$*OUTPUT, FIELD, VARIABLE = PRESELECT, FREQUENCY = 99999$
**
$**HISTORYOUTPUT : H - OUTPUT - 1$
**
$*OUTPUT, HISTORY, VARIABLE = PRESELECT, FREQUENCY = 99999$
$*ENDSTEP$
Normal load analysis (3d symmetric model generation)
$*HEADING$
$*NODE, NSET = ROAD$
$99999, 0, 0.252958298, -338.200012$
$*RESTART, WRITE, FREQ = 1$
$*SYMMETRICMODELGENERATION, REVOLVE, ELEMENT = 800, NODE = 800$
$0, 0, 0, 0, 1, 0$
$0, 0, 1$
$90, 3$
$70, 3$
$15, 7$
$10, 4$
$15, 7$
$70, 3$
$90, 3$
$*ELSET, ELSET = FOOT, GEN$
$5151, 18751, 800$
$5150, 18750, 800$
$5149, 18749, 800$
$5148, 18748, 800$
$5147, 18747, 800$
$5128, 18728, 800$
$5146, 18746, 800$
$5200, 18800, 800$
$5126, 18726, 800$
$5144, 18744, 800$
$5190, 18790, 800$
$5194, 18794, 800$
$5120, 18720, 800$
$5140, 18740, 800$
$5119, 18719, 800$
$5192, 18792, 800$
$5142, 18742, 800$
$5117, 18717, 800$
$5111, 18711, 800$
$5181, 18781, 800$
$5140, 18740, 800$

5107, 18707, 800
5110, 18710, 800
5183, 18783, 800
5135, 18735, 800
5182, 18782, 800
5136, 18736, 800
5137, 18737, 800
5138, 18738, 800
5204, 18804, 800
5233, 18833, 800
$*SURFACE, TYPE = CYLINDER, NAME = SROAD$
0, 0.252958298, −338.200012, 3, 0.252958298, −338.200012
0, 3.252958298, −338.200012
$START$, −1000, 0.252958298
$LINE$, 1000, 0.252958298
$*RIGIDBODY, REFNODE = ROAD, ANALYTICALSURFACE = SROAD$
$*SURFACE, NAME = STREAD$
$FOOT$
$*CONTACTPAIR, INTERACTION = SRIGID, TYPE = SURFACETOSURFACE$
$STREAD, SROAD$
$*SURFACEINTERACTION, NAME = SRIGID$
$*FRICTION$
0.0
$*NSET, NSET = FOOT, ELSET = FOOT$
$*NSET, NSET = PATH1, GENERATE$
5173, 19573, 800
$*NSET, NSET = PATH2, GENERATE$
5183, 19583, 800
$*NSET, NSET = PATH3, GENERATE$
5193, 19593, 800
$*NSET, NSET = PATH4, GENERATE$
5204, 19604, 800
$*FILEFORMAT, ZEROINCREMENT$
****
$*STEP, INC = 100, NLGEOM = YES$
$1 : INFLATION$
$*STATIC$
.25, 1, .25, 1
$*BOUNDARY$
RIM, 1, 6
$ROAD$, 1, 2
$ROAD$, 4, 6
$*DSLOAD$
IP_IL, P, 0.2
$*OUTPUT, FIELD, FREQUENCY = 1$

$*NODEPRINT, NSET = ROAD, FREQ = 1$
$U,$
$RF,$
$*ELPRINT, FREQ = 0$
$*OUTPUT, FIELD, FREQ = 1$
$*NODEOUTPUT$
$U,$
$*ELEMENTOUTPUT, POSITION = INTEGRATIONPOINTS$
$S,$
$LE,$
$*OUTPUT, HISTORY, FREQ = 1$
$*CONTACTOUTPUT, MASTER = SROAD, SLAVE = STREAD$
$CAREA,$
$*PRINT, SOLVE = YES$
$*ENDSTEP$
$**********$
$*STEP, INC = 100, NLGEOM = YES$
$2 : FOOTPRINT(Displacementcontrolled)$
$*STATIC$
$1e-9, 1, 1e-9,$
$*BOUNDARY, OP = NEW$
$RIM, 1, 6$
$ROAD, 1, 2$
$ROAD, 4, 6$
$ROAD, 3, , 2.5$
$*OUTPUT, FIELD, FREQ = 1$
$*NODEOUTPUT$
$U,$
$*OUTPUT, FIELD, FREQ = 1$
$*ELEMENTOUTPUT, POSITION = INTEGRATIONPOINTS$
$S,$
$LE,$
$*OUTPUT, HISTORY, FREQ = 1$
$*NODEOUTPUT, NSET = ROAD$
$U3, RF3$
$*CONTACTOUTPUT, MASTER = SROAD, SLAVE = STREAD$
$CAREA,$
$*print, solve = yes$
$*ENDSTEP$
$**********$
$*STEP, INC = 100, NLGEOM = YES$
$3 : FOOTPRINT(Displacementcontrolled)$
$*STATIC$
$1e-9, 1, 1e-9,$
$*BOUNDARY, OP = NEW$

$RIM, 1, 6$
$ROAD, 1, 2$
$ROAD, 4, 6$
$ROAD, 3, , 5.0$
$*OUTPUT, FIELD, FREQ = 1$
$*NODEOUTPUT$
$U,$
$*OUTPUT, FIELD, FREQ = 1$
$*ELEMENTOUTPUT, POSITION = INTEGRATIONPOINTS$
$S,$
$LE,$
$*OUTPUT, HISTORY, FREQ = 1$
$*NODEOUTPUT, NSET = ROAD$
$U3, RF3$
$*CONTACTOUTPUT, MASTER = SROAD, SLAVE = STREAD$
$CAREA,$
$*print, solve = yes$
$*ENDSTEP$
$**********$
$*STEP, INC = 100, NLGEOM = YES$
$4 : FOOTPRINT(Displacementcontrolled)$
$*STATIC$
$1e-9, 1, 1e-9,$
$*BOUNDARY, OP = NEW$
$RIM, 1, 6$
$ROAD, 1, 2$
$ROAD, 4, 6$
$ROAD, 3, , 7.5$
$*OUTPUT, FIELD, FREQ = 1$
$*NODEOUTPUT$
$U,$
$*OUTPUT, FIELD, FREQ = 1$
$*ELEMENTOUTPUT, POSITION = INTEGRATIONPOINTS$
$S,$
$LE,$
$*OUTPUT, HISTORY, FREQ = 1$
$*NODEOUTPUT, NSET = ROAD$
$U3, RF3$
$*CONTACTOUTPUT, MASTER = SROAD, SLAVE = STREAD$
$CAREA,$
$*print, solve = yes$
$*ENDSTEP$
$**********$
$*STEP, INC = 100, NLGEOM = YES$
$5 : FOOTPRINT(Displacementcontrolled)$

$*STATIC$
$1e-9, 1, 1e-9,$
$*BOUNDARY, OP = NEW$
$RIM, 1, 6$
$ROAD, 1, 2$
$ROAD, 4, 6$
$ROAD, 3, , 10.0$
$*OUTPUT, FIELD, FREQ = 1$
$*NODEOUTPUT$
$U,$
$*OUTPUT, FIELD, FREQ = 1$
$*ELEMENTOUTPUT, POSITION = INTEGRATIONPOINTS$
$S,$
$LE,$
$*OUTPUT, HISTORY, FREQ = 1$
$*NODEOUTPUT, NSET = ROAD$
$U3, RF3$
$*CONTACTOUTPUT, MASTER = SROAD, SLAVE = STREAD$
$CAREA,$
$*print, solve = yes$
$*ENDSTEP$
$**********$
$*STEP, INC = 100, NLGEOM = YES$
$6 : FOOTPRINT(Displacementcontrolled)$
$*STATIC$
$1e-9, 1, 1e-9,$
$*BOUNDARY, OP = NEW$
$RIM, 1, 6$
$ROAD, 1, 2$
$ROAD, 4, 6$
$ROAD, 3, , 12.5$
$*OUTPUT, FIELD, FREQ = 1$
$*NODEOUTPUT$
$U,$
$*OUTPUT, FIELD, FREQ = 1$
$*ELEMENTOUTPUT, POSITION = INTEGRATIONPOINTS$
$S,$
$LE,$
$*OUTPUT, HISTORY, FREQ = 1$
$*NODEOUTPUT, NSET = ROAD$
$U3, RF3$
$*CONTACTOUTPUT, MASTER = SROAD, SLAVE = STREAD$
$CAREA,$
$*print, solve = yes$
$*ENDSTEP$

$**********$
$*STEP, INC = 100, NLGEOM = YES$
$7 : FOOTPRINT(Displacementcontrolled)$
$*STATIC$
$1e-9, 1, 1e-9,$
$*BOUNDARY, OP = NEW$
$RIM, 1, 6$
$ROAD, 1, 2$
$ROAD, 4, 6$
$ROAD, 3, , 15.0$
$*OUTPUT, FIELD, FREQ = 1$
$*NODEOUTPUT$
$U,$
$*OUTPUT, FIELD, FREQ = 1$
$*ELEMENTOUTPUT, POSITION = INTEGRATIONPOINTS$
$S,$
$LE,$
$*OUTPUT, HISTORY, FREQ = 1$
$*NODEOUTPUT, NSET = ROAD$
$U3, RF3$
$*CONTACTOUTPUT, MASTER = SROAD, SLAVE = STREAD$
$CAREA,$
$*print, solve = yes$
$*ENDSTEP$
$**********$
$*STEP, INC = 100, NLGEOM = YES$
$8 : FOOTPRINT(Displacementcontrolled)$
$*STATIC$
$1e-9, 1, 1e-9,$
$*BOUNDARY, OP = NEW$
$RIM, 1, 6$
$ROAD, 1, 2$
$ROAD, 4, 6$
$ROAD, 3, , 17.5$
$*OUTPUT, FIELD, FREQ = 1$
$*NODEOUTPUT$
$U,$
$*OUTPUT, FIELD, FREQ = 1$
$*ELEMENTOUTPUT, POSITION = INTEGRATIONPOINTS$
$S,$
$LE,$
$*OUTPUT, HISTORY, FREQ = 1$
$*NODEOUTPUT, NSET = ROAD$
$U3, RF3$
$*CONTACTOUTPUT, MASTER = SROAD, SLAVE = STREAD$

$CAREA,$
$*print, solve = yes$
$*ENDSTEP$
$**********$
$*STEP, INC = 100, NLGEOM = YES$
$9 : FOOTPRINT(Displacementcontrolled)$
$*STATIC$
$1e-9, 1, 1e-9,$
$*BOUNDARY, OP = NEW$
$RIM, 1, 6$
$ROAD, 1, 2$
$ROAD, 4, 6$
$ROAD, 3, , 20.0$
$*OUTPUT, FIELD, FREQ = 1$
$*NODEOUTPUT$
$U,$
$*OUTPUT, FIELD, FREQ = 1$
$*ELEMENTOUTPUT, POSITION = INTEGRATIONPOINTS$
$S,$
$LE,$
$*OUTPUT, HISTORY, FREQ = 1$
$*NODEOUTPUT, NSET = ROAD$
$U3, RF3$
$*CONTACTOUTPUT, MASTER = SROAD, SLAVE = STREAD$
$CAREA,$
$*print, solve = yes$
$*ENDSTEP$
$**********$
Steady state analysis (braking and traction analysis)
$*HEADING$
$STEADY - STATEROLLINGANALYSISOFATIRE :$
$*RESTART, READ, STEP = 9, INC = 51$
$**********$
$*STEP, INC = 300, NLGEOM = YES, UNSYMM = YES$
$1 : STRAIGHTLINEROLLING(Fullbraking)$
$*STEADYSTATETRANSPORT$
$0.5, 1.0$
$*CHANGEFRICTION, INTERACTION = SRIGID$
$*FRICTION, SLIP = 0.017$
$.85$
$*TRANSPORTVELOCITY$
$TIRENODE, 8.0$
$*MOTION, TYPE = VELOCITY, TRANSLATION$
$TIRENODE, 1, , 2777.8$
$*NODEPRINT, FREQ = 1$

$*ELPRINT, FREQ = 1$
$*OUTPUT, FIELD, OP = NEW, FREQ = 1$
$*ELEMENTOUTPUT$
S, LE
$*NODEOUTPUT$
U, V, VR
$*OUTPUT, HISTORY, FREQ = 1$
$*NODEOUTPUT, NSET = RIM$
U, RF
$*NODEOUTPUT, NSET = ROAD$
U, RF
$*ENDSTEP$
$**********$
$*STEP, INC = 300, NLGEOM = YES, UNSYMM = YES$
$2 : STRAIGHTLINEROLLING(FULLTRACTION)$
$*STEADYSTATETRANSPORT$
$0.1, 1.0, , 0.1$
$*RESTART, WRITE, FREQ = 1$
$*TRANSPORTVELOCITY$
$TIRENODE, 9$
$*ENDSTEP$
$**********$
Steady state analysis (partial traction analysis)
$*HEADING$
$*RESTART, READ, STEP = 11, INC = 4, ENDSTEP, WRITE, FREQ = 1$
$*FILEFORMAT, ZEROINCREMENT$
$**********$
$*STEP, INC = 300, NLGEOM, UNSYMM = YES$
$1 : STRAIGHTLINEROLLING$
$*STEADYSTATETRANSPORT$
$1.0, 1.0,$
$*TRANSPORTVELOCITY$
$TIRENODE, 8.42$
$*ENDSTEP$
$**********$
$*STEP, INC = 300, NLGEOM, UNSYMM = YES$
$2 : STRAIGHTLINEROLLING(Partialtraction)$
$*STEADYSTATETRANSPORT$
$0.25, 1.0, , 0.25$
$*TRANSPORTVELOCITY$
$TIRENODE, 8.43$
$*ENDSTEP$
$**********$
Steady state analysis (free-rolling at various slip angles analysis)
$*HEADING$

$STEADY-STATEROLLINGANALYSISOFATIRE:$
$*RESTART, READ, STEP = 5, INC = 1, ENDSTEP, WRITE, FREQ = 1$
$*FILEFORMAT, ZEROINCREMENT$
$**********$
$*STEP, INC = 300, NLGEOM, UNSYMM = YES$
$1 : STRAIGHTLINEFREEROLLING$
$*STEADYSTATETRANSPORT$
$1.0, 1.0,$
$*TRANSPORTVELOCITY$
$TIRENODE, 8.4225$
$*ENDSTEP$
$**********$
$*STEP, INC = 10000, NLGEOM, UNSYMM = YES$
$2 : SLIP(6degrees)$
$*STEADYSTATETRANSPORT, LONGTERM$
$0.25, 1.0, ,$
$*MOTION, TYPE = VELOCITY, TRANSLATION$
$TIRENODE, 1, , 2762.5829$
$TIRENODE, 2, , 290.3591$
$*ENDSTEP$

Appendix B

Code for Fourier Analysis

$X_cord = [.263157895$
.315789474
.368421053
.421052632
.473684211
.526315789
.578947368
.631578947
.684210526
.736842105
.789473684
.842105263
$]; l = length(X_cord);$

$FFTProcedure$
$Sensor1$
$Samplingfrequency$
$Fs = 1024;$

$nfft = 1024;$
$F = [0 : Fs - 1] * (Fs/nfft);$

$figure(1)$
$subplot(211);$
$plot(X_cord, s0_1,' - ok', X_cord, s1_1,' - dk', X_cord, s2_1,' - sk', X_cord, s3_1,' - xk', X_cord, s4_1,$
$' - pk',' LineWidth', 4);$
$xlabel('\mathbf{Contactduration(sec)'); \mathbf{ylabel}('\mathbf{Hoopstrain}\epsilon'_{\theta\theta});$
$z = legend('Sensor1@0^oSA','Sensor1@1.5^oSA','Sensor1@3^oSA','Sensor1@4.5^oSA',$
$'Sensor1@6^oSA', 5);$
$set(z,'Interpreter','tex')$
$Xejw0_1 = fft(s0_1, nfft);$
$Xejw1_1 = fft(s1_1, nfft);$
$Xejw2_1 = fft(s2_1, nfft);$
$Xejw3_1 = fft(s3_1, nfft);$
$Xejw4_1 = fft(s4_1, nfft);$
$amplitudeextraction$

$FF = [F(3:7)];$
$Ampl_s1_0deg = [abs(Xejw0_1(2:6))];$
$Ampl_s1_1deg = [abs(Xejw1_1(2:6))];$
$Ampl_s1_2deg = [abs(Xejw2_1(2:6))];$
$Ampl_s1_3deg = [abs(Xejw3_1(2:6))];$
$Ampl_s1_4deg = [abs(Xejw4_1(2:6))];$
$subplot(212);$
$semilogx(F, abs(Xejw0_1), '-ok', F, abs(Xejw1_1), '-dk', F, abs(Xejw2_1), '-sk', F, abs(Xejw3_1),$
$'-xk', F, abs(Xejw4_1),$
$'-pk', 'LineWidth', 4);$
$xlabel('\mathbf{Frequency}'); \mathbf{ylabel}('\mathbf{Amplitude}'); \mathbf{axis}([\mathbf{0\ 5\ 1\ 2\ 0\ max}(\mathbf{Xejw0_1})]);$
$z = legend('Sensor1@0^oSA', 'Sensor1@1.5^oSA', 'Sensor1@3^oSA',$
$'Sensor1@4.5^oSA', 'Sensor1@6^oSA', 5);$
$set(z, 'Interpreter', 'tex')$
$subplot(313); holdon; boxon;$
$set(gca, 'XTick', 2:1:6)$
$set(gca, 'XTickLabel', '2', '3', '4', '5', '6')$
$stem(FF, Ampl_s1_0deg, 'r', 'LineWidth', 2); xlabel('\mathbf{Frequency}'); \mathbf{ylabel}$
$('\mathbf{Amplitude}');$
$stem(FF, Ampl_s1_1deg, 'g', 'LineWidth', 2);$
$stem(FF, Ampl_s1_2deg, 'b', 'LineWidth', 2);$
$stem(FF, Ampl_s1_3deg, 'c', 'LineWidth', 2);$
$stem(FF, Ampl_s1_4deg, 'k', 'LineWidth', 2);$
$z = legend('Sensor1@0^oSA', 'Sensor1@1.5^oSA', 'Sensor1@3^oSA',$
$'Sensor1@4.5^oSA', 'Sensor1@6^oSA', 5);$
$set(z, 'Interpreter', 'tex')$

Appendix C

Code for Weibull Curve Fiting

$$
\begin{aligned}
&\quad function createFit1(t, s0_1, s1_1, s2_1, s3_1, s4_1)\\
&f_{=}clf;\\
&figure(f_{)};\\
&set(f_{,}'Units',' Pixels',' Position', [445129688485]);\\
&legh_{=}[];\\
&legt_{=};\\
&xlim_{=}[Inf - Inf];\\
&ax_{=}axes;\\
&set(ax'Units',' normalized',' OuterPosition', [0011]);\\
&set(ax_{,}'Box',' on');\\
&axes(ax_{)};\\
&holdon;\\
&t = t(:);\\
&s0_1 = s0_1(:);\\
&h_{=}line(t, sm\_y1,' Parent', ax_{,}'Color',' r', ...\\
&'LineStyle',' none',' LineWidth', 1, ...\\
&'Marker',' .',' MarkerSize', 15);\\
&xlim_{(}1) = min(xlim_{(}1), min(t));\\
&xlim_{(}2) = max(xlim_{(}2), max(t));\\
&legh_{(}end + 1) = h_{,}\\
&legt_{end+1} =' FEMdata- > Sensor1@0SA';\\
&s1_1 = s1_1(:);\\
&h_{=}line(t, sm\_y2,' Parent', ax_{,}'Color',' g', ...\\
&'LineStyle',' none',' LineWidth', 1, ...\\
&'Marker',' .',' MarkerSize', 15);\\
&xlim_{(}1) = min(xlim_{(}1), min(t));\\
&xlim_{(}2) = max(xlim_{(}2), max(t));\\
&legh_{(}end + 1) = h_{,}\\
&legt_{end+1} =' FEMdata- > Sensor1@1.5SA';\\
&s2_1 = s2_1(:);\\
&h_{=}line(t, sm\_y3,' Parent', ax_{,}'Color',' b', ...\\
&'LineStyle',' none',' LineWidth', 1, ...\\
&'Marker',' .',' MarkerSize', 15);\\
&xlim_{(}1) = min(xlim_{(}1), min(t));\\
&xlim_{(}2) = max(xlim_{(}2), max(t));\\
&legh_{(}end + 1) = h_{,}
\end{aligned}
$$

$legt_{end+1} =' FEMdata- > Sensor1@3SA';$
$s3_1 = s3_1(:);$
$h_{=}line(t, sm.y4,' Parent', ax,'Color',' c', ...$
$'LineStyle',' none',' LineWidth', 1, ...$
$'Marker',' .',' MarkerSize', 15);$
$xlim_(1) = min(xlim_(1), min(t));$
$xlim_(2) = max(xlim_(2), max(t));$
$legh_(end + 1) = h_{;}$
$legt_{end+1} =' FEMdata- > Sensor1@4.5SA';$
$s4_1 = s4_1(:);$
$sm.y5 = smooth(t, s4_1, 5,' moving', 0);$
$h_{=}line(t, sm.y5,' Parent', ax,'Color',' k', ...$
$'LineStyle',' none',' LineWidth', 1, ...$
$'Marker',' .',' MarkerSize', 15);$
$xlim_(1) = min(xlim_(1), min(t));$
$xlim_(2) = max(xlim_(2), max(t));$
$legh_(end + 1) = h_{;}$
$legt_{end+1} =' FEMdata- > Sensor1@6SA';$
$if all(isfinite(xlim_))$
$xlim_{=}xlim_{+}[-11] * 0.01 * diff(xlim_);$
$set(ax,'XLim', xlim_)$
$else$
$set(ax,'XLim', [0.41684210568999996, 0.84631578930999996]);$
end
$ok_{=}isfinite(t)isfinite(sm.y1);$
$if\ all(ok_)$
$warning('GenerateMFile : IgnoringNansAndInfs',' IgnoringNaNsandInfsindata.');$
end
$st_{=}[0.505528006113628250.974681752559468540.52991989837207953];$
$ft_{=}fittype('(c/a)^(1/a) * (x/a)^(b/c - 1) * exp(-x/a)^(b)/c',' dependent','y',$
$'independent','x',' coefficients','a',' b',' c');$
$cf_{=}fit(t(ok_), sm.y1(ok_), ft,'Startpoint', st_);$
$h_{=}plot(cf,'fit', 0.95);$
$set(h_(1),' Color',' r',' LineStyle',' -',' LineWidth', 4,' Marker',' none',' MarkerSize', 6);$
$legendoff;$
$legh_(end + 1) = h_(1);$
$legt_{end+1} =' Weibullfit- > Sensor1@0SA';$
$ok_{=}isfinite(t)isfinite(sm.y2);$
$if\ all(ok_)$
$warning('GenerateMFile : IgnoringNansAndInfs', ...$
$'IgnoringNaNsandInfsindata.');$
end
$st_{=}[0.505528006113628250.974681752559468540.52991989837207953];$
$ft_{=}fittype('(c/a)^(1/a) * (x/a)^(b/c - 1) * exp(-x/a)^(b)/c',$
$'coefficients','a',' b',' c');$

$cf_{=}fit(t(ok_{)}, sm.y2(ok_{)}, ft_{,}'Startpoint', st_{)};$
$h_{=}plot(cf_{,}'fit', 0.95);$
$set(h_{(}1),' Color',' g',' LineStyle',' -',' LineWidth', 4,' Marker',' none',' MarkerSize', 6);$
$legendoff;$
$legh_{(}end + 1) = h_{(}1);$
$legt_{end+1} =' Weibull fit- > Sensor1@1.5SA';$
$ok_{=}isfinite(t)isfinite(sm.y3);$
$if\ all(ok_{)}$
$warning('GenerateMFile : IgnoringNansAndInfs',' IgnoringNaNsandInfsindata.');$
end
$st_{=}[0.505528006113628250.974681752559468540.52991989837207953];$
$ft_{=}fittype('(c/a)^(1/a) * (x/a)^(b/c - 1) * exp(-x/a)^(b)/c',' dependent','y',$
$'independent','x',' coefficients','a',' b',' c');$
$cf_{=}fit(t(ok_{)}, sm.y3(ok_{)}, ft_{,}'Startpoint', st_{)};$
$h_{=}plot(cf_{,}'fit', 0.95);$
$set(h_{(}1),' Color',' b',' LineStyle',' -',' LineWidth', 4,' Marker',' none',' MarkerSize', 6);$
$legendoff;$
$legh_{(}end + 1) = h_{(}1);$
$legt_{end+1} =' Weibull fit- > Sensor1@3SA';$
$ok_{=}isfinite(t)isfinite(sm.y4);$
$if\ all(ok_{)}$
$warning('GenerateMFile : IgnoringNansAndInfs',' IgnoringNaNsandInfsindata.');$
end
$st_{=}[0.505528006113628250.974681752559468540.52991989837207953];$
$ft_{=}fittype('(c/a)^(1/a) * (x/a)^(b/c - 1) * exp(-x/a)^(b)/c',' dependent','y',$
$'independent','x',' coefficients','a',' b',' c');$
$cf_{=}fit(t(ok_{)}, sm.y4(ok_{)}, ft_{,}'Startpoint', st_{)};$
$h_{=}plot(cf_{,}'fit', 0.95);$
$set(h_{(}1),' Color',' c',' LineStyle',' -',' LineWidth', 4,' Marker',' none',' MarkerSize', 6);$
$legendoff;$
$legh_{(}end + 1) = h_{(}1);$
$legt_{end+1} =' Weibull fit- > Sensor1@4.5SA';$
$ok_{=}isfinite(t)isfinite(sm.y5);$
$if\ all(ok_{)}$
$warning('GenerateMFile : IgnoringNansAndInfs',' IgnoringNaNsandInfsindata.');$
end
$st_{=}[0.505528006113628250.974681752559468540.52991989837207953];$
$ft_{=}fittype('(c/a)^(1/a) * (x/a)^(b/c - 1) * exp(-x/a)^(b)/c', ...$
$functioncreateFit1(t, s0_{1}, s1_{1}, s2_{1}, s3_{1}, s4_{1})$
$f_{=}clf;$
$figure(f_{)};$
$set(f_{,}'Units',' Pixels',' Position', [445129688485]);$
$legh_{=}[];$
$legt_{=};$
$xlim_{=}[Inf - Inf];$

$ax_{=}axes;$
$set(ax,'Units','normalized','OuterPosition',[0011]);$
$set(ax,'Box','on');$
$axes(ax_{)};$
$holdon;$
$t = t(:);$
$s0_1 = s0_1(:);$
$h_{=}line(t, sm.y1,'Parent', ax,'Color','r', ...$
$'LineStyle','none','LineWidth', 1, ...$
$'Marker','.','MarkerSize', 15);$
$xlim_{(}1) = min(xlim_{(}1), min(t));$
$xlim_{(}2) = max(xlim_{(}2), max(t));$
$legh_{(}end + 1) = h_{;}$
$legt_{end+1} =' FEMdata- > Sensor1@0SA';$
$s1_1 = s1_1(:);$
$h_{=}line(t, sm.y2,'Parent', ax,'Color','g', ...$
$'LineStyle','none','LineWidth', 1, ...$
$'Marker','.','MarkerSize', 15);$
$xlim_{(}1) = min(xlim_{(}1), min(t));$
$xlim_{(}2) = max(xlim_{(}2), max(t));$
$legh_{(}end + 1) = h_{;}$
$legt_{end+1} =' FEMdata- > Sensor1@1.5SA';$
$s2_1 = s2_1(:);$
$h_{=}line(t, sm.y3,'Parent', ax,'Color','b', ...$
$'LineStyle','none','LineWidth', 1, ...$
$'Marker','.','MarkerSize', 15);$
$xlim_{(}1) = min(xlim_{(}1), min(t));$
$xlim_{(}2) = max(xlim_{(}2), max(t));$
$legh_{(}end + 1) = h_{;}$
$legt_{end+1} =' FEMdata- > Sensor1@3SA';$
$s3_1 = s3_1(:);$
$h_{=}line(t, sm.y4,'Parent', ax,'Color','c', ...$
$'LineStyle','none','LineWidth', 1, ...$
$'Marker','.','MarkerSize', 15);$
$xlim_{(}1) = min(xlim_{(}1), min(t));$
$xlim_{(}2) = max(xlim_{(}2), max(t));$
$legh_{(}end + 1) = h_{;}$
$legt_{end+1} =' FEMdata- > Sensor1@4.5SA';$
$s4_1 = s4_1(:);$
$sm.y5 = smooth(t, s4_1, 5,'moving', 0);$
$h_{=}line(t, sm.y5,'Parent', ax,'Color','k', ...$
$'LineStyle','none','LineWidth', 1, ...$
$'Marker','.','MarkerSize', 15);$
$xlim_{(}1) = min(xlim_{(}1), min(t));$
$xlim_{(}2) = max(xlim_{(}2), max(t));$

$legh_(end+1) = h_;$
$legt_{end+1} =' FEMdata- > Sensor1@6SA';$
$ifall(isfinite(xlim_))$
$xlim_=xlim_+[-11] * 0.01 * diff(xlim_);$
$set(ax_,'XLim', xlim_)$
$else$
$set(ax_,'XLim', [0.41684210568999996, 0.84631578930999996]);$
end
$ok_=isfinite(t)isfinite(sm_y1);$
$if\ all(ok_)$
$warning('GenerateMFile : IgnoringNansAndInfs','IgnoringNaNsandInfsindata.');$
end
$st_=[0.505528006113628250.974681752559468540.52991989837207953];$
$ft_=fittype('(c/a)^1/a) * (x/a)^b/c - 1) * exp(-x/a)^b)/c','dependent','y',$
$'independent','x','coefficients','a','b','c');$
$cf_=fit(t(ok_), sm_y1(ok_), ft_,'Startpoint', st_);$
$h_=plot(cf_,'fit', 0.95);$
$set(h_(1),'Color','r','LineStyle','-','LineWidth', 4,'Marker','none','MarkerSize', 6);$
$legendoff;$
$legh_(end+1) = h_(1);$
$legt_{end+1} =' Weibullfit- > Sensor1@0SA';$
$ok_=isfinite(t)isfinite(sm_y2);$
$if\ all(ok_)$
$warning('GenerateMFile : IgnoringNansAndInfs', ...$
$'IgnoringNaNsandInfsindata.');$
end
$st_=[0.505528006113628250.974681752559468540.52991989837207953];$
$ft_=fittype('(c/a)^1/a) * (x/a)^b/c - 1) * exp(-x/a)^b)/c','coefficients','a','b','c');$
$cf_=fit(t(ok_), sm_y2(ok_), ft_,'Startpoint', st_);$
$h_=plot(cf_,'fit', 0.95);$
$set(h_(1),'Color','g','LineStyle','-','LineWidth', 4,'Marker','none','MarkerSize', 6);$
$legendoff;$
$legh_(end+1) = h_(1);$
$legt_{end+1} =' Weibullfit- > Sensor1@1.5SA';$
$ok_=isfinite(t)isfinite(sm_y3);$
$if\ all(ok_)$
$warning('GenerateMFile : IgnoringNansAndInfs','IgnoringNaNsandInfsindata.');$
end
$st_=[0.505528006113628250.974681752559468540.52991989837207953];$
$ft_=fittype('(c/a)^1/a) * (x/a)^b/c - 1) * exp(-x/a)^b)/c','dependent','y','independent','x'$
$cf_=fit(t(ok_), sm_y3(ok_), ft_,'Startpoint', st_);$
$h_=plot(cf_,'fit', 0.95);$
$set(h_(1),'Color','b','LineStyle','-','LineWidth', 4,'Marker','none','MarkerSize', 6);$
$legendoff;$
$legh_(end+1) = h_(1);$

$legt_{end+1} =' Weibullfit- > Sensor1@3SA';$
$ok_{=}isfinite(t)isfinite(sm.y4);$
$if\ all(ok_{)}$
$warning('GenerateMFile : IgnoringNansAndInfs','IgnoringNaNsandInfsindata.');$
end
$st_{=}[0.505528006113628250.974681752559468540.52991989837207953];$
$ft_{=}fittype('(c/a)^(1/a) * (x/a)^(b/c - 1) * exp(-x/a)^(b)/c','dependent','y','independent','x'$
$cf_{=}fit(t(ok_{)}, sm.y4(ok_{)}, ft_{,}'Startpoint', st_{)};$
$h_{=}plot(cf_{,}'fit', 0.95);$
$set(h_{(}1),'Color','c','LineStyle','-','LineWidth',4,'Marker','none','MarkerSize',6);$
$legendoff;$
$legh_{(}end + 1) = h_{(}1);$
$legt_{end+1} =' Weibullfit- > Sensor1@4.5SA';$
$ok_{=}isfinite(t)isfinite(sm.y5);$
$if\ all(ok_{)}$
$warning('GenerateMFile : IgnoringNansAndInfs','IgnoringNaNsandInfsindata.');$
end
$st_{=}[0.505528006113628250.974681752559468540.52991989837207953];$
$ft_{=}fittype('(c/a)^(1/a) * (x/a)^(b/c - 1) * exp(-x/a)^(b)/c', ...$
$'dependent','y','independent','x','coefficients','a','b','c');$
$cf_{=}fit(t(ok_{)}, sm.y5(ok_{)}, ft_{,}'Startpoint', st_{)};$
$h_{=}plot(cf_{,}'fit', 0.95);$
$set(h_{(}1),'Color','k', ...'LineStyle','-','LineWidth',4, ...'Marker','none','MarkerSize',6);$
$legendoff;$
$legh_{(}end + 1) = h_{(}1);$
$legt_{end+1} =' Weibullfit- > Sensor1@6SA';$
$holdoff;$
$leginfo_{=}'Orientation','vertical','Location','NorthEast';$
$h_{=}legend(ax_{,}legh_{,}legt_{,}leginfo_{)};$
$set(h_{,}'Interpreter','none');$
$xlabel(ax_{,}'');$
$ylabel(ax_{,}'');$
$'dependent','y','independent','x','coefficients','a','b','c');$
$cf_{=}fit(t(ok_{)}, sm.y5(ok_{)}, ft_{,}'Startpoint', st_{)};$
$h_{=}plot(cf_{,}'fit', 0.95);$
$set(h_{(}1),'Color','k', ...'LineStyle','-','LineWidth',4, ...'Marker','none','MarkerSize',6);$
$legendoff;$
$legh_{(}end + 1) = h_{(}1);$
$legt_{end+1} =' Weibullfit- > Sensor1@6SA';$
$holdoff;$
$leginfo_{=}'Orientation','vertical','Location','NorthEast';$
$h_{=}legend(ax_{,}legh_{,}legt_{,}leginfo_{)};$
$set(h_{,}'Interpreter','none');$
$xlabel(ax_{,}''); ylabel(ax_{,}'');$